Novel Integrated Approaches to Greenhouse Gas Sensing

MATTHEW S. RAHME

B.Sci (Hons), B.Com

THE UNIVERSITY OF
SYDNEY

Supervisor: Prof. Sergio Leon-Saval
Associate Supervisor: Dr. Christopher Betters

A thesis submitted in fulfilment of
the requirements for the degree of
Doctor of Philosophy

School of Physics, Faculty of Science
The University of Sydney
Australia

This research reported in this thesis was supported by the award of a Research Training Program scholarship to the PhD Candidate.

23 January 2025

Dedications

Dedicated to Said Rahme, Mary O'Brien, and Hellen Rahme. Whose memories of hard work, dedication, perseverance, and encouragement I hope to have done proud.

Quote

“Perplexity is the beginning of knowledge.”

— Khalil Gibran

Abstract

The effects of anthropogenic climate change pose a significant risk to both the environment and human property, with the most serious impact being the loss of human life. Even if greenhouse gas emissions are reduced in the near future, global temperatures are still expected to rise by at least $1.5\ ^{o}$C. Addressing this issue requires accurate monitoring of all contributing greenhouse gases, including trace gases such as methane and nitrous oxide, which are particularly challenging to detect due to their low concentrations. Studies increasingly suggest that human activities are releasing much more of these gases than previously estimated. Consequently, there is an urgent need for improved gas detectors that are both lightweight and portable, so that they are capable of monitoring large areas, yet maintain high levels of selectivity and sensitivity.

Absorption spectroscopy is a well-established technique that enables the precise detection and monitoring of specific gas species. Within this field, modulation spectroscopy offers pathways to sensitive, low-cost detection solutions. This thesis explores two distinct applications of modulation spectroscopy for "fingerprint" gas detection, that is highly sensitive and selective molecular species identification and monitoring. The first focuses on cross-correlation using a complex aperiodic fiber Bragg grating (FBG). This complex grating mimics the multiple absorption features of acetylene's P-band. For the first time, we demonstrate that complex FBGs can selectively identify different concentrations of a target gas species. Additionally, we show that the system maintains high selectivity even in the presence of overlapping absorption features from other gases. These findings are reinforced by simulated data, establishing the potential of this technique for selective gas detection.

The second part of the thesis investigates wavelength modulation spectroscopy through quartz-enhanced photoacoustic spectroscopy (QEPAS), a method that leverages the photoacoustic effect to detect low gas concentrations. QEPAS generates sound waves from the target gas using a modulated light source, with the sound amplitude correlating to the gas

concentration. A quartz tuning fork (QTF) is used to convert these sound waves into electrical signals, allowing the creation of small, highly sensitive detection units. In this thesis, we present the design and build of dedicated voltage amplifiers to enhance the piezoelectric signal from the QTF. In addition we also developed two custom-built QEPAS units made using 3D-printed materials, to test the amplifiers performance in direct methane detection. These chambers incorporate a chemical annealing process to provide a better material finish for use in gas detection. The 3D-printed detection units allow for a direct comparison of amplifier performance, and we demonstrate methane detection with a minimum detection limit of 6.4 ppm. The combination of custom-built chambers and amplifier design showcases a practical, customisable approach for sensitive gas detection.

Acknowledgements

When one sets off to war, one does not do so alone. You need your commanders giving direction, support staff keeping the wheels turning, the right equipment (or at least equipment that works *some* of the time), and the unwavering support of the home front. Embarking on a PhD journey, I argue, is little different. Both require strategy, perseverance, and the ability to charge headlong into challenges — often with questionable sanity. Success in either venture is only possible with a dedicated team and the occasional lucky break, preferably involving large supplies of tea.

Firstly, I would like to acknowledge the home front—my family and friends. My PhD journey began in March 2020, two weeks before COVID-19 reached the country, making an already treacherous path even harder. Yet, no matter what, you were there to support me and keep me moving towards completion. Graduation this year would mark three generations at this university, from my grandfather in 1950 to me in 2025. It has been a long road, but one worth travelling upon.

Mum and Dad, you played many roles, and I can never thank you enough for all you did, even just in regard to my PhD. You were my propaganda ministers (it did not matter what happened, you only ever had positive things to say about me), food supply officers, and constant sources of grounding. My siblings—Dan, Nick, Kate, and Peach (*woof*)—no matter how much you tried to piss me off, you were always in my corner, ready to be my frontline forces. Dan… enough said. Nick, I think 53 pairs of cowboy boots. I'll explain why when you're old enough. Kate, there will always be a chair for you to have dinner in the office — and what's more, I've removed the armrests so there's enough space. Peach, even though you constantly try to steal kisses, I'll make sure you get plenty of treats. I love you all.

As for my friends, there are too many wonderful people to thank all of you individually. Whether you were my coffee (*correct to tea), climbing, lunch, or drinking buddies, you ensured I always had something to look forward to.

James, Nick, and Kyle—my fellow comrades—thank you for sharing in moments fuelled by *Victory Gin* and the spirit of wanting to drive a tank through any barriers in my way. I may not know what is at the top of the fridge like all of you, but you were my manufacturers of good times, production lines of good bants, and magnates of support.

Alex, you were there from before the beginning right through to the end, and I look forward to more to come now that I finally have a degree in a *real* science.

Sarah, thank you for being there alongside me as I walked, ran, and maybe—just maybe—occasionally stumbled my way along this path.

DD, thank you for all your support and advice throughout everything. You were like a cattle prod—albeit a hell of a lot gentler. *Moo Moo.*

Chris, thank you for punching walls with me and constantly reminding me that sanity is overrated. You were in my corner like a saint with cybernetic ambitions… or was it Hadouken powers?

Ali, my longest-running friend still at uni—from when we literally stood rank and file together to now, where neither of us knows how to leave this place. Thank you for all the memories and advice. From your *interesting* questions to your deep insights over good meals, I truly appreciate it. I hope you and Lucy understand just how helpful your words and advice at crucial moments were—I will not forget them.

Ally, Erin, Maggie, and Bryce—sorry to betray you for physics, but thank you for all the moments: our regular catch-ups, friendship llamas, and COVID trivia nights. We all made it this far, and I can't wait to see what the next chapters bring us. Issy, thank you also for reminding me to be brave enough to take challenges head-on, even if it means copping one on the jaw every once in a while.

I cannot forget to mention my command HQ, office 325A, and, more importantly, everyone who shared in my ramblings and cursing as I trudged through the campaign that was this thesis. You were all incredibly supportive, and I look forward to more hot chocolates and hot pot with you. (Good luck to those still to submit)

However, the weapons of war do not run solely on stress and the tears of PhD students, even with an overabundance of both. So, thank you, Neil — my tea supply officer — for providing insight into the most crucial element that fuelled this thesis. In addition, thank you

for all your mentoring and guidance. I look forward to sharing more tea and whisky with you and Sonia.

As for my support staff, I want to thank Peter for helping me design and manufacture my *weapons of war*. Without your tireless help, the electronics for the QEPAS chapter would have functioned about as effectively as the Mark 14 torpedo. Instead, the amplifiers picked up a signal as effectively as the Type 95 redressed the problem of positive warship buoyancy. On this note I would also like to thank the mechanical workshop staff for their help in manufacturing parts for my experiments and providing invaluable design advice.

Finally, I extend my sincere gratitude to my supervisors, Prof. Sergio Leon-Saval and Dr. Chris Betters. Their guidance and support, in ways both seen and unseen, helped shape the course of this work. The completion of this thesis would not have been possible without their contributions, from facilitating access to essential resources to providing valuable feedback in key moments. I appreciate the time and effort they dedicated along the way, and I am truly grateful for their support and encouragement throughout this journey. Their insights and mentorship have played a part in shaping me into the scientist I am today, and for that, I am deeply appreciative.

Contents

List of Figures

List of Tables

CHAPTER 1

Introduction

Detecting trace gases with high sensitivity and selectivity has become increasingly important in various fields, particularly environmental monitoring. Spectroscopy, which investigates the interaction between light and matter, has played a critical role in this endeavour. Ever since the early pioneering work of Isaac Newton in the 17^{th} century and Joseph Fraunhofer's development of the spectroscope in the early 19^{th} century, the field has evolved into a powerful tool for identifying and quantifying substances in complex environments. Today, the demand for portable and efficient detectors is growing as they offer significant advantages in applications that require real-time monitoring in remote or challenging settings. The development of compact and lightweight spectroscopic devices presents an opportunity to improve the accessibility and accuracy of environmental assessments.

1.1 Need for Detectors

The 2019/2020 Australian bushfire season saw a devastating series of fires that tore through New South Wales and Victoria. These fires were the worst on record and led to the destruction of nearly 19 million hectares, equivalent to the entire area of the low countries in Europe [1]. The fires ravaged the country from September through February and directly resulted in the deaths of 35 people [2], and over a billion animals [3]. In addition to the loss of life these fires caused nearly $\$5$ billion in damage, not including the ongoing and future costs of health care and further environmental disasters [4].

Environmental disasters such as this, which occurred only months before the work on this thesis commenced, are predicted to become more common. The frequency and severity of

Australian bushfires are tied to several natural cycles including: El Nino, the Southern Annular Mode, and the Indian Ocean Dipole [5, 6]. However, studies have shown that there has been a general increase in the conditions that lead to devastating bushfire seasons, independent of these cycles, instead being attributed to the effects of anthropogenic climate change [7].

Bushfires are only one example of the increasing costs, both in lives and in property, of global warming. According to the Sixth Assessment Report of the Intergovernmental Panel on Climate Change (IPCC), global average temperatures are on track to reach an increase of 1.5^oC between 2030 and 2035, if current emission trends are not curtailed [8]. The report states that many ecosystems, such as coral reefs and low-lying coastal communities, are reaching the limits of their adaptability, and further increases to temperature will see unmitigated levels of irreversible damage.

The report emphasises the importance of the following decade in taking action to avert the most catastrophic outcomes. To remain within the stated 1.5^oC temperature rise, greenhouse gas emissions must be reduced by 43% by 2030. Carbon dioxide (CO_2) remains the largest contributor by volume, with atmospheric concentrations now at 410 ppm. However, carbon dioxide emissions are not the only ones that need to be curtailed, as trace greenhouse gases also present a growing threat. Although trace greenhouse gases exist at concentrations 2 to 6 orders of magnitude less than carbon dioxide, their combined potential contribution to anthropogenic warming is greater [9]. However, accurate monitoring of trace greenhouse gases emissions is more difficult due to their much lower concentrations.

The two largest trace gases by concentration are methane (CH_4) at 1.866 ppm, and nitrous oxide (NO_2) at 0.332 ppm [8]. Looking specifically at methane we can see why it poses great risk, despite its lower concentration. The radiative forcing, proportion of IR radiation absorbed, is 21 times greater (by mass) than carbon dioxide [10]. When atmospheric half-lives are considered, methane alone has a global warming potential 3.7 times larger than that of carbon dioxide [9]. However, despite the risk posed by methane, emission levels are not well understood. A specific study in British Columbia, Canada, combined LIDAR and ground emission data for methane and showed that emission levels were 1.6-2.2 times higher than

federal inventory estimates [11]. This is supported by isotope analysis which suggests that emission levels from human activity could be underestimated by up to 58% [12, 13].

To address the effect of methane and other trace greenhouse gases on anthropogenic climate change, accurate monitoring is required. Monitoring not only would allow for the contribution of these gases to be tracked, but it would also enable a better understanding of the release processes and mechanisms. Specifically, lightweight, low-cost detectors that are capable of low detection limits are required. For this thesis we look at two specific applications of absorption spectroscopy, with the aim of achieving highly sensitive, and selective "fingerprint" spectroscopic detection.

1.2 Absorption Spectroscopy

The science of spectroscopy owes much of its central place in optical physics to its ability to reveal details of the chemical composition and physical environment from the analysis of signals encoded with wavelength upon a beam of light. However, equipment required to perform accurate measurements can be cumbersome and expensive; producing a relatively large volume of data (spectra) that must be distilled to what are often only a select number of desired quantities (e.g. concentrations). To help address these issues, we specifically look to applications of absorption spectroscopy.

Absorption spectroscopy is a well-established approach for implementing gas detection. At its core, it relies on measuring the light that is absorbed by the target atoms or molecules in a sample. The wavelengths absorbed by a target molecule are determined through quantum effects. Each molecule has quantised energy states that it can occupy, and can only transition between these by gaining or losing discrete packets of energy that also match the differences in these levels. The electronic structure of each molecule is the largest determining factor in determining the energy at which these transitions occur and what transitions are allowed. Since the energy of a photon is tied to its wavelength through $E = hc/\lambda$, where h is Planck's constant, c is the speed of light, and λ is the wavelength, then the wavelengths that are absorbed by exciting these transitions will match. However, it is important to note that the

lineshape and exact wavelength at which these transitions occur will vary with other variables, including temperature, pressure, and interactions with other molecular species [14]. Since this thesis is interested in determining the concentration of gases, we will focus on the condition in which the target sample is comprised of mixed gases.

To determine the concentration of a target gas species, we correlate the intensity of absorbed light with the number of those target molecules in a sample. The nature of this correlation arises from the probability that any individual photon of a given wavelength will be absorbed by a gas sample. To do this, we can look at the interaction cross section of each molecule, which is the effective size of a molecule with regard to a photon. To quantify the amount of light absorbed we treat our sample as a series of slices, where each individual slice has no overlapping cross sections. To have this non-overlapping assumption, the slices must be thin enough that the absorption can be considered interdependent from other slices. For low concentrations, such as that of greenhouse trace gases, interferences between photons and molecules is low enough that the response is linear. The linear response of absorption (A) is expressed in the Beer-Lambert law:

$$\log\left(\frac{I_0}{I}\right) = A = \epsilon c l \tag{1.1}$$

Where ϵ is the extinction coefficient related to the cross-sectional absorption coefficient, c is the concentration, and l is the path length through which light travels through the sample [15]. This means that, at low concentrations, since c is directly proportional to A, which is important for concentration determination of gases in low amounts.

However, this introduces a few limitations. Firstly, if the concentration is low, then the relative proportion of absorbed light will also be low, making sensitive detection more difficult. To offset this and increase absorption, the magnitude of ϵ or l must be increased. Maximising ϵ can be achieved by careful selection of the light source used. It is dependent on the interaction probability for each energy transition in a molecule and is thus highly wavelength-dependent. However, the choice of target wavelength(s) is often limited. In order to achieve selective detection, two approaches can be taken. The first is to target an isolated absorption feature,

with no overlapping features from other gases. Here the chosen light source should not emit wavelengths that can be absorbed by other gases in the sample. i.e. Absorption linewidths should not overlap. The second approach is using a multivariate approach, monitoring multiple absorption features simultaneously. This method does allow for features to still be exploited, even when there is overlap from the optical features of other gases. However, this approach is not always desireable as it can increase the complexity of the setup, all else being equal between both approaches.

One of the largest constraints that determines which method can be used is the available light sources that are capable of targeting a chosen gas species. Different light sources are available for targeting different wavlengths, each with advantages and disadvantages. For example, distributed feedback (DFB) diode lasers provide excellent low-power light sources for remote sensing, however, their performance is limited at longer wavelengths and cannot exceed 3.5 μm [16]. To reach other absorption features at longer wavelengths, optical emitters, such as quantum cascade lasers (QCLs) and interband cascade lasers (ICLs), need to be used [17, 18], however, these are much larger, more expensive, and have higher power and temperature control requirements. Beyond wavelength selection, this leaves the path length as the only other variable that can increase absorption sensitivity. For longer range column detection, this may not be an issue. However, for miniaturised modules aimed at localised detection, this is constrained by the detector itself. To achieve long path lengths, other design considerations must be implemented, such as Herriott- and White-type multipass cells [19–21].

1.2.1 Direct Measurement

Perhaps the most intuitive method for measuring the absorption peak of a molecule is direct absorption (DA). As the name suggests, this technique involves passing a light source through the sample and measuring the transmitted intensity directly. According to the Beer-Lambert law ((1.1)), the absorption is determined by comparing the transmitted light intensity to the incident light intensity. This requires knowledge of both I_0, the initial intensity of the light, and I, the intensity after passing through the sample. This straightforward approach provides a direct measurement of absorbance, making it particularly suitable for systems

where the target molecule's concentration is sufficiently high to produce detectable changes in transmitted intensity. DA methods, therefore, lend themselves well to stand off/open path detection methods.

The most straightforward method to achieve this is using a fixed-wavelength approach. The wavelength of the light source is fixed, ideally, to the peak of the absorption feature being probed. The transmitted intensity is then measured directly after the light has passed through the gas sample. This can then be compared with the incident intensity to calculate the absorption; and there are several ways in which this can be monitored. Incident light can be measured through multiple means including the use of a 0% concentration reference cell to calibrate detection, or by splitting a portion of the beam through a reference cell [22].

Although the fixed-wavelength method offers a simple approach, it is the least sensitive. It cannot directly measure changes to the line-shape and shifts in the peak wavelength. As mentioned above, these are affected by multiple factors, including interactions with other gases, temperature, and pressure [14]. For this reason, many spectrometers use a scanned-wavelength approach. The setup is similar to that of fixed wavelength detection, though here the wavelength of the light source is scanned across the target absorption peak. Whilst this allows for monitoring of the absorption line-shape, this method also is still prone to noise from various sources. This includes, detector noise - thermal fluctuations, wavelength instability, electronic (both analogue and digital) [23] - as well as broadening effects (including Doppler and pressure boarding, both of which also can impact any spectral overlap) [24].

Despite strong demand arising from myriad applications across science and industry, widespread adoption of miniaturised gas sensors has been hampered by the inability to meet the twin demands of sensitivity and specificity. High sensitivity using DA methods demands large, expensive, and complex spectrometers; smaller devices generally require compromise and trade-offs that limit sensitivity [25].

1.2.2 Indirect Absorption

In contrast to DA methods that directly rely on measuring absorption of light attenuation, indirect absorption (IA) uses secondary features to determine the presence and concentration of chosen gases. Secondary features can include heat generation as used in photoacoustic spectroscopy (PAS, which will be expanded greatly in Chap. 4), refractive index changes as used in cavity ring-down Spectroscopy [26], and scattering as used in cavity enhanced absorption spectroscopy [27].

In contrast to DA methods that directly rely on measuring the attenuation of light, indirect absorption (IA) techniques use secondary effects arising from the absorption process to determine the presence and concentration of target gases. These secondary features can include heat generation, as exploited in photoacoustic spectroscopy (PAS, which will be expanded upon in Chap. 4), refractive index changes, as utilised in cavity ring-down spectroscopy (CRDS) [26], and scattering effects, as seen in cavity enhanced absorption spectroscopy (CEAS) [27].

Indirect methods are particularly well-suited to point detection, where measurements are confined to a small and localised region within the sample. In point detection, the interaction volume is typically well-controlled, such as within an acoustic cell (as in PAS) or an optical resonator (as in CRDS or CEAS), allowing for enhanced sensitivity to trace gases. By exploiting the secondary effects that scale with the absorption process, IA methods often achieve significantly improved signal-to-noise ratios (SNR) compared to DA techniques, making them ideal for detecting gases at very low concentrations.

The reliance on confined geometries and secondary effects gives IA techniques their characteristic sensitivity and robustness, but it also introduces greater complexity into the experimental setup. For example, PAS requires precise acoustic resonance tuning, and CRDS and CEAS depend on highly reflective mirrors to maintain long effective optical path lengths. Despite these challenges, the enhanced performance of IA methods has made them invaluable in applications where extreme sensitivity is required, such as environmental monitoring, medical diagnostics, and industrial process control.

1.2.3 Modulation Spectroscopy

An approach that can greatly enhance measurement sensitivity is the use of modulation spectroscopy [28, 29]. Here, instead of monitoring the signal directly, a distortion to the measured signal is observed, and absorption properties are inferred by changes over time to this distortion. There are multiple ways in which modulation spectroscopy can be performed, though, for the purposes of this thesis, we will cover the two used herein: Cross-correlation and wavelength modulation spectroscopy (WMS).

To increase the selectivity of a detector, an ideal approach is to monitor multiple absorption features simultaneously. By targeting many features, sensitivity can be increased while simultaneously the effects of non-target gas species can be minimised, with specificity dramatically enhanced by matching a more complete fingerprint unique to the desired chemical. Cross-correlation spectroscopy is one approach to achieve this and involves the direct comparison of spectral features with a known reference. One common method to perform cross-correlation is to use a custom filter that targets known absorption features. This filter is then modulated back and forth between these features to generate a differential signal. If there are other gases with overlapping features, then their impact is minimised as the overlap only affects a small portion of the filter.

For the second approach, WMS, a high-frequency modulation is applied to the centre wavelength of the incident light beam. The signal arising from the transmitted intensity is then demodulated through the use of lock-in amplification (LIA). In general, the differential response is monitored in the frequency domain. Within the frequency domain, multiple harmonics of the signal are produced. The most common and established method for implementing WMS is tunable diode laser spectroscopy (TDLS) [16, 30]. TDLS, as the name suggests, relies on a diode laser as the light source. Given that the output wavelength and power are easy to control through the diode's operating current, they provide a highly tuneable, relatively low-cost light source. Although, TDLS has been used to achieve highly sensitive detection [31–33], it is still bound by the limitations imposed by optical path length and detection requirements [16].

In this thesis, two distinct approaches to spectroscopic gas detection through integrated optical solutions are explored. The first focuses on a novel notch filter designed for cross-correlation spectroscopy, utilising a complex, aperiodic fibre Bragg grating. The second investigates WMS via quartz-enhanced photoacoustic spectroscopy (QEPAS), where advances in electronic signal processing and the flexibility of 3D printing are combined to develop methane monitoring detection units. These two approaches provide complementary perspectives for the advancement of portable gas detection technologies, balancing novel innovation with practical engineering solutions.

CHAPTER 2

Introduction to Complex Fibre Bragg Gratings

The following two chapters present a novel approach to cross-correlation spectroscopy through the use of a complex aperiodic fibre Bragg grating (FBG). Here, in this chapter, we outline the use of optical filter devices within spectroscopy and provide an outline as to their use in modulation spectroscopy. The following chapter will then describe the first customised complex FBG device designed to mimic the absorption bands of acetylene C_2H_2. An experimental methodology is then presented, outlining how this device can be used for spectroscopic measurements. Subsequent results provide a proof of concept; with these results being supported through simulations. Much of the content in these chapters has been adapted and expanded from the work published in the following paper:

M. Rahme et al., 'A new gas detection technique through cross-correlation with a complex aperiodic FBG', Scientific Reports **14**, Publisher: Nature Publishing Group, 9939 (2024)

2.1 Cross-Correlation Using Complex FBG devices

Optical cross-correlation (OCS) offers avenues to achieve fingerprint gas detection in compact devices. Rather than sensing by matching unknown sample data to library spectra by computer, this step is accomplished optically prior to the photosensor. In addition to enhanced fingerprint detection, it can also reduce the requirements on the volume of data collected while allowing for a simpler, more efficient device that can perform without loss of sensitivity. This can be accomplished by modulating the response of the spectral matched filter (conceptually, the location of the wavelength notches in the filter transmission profile). For spectroscopic measurement, such techniques are used to increase measurement sensitivity

over limits obtained by traditional DA methodologies by calibrating for and removing sources of background noise and variation [35].

Whilst OCS is a promising technique for gas detection, the key challenge regarding its implementation is the realisation of the spectral filter. The use of differential optical cross-correlation techniques have been demonstrated to great effect, specifically in a number of astronomical measurement settings. However, traditional spectroscopic data is taken using large, highly complex and costly instruments, such as echelle spectrographs [35], which cannot be utilised in smaller devices. Simpler solutions to this problem were explored decades ago [36, 37]; however, again these devices were still too complex and costly to develop into general-purpose gas detectors.

More recently, interest has grown in this field as other potential solutions have become more viable. A system employing a notch filter has been modelled by *Cheriton et al* [38], who demonstrated recovery of the IR spectrum of Venus. Various groups have independently pursued architectures to deliver improved sensors based on the ability of FBGs to create complex wavelength-selective filters, including the work of *Tuthill* [39] and *Sivanadam et al.* [35]. However, prior to the work presented here, a major challenge has been in the fabrication of the required bespoke tailored filters to exactly match the spectral response of target molecules.

Many optical techniques and configurations to generate the complex featured wavelength response have been trialled. Varying levels of success have been demonstrated by approaches ranging from multi-wavelength gratings, Lyot filters [40], Fabry-Perot cavities [38, 41] and Michelson interferometry [42]. Of particular note are filters generated from silicon waveguides [43] and ring resonators [44, 45], which produce periodic filters with the ability to shift wavelength features. A key feature of almost all these approaches is that, to keep the optical setup relatively simple, the wavelength response of the filter produced typically results in regularly spaced notches at a repeating cadence dictated by the physics of the optical apparatus. Whilst these types of filters can be effective over limited ranges for chemicals with pseudo-periodic absorption features, they lack the fingerprint sensitivity and flexibility of aperiodic optical devices that can cover more absorption features. The match

they provide with the true molecular response is limited in both precision and wavelength extent. What is required is the capability of producing photonic molecules that exactly match complex aperiodic features over wide spectral ranges; a capability that FBGs stand ready to deliver. Aperiodic FBGs with customised transmission notches to match molecular absorption features make an ideal matched-filter for use in an optical gas detection sensor based on cross-correlation methods [46].

In general, FBGs have found widespread application across science and industry since their invention nearly a half-century ago. Their optical response is highly sensitive to both strain and temperature, making them ideal for use to sense changes in environment in many contexts. In addition to their high sensitivity, they are also largely immune to high voltage electrical fields, favouring their deployment in conditions where traditional electronic sensors would fail [47]. From material strain monitoring to sonar, FBGs have already been demonstrated to be extremely versatile and cost-effective solutions [48–51]. Of recent interest is their growing use in chemical monitoring, where they offer low-cost, compact, yet highly sensitive options in the development of new gas detectors [48, 51, 52].

Our method of creating an optical template with which to perform this match employs a FBG fabricated to encode multiple aperiodic Bragg wavelengths [53]. This FBG has been customised so that its Bragg wavelengths provide an excellent match the absorption bands of the target gas. In other words, our custom FBG acts as a "photonic molecule" engraved in glass fibre: an optical facsimile capable of exactly mimicking the spectral features of the target gas species over the wavelength range of interest.

However, the writing and demonstration of customised FBGs with the desired characteristics is not without precedent. Such devices, fabricated to reproduce (in absorption) atmospheric molecular emission lines, have shown promising results and the potential to offer new capabilities in the field of Astrophotonics [54]. This use of complex aperiodic FBGs, configured as an optical filter in the near-infrared region of the spectrum, have been deployed to reject specific molecular emission lines. The sum total of many (of order a $\sim \mathcal{O}(100)$) bright but narrow lines occurring at quasi-regular intervals combine to contaminate a spectral window important to ground-based astronomy. This near-infrared bright sky background problem

[55] is predominantly caused by the relaxation of hydroxyl (OH) molecule's rotational and vibration modes in the upper atmosphere. Widely regarded as one of the intractable problems plaguing ground-based infrared astronomy for decades, this bright and highly variable telluric emission has presented a significant barrier in studying faint astronomical objects with important signatures in the near-infrared, from galaxies to exoplanets.

Spectrographs that incorporate bespoke FBGs that suppress the problematic OH lines are now being developed; specifically, the GNOSIS [56] and later PRAXIS [57] instruments both deploy customised FBGs capable of suppression of more than 100 OH emission lines simultaneously. Configured as optical notch filters, they reject unwanted background radiation in reflection, transmitting only clean interline regions of the spectrum through to the science detector. GNOSIS demonstrated that the targeted OH lines could be suppressed by 30 dB, improving the interline background by a factor of 4. PRAXIS was further able to improve the signal to noise ratio (SNR) in the interline regions between the targeted lines by up to a factor of 17. Although these devices did not involve the direct detection of any gases, they pioneered the fabrication of FBGs that could be written to replicate any given spectral fingerprint. Building upon this foundation, these same design and fabrication technologies for the creation of custom FBG devices are carried over to a new application: an active sensor of novel architecture purposed for gas sensing and analysis.

Another advantage of employing complex FBGs for OCS is that their modest physical footprint makes it straightforward to operate several or many in parallel, scaling up the possibilities so that multiple FBGs can be incorporated into a single device. For example, an architecture which also incorporates photonic lanterns – fibre devices that enable the coupling of multimode fibres to multiple single mode fibres [58] – would be one way to upscale the capabilities of a sensor. Based on these technologies, devices could embody several or many complex FBGs implemented in "multiline" gas detectors [59] that operate in parallel so that the eventual specificity and complexity of possible filter combinations is almost unlimited. In addition, the use of lanterns enables the strictly single-moded technology of complex FBGs to be used in a setting where light collection by means of multimode fibres is desired, for example, better coupling for light collection.

2.2 Theory

Cross-correlation spectroscopy is usually performed by translating a template filter across spectral features of interest. For simplicity, we might envisage the filter to consist of multiple notches, each tailored to target corresponding molecular features. As the filter is scanned through the wavelength regime, its varying overlap with spectral features from the molecular structure means that the transmitted intensity will be modulated. Using the model presented by *Sivanandam et al* [35] the transmitted intensity for a given spectral feature can be expressed as:

$$C(v) = S(\lambda)T(\lambda) \tag{2.1}$$

Where T is the transmission profile of the notch filter, S is the spectrum of the target object, C is the observed cross-correlation lag. Here $v = \Delta\lambda/\lambda_0 \times c$ where $\Delta\lambda$ is the offset from the rest wavelength and λ_0 is the wavelength that corresponds to the spectral feature in question. Overall, the transmitted intensity will be maximised when the notch filter is most closely aligned with the series of corresponding molecular spectral features that it was designed to mimic. When using an FBG, we have the advantage of having a well-defined transmitted and reflected signal. Therefore, at the same location one obtains maximum transmission, we will witness a minimum in the reflected signal: that is, when the filter and the spectral features are aligned. Hence, the sensor should ideally be constructed so as to monitor both transmitted and reflected ports of the FBG, where an intensity maximum and minimum, respectively would then be expected as the filter passes through alignment with the molecular spectrum.

To achieve this OCS, all the structures in the template filter must be modulated simultaneously. Two possible methods to accomplish this suggest themselves: varying the temperature or the tension of a complex FBG can produce the required modulation. This is because the Bragg wavelength (λ_B) of an FBG is affected by both temperature and applied strain by an amount ($\Delta\lambda_B$) that can be expressed as:

$$\frac{\Delta\lambda_B}{\lambda_B} = (\alpha_s + \alpha_e)\Delta T + (1 - p_e)\epsilon \tag{2.2}$$

where α_s is the thermal expansion coefficient, α_e the thermo-optic coefficient, ΔT the temperature change, p_e the effective strain and ϵ the strain [60]. If we adopt strain as our primary method of tuning the grating (so that the temperature is kept stable, i.e. $\Delta T = 0$) then Eqn. 2.2 simplifies to:

$$\Delta\lambda_B = (1 - p_e)\epsilon\lambda_B \tag{2.3}$$

This equation quantifies the relationship between varying the strain applied to the FBG and the resulting modulated response in the Bragg wavelengths. Because the change occurs simultaneously for all Bragg wavelengths, this mechanism can be used to perform cross-correlation gas measurements over all of the features written in our complex FBG.

In the following chapter, we present the first complex FBG written to mimic the absorption profile of a target gas using a novel writing technique [39]; specifically, the P-band absorption lines of acetylene (C_2H_2) have been used for the purposes of this demonstration. Furthermore, an apparatus constructed around this grating that delivers gas detection using cross-correlation techniques is described. A successful demonstration of the apparatus and the methods delivered data capable of determining the relative concentration of gases contained in various standard cells, utilising a fixed light source. Furthermore, we explore the impact of contaminant gases, comparing our experimental results with simulation. As shown in the following sections, these results together constitute a significant step toward an architecture for the deployment of FBGs as low-cost, compact photonic devices for gas detection with high sensitivity and specificity.

CHAPTER 3

Fibre Bragg Grating Gas Sensor Testbed and Analysis

3.1 Experimental Methods

3.1.1 Novel Grating Structure

Gratings in fibres are made by imprinting a section of varying refractive index that is specifically tailored to the desired Bragg wavelength(s). The technology for writing gratings into fibres is mature and involves generating an interference pattern in UV light. Sufficiently intense UV light incident on the glass generates a slight change in refractive index. Various methods to produce the desired interference pattern are well established and can involve: interferometric, phase mask, and point-by-point methods [61]. Whilst these techniques have been used to write single-wavelength FBGs for decades, aperiodic gratings with multiple Bragg wavelengths are significantly more complex. Here we utilise a design process that treats all N channels simultaneously (as employed for the GNOSIS spectrograph; a detailed description is contained in *Bland-Hawthorn et al* [54]).

To fabricate the aperiodic multi-notch FBG with complex kappa (κ) amplitude and phase design, a versatile interferometry-based inscription setup using a Sagnac interferometer and acousto-optic modulators (AOMs) was used. The aperiodic complex FBG period and index modulation intensity (κ) design can be seen in Fig. 3.1 a). In our system, the laser used is the Innova FreD (Frequency-Doubled) ion laser from Coherent, generating 244 nm continuous-wave laser light. The phase mask generates a diffraction pattern, and its $\pm 1^{st}$ order forms a Sagnac loop. The phase of each beam inside the loop is modulated by two AOMs individually. The resultant index modulation can be tuned independently by both

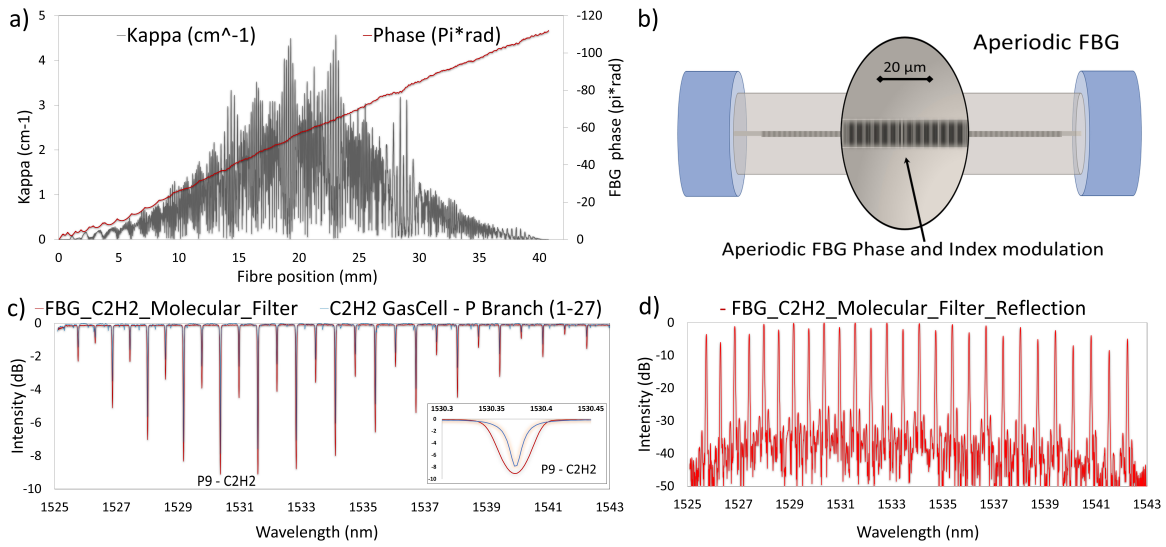

FIGURE 3.1: a) Custom design of the aperiodic FBG as represented by amplitude (κ) and phase (θ) along the axis of the fibre. b) Schematic representation of the index modulation and phase variation in the core of a complex aperiodic FBG optical fiber. c) Comparison of the complex FBG transmission response (red) with the p-band absorption features of C_2H_2 (black) which it was designed to mimic. d) Reflection spectrum of the complex FBG filter.

period and magnitude (as shown schematically in Fig. 3.1 b)). This enables the ability to detune the central wavelength, which allows inscription of complex structure into the fibre core [62]. The resultant transmission and reflection spectra can be seen in Fig. 3.1 c) and d), respectively. The grating was written to mimic the absorption features of the P branch of C_2H_2 and the strong overlap can be seen in the insert of Fig. 3.1 c) with all major features aligned. To the best of our knowledge this constitutes the first such device reported in the open literature.

3.1.2 Optical Testbed and Data Analysis

A fibre-coupled benchtop Superluminescent Diode (SLD; ThorLabs model S5FC1005P with centre $\lambda = 1550$ nm, bandwidth = 50 nm, power = 22 mW, $T = 22.5$ ^{o}C) was used as the light source for the experiment. The SLD was coupled to a calibrated reference gas cell or to multiple cells in series. The light was then passed through the complex FBG, which was placed on a large copper block connected to a heater and kept at a constant temperature of

($T = 24.5 \pm 0.1$ °C) for all experiments. A photodetector was used to monitor transmitted light while an optical circulator enabled a second detector to simultaneously monitor the reflected signal. The detector outputs were recorded using the data logger function on a Moku-Pro precision oscilloscope (50 000 samples/s). The aperiodic FBG was secured in place, clamped at each end. One clamp was attached to a linear translation stage moving under computer control with a 25 mm actuator. The applied strain was measured using a scale (calibrated in grams) attached to the stage. This setup can be seen in Fig. 3.2.

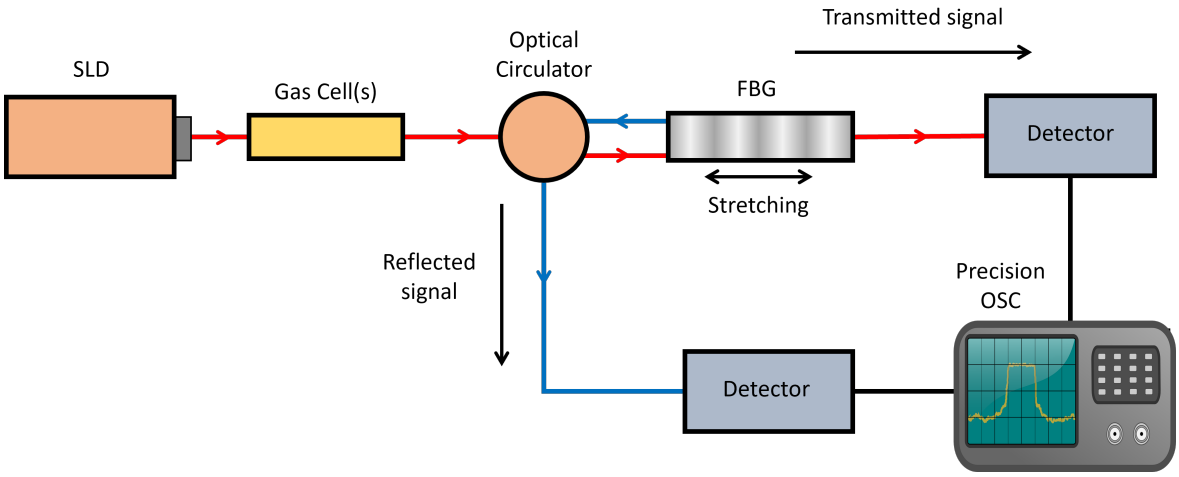

FIGURE 3.2: Schematic of the experimental setup. Transmitted (red) and reflected (blue) light paths are shown. The fibre is stretched using clamps and a motor to precisely control the strain.

Motor retractions increased tension on the complex FBG structure, resulting in the grating wavelength response shifting longwards, as expected from Eqn. 2.3. Fig. 3.3 a) shows the shift of a single peak to longer wavelengths as the tension is increased. A change in tension will shift all of the Bragg wavelengths. The exact shift will vary slightly for each peak, being dependant on the design of the device, temperature variability, and how evenly the strain is applied. However, the variation between peaks is negligible compared to the overall shift, as will be highlighted later.

Following from this, modulating the motor position allowed all Bragg wavelengths to periodically cycle in and out of alignment with the absorption peaks of the P band of C_2H_2. Examining the total reflected intensity then enabled this effect to be carefully monitored. As

seen in Fig. 3.3 b), when tuned so that the peaks coincide, the intensity of reflected light decreases, as expected.

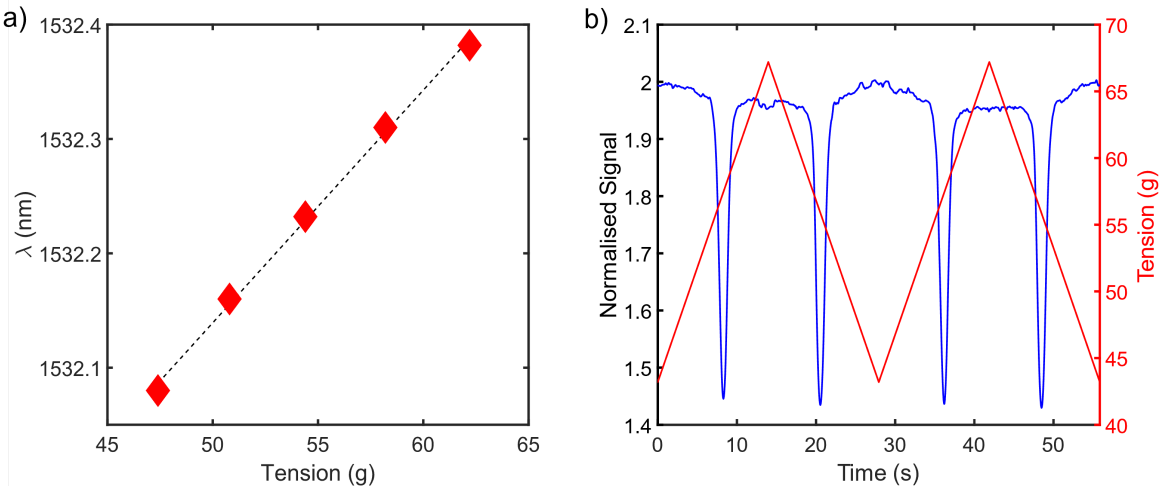

FIGURE 3.3: a) The wavelength of a single peak from the complex FBG spectrum as a product of applied strain. The observed shift exhibits a direct proportionality to the applied strain, underscoring a consistent correlation between the strain and the wavelength alteration. d) Example trace using a single C_2H_2 gas cell showing the intensity of reflected light (blue) as the tension applied (red) to the FBG is modulated. This shows the total intensity of reflected light as stretching occurs.

To characterise the optical response of different C_2H_2 concentrations, standard calibrated gas reference cells were employed. Three fibre-coupled cells of increasing $^{12}C_2H_2$ concentration were used: NIST SRM2517a (6.7 kPa, 5.5 cm path length), the output reference from the ANDO AQ6317B spectrum analyser, and NIST SRM2517a (6.7 kPa, 3 cm path length). For ease of reference, the NIST SRM2517a will be labelled as the testbed reference, since simulations were performed using the spectrum from this cell. The other two cells will be referred to as reduced cells 1 and 2 respectively. Gas cells of ^{12}CO (Wavelength References CO-12-200, 26.7 kPa), and $H^{13}C^{14}N$ (NIST SRM2519, 13.3 kPa, 5.5 cm path length) were also employed to test the effect of contaminant gases. When multiple gases were tested simultaneously, cells were concatenated in series allowing the accumulated spectra to emulate mixed chemical environments.

The positions of each peak were tracked with custom software (written in MATLAB), wherein a Gaussian profile was fitted to each to obtain the intensity. To account for different coupling

losses between each cell, the signal was normalised to a baseline level defined to occur between each second peak. Peaks were analysed two at a time to account for the background asymmetry that arises from the hysteresis observed with motor direction. This asymmetry is noticeable in Fig. 3.4, where differences in the baseline are clearly seen, though there is strong overlap in the peak positions between the two.

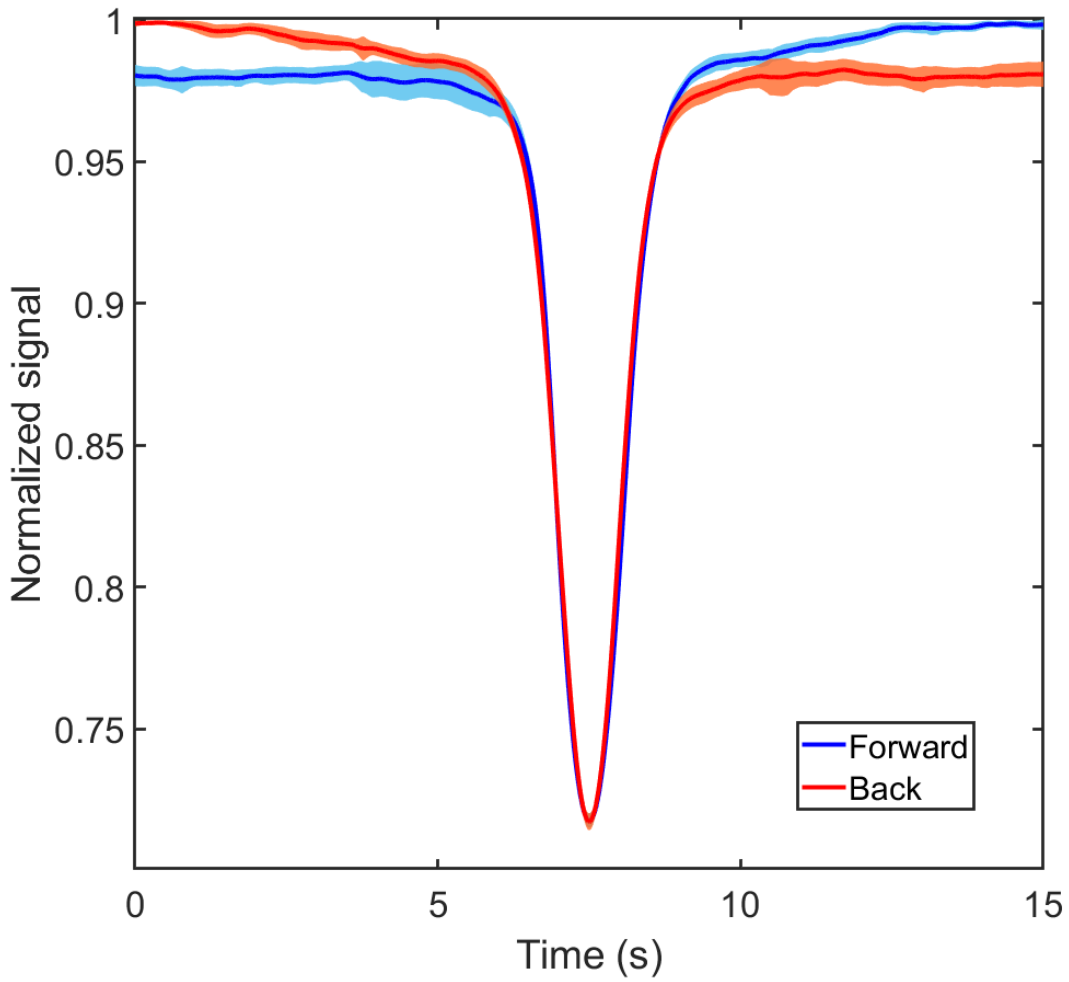

FIGURE 3.4: Example traces of the two different directions of the motor showing the asymmetry in the baseline. These are the average, with the standard deviation shown as the shaded region.

As noted above, both the transmitted signal and the reflected signal can be used to obtain the final output: the gas concentration. However, the reflected signal had a higher signal-to-noise ratio (SNR), so it was used for the measurements in this study. To obtain a measure of

concentration using this reflected signal, the difference between the baseline and the fitted location of each minima was used: a greater magnitude indicated a higher gas concentration.

3.1.3 Simulating the Effect of Contaminant Gases

The impact of unwanted gases in a mixed environment together with the target species by comparing the reflection spectra of the FBG to C_2H_2 in the presence of CO and HCN. Designating these latter two as "interlopers", for this section the combined optical effects of all gases was projected from measured data on each individually using MATLAB code. Both absorption and FBG spectra were converted from dB to a linear scale to match the measured voltage scale used above and kept as simple vector arrays. Only a segment of the full absorption spectra obtained for C_2H_2 was used (1525.5 - 1540 nm). A corresponding segment was also taken from the FBG spectrum with an offset applied to the index arrays. The offset was increased, while the wavelength vector was not changed, to simulate a strain-induced shift in the Bragg grating response.

For a given offset, the molecular absorption array was multiplied by its corresponding value in the FBG template array, and this new array was summed. This summed value can then be used as a metric for the total light reflected by the FBG array. The results were then normalised using the same method as described above for the measured data. This procedure was then repeated after adding the absorption spectra of interlopers HCN or CO to that of C_2H_2. A weighting factor was also applied to account for coupling losses in the experimental segment of this study. The weighting factor was determined by measuring the direct output loss of each component.

3.2 Results and Discussion

In this section, we outline the use of the FBG to sense different concentrations using standard gas cells and to test the impact of contaminant gases. The presence of the target gas C_2H_2 was probed by modulating the applied tension to the custom FBG.

3.2.1 Differing Concentrations

Recall from the above that when the Bragg wavelengths align with the p-band C_2H_2 absorption, a minimum in reflected intensity occurs. Establishing the relative concentration of each gas cell can be done by measuring the magnitude of each minima after normalisation. As the concentration of the C_2H_2 was increased a positive trend was observed in the magnitude of the measured dip. This clear trend is seen in Fig. 3.5, with the most concentrated cells producing a stronger drop in the reflected signal when the customised FBG and molecular absorption features are in tune.

We also noticed variation in the signal recorded, most notably in the baseline. To account for this, we recorded 43 sweeps over a 10 minute window, repeating for each gas cell configuration and combination. In Fig. 3.5 we show the average (solid lines) and standard deviation (shaded region) for each configuration. In an initial comparison of sweeps, an asymmetry was observed between alternating sweeps (as shown above), attributable to differences in motor direction. Consequently, to calculate the average and standard deviation, only one motor direction was used. However, it is pertinent to mention that this variation is unlikely to arise from motor control. The 25 mm actuator has a resolution of 40 nm and a minimum step size of 50 nm. The minimum step in the wavelength of the grating can be deduced by taking into account two factors: firstly, the tension shift is 24 g/mm, and secondly, based on regression analysis performed on the data presented in Fig. 3.3 a), the wavelength shift amounts to 20.4 nm/pg. Given the linear nature of all responses, a minimum step size of 153 fm is derived. As this value significantly falls below the detection limit of the utilised equipment, it is unlikely to contribute to any observed variation.

Overall while there was notable variability in the level of the baseline signal (regions where the filter is detuned), there was little deviation in the magnitude of each minima ($< 3\%$ for all measured configurations). Furthermore, this stability indicates that any variation in the shift of individual Bragg wavelengths is minimal when compared with the overall shift of the grating, as expected. Since the magnitude of the minima is the primary key to determination

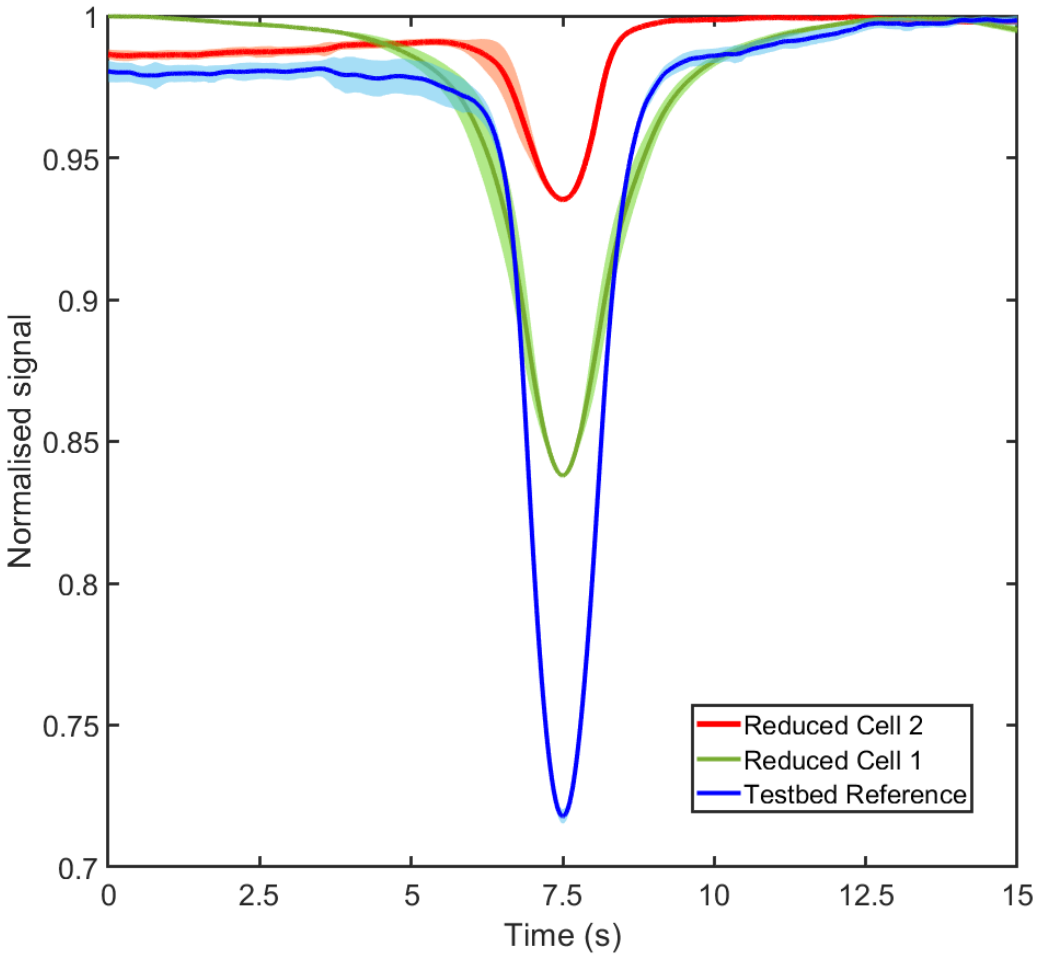

FIGURE 3.5: Averaged and normalised sweeps for three different gas cell concentrations of C_2H_2. Increasing concentration correlates with lower minima for each gas chamber.

of gas concentration, the low variability in the measured data is encouraging for the eventual translation of this technology to a calibrated sensor.

3.2.2 Impact of Other Gases

C_2H_2 was chosen for this study as it is an ideal test molecule with strong pseudo-periodic absorption features over a wavelength range convenient for our optical fibre technologies. It

is also a common standard for optical calibration, so that a range of calibrated chambers are readily available for testing.

Establishing a clear trend between concentration and intensity of the reflected light from the FBG constitutes a significant step toward establishing the basis of such devices in gas detection. However, chemical monitoring is almost always performed in impure, mixed gas environments. We, therefore, tested the capabilities of our custom FBG template to operate in such conditions using CO and HCN as 'contaminant' gases. As before, multiple sweeps of the OCS apparatus were averaged and combined to produce our data plots. These tests were first performed individually with single gas cells in isolation, and later cells were grouped in series together with the highest concentration C_2H_2 cell.

Turning first to signals arising from CO alone, no clear peaks were observed over the range scanned. This indicates that we should expect minimal impact from CO as an interloper species. Indeed, we see from Fig. 3.6 a) that there is no overlap in absorption features between C_2H_2 and those of CO in the region of interest, making it an ideal control gas. The sweeps performed with only C_2H_2 returned a minima at 0.732 ± 0.003, which was within error of the sweeps with both CO and C_2H_2 which returned a minima of 0.741 ± 0.010. This can be visually seen in Fig. 3.7 a), with strong overlap between the average traces for these gas setups. This measurement also provided a validation of the simulation, which indicated a difference of less than 0.1% between a pure and mixed environment, which is well within the error of the measured results. In summary, we anticipated minimal impact from CO, and our results did not show detectable influence.

Next, we turn to HCN which presents a far more challenging case for our sensor as this contaminant gas is expected to have some impact on the measured concentrations of the target. The R and P absorption branches of HCN overlap with the P branches of C_2H_2, and as a consequence, they also overlap with our template FBG. This can be clearly seen in Fig. 3.6 c): some features overlap almost directly while a significant number lie between those of C_2H_2. It is also important to note that the linewidth of individual peaks created by the FBG template is larger than that of the target gases. Therefore, the potential for confusion and unwanted signals generated by this interloper species is somewhat under-represented by

simple comparison of the spectra at their native molecular linewidths, as in Fig. 3.6 c). For all these reasons, disentangling HCN from target C_2H_2 presents an excellent challenge in recovering the measured signals from our candidate sensor.

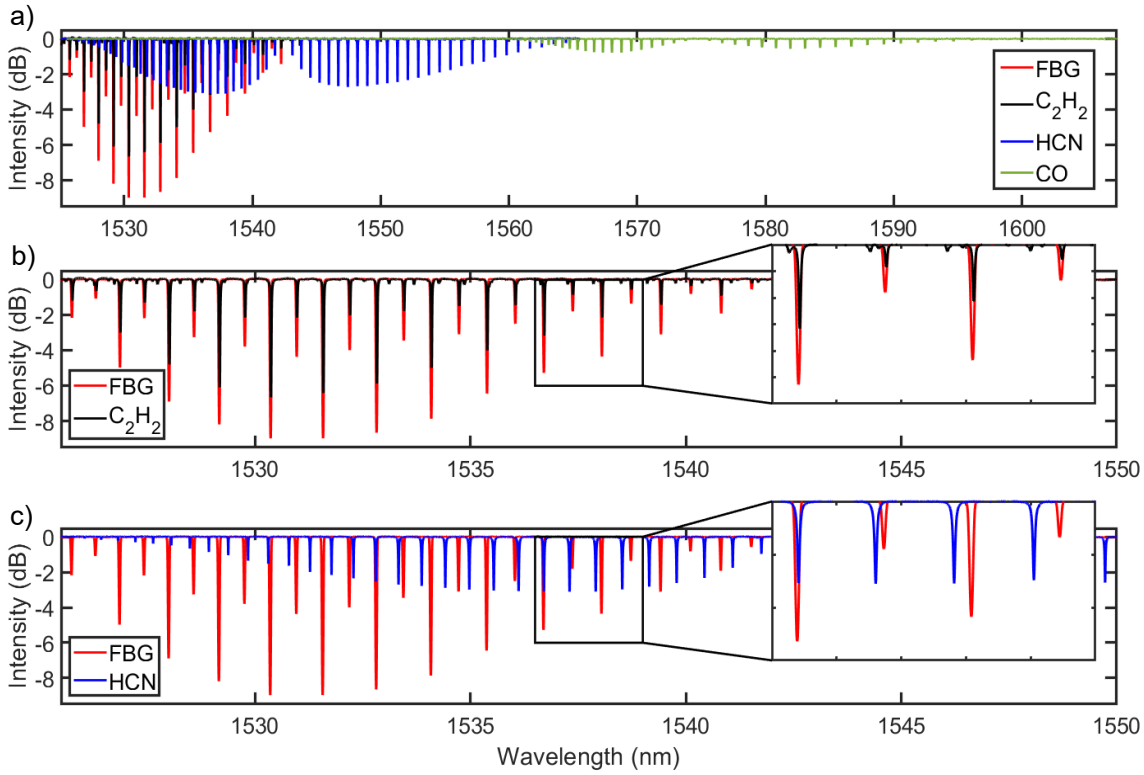

FIGURE 3.6: a) Transmission spectrum of the complex FBG (red) compared with the absorption spectra of C_2H_2 (black), HCN (blue), CO (green). b) Absorption spectrum of C_2H_2 (black), compared with the transmission of the complex FBG (red). c) Absorption spectrum of HCN (blue), compared with the transmission of the complex FBG (red).

OCS signals were first recovered from a setup incorporating only a HCN standard cell. As in the earlier case with CO, no discrete narrow peaks were present over the scanned range, although unlike the previous case, here a prominent variation was observed. The simulation of the correlation spectrum arising from pure HCN show the variation given by the red trace in Fig. 3.7 b). Experimental signals obtained from ganged cells simulating a mixed gas environment still preserved the strongly peaked signal when strain brings the sensor in tune with the C_2H_2 target. However, it can also be seen from the figure that variations from HCN persist in the background, and indeed their shape is largely preserved except near the peak where C_2H_2 dominates. A difference of $3.7 \pm 1.0\%$ was measured between a pure C_2H_2 and

a mixed HCN and C_2H_2 configuration. The variation in the background is consistent across all scans, and the close match with the simulated traces. As expected, the outcome is then that the basic robust detection made by the sensor suffers little impact, although influence from the interloper is clearly present. This is consistent with the simulated response, which predicted that the presence of HCN would produce a difference of order 3.3%: an excellent match to the measured difference in normalised intensity. We further note that these results imply that should the presence of the contaminant be known in advance, or determined from the shape of the signals, then the effects are entirely predictable and therefore could in principle be calibrated out, ameliorating any impact on sensing the target.

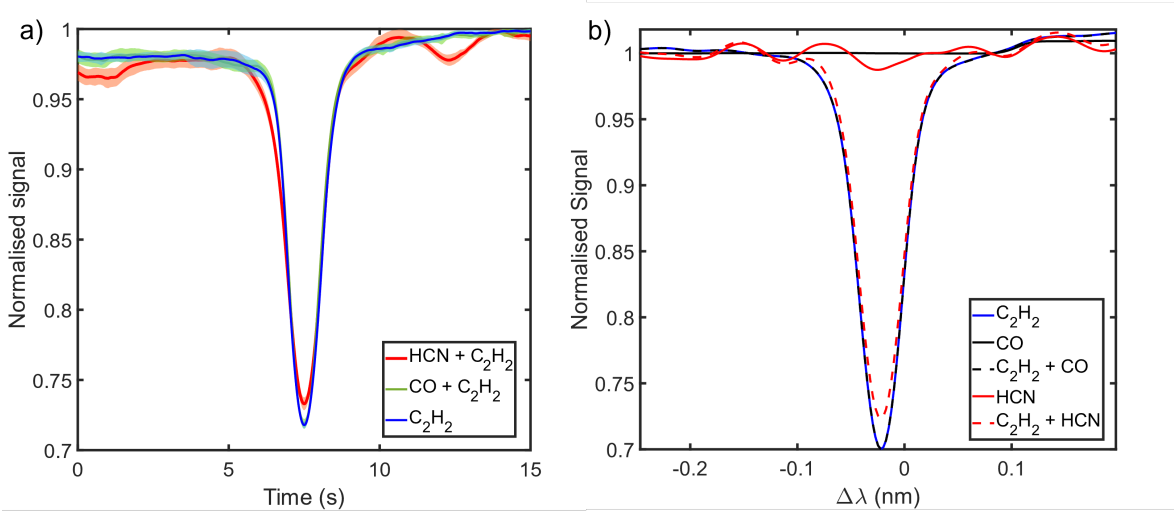

FIGURE 3.7: a) OCS signals for C_2H_2 compared to mixed gas configurations that also include CO and HCN as "contaminants". The shaded regions in both graphs represent the standard deviation (1σ) of the averaged sweeps. b) Simulation results for C_2H_2 and contaminating gases, including those in mixed gas environments. The simulations involving HCN and C_2H_2 exhibit features in the interline period that closely mirror those observed in the experimental data presented in the previous panel.

Although they do not alter the underlying conclusions, there are a few caveats to be aware of with regard to these simulation and experimental outcomes. First, the spectra used in the simulation are from data obtained from a setup whose resolution is lower than the intrinsic spectral linewidth of each peak. Second, the simulation does not account for noise arising from instability in the imposed strain (arising from imperfections in the motorised actuator). Also, the scan rate here was ~ 0.4 Hz (14 s per sweep). It would be important for future work

to investigate faster scan rates. In addition, these tests do not account for inhomogeneous spectral broadening, that would occur in a mixed environment, owing to testing being performed in series. However, despite these minor points, the close match between expectations and experimental results is an encouraging step in validating sensor performance in multi-species environments. The fact that the observed signals were overwhelmingly dominated by resonance with the target gas bodes well for accurate measurements of concentration, despite the presence of contaminants. Furthermore, the finding that the background variation for the blended HCN experiment could be well simulated indicates that more information, and perhaps even the sensing of gases not directly tailored into the grating, could be recovered from the OCS data in future work.

3.3 Conclusions

We have presented results from the first optical testbed to perform optical cross-correlation spectroscopy using an aperiodic fibre Bragg grating. This complex FBG was custom designed and shown to yield an excellent match to a ~ 20 nm region of the p-band absorption spectrum of C_2H_2. As an optical simulacrum of the molecule itself, it provides the ideal matched-filter template to perform optical cross-correlation, probing for the presence of the target species. Acting as a complex notch filter and employing strain as a mechanism to cyclically tune/detune the device from resonance with the molecular spectrum, we demonstrated that our device is capable of distinguishing varying levels of concentrations of the target gas. Our prototype sensor also exhibited robust insensitivity to the presence of unwanted contaminant gases. Overall, our findings indicate the viability of customised FBGs as compact, cost-effective devices for use in the spectral fingerprinting of specific target gases.

CHAPTER 4

Introduction to Quartz Enhanced Photoacoustic Spectroscopy

The following chapter covers the operation of quartz enhanced photoacoustic spectroscopy (QEPAS) and the importance of piezo signal amplification. First general photoacoustic spectroscopy will be discussed, including the advantages of such an approach to the fingerprint detection of gasses. Following from this, the specifics of QEPAS, including various key components and their physical operations, will be covered. This will include a discussion of general QEPAS detection methods and the modules used to implement them. Finally, the specifics of electrical amplification and its importance to the overall operation of a QEPAS detector will be covered. This will include different amplifier typologies and outline the objectives for the following two results chapters in this thesis.

4.1 Photoacoustic Spectroscopy

The photoacoustic effect, the ability to generate sound from light, has been known for nearly a century and a half. Alexander Graham Bell first described the photoacoustic effect in 1880 [63], though, technology at the time precluded any useful applications. It took more than half a century for the technology relating to microphones and optics to develop far enough that this effect could be applied to gas detection. In 1938 *Viegerov* demonstrated the first instance of photoacoustic spectroscopy (PAS), detecting both CO_2 and CH_4 [64]. The field saw rapid development in the late 1960s as laser technology advanced sufficiently to harness its inherent advantages in beam quality and monochromatic wavelength, making lasers practical as light sources [65]. Since then PAS-based detectors have gathered much attention and have been applied to a wide range of applications including medical diagnosis and monitoring [66–71],

industrial production and pollution monitoring [72–74], and even fruit quality monitoring [75]. Most importantly for this thesis is the application of PAS to environmental monitoring [73, 76].

PAS, as the name suggests, operates by generating an acoustic signal in order to monitor a target gas. Although there are many ways to implement a PAS detector, the general configuration is consistent, and we will outline this below. Each PAS setup requires at least one light source, which is chosen at a suitable wavelength to target an absorption band of the molecule that one wishes to monitor. A small portion of the absorbed photon energy is transferred into sound waves [77]. These sound waves are then detected using a microphone and the electrical signal from this is then processed to determine the concentration of gas present. This general outline can be seen in Fig. 4.1.

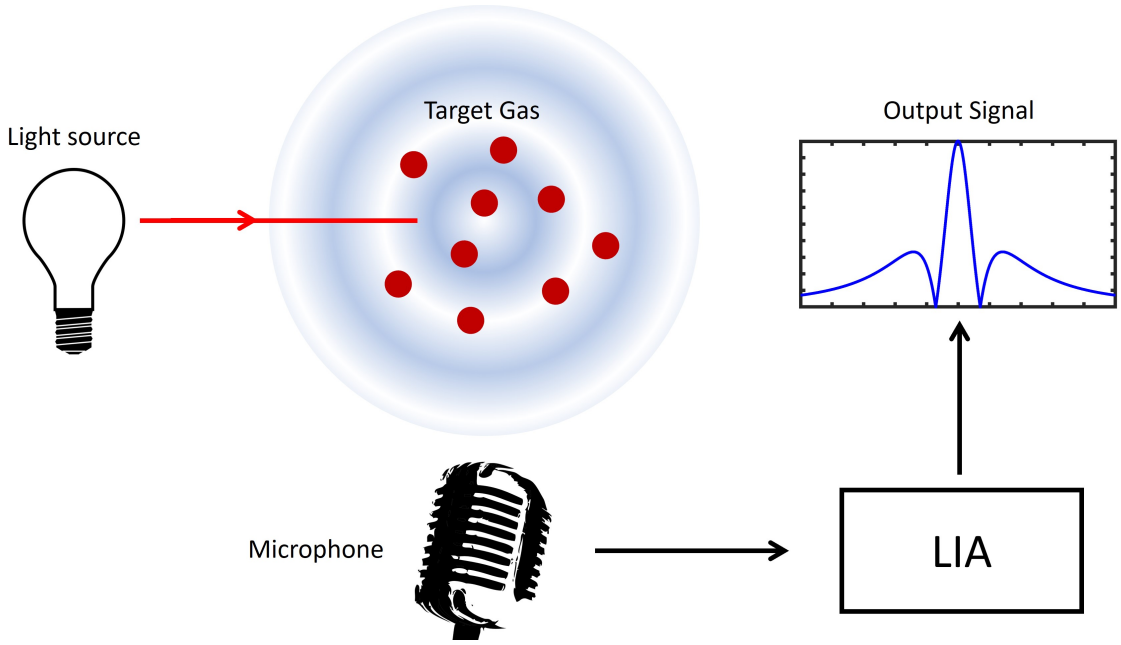

FIGURE 4.1: Schematic depicting the generalised setup of a PAS detector. A modulated light source is used to generate an acoustic wave that is then measured and processed into a meaningful signal. Here the signal is demodulated through the use of a Lock in Amplifier.

Unlike most optical detection methods, which determine concentrations by monitoring the intensity of light absorbed by a target gas [30], PAS goes further and utilises the relaxation pathways of the gas molecules excited by absorption. Once excited these molecules can relax

through either radiative or non-radiative pathways. Energy lost through non-radiative decay causes a temperature increase in the local of the light pathway. We can relate this localised heating to the photoacoustic effect from the correlation between pressure and temperature, as given by the ideal gas law:

$$PV = nRT \tag{4.1}$$

where P is the pressure, V is the volume, n is the number of moles, R is the gas constant, and T is the temperature. The direct proportionality between pressure and temperature implies that an increase in temperature will result in a proportional increase in pressure. By modulating the light source, we can subsequently modulate the temperature and, therefore, the pressure, which is a sound wave. Careful modulation of the light source enables the precise control of the resultant acoustic wave, facilitating the accurate determination of gas concentrations even at low levels.

The key benefit of PAS is that it does not rely on an optical detector, instead only a microphone is required for detection. A range of possible microphones can be used; however, they can be as simple as those used in a commercial hearing aid [78]. As a result, the signal from a PAS detector is determined by how much energy can be transferred to the acoustic signal and then to the microphone. This signal (S) is determined by:

$$S = \epsilon C P \alpha \tag{4.2}$$

where ϵ represents the radiation to sound transduction efficiency, C represents the instrument constant, P denotes the incident optical power, and α corresponds to the absorption coefficient of the target peak. From this, there are two key takeaways: The first is that the signal is directly proportional to the intensity of the light source being used, and the second is that the PAS signal does not depend on the path length of the detector. Combining these factors, the most significant advantage of PAS can be seen, in that the detector can be kept small, whilst maintaining sensitivity, as minimal path lengths can be kept [78]. Instead, other

design features can be used to increase the sensitivity of a detector such as increasing optical power, reducing background noise, improving the sensitivity of the microphone used, and improving the electrical signal being fed to the lock in amplifier (LIA). As a result, PAS offers a methodology to achieve highly sensitive detectors that are compact and portable.

There are two different modes of operation for a PAS cell; those being resonant and non-resonant [79]. All PAS cells can operate in both modes, with the distinguishing factor being the modulation frequency of the excitation light source. In the latter case, the modulation frequency is much lower than the resonance frequency of the cell. In this non-resonant mode, the sound wavelength is longer than the lowest frequency that a given cell can operate at. The advantage of this approach is that the PAS detector is not confined by the physical parameters of the cell, which allows for much simpler, and importantly, smaller cells to be employed. However, non-resonant PAS comes with two significant disadvantages [80]: First, it is not possible to detect flowing gases, as the flow rate drastically reduces the signal. Secondly, non-resonant cells are limited to operate at relatively low frequencies. Current noise, gas flow noise, and ambient noise are all inversely proportional to frequency. This is known as $1/f$ noise and means that the signal-to-noise ratio (SNR) is significantly reduced at these lower frequencies. Both of these parameters pose significant problems when considering non-resonant PAS detectors for environmental monitoring.

Resonant PAS, does help overcome these issues by operating at higher frequencies. A PAS cell operating in resonant mode ties the modulation frequency directly to the cell itself to create a standing wave. Although this allows for both flowing gases to be detected and reduces the $1/f$ noise, more attention needs to be given to the design of the chamber itself. However, the dimensions and exact shape of the chamber are now tied directly to the modulation frequency. This puts limits on the size and dimensions of the chamber. Furthermore, although significant improvements have been made to the chamber design, resonant PAS is still affected by $1/f$ noise [80].

4.2 Quartz Enhanced Photoacoustic Spectroscopy

A promising area of PAS that can help overcome some of the previous limitations is QEPAS. First demonstrated in 2002 by *Kosterev et al* [81] in which a quartz tuning fork (QTF) was used as a microphone to detect the photoacoustic signal. In this first paper, a simple watch QTF was used, which opened the door to the possibility of implementing PAS with a relatively simple and cost effective detection unit.

A typical QEPAS setup consists of a function generator, a light source (typically a laser), a QTF attached to an electrical amplifier, and a lock-in amplifier (LIA). The function generator is used to control the modulation of the laser. The laser beam is then focused directly through the middle of the prongs of the QTF, with this arrangement depicted in Fig. 4.2 a). The generated acoustic pressure pushes outwards upon the prongs of the QTF, generating a small piezoelectric signal. This is shown in Fig. 4.2 b), which depicts the most common beam orientation used in QEPAS. The piezoelectric signal is then boosted by the use of an electrical amplifier, providing a voltage response that is large enough to be effectively extracted using a LIA.

In order to understand the specific benefits of QEPAS, we must look at several parameters that determine the signal measured in PAS. Although C in Eqn. 4.2 depends on multiple factors that correspond to the exact design of the acoustic resonator that is used, several key factors can be extracted to give the following relation:

$$S \propto \epsilon \frac{\alpha Q P}{f} \tag{4.3}$$

where f is the resonant frequency, and Q is the Q or quality factor [82]. f is most commonly tied to the resonant frequency of the QTF, which is represented as f_0. The Q-factor is the ratio of the energy stored in an oscillator to the fraction of that energy lost in one oscillation cycle. The Q-factor can be defined mathematically as:

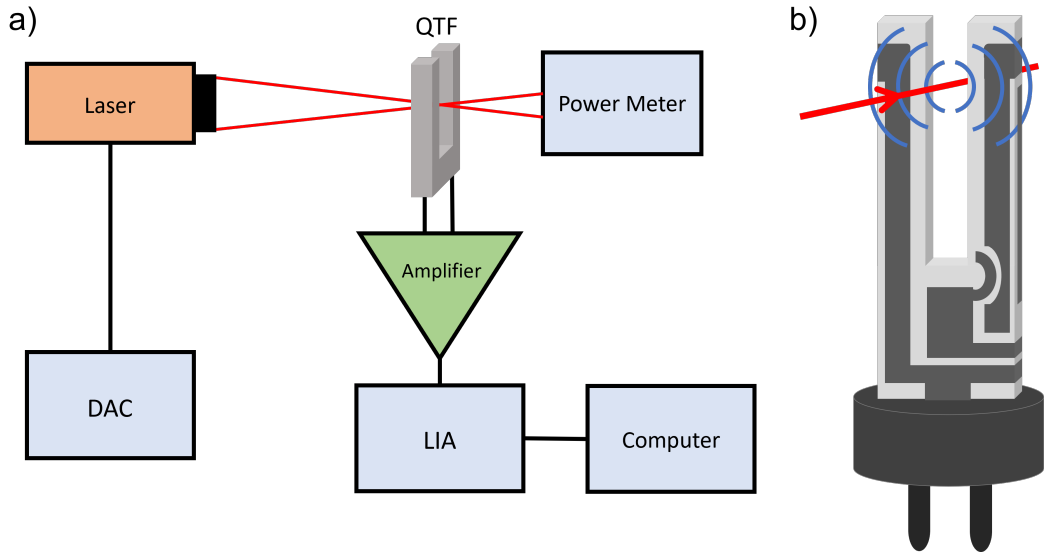

FIGURE 4.2: a) Schematic depicting the generalised, common setup for a QEPAS detector. This setup utilised a digital to analog converter (DAC) as the signal generator and the signal is filtered using a LIA. b) Schematic showing the orientation of the laser beam path through the prongs of the QTF. Here this QTF is depicted with an example of electric plating in a quadrupole pattern.

$$Q = \frac{f_0}{f_{FWHM}} \tag{4.4}$$

where f_0 is the resonant frequency of the QTF, and f_{FWHM} is the full width half-maximum for the resonant peak. When considering the Q factors of resonant PAS detectors, they typically have values of the order $\mathcal{O}(100)$, while basic QTFs typically have Q factors in the order of $\mathcal{O}(10^4)$ under atmospheric conditions [83]. The reason for such a stark difference is how the energy is stored. In a resonant PAS detector the acoustic energy is contained within the gas itself, so is limited by the fluid dynamics within the cell. On the other hand, in QEPAS the energy is stored within the microphone itself [84]. The solid quartz is capable of storing more vibrational energy than a gas medium, and this is reflected in the corresponding Q factor. Furthermore, for photoacoustic resonant cells, the signal generation is also directly tied to the Q-factor. Since $S \propto Q$, from Eqn. 4.3, this significantly higher Q factor enables a greatly increased signal.

Another important parameter to consider when comparing QEPAS with more traditional PAS is the operating frequency. Typically PAS detectors are designed to operate in the range of $\mathcal{O}(100) - (1000)\ Hz$ [84], whereas QEPAS detectors are bound by the f_0 of the QTF being employed. Most often, this is a typical watch QTF with $f_0 = 2^{15} = 32768$ Hz [85]. Although f of a QEPAS system is, therefore, significantly higher, the reduction in signal is offset by $1/f$ noise. This in turn means that the higher operating frequency does not proportionally affect the SNR [82].

4.2.1 Quartz Tuning Forks

Now that the role and key advantages of the QTF in QEPAS have been introduced, let us now look into the operation of the QTF in more detail. On a relatively basic level, the QTF is fundamentally the same as a regular metal tuning fork. There are two prongs connected to a substrate, each of which acts as a clamped beam. Each of the prongs can be treated as a damped oscillator bound at one end [86]. Owing to the fact that both prongs are tied to each other and are symmetric, the number of modes with significant Q-factors is restricted [87] making it easy to isolate modes for measuring signals. The most important mode in QEPAS operation is f_0 where the system will oscillate at the highest amplitude. This can be determined mathematically by the Euler-Bernoulli model: [88]

$$f_0 = \frac{\pi K}{8L^2}\sqrt{\frac{E}{\rho}} \tag{4.5}$$

where K is the width of the prongs, L is the length of each prong, E is the Young modulus, and ρ is the density of the quartz. The dimensions in this formula are schematically depicted in Fig. 4.3 a), where h represents the dampening force. This force arises predominantly from friction between the prongs and the surrounding medium, which for the purposes of this thesis will always be an air mix. This dampening is apparent when comparing Q in a vacuum with that in an air mixture under standard conditions; in the later case the Q-factor typically lower by an order of magnitude [85]. This means that the gas medium remains an important factor to consider when operating a QEPAS detector [89].

Given that quartz exhibits piezoelectric properties, mechanical energy is converted into electrical charges. This allows the QTF to act as a transducer that converts the original acoustic energy into electrical potential. Here we can also model the QTF as an electrical oscillator using a Butterworth-Van Dyke model [90]. The model consists of a resistor, inductor, and capacitor (RLC) circuit. We can model the electrical equivalent of the mechanical oscillator and determine the resonant frequency based on the physical parameters:

$$f_0 = \frac{1}{2\pi}\sqrt{\frac{1}{LC}} \tag{4.6}$$

where L is the inductance, and C is the capacitance. This is schematically depicted in Fig. 4.3 b), with an additional parallel capacitor (C_0) to account for the capacitance between the prongs of the QTF, and the quartz substrate (C_0). The QTF acts as an acoustic quadrupole, and the corresponding metal plating is arranged to generate a corresponding electrical quadrupole. As a result, only asymmetric vibrational modes will result in a detectable signal, whereas symmetric vibrations are quenched [91] . The only vibrations that generate a signal will primarily be from acoustic sources between the two prongs. Since a QEPAS signal is generated from the laser beam passing through the gap between the prongs, this will be the primary source of any acoustic QEPAS signal and therefore the system provides excellent noise immunity to any external acoustic pressure [92, 93]. However, the QTF is very sensitive to noise from the light source itself, due to the photothermal effect [94]. Incident light upon the QTF can generate a pieozo signal, since the light source is modulated at a frequency that directly excites f_0 it is important to ensure that the beam passes cleanly through the prongs and no light is incident upon the QTF itself.

Furthermore, QTFs can also offer significant cost advantages as many QEPAS detectors utilise standard commercial QTFs ($f_0 = 32.76$ kHz) [95–97]. These common electrical components and can be sourced for a less than a $\$1$ [98].

Since the first demonstration of QEPAS in 2002 standard, commercially available, 32.768 kHz QTFs have been employed to develop gas detectors that have demonstrated successful gas detection on many occasions [99–104]. The use of a custom QTF designed for use in QEPAS

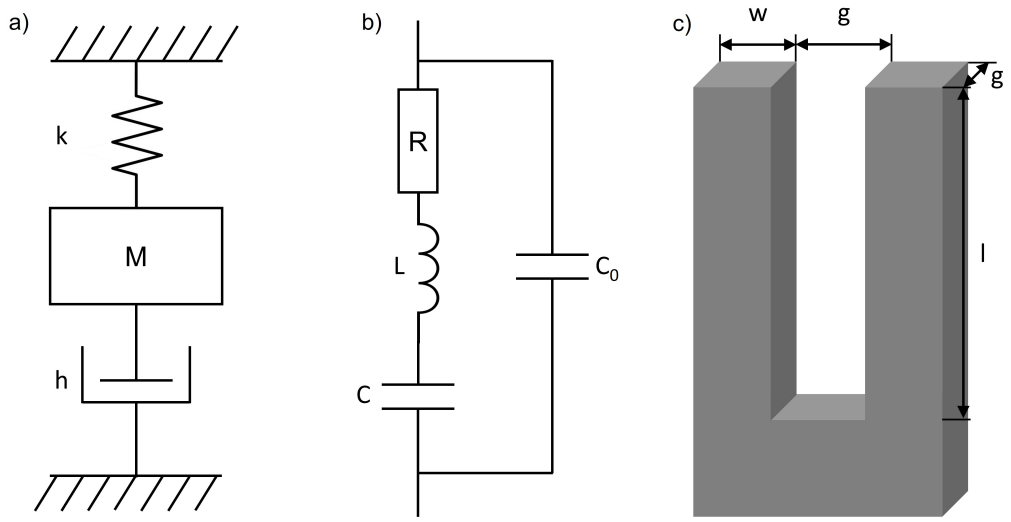

FIGURE 4.3: a) Model of a damped oscillator pertaining to the operation of a QTF. Here it can be modeled in respect to the stiffness of the spring (k), the mass (M), and a dampening force (h) b) The equivalent electrical model of the QTF, represented as an RLC circuit with a parallel capacitor. c) Schematic with QTF dimension notations listed.

was first demonstrated by *Patimisco et al.* in 2013 [105]. This QTF operated with a much lower resonant frequency ($f_0 = 4246$ Hz). Although earlier simulations had shown that this would result in less sensitivity [106], this QTF had a much larger prong spacing of 1 mm, which enabled a THz laser to be used for the first time. This paved the way for QTFs to be modified for use in QEPAS. Both f_0 and Q can be modified by varying the dimensions described in Fig. 4.3 c) [107].

Given that $S \propto 1/f_0$, this has led to multiple studies looking at QTFs with lower resonant frequencies, whilst maintaining high Q-factors. This has included QTFs where the fundamental frequency was lowered sufficiently to allow the use of the first overtone mode [108, 109], leading to the implementation of a double anti-node QEPAS module [110]. This development enabled dual gas detection where two separate laser sources were modulated to excite both the fundamental and first overtone modes [111]. Further studies have also looked at other physical factors, such as the addition of rectangular groves and T-shaped prongs which were shown to help improve the SNR of QTFs with a lower resonant frequency ($f_0 \approx 16$ kHz) by a factor of 60, compared to a standard bare QTF [112]. Gas detection was also performed using pilot line QTFs specifically designed for use in QEPAS (with $f_0 \sim 28$ kHz) was also

performed, which produced a ~ 10 increase in SNR over standard QTFs [97]. This custom design was later used in the successful monitoring of CO_2 in a greenhouse [113], further demonstrating the potential of custom QTFs. Although custom QTFs are not the focus of this thesis, their growing use in QEPAS as well as the ease of implementation should still be considered.

4.2.2 Micro-resonators

A design feature that most QEPAS setups incorporate to further improve signal is the use of acoustic micro-resonators (MRs). These consist of a tube or tubes to increase the acoustic pressure at the QTF, and subsequently increase the signal measured. The MRs acoustically couple with the QTF and this system is called the acoustic detection module (ADM). Given that MRs can have a significant impact on the signal and are incorporated in nearly all systems, it is important to consider the factors that will allow us to best use them in a QEPAS system.

The standard and most common configuration consists of two separate tubes placed either side of the QTF, with the laser being passed through both tubes. This setup is shown in Fig. 4.4 a). Another configuration is off-beam, or OB-QEPAS, where a single tube is used. This tube runs along the side of the QTF with a small slit cut in the centre of the pipe, in line with the centre of the QTF. Here, the laser passes only through the MR and does not pass through the QTF. OB-QEPAS was first reported by *Liu et al* [95]. Although both of these configurations are quite different, they both utilise the physics of longitudinal acoustic resonance in a pipe, where this standing wave is coupled with the vibrational resonance of the QTF [114]. This reduces the Q-factor of the ADM as the high Q QTF is losing energy via coupling to the relatively lower Q factor MRs. However, this does not reduce the signal, as one might intuitively expect, instead, it increases the energy transfer to the QTF and speeds up the response time [114].

When designing an ADM we can treat the MRs as supporting a standing wave in an open-ended tube. With this in mind, we can model the system in one of three ways: The first two being as either a single continuous resonator, or as two completely independent resonators. In

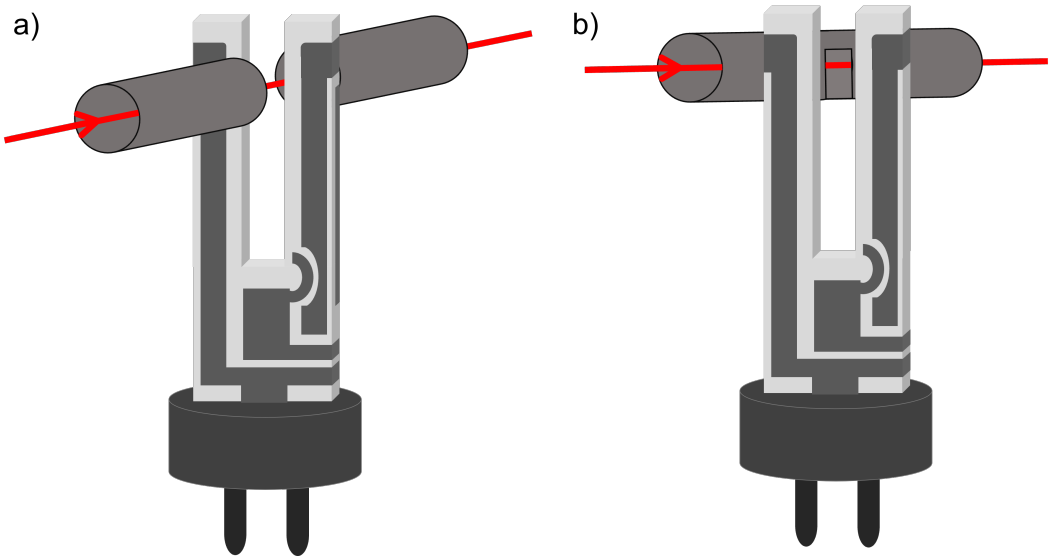

FIGURE 4.4: Schematic showing two of the most common MR setups using a) standard and b) off-beam configurations

the first case the spacing between the tubes is assumed as negligible, and so the system can be modelled as one continuous resonator, as seen in Fig. 4.5 a). Early QEPAS systems operated under the assumption that the MRs function as a continuous resonator, as highlighted in one of the earliest reviews [84]. As a result, initial QEPAS detectors had their MRs cut to a length of $\lambda_s/4$, where λ_s is the acoustic wavelength. In this case, the combined length of both tubes is half the sound wavelength. However, further studies showed that better performance could be achieved when each tube was cut to $\lambda_s/2$ [115]. This indicated that the gap between the tubes was significant enough to potentially consider the system as operating in the second case, where the tubes acted as two separate resonators (depicted in Fig. 4.5 b)).

However, later studies demonstrated that they should be treated as somewhere in-between the two cases, with *Serebryakov et al* [116] showing that the optimal length for each tube lies between $\lambda_s/4$ and $\lambda_s/2$. This indicates that the optimal length of the MRs should be determined by treating them as two overlapping, and not separate resonators. A further study by *Rello Russo et al.* [117] developed a model that could better predict the optimal length of the resonator tubes. This model incorporated a factor, that accounted for the fact that the true anti-nodes of the standing waves were positioned just outside the ends of the tubes, known open-end correction: [118]

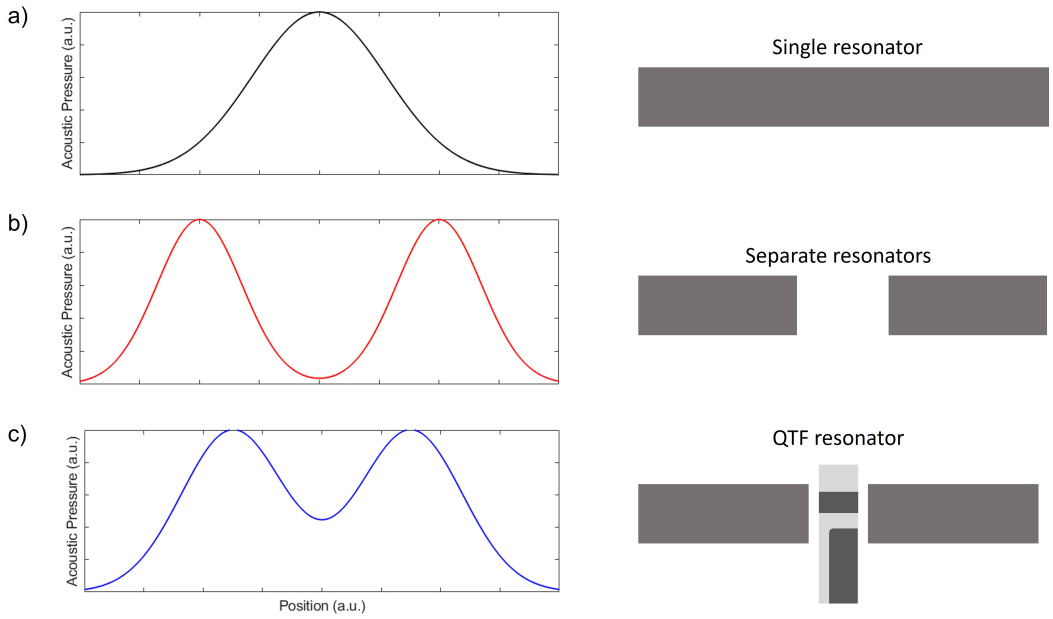

FIGURE 4.5: Resonance models for the tubes used in QEPAS MRs. a) The tubes can be treated as single resonator. This works well for modelling OB-QEPAS. b) Tubes treated as two separated resonators. This assumes significant enough spacing between the tubes that they act as independent resonators. c) Intermediate case, where the tubes are positioned such that the they cannot be treated as fully separate resonators or one continuous resonator. This has been shown to be the case for QEPAS standard configurations.

$$\Delta\lambda = \frac{8a}{3\pi} \tag{4.7}$$

where a is the radius of the resonator. Incorporating this into the model for the acoustic resonator *Rello Russo et al.* were able to estimate the optimal length as:

$$\lambda_n = \frac{n\nu_s}{2f_0} - \frac{16a}{3\pi} \tag{4.8}$$

Another important variable to consider when designing and optimising QEPAS MRs is the inner diameter of the tubes. The diameter of the tubes directly impacts the nature of the coupling between them and the QTF spectrophone. Studies have shown that a narrower inner diameter improves the SNR of the QEPAS signal [114]. However, this comes at a cost of both sensitivity and increased beam confinement. Although a narrower tube was found to increase

the coupling strength, it also increased the coupling sensitivity with respect to other variables, such as pressure, temperature, and gas composition [114]. Given this, it is likely difficult to fully optimise a system where the test conditions are likely to vary significantly. It may be preferable then to use a wider tube in such circumstances.

As to beam confinement, this is an important parameter to consider when designing a QEPAS detector. Light that is scattered off the sides of the MRs contributes to background thermal noise, and as discussed previously with the QTF, the beam must be confined to pass completely through the MRs and the QTF. However, this is not necessarily a significant problem, as the spacing between the QTF prongs is often smaller than the inner diameter of the MRs. Standard QTFs ($f_0 = 32.76$ kHz) have a prong spacing of 0.3 mm, whereas the narrowest MRs tested in *Dong et al* was 0.41 mm [114]. However, this may still cause problems when beam divergence is significant. This was also one of the proposed benefits of the OB-QEPAS in that wider MRs can be used, so the system is not limited by the spacing between the QTF. However, OB-QEPAS comes at the cost of weaker acoustic coupling to the QTF [114], which results in a smaller signal.

4.2.2.1 Lock in Amplification

Lock in amplification (LIA), is an important tool for measuring the differential signal produced in WMS. LIAs utilise phase-sensitive detection (PSD) to isolate a selected modulated signal from a given trace, essentially acting as a very narrow filter. LIAs typically operate with bandwidths <1 Hz. As a result, a LIA is capable of measuring incredibly weak AC signals, with some devices capable of detecting signals in the order of nVs [119]. This can even be performed when the noise level is higher than the desired signal and as a result provides an incredibly useful tool in QEPAS when measuring the small electrical signals from a QTF.

LIAs require both an input trace that contains the desired experimental signal, and a reference signal to work. LIAs use this reference signal to isolate a single frequency and extract it from the input trace. To understand how this works, let us first consider the desired signal, which can be represented by:

$$V_{sig}\sin(\omega_{sig}t + \theta_{sig}) \tag{4.9}$$

where V_{sig} is the amplitude of the desired signal, ω_{sig} is the frequency, t is time, and θ_{sig} is the phase. Likewise, we can also similarly represent the reference by:

$$V_{ref}\sin(\omega_{ref}t + \theta_{ref}) \tag{4.10}$$

where V_{ref} is the amplitude of the reference signal, ω_{ref} is the reference frequency, and θ_{ref} is the reference phase. All LIAs generate their own reference signal; however, this can be done in one of two ways. The first is internally, where the LIA generates it's own reference signal. The second is to use a phase-locked loop tied to an external reference input. This external reference does not necessarily have to be a sine wave and can be, for example, a square or triangle wave, as the LIA converts this into an equivalent AC sine signal. The LIA then obtains an output of the PSD (V_{psd}) by multiplying these two signals together, which results in the following:

$$\begin{aligned} V_{psd} &= V_{sig}V_{ref}\sin(\omega_{sig}t + \theta_{sig})\sin(\omega_{ref}t + \theta_{ref}) \\ &= 1/2V_{sig}V_{ref}\cos((\omega_{sig} - \omega_{ref})t + \theta_{sig} - \theta_{ref}) \\ &+ 1/2V_{sig}V_{ref}\cos((\omega_{sig} + \omega_{ref})t + \theta_{sig} + \theta_{ref}) \end{aligned} \tag{4.11}$$

This provides us with one component at the sum of the frequencies and one at the difference. A low-pass filter is then applied, which removes any higher frequency components. This will always remove the component arising from the sum of the frequencies and leave only the difference. The difference here is incredibly useful since, ideally, both the reference and the desired signal should have the same frequency, i.e. $\omega_{ref} = \omega_{sig}$, which then gives us:

$$V_{psd} = 1/2V_{sig}V_{ref}\cos(\theta_{sig} - \theta_{ref}) \tag{4.12}$$

This is a DC signal proportional to the amplitude of the desired signal. This process can be performed by either analogue and digital processors; however, for this thesis, we will focus on digital demodulation. Now, we must also consider a noisy signal. For now we have only considered multiplying the reference by a signal with a single sine wave; however, experimentally this will not be the case as there will be other components that comprise the experimental signal, including noise. We can consider noise to be made up of sine waves with frequencies that differ from the reference signal. In that case, we return to Eqn. 4.11 and consider the case where the signal is made up of components whose frequencies do not match the reference signal ($\omega_{ref} \neq \omega_{sig}$). If the frequency of these noise components are sufficiently different from the reference, then both the sum and difference components will be removed by the low-pass filter. By restricting the roll-ff point of the low-pass filter to very low frequencies, the LIA becomes a narrow-band filter, which will hopefully remove most of the undesired noise. However, this increases the acquisition time. In order to narrow the filter bandwidth, the time constant τ of the LIA must be increased, which reduces the response time. This is not a problem if the desired signal from an experiment has a slow response time, though, it may restrict sweep speed when modulation spectroscopy is performed. With this in mind, it is then important to consider both the response time of the QTF and the LIA when designing a QEPAS setup.

There is another significant factor to consider in PSD. Here we have assumed that $\theta_{sig} - \theta_{ref}$ remains constant, whereas this is not necessarily the case. Using a single PSD measurement, it is not possible to isolate the signal magnitude from any change in phase between the reference and the desired signal. However, this can be overcome by introducing a second reference signal. This second reference does not need to be generated externally and is most often generated internally in the LIA. This is typically done within the LIA by generating a second identical reference signal, phase offset from the first by 90^o, and separately multiplying this by the input signal to give a second PSD output. Conventionally, the first PSD output is labelled X and the second Y. Given the 90^o offset in the second reference this, after the low pass filters, gives us:

$$\begin{aligned} X &= V_{sig}\cos(\theta_{sig} - \theta_{ref}) \\ Y &= V_{sig}\sin(\theta_{sig} - \theta_{ref}) \end{aligned} \tag{4.13}$$

Here, the magnitude of the signal can be extracted as a single component R:

$$R = \sqrt{X^2 + Y^2} \tag{4.14}$$

The phase difference between the reference and the desired signal (θ) can also be extracted by:

$$\theta = \tan^{-1}(Y/X) \tag{4.15}$$

This then results in an output where the signal magnitude and the phase difference between the reference and the desired signal are now fully isolated. Furthermore, signals can be demodulated at different harmonics. A PAS signal will generate a nonlinear response that, in the frequency domain, produces signals at the first, as well as higher harmonics. Typically, QEPAS signals can be demodulated at the first or second harmonics. If demodulated at the first harmonic, the laser is modulated at f_0, commonly referred to as the 1f-QEPAS signal. If demodulated in the second harmonic, the laser is modulated at $f_0/2$, referred to as the 2f-QEPAS signal.

Wavelength modulation spectroscopy (WMS) can be performed using both fixed or scanned wavelength techniques. For fixed wavelength measurements, the laser wavelength is modulated around a fixed point, ideally a target absorption peak. Although this provides a relatively simple method of detection, it is generally not the primary method for measuring QEPAS signals. Though it does have some specific uses such as longer-term Allan deviation studies [120]. The primary method for acquiring concentration measurements is to combine WMS with the scanned wavelength method.

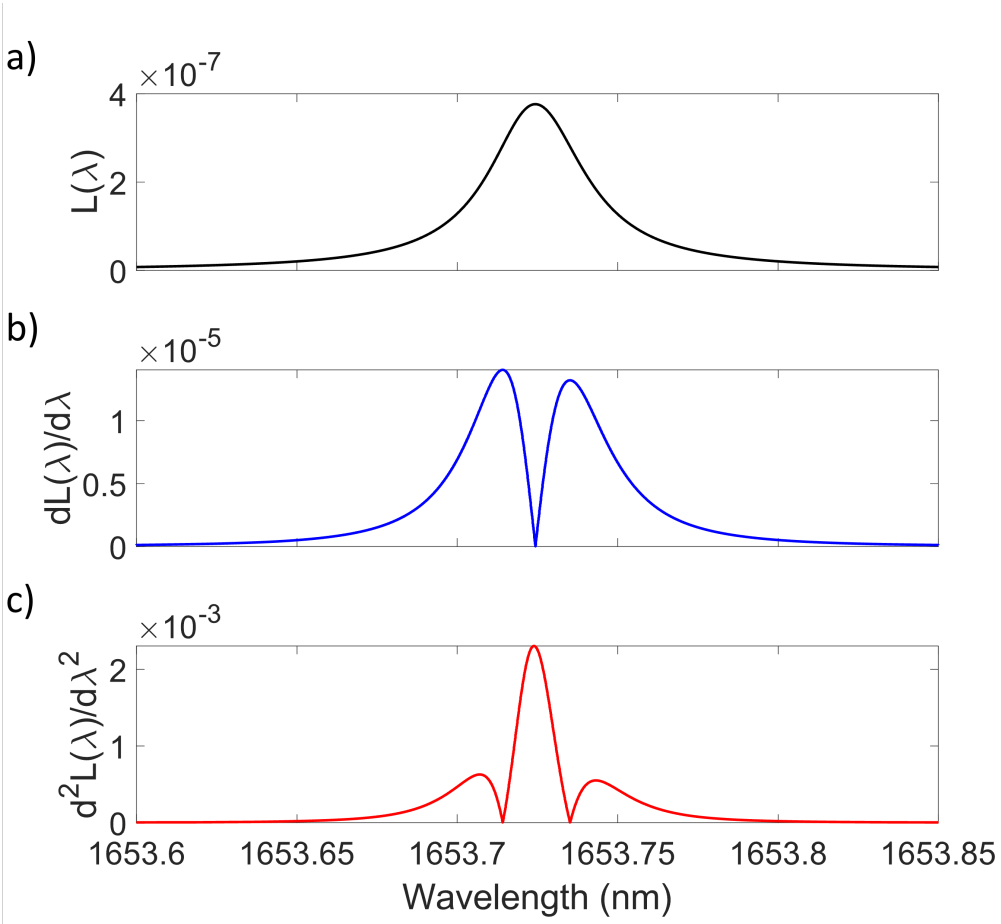

FIGURE 4.6: a) Example methane absorption peak, modelled using a Lorentzian function around 1653.7 nm, using a methane of concentration of 500 ppm in air, at a pressure of 1 atm. b) Model of the 1f-QEPAS response. c) Model of the 2f-QEPAS response.

In this study, we used the absorption peak at 1653.7 nm ($\nu = 6046$ cm^{-1}), and here we can use it to provide an approximate lineshape model for the expected 1f and 2f-QEPAS responses, in the scanned mode. For the 1f-QEPAS signal, the output will be the differential signal as the high-frequency modulation is passed over the absorption peak, resulting in the output line shape following the 1st derivative. The 2f-QPEAS signal will likewise follow the second derivative. If we model this absorption feature as a Lorentzian function, as seen in Fig. 4.6 a), then we can also model the expected 1f and 2f-QEPAS signals. For the 1f-QEPAS signal we get a double peak feature, shown in Fig. 4.6 b). For the 2f-QEPAS signal, this results in a large centre peak, with two smaller side peaks, as shown in Fig. 4.6 c). Note that these have been modelled as the absolute value of the derivative, since R was used to measure the signal

for this thesis. We use R here because it separates the phase from the magnitude of the signal, and so is not prone to shifts if the phase shift differs across sweeps. Furthermore, while the lineshape is modelled around the methane absorption peak at 1653.7 nm - using data from the HITRAN database [121] - the magnitude is arbitrary and used purely for illustrative purposes. For a more detailed explanation of the modelling of the 1f, and 2f signals, inlcuding Taylor expansions, see *Supplee et al.* [122].

4.3 Main Analysis

Now that the general configuration of QEPAS, and how signals are measured have been introduced, we will look at some specific examples that pertain to the detection of methane in this thesis. The following section covers a range of methane detectors and compares their performance with respect to specific parameters. This will include laser power, the type of laser, and scan speed. Following that, two other applications of this technology - beat-frequency QEPAS (BF-QEPAS) and quartz-enhanced photothermal spectroscopy (QEPTS) - will also be introduced.

4.3.1 Detection Limits

In order to compare detectors, we must first introduce two parameters that will enable us to quantify detector performance: The minimum detection limit (MDL) and the normalised noise equivalent absorption (NNEA). The MDL, sometimes referred to as the limit of detection (LOD), is a straightforward measurement that uses the SNR for a given concentration to determine the lowest gas concentration that can be identified with a given setup. It is given by:

$$MDL = \frac{c}{SNR} \tag{4.16}$$

here SNR is the signal-to-noise ratio for a given concentration (c). The SNR in QEPAS is often calculated as the ratio of the signal peak to the 1σ variation of the interline region; that

is, the standard deviation when the laser is sufficiently off the absorption peak of interest. For the rest of this chapter, we will assume this calculation for SNR, unless otherwise stated.

Although the MDL is a convenient measurement to compare similar systems, it is not a valid comparison between different systems. In order to account for a wider array of variables, the NNEA can be used. The NNEA is given by:

$$NNEA = \frac{\alpha_{min} P}{\sqrt{BW}} \tag{4.17}$$

where α_{min} is the minimum detectable absorption coefficient, P is the laser power, and BW is the equivalent noise detection bandwidth. α_{min} is given by:

$$\alpha_{min} = \sigma N MDL \tag{4.18}$$

where N is the number of absorbing molecules per cm^3, and $\sigma(\lambda)$ is the absorption cross section per molecules for a given wavelength [123]. Although more complex to determine, the NNEA enables comparisons between different detectors to be made. The NNEA takes various parameters, such as LIA filter settings, incident optical power, and is independent of the type of gas [124]. Here, a lower NNEA is desirable.

4.3.2 Methane Detection

QEPAS detectors have been demonstrated to work with a wide range of gases, including ammonia [116, 125], carbon disulfide [126], triacetone triperoxide [127], and acetylene [128]. One of the significant advantages of QEPAS is its flexibility in hardware and software, since most components remain unchanged regardless of the gas being detected. The primary exception is the light source, which must be adjusted to target the specific absorption features of the gas in question. This adaptability means that, as long as the light source can be modulated around desired absorption features, the rest of the setup generally remains the

same. Nevertheless, careful consideration of both the light source and the target gas is essential to ensure accurate fingerprint detection.

To this end, let us look at methane, which is of key importance to this thesis. Table 4.1 below shows a selection of recent QEPAS studies that directly measured methane, using a variety of light sources and measurement techniques. The following sections will cover key points.

TABLE 4.1: Comparison of methane QEPAS Systems. Here S represents a standard ADM setup, S-C represents a standard setup that uses a custom QTF, OB represents an OB-QEPAS system, BF beat frequency, and H heterodyne.

QEPAS type	Laser Type	Laser Power (mW)	MDL (ppm)	Ref.
S	DFB	38	14.93	*Chen et al* [129]
S	A-DFB	246	0.094	*Zatorska et al* [130]
S	ICL	12.5	0.18	*Elefante et al* [131]
S	ICL	11	0.09	*Sampaolo et al* [132]
S-C	DFB	6.7	34	*Twomey et al* [133]
S-C	MIR-OPO	53	0.023	*Christensen et al* [134]
S-C	DFB	6.3	7.0/2.2	*Li et al* [135]
S-C	DFB	12	0.76	*Menduni et al* [136]
S-C	QCL	48	0.048	*Zifarelli et al* [137]
S-C	QCL	74	0.028	*Menduni et al* [138]
OB	DFB	10	2.41/0.288	*Lin et al* [139]
BF	DFB	0.64	28.35	*Ye et al* [140]
H	CW-DFB	$\sim$31	0.711/1.06	*Liang et al* [120]

4.3.2.1 Optical Source

Many QEPAS systems utilise distributed feedback (DFB) laser diodes as the light source. This offers several advantages since diode lasers are commercially available, have relatively low power requirements, are compact and lightweight, and crucially the output is easy to tune and modulate [141]. However, this poses a limitation on the acoustic signal that can be generated. Although high output power can be achieved, it is difficult and often comes at the cost of poor beam quality, an increased risk of optical misalignment, and requires more complicated thermal regulation [78]. Recall from Eqn. 4.3 that $S \propto P$, which means that a stronger light source will give a larger QEPAS signal, everything else being equal. Examples of this can be see in specific cases such as, *Zifarelli et al* [137] and *Menduni et al* [138] (where increasing

the output from $48 \rightarrow 74$ mW improved the detection limit from $0.48 \rightarrow 0.28$ mW) as well as *Li et al* [135] and *Zatorska et al* [130] (where increasing the output from $6.3 \rightarrow 246$ mW improved the detection limit from $2.2 \rightarrow 0.094$ ppm), demonstrate this experimentally. This shows that increasing the acoustic signal by increasing the laser power is straightforward; however, it may not be practically achieved when constructing lightwiehgt detection modules.

Fibre amplifiers are one established method for increasing the laser power in both PAS [142] and QEPAS [128]. Erbium-doped fibre amplifiers have also been used to achieve low detection limits of ammonia, for biomedical monitoring [125]. An output of 246 mW (as seen in Tbl. 4.1) was used to obtain a very low MDL, though, this was achieved through the use of a specialised bismuth-doped fibre amplifier. When considering the development of portable detectors for environmental monitoring, increasing the laser power using fibre amplifiers may not always be practical, and they are restricted by the extent to which wavelengths can be amplified using available devices.

Another solution is to use non-diode lasers as the light source. As seen in Tbl. 4.1, many of the recent QEPAS detectors use an inter-band cascade laser (ICL) or a quantum cascade laser (QCL) to achieve low MDLs. The use of these light sources opens up the possibility of using wavelengths further into the IR allowing for other absorption features to be targeted. Similar to diode lasers ICLs are lightweight, relatively low power, and easy to modulate light sources [143] which makes them suitable for QEPAS. They enable targeting of absorption bands in the mid-IR and can operate effectively up to ~ 5 μm [144]. QCLs further extend this range and allow multi-gas detection due to their wide tuning ranges [145]. Their narrow linewidths are desirable and they enable the probing of absorption features even up to the terahertz regime. As previously discussed, this has already been seen in QEPAS; however, due to much wider beam diameters at longer wavelengths, this required the use of custom QTFs with much larger prong spacing. Although QCLs can achieve very low detection limits, they do, nonetheless, come with several disadvantages. They have much higher power thresholds for lasing, require more complex thermal regulation, and can suffer from reduced beam quality at higher powers [146]. Furthermore, because of their complexity they are less cost effective than both regular diode lasers and ICLs. All this considered, they provide significant benefits; however, they

are not suitable for all QEPAS applications, especially when low cost and minimised physical footprints are required.

4.3.2.2 Scan Time

An additional factor worth exploring is the signal acquisition time. In order to measure a signal, the acoustic energy needs sufficient time to be transferred into the QTF. From classical oscillator theory the time constant (τ) is given by:

$$\tau = \frac{Q}{\pi f_0} \tag{4.19}$$

Here, τ is defined as the time it takes for the oscillation amplitude to decay to $1/e$ of an initial value [147]. Although QTFs have relatively high f_0 values, the high Q factor generally results in a longer time constant. For a typical 32.768 kHz QTF, this results in $\tau \approx 100$ ms under atmospheric conditions.

This is reflected in the integration time settings used for the LIA. It takes longer to fully scan an absorption peak with typical times in the order of $5 - 10$ s. Although this is not a problem for some applications, it is not ideal for use cases that require more rapid spectral scans with faster scan rates potentially introducing spectral smearing [134]. This can be a significant issue when trying to resolve several close spectral features, which can impact the ability to perform selective fingerprint detection.

Slower acquisition times become a more pronounced problem for custom QTFs that operate at lower frequencies. One of the more common variants of custom QTF is one with $f_0 = 12.5$ kHz, accounting for 4/6 of the above custom QTF references above (Tbl. 4.1). This lower resonant frequency further increases the time constant to $\tau \approx 300$ ms. The paper in which this variant was first reported had scan times of 50 s [112], these lower scan rates may further limit the use of custom QTFs in cases where rapid spectral measurements are required.

4.3.2.3 The Use of Beat Frequencies

One potential solution to slower acquisition times is to use the beat frequency QEPAS (BF-QEPAS) technique, first demonstrated by *Wu et al* in 2017 [148]. The response of a mechanical oscillator is comprised of two components: steady-state and transient. Up to this point, all the QEPAS work presented relies on the steady-state response, which is stimulated by a modulation signal that is slowly swept and forces the QTF to oscillate at the resonant frequency. In BF-QEPAS the signal is modulated away from the resonance by Δf and the sweep is replaced by a rapid pulse. After this initial excitation the QTF is left to freely vibrate without additional acoustic pressure being generated. The LIA is also set with a very short time constant ($\tau \sim 10$ ms), which not only allows for the faster transient response to be monitored, but it also increases the filter bandwidth so that despite the difference in frequency the f_0 response of the QTF can still be easily measured. This results in a pulsed response that decays over time. f_0 can be recovered by looking at the time difference between the peaks in the response (Δt) given that this is related to the resonant frequency through:

$$\Delta f = \frac{1}{\Delta t} = |f - f_0| \tag{4.20}$$

Where f is the driving modulation frequency. The speed at which the transient response decays can be used to determine the Q of the ADM. This makes it possible to constantly monitor both f_0 and Q which reduces the need for calibration.

4.3.3 Quartz Enhanced Photothermal Spectroscopy

Quartz enhanced photothermal spectroscopy (QEPTS) shares a similar configuration with QEPAS, however, is used for column detection of gases. QEPTS, also referred to as light-induced thermoelastic spectroscopy (LITES), uses a QTF as a highly sensitive photodetector. A modulated light source is first passed through a gas sample before being focused directly onto one of the prongs of the QTF. The light energy is directly absorbed by the quartz, or chrome (used in the metal plating), which is then released within the QTF structure generating

a piezo signal. [149] Whilst this generates photothermal noise in QEPAS, this process can be used here to turn the QTF into a photodetector. The QTF is connected to an electrical amplifier, and the output signal is demodulated through the use of an LIA. This setup can be seen in Fig. 4.7, with most of the signal generation and processing components being functionally identical to those used in QEPAS.

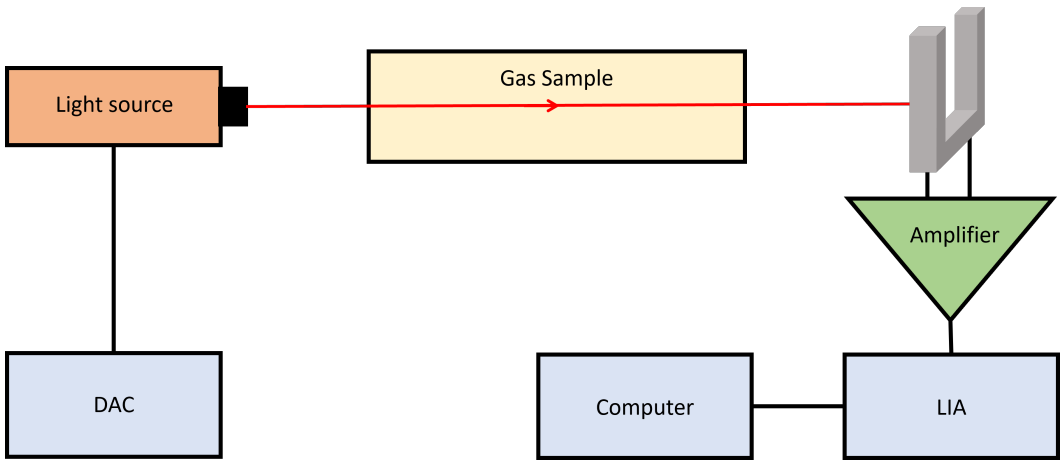

FIGURE 4.7: QEPTS schematic, with a laser as the light source. The light source, DAC, amplifier, and LIA are not functionally different to QEPAS.

QEPTS was first demonstrated by *Ma et al* in 2018 [94] and has been shown to offer several benefits in specific cases to QEPAS. QEPTS is a non-contact technique that offers benefits in remote trace gas detection since it is easier to keep components isolated from environmental deposits that may otherwise require the QTF to be regularly cleaned, though, it is possible to achieve similar results in QEPAS through the use of novel ADM structures such as ellipsoidal gas cells [150]. The beam quality is less important for QEPTS [88], and can be used in combination with other more traditional spectroscopic techniques, such as multipass cells [151]. The use of a second reference light source [152], and the use of gold plating on the QTF to reflect the back, increasing the path length through the quartz substrate [153] can also be used to further increase the SNR in a QEPTS detector. QEPTS has even been recently used to detect methane using a custom heterodyme QTF [154]. However, QEPTS does reintroduce the need to consider path length in the development of the gas chamber and is only suitable for stand-ff/open path sensing, and so the benefits may not always be applicable to the use cases that require small, sensitive detectors.

4.4 Electrical Amplifiers

When the QTF is mechanically loaded, charges will form on the opposite faces of the prongs, which are picked up by the metal plating on the surface [155]. When considering acoustic forces upon the quartz substrate, the QTF is only capable of producing a very small electrical signal, on the order of $\sim 1 - 100\mu V$, depending on the exact conditions [85, 156]. This limitation requires the integration of both an electrical amplifier and a subsequent LIA into the experimental setup [84], as depicted in Fig. 4.2. The electrical amplifier is instrumental in addressing the raw output of the QTF, significantly improving the detectability of trace gas concentrations. Boosting the magnitude of the raw signal from the QTF ensures that even minute photoacoustic signals arising from low gas concentrations can be effectively captured. Incorporating a suitable amplifier circuit is therefore indispensable in optimising the QEPAS technique for gas-sensing applications. Furthermore, the QTF and the amplifier operate independently of the optical source, which means that a suitable amplifier can be used across a wide range of gas detectors. This essentially means that an improvement to the design of an electrical amplifier can be applied to any of the previously discussed QEPAS, and QEPTS techniques. In cases where there are other hardware limitations, such as the use of more powerful optical sources or the use of custom QTFs, an improved amplifier may be one solution to achieve a larger SNR without demanding power requirements. Even in cases where other hardware improvements can be made, an improved amplifier can still be implemented. However, despite the importance of this amplifier circuit, there have been very few changes to the basic amplifier design since QEPAS was first demonstrated.

Three distinct amplifier architectures can be employed to initially boost the a piezoelectric signal: a transimpedance amplifier (TA), a charge amplifier (CA), and a voltage amplifier (VA) [157]. Careful selection and design of the pre-amplifier is crucial in ensuring it achieves sufficient signal enhancement for subsequent analysis and processing. The following section covers their operation in relation to use in QEPAS.

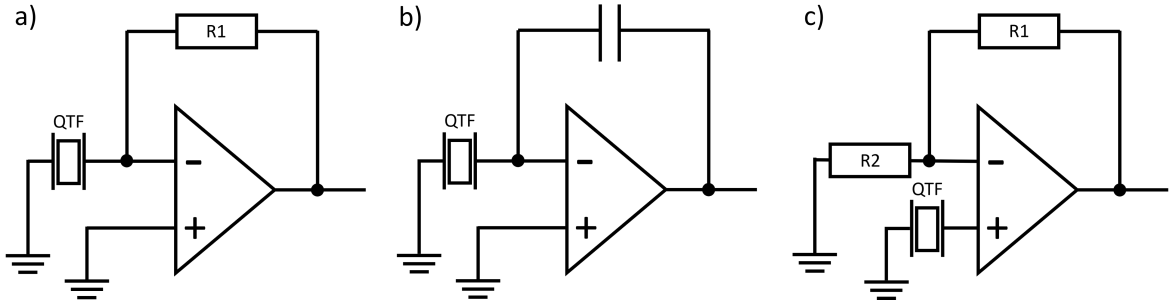

FIGURE 4.8: Schematic showing three common electronic topologies used to amplify a small piezoelectric signal: a) Transimpedance amplifier, most commonly used amplifier in QEPAS with the gain determined by the value of R1. b) Charge amplifier, where the gain is determined by the value of the feedback capacitor. c) Voltage amplifier, where the gain is determined by the ratio of R1:R2.

4.4.1 Transimpedance Amplifier

A TA works by converting a small current into a large voltage output. It consists of an operational amplifier (op-amp) with a large resistor wrapped around connecting the inverting input to the output. This is the most common amplifier design in QEPAS with all studies previously referenced using this design. The original QEPAS design used a 4.4 MΩ feedback resistor (in place of R1 in Fig. 4.8 a)), since then the vast majority of published detectors using a 10 MΩ resistor (all methane studies reported in Tbl. 4.1 use this as their feedback resistor). The use of such a feedback resistor will mean that the TAs begin to attenuate any signal higher than 6.4 kHz [158]. As this is well below f_0 for most QTFs used in QEPAS any TA will likely be operating well outside of their pre-amplifier bandwidth. This means that the vast majority of QEPAS amplifiers are not optimal for the frequencies being used.

4.4.2 Charge Amplifier

A CA works by converting a small charge to a large voltage output. It has a similar structural layout to the TA, with the resistor being replaced with a capacitor, as seen in Fig. 4.8 b). A CA has a very narrow operating frequency, which makes it suitable for use with the QTF with its high Q factor and stable f_0. The gain is determined by the ratio of the capacitance of the QTF to the feedback capacitor. However, this means that parasitic capacitance limits the

effective gain given the relatively low capacitance of the QTF (in the order of pF). To achieve better gain it is possible to place a resistor parallel to the capacitor being used; however, for higher resistor values, the charge amplifier will convert to transimpedance amplification.

4.4.3 Voltage Amplifier

A VA is somewhat different in topology. The QTF is connected directly to the non-inverting input of the op-amp, and two resistors are used to generate a feedback circuit around the inverting node, as seen in Fig. 4.8 b). The gain is determined by the ratio of R1/R2, which provides great flexibility in choosing the gain of the system. Here, resistor values can be chosen that achieve a high gain, without attenuating the frequencies that a QTF will likely be operating at. Since the QTF is connected directly to the op-amp, its high input impedance can also be easily maintained, which reduces signal reflection and allows for better electronic energy transfer between the QTF and the input of the amplifier. Furthermore, quartz has a better voltage constant (118 $\mathrm{VmN^{-1}}$) versus its charge constant (4.6 $\mathrm{pCN^{-1}}$) [156, 159]. Even compared to a TA working at the QTF noise floor, this suggests a signal roughly an order of magnitude greater than relying the on the charge response. This further increases the effectiveness of a VA compared to a TA for use in amplifying the piezoelectric signal from a quartz substrate. TAs are commonly used for piezo materials where the charge constant is greater than the voltage constant, such as perovskites [160].

The advantages of VAs have been shown in studies initiated by *Starecki and Wieczorek* [161] and *Winkowski and Stacewicz* [162]. In their research, *Starecki and Wieczorek* modelled and compared all three types of amplifiers, and their results favoured the VA for providing the highest SNR. This advantage in SNR was further cemented by *Winkowski and Stacewicz* this notion by achieving an SNR of 55.56 dB using a VA, in contrast to the 32.46 dB obtained with a traditional TA, when measuring water vapour. Both studies used a three-stage amplifier design to achieve their output. Further studies have also supported this result, giving strong support to the benefits of the VA configuration over the traditional TA [163–165]. However, despite this 10 MΩ TAs are still the dominant amplifier in publications [129, 130, 138, 166, 167]

4.4.4 Balanced Detection

The electronic topologies described so far have been single-ended amplifiers, that is, with one active loop that provides a gain whilst the other side is grounded. In regards to monitoring QTF activity, this is the equivalent of holding one prong still and looking for the movement of the other. Balanced detectors roughly mirror the amplifier topology so that both prongs of the QTF can be monitored simultaneously. Not only does this increase the measured signal, it can also decrease the measured noise. Experimental analysis has shown that both balanced VA and TA detectors achieve improved SNRs compared to their single-sided counterparts [163]. However, this advantage also results in increased complexity of the pre-amplifier design, requiring more sophisticated circuitry. This added complexity may further decrease the likelihood of widespread adoption in QEPAS systems.

4.5 In This Thesis

In the following two chapters, we introduce two versions of a two-stage pre-amplifier. One version was developed specifically for capturing signals at $\sim$33 kHz, while the other captures frequencies closer to $\sim$12.5 kHz. This provides flexibility when considering the use of standard QTFs or custom QTFs. For each board, the initial stage comprises a balanced detector that has a substantial gain of +30 dB, and a subsequent stage, with a gain of +3 dB that serves to convert the balanced detection into a single output. Filter gain blocks are also designed and modelled to provide additional optional gain. A key consideration with these designs is simplicity of use, where all this is implemented in a system that can be powered on and does not need constant maintenance. In the following chapter (Chap. 5) the design and electronic modelling of each board are presented. Each board is then electronically characterised. Following from this, the design and build of a basic QEPAS ADM and gas chamber is laid out and discussed. The QEPAS chamber uses 3D printing and chemical treatment to provide a cost-effective test chamber which is then used to demonstrate the operation of QEPAS with one of the developed VAs. The next chapter builds upon this work, where we lay out the design and build of an optically improved ADM and detection

chamber. This chamber is then used in the direct detection of methane, which to the best of our knowledge is the first time a VA electronic amplifier has been used for this. This chamber is then used to compare the output signal for our developed VAs with a control TA. The performance of the chamber is also characterised and compared with the literature.

CHAPTER 5

Electronic Amplifier Design, Build, and Early Testing

In the following chapter, we cover work relating to the development and testing of two voltage amplifier (VA) circuits for use in QEPAS. We will present the electrical designs for both voltage pre-amplifiers (PAs), as well as additional secondary gain block filters (GBs), which can be chained to the PA output, to further increase the QEPAS signal. Firstly, the design of two voltage PAs, one more suitable for lower frequencies and one for higher frequencies will be covered. This will then be followed by the design and modelling of two GB designs that correlate with the expected operational frequencies domains for the PAs. The assembly and electrical characterisation of these components will then be covered to demonstrate their operation and frequency responses. In order to test the QEPAS capabilities of the higher-frequency designs, the development of a gas chamber and acoustic detection module (ADM) are subsequently covered along with initial QEPAS measurements.

5.1 Electronics Design

5.1.1 Pre-amplifiers

Designing PAs for use in QEPAS detection involves overcoming several key challenges that culminate in enhancement of the small electrical signal from the QTF whilst minimising noise. The design of the amplifier must also balance obtaining a high gain and SNR, with other factors including power demand, the operational frequency of the ADM, and compatibility with other integrated electronics. As highlighted in the previous chapter (Chap. 4), despite the widespread use and relative simplicity of transimpedence amplifiers (TAs), VAs have

been shown to achieve a better SNR both theoretically and experimentally. Based on this, pre-amplifiers were designed that do not require adjustment once implemented within a QEPAS detection unit. To provide a significant gain and easy-to-use output, we designed our amplifier with two gain stages. The first stage was a balanced VA with a gain of 30 dB, and the second stage was an instrumentation amplifier with a gain of 3 dB.

The first stage comprised of a balanced VA utilising two separate operational amplifiers (op-amps), and the second stage took the balanced input and output a single trace for measurements. This layout can be seen in Fig. 5.1 where the gain of the first stage is set by the ratio of R1:R2, and the second stage is set by the ratio of R4:R3. The design of the first was formulated so that it should provide the aforementioned benefits of using a voltage amplifier. The balanced nature should help reduce the effects of any unwanted electrical noise that would otherwise have a significant impact given the high gain of this stage. In addition these benefits would also carry over to the electrical characterisation of QTFs. Due to differences in the impedance of this design compared to standard TAs, the f_0 would be slightly different for an ADM using this design. However, the higher voltage response of quartz and lower noise floor would enable a clearer and more accurate characterisation of QTFs, so this should not be an issue. The amplifier design for the second stage was chosen specifically to extract the differential signal from the first stage. This is achieved by taking each of the balanced outputs from the first stage and routing one to the inverting inputs and one to the non-inverting inputs of the second stage op-amp. The second stage converts the balanced signal into a single output which makes the system easier to integrate into a general QEPAS system, whether that is to further gain stages or to a LIA for direct signal measurement.

The circuit boards were designed in two stages using Autodesk's EAGLE software. The first stage involved creating the schematics and selecting the appropriate components. The physical CAD layout for the corresponding PCBs was developed directly from these schematics. Two board variants were designed: one to operate at AC frequencies typical of some common custom QTFs, and the other to operate primarily around the standard 32.8 kHz QTF frequency. Although the physical layout of the boards are largely similar, each was tailored with specific electronic components that suited its respective frequency range. For clarity, we will refer

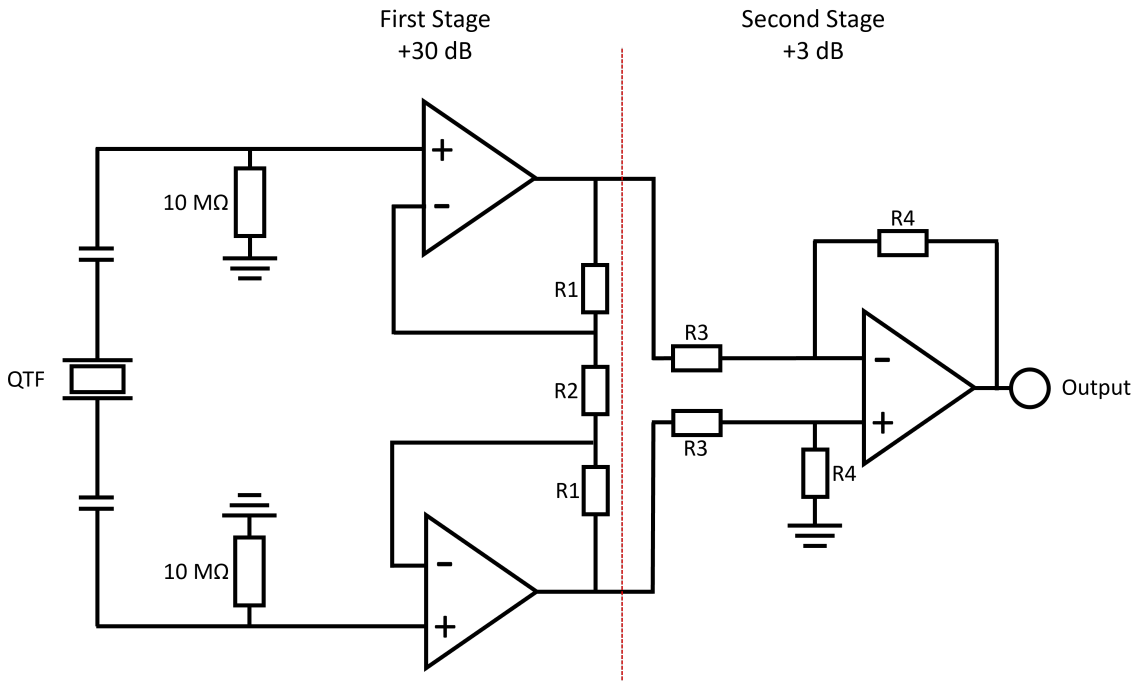

FIGURE 5.1: Schematic outlining the general design of the voltage pre-amplifier circuits, with the dotted red line demarcating the two gain stages. The gain of the first stage is set by the ratio of R1:R2. Likewise the gain of the second stage was determined by the ratio of R4:R3. Both the lower and the higher frequency boards had the same general design, however the operational amplifiers of the first stage differed.

to the first variant as the low-frequency (centred at 12.5 kHz) board and the second as the high-frequency (centred at 31 kHz) board, reflecting the primary frequency considerations in their design.

Both PCB designs feature a two-layer structure, with the lower secondary layer filled with a ground pour, ensuring protection of the components from external interference. The diameter of the trace widths was set to 0.30 mm, and the diameters of the vias was set to 0.35 mm. A right angle SMA adaptor mount was included for output channels.

Although the QTF is fairly resistant to acoustic noise, its high impedance makes it prone to electrical noise. Some of this is helped by the differential design that does help filter out external electromagnetic interference, however, the boards are still sensitive to noise introduction in a few key places. When coupled with the high gain of the system, several steps were taken to mitigate the risk of noise through several design features.

The area most exposed to the incorporation of noise is between the QTF and the inputs of the first op-amps. The boards were designed with two solder points to incorporate press-pin mounts that would connect the QTF prongs to the board. The area from each of these solder points to the input pins of the first-stage op-amps were boarded with guard shielding. The pin mounts are the only location where this initial input also carries to the lower layer, and the guard shielding was extended to here as well. The ground pour was also excluded from this area in order not to introduce a path for any potential ground noise to be carried to these inputs, potentially creating a feedback pathway. Furthermore, voltage regulators were incorporated to stabilise the power supply to both the positive and negative rails of the three PA op-amps. For the low-frequency board these were set to 5 V, and for the higher frequency board to 10 V, as guided by data sheet specifications for their respective op-amps.

Careful component selection, with a particular emphasis on the choice of op-amps, was also crucial in reducing the noise of the system. For the 31 kHz, high-frequency design, we opted for the ADA4627 model [168] for all three op-amps. Conversely, for the lower frequency design, we employ the LMC6001 [169] for the first two op-amps, keeping the ADA4627 for the second stage instrumentation amplifier. The selection of the ADA4627 for higher frequencies was based on its optimal impedance matching to the QTF, a low $1/f$ flicker noise corner at the expected operational frequencies, and a suitable gain-bandwidth product with a remarkably high power supply rejection ratio (PSRR) [168]. The latter characteristic is especially crucial for maintaining stability and noise control, important considerations given the large gain in this initial stage. Similarly, the LCM6001 is chosen for its optimal impedance matching and low $1/f$ flicker noise corner [169], but with better suitability for lower frequencies. Moreover, the gain-bandwidth product and the power supply rejection ratio of the LCM6001 also align with the requirements for operations at these lower frequencies.

In addition, both op-amps exhibit exceptionally low bias currents (see Tbl. 5.1), a critical factor in managing the offset across the entire board's biasing network. This feature is particularly significant, as it means that we can maintain low power consumption across the entire system while still achieving substantial gains, especially when coupled with the filter gain block.

TABLE 5.1: Summary of key Op-amp performance parameters.

Op-amp	1 kHz Noise (nV/$\sqrt{\text{Hz}}$)	PSRR ($\pm$V)	Input bias current (pA)
ADA4627 [168]	6.1	$5 \rightarrow 15$	5
LMC6001 [169]	22	$5 \rightarrow 15$	0.025

5.1.2 Gain Blocks

Although the initial gain stage imparts substantial amplification, in numerous QEPAS configurations, low-cost, low-power, and portable devices further signal enhancement can be beneficial. This additional amplification may prove particularly pragmatic in facilitating simplified processing with more straightforward or less sensitive ADCs. In addition, by combining the GB with a filter, this may not only increase the output signal but also help filter out noise, subsequently improving the SNR. To address this requirement, we devised two filter gain blocks tailored for each of the distinct frequency ranges — one chained to the lower frequency PA and the other optimised for chaining with the higher frequency PA. Both filter designs share a common layout, but differ in their resistor and capacitor values to generate different passband regions. The designs were modelled using the freely available Analogue Devices filter design tool [170]. The selected configuration for both filter blocks employs a 6^{th} order (0.3 dB) Chebyshev filter, with a gain of 40 dB. A simplified schematic of this is shown in Fig. 5.2. This specific design choice facilitates easy and precise frequency range selection and rapid roll-off characteristics, enabling robust noise suppression outside the selected frequency range.

For the higher frequency board, the centre frequency was set at 31 kHz with a 6.2 kHz pass-band. The lower frequency board had its centre frequency set to 12.5 kHz with a 2.4 kHz pass-band. The stop-band for both boards was set to -40 dB at 20 kHz. Both of these passband ranges enable standard and most custom QTFs to be used whilst still working to suppress unwanted signal. For example the higher frequency board still allowed the use of pilot line 28 kHz QTFs [97], and the lower frequency board was specifically designed for the use of QTFs with $f_0 \approx 12.5$ kHz as seen in numerous studies covered in the previous chapter (Chap. 4). In addition, a careful choice of operational amplifier was also employed in the

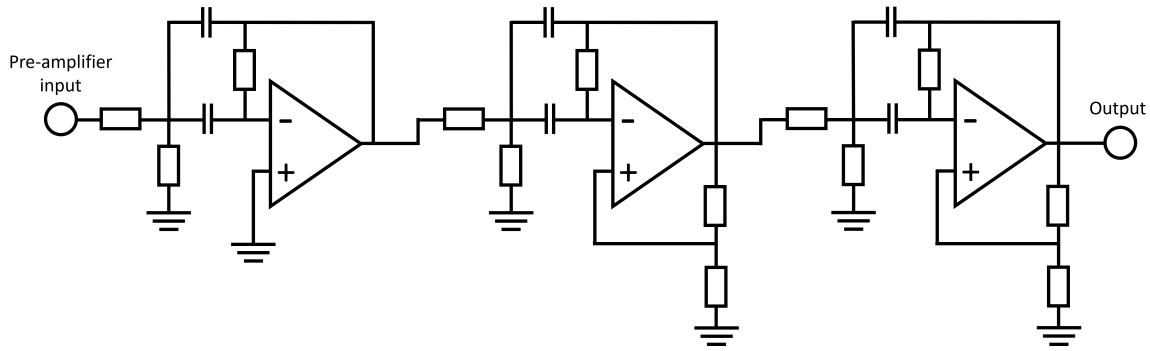

FIGURE 5.2: Schematic depicting the layout of the GBs. The topology follows a 6th order 0.3 dB Chebyshev filter with a gain of 40 dB. The physical layout and operational amplifiers remain consistent between the lower and higher frequency designs, however there is significant variation in the resistor and capacitor values.

design of these filter blocks. Here, we used the ADA series that employs three 4001 devices for each. The ADA4001, has desirable noise characteristics, a high PSRR, [171] and is compatible with the aforementioned software. For specific part values see Appx. A. Whilst QEPAS incorporates LIAs that utilise narrow-band filtering, the use of the Chebyshev filter was incorporated to allow greater flexibility in future designs. This filter design offers a highly flexible band-pass region that can obtain significant gain. Whilst we have designed ours to each fit a wide range of QTF fundamental frequencies, in cases where the QTF parameters can be more rigid the band-pass region can easily be either shifted or narrowed without significant topology changes. As such it is envisaged to compliment the LIA filter whilst still enabling significant gain without reducing the SNR. Specifically this filter design would help protect from low frequency 1/f noise. Whilst LIAs do incorporate a narrow band filter they are still susceptible to low frequency 1/f noise (arising from the use of low-pass filters to provide their narrow-band filtering effects). The narrow-band nature, and sharp roll off of the Chebyshev filter can help filter this out before it reaches the LIA.

5.1.3 Adder Circuit

To implement wavelength modulation spectroscopy (WMS) combined with a scanned wavelength approach, a high-frequency signal must be combined with a slow ramp. To combine these

signals with minimal noise and feedback, we designed and built an adder circuit. This circuit consisted of two primary input's and a single output. One input was designed for the high-frequency sine wave, which we will designate the HF signal. The second input was for the low-frequency ramp signal. Both channels had set gains as seen in Fig. 5.3, with the gains determined by the ratio of R1 to R2 (for the HF trace) and R3 (for the triangle wave input trace). These gains enabled the signal generators to run at more optimal voltages while maintaining a suitable modulation depth. Initially, we incorporated resistor values of: R1=10 kΩ, R2 =7.7 kΩ, and R3=69.8 kΩ.

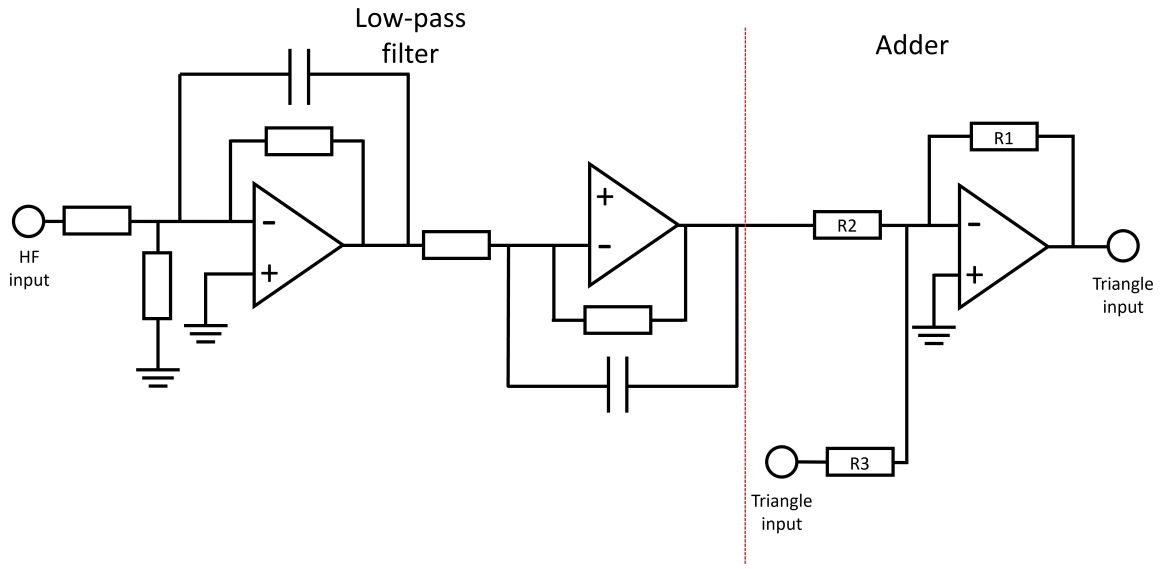

FIGURE 5.3: Schematic of the adder circuit, and high pass filter on the HF input. The adder circuit also performed voltage division with the gain set by the ratio of R1:R2 for the HF sign input, and R1:R3 for the triangle input. The triangle input could also be used for other waveform, such as saw-tooth, or BF-QEPAS signals.

The board had two additional integrated circuits. The first, also depicted in Fig. 5.3, was a low-pass filter on the HF line. This served two purposes; the first was to prevent noise from being added to the high frequency (HF) signal as this was the primary signal being locked to. This was to ensure that the HF signal was kept isolated from the ramp, primarily to keep a cleaner reference signal for the LIA. The full details of the design and layout, as well as part models, resistor and capacitor values, can be seen in Appx. A.

5.1.4 Assembly: Electronics

The printed circuit boards (PCBs) were commercially manufactured through JLCPCB [172], with all parts mounted in-house to enable flexibility if changes were needed. The printed boards can be seen in Fig. 5.4. Given the sensitivity of the op amps, all components were soldered with electrostatic discharge (ESD) protection. Metal film resistors with tolerances $\leq 1\%$ were exclusively chosen to ensure precise alignment between the actual outputs and the design specifications. To address the challenges posed by piezoelectric effects and temperature-induced drifts, multilayered ceramic capacitors were chosen, with tolerances $\leq 5\%$ wherever feasible. Exceptions to this practice were applied to larger value bypass capacitors on power supply lines, which was a concession made because of the high power supply rejection ratio (PSRR) exhibited by the selected op-amps. All solder joints were examined under microscope to ensure clean connectivity had been achieved.

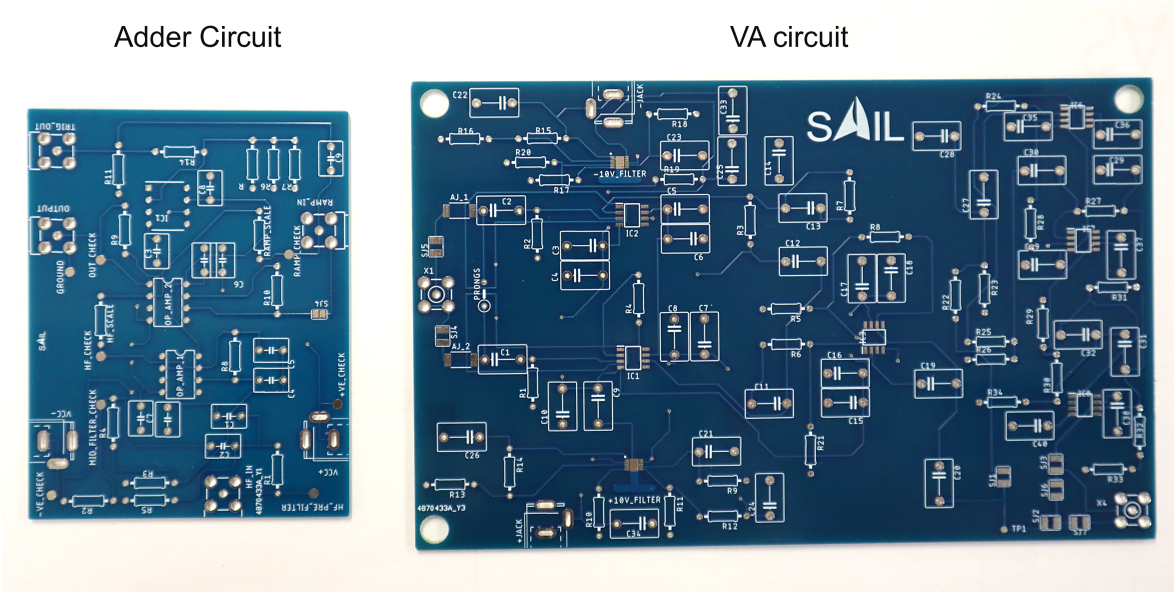

FIGURE 5.4: Picture of the printed PCBs prior to any part placements.

5.2 Electronic Characterisation

The following section covers initial electronic testing prior to the development of a QEPAS detection unit. Firstly, we cover the results obtained from noise modelling software, to

determine the expected frequency response which is then compared to the measured frequency response of each board. The noise floors of both boards are measured, with additional measurements of higher frequency board after the incorporation of a standard QTF. Finally, the voltage response of each board is tested for emulated QTF signals.

5.2.1 Frequency Response

5.2.1.1 Noise and Gain Modelling

Noise and gain modelling for the PAs was conducted using the Signal Chain Designer (Beta) from Analog Devices [173]. A differential voltage source was used as the sensor in the software. For the higher frequency board, the resistance was set at 100 kΩ and capacitance at 2.5 pC to reflect the values of a standard $f = 32.768$ kHz QTF [161]. For the lower frequency board the resistance was adjusted to 160 kΩ to better match custom QTFs operating at the expected lower frequencies [112]. Four stages were chained to this source, starting with a low pass filter, a differential gain block (representing the first stage of our amplifier designs), then a differential to single output gain block (to model the second stage), then finally to pass-band gain block. The inputs for the final block were directly linked to the software used in designing the gain blocks. Adjusting the parameters in each of the stages above allowed for the expected changes to the noise floor to be modeled. The output for the designs laid out in Section 5.1 can be seen in Fig. 5.5.

5.2.1.2 Experimental Methods

Frequency response sweeps were performed on both boards, housed in the metal box for shielding. The boards were powered by an external battery bank with two voltage settings that corresponded to the regulators on the low- and higher-frequency boards. Both boards and battery banks were placed on an electrostatic safe discharge (ESD) mat and all physical interactions were performed with ESD precautions in place. In addition a metal box was used to house the electronic boards during testing, and provide shielding from potential electromagnetic interference in the lab. The metal box was purchased and then customised

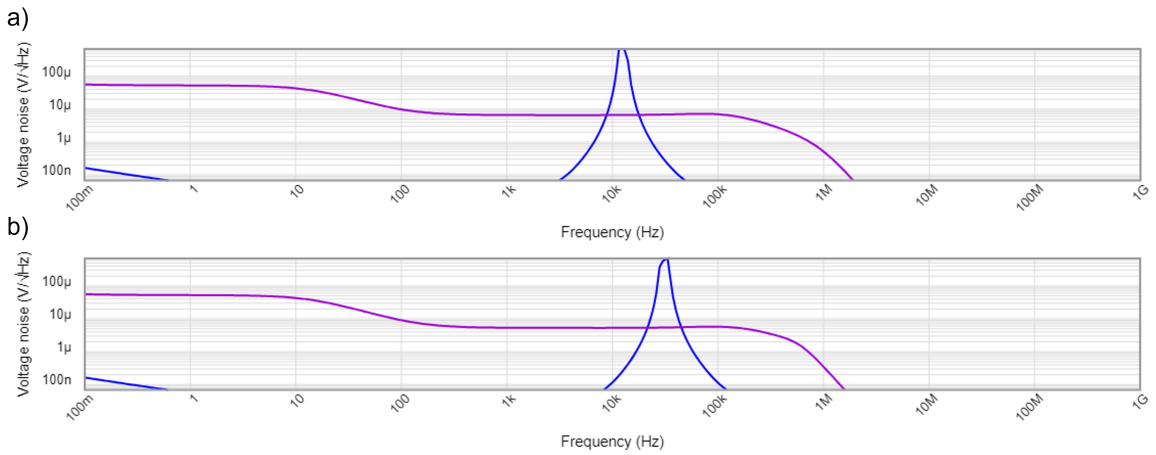

FIGURE 5.5: Output captures from the Analogue Electronics Signal chain designer. Noise modeling is shown for the a) lower and b) higher frequency boards.

by the School of Physics' engineering workshop. A milling machine was used to drill holes around the SMA and power jack ports, as well as smaller holes that enabled the board to be bolted inside the box.

For the battery bank twenty rechargeable Ni-Mh batteries, each rated at 1.2 V, were used to construct a long-life stable power supply for the boards. The batteries were separated into four smaller banks. Two banks consisted of 6 batteries in series and a common ground allowed them to provide both positive and negative 7.2 V rails. Two smaller banks were also included, each consisting of 4 batteries. These smaller banks could be connected in series with the others to increase the rails to 12 V each. The general schematic is laid out in Fig. 5.6 a). The batteries were housed in a 3D printed casing and had a single double three-way switch controlling both rails. Importantly, this bank also had two fuse housings with 100 mA fuses connected to ensure that no op amps were overloaded on the boards. The container was also coated in metal tape to protect it from electromagnetic interference. A picture of the finalised bank can be seen in Fig. 5.6 b).

A Liquid Instruments Moku-Pro [174] was used as a function generator. Two output lines were connected to each of the input pins on the amplifier boards. This conversion was done using a BNC cable from the Moku-Pro to a custom-made connector. The connector consisted of two parallel SMA cables terminated with metal pins, analogous to the output pins on a QTF.

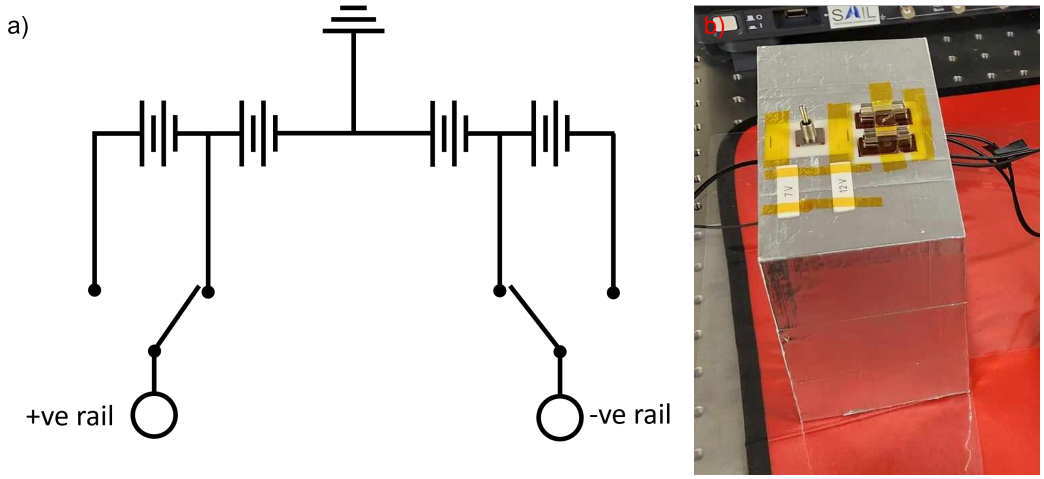

FIGURE 5.6: a) Schematic of the battery bank design. b) Picture of the battery finished battery bank, ready for use.

This connector can be seen in Fig. 5.7, where panel a) shows it connected to the electronic board as it is housed in the metal box for shielding and panel b) shows the alignment of the press-fit pin mounts to the connector output pins.

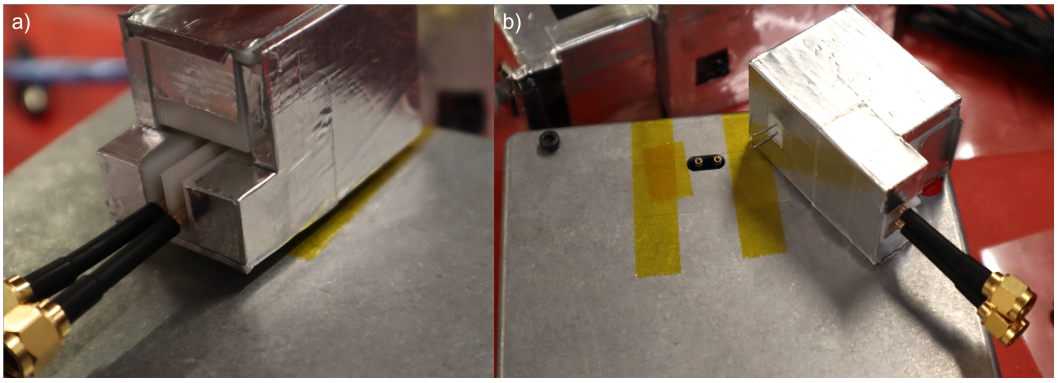

FIGURE 5.7: Pictures showing the customised connector. a) Connector fitted to the input pins of the board. b) Connector pulled back to show the alignment of the pints with the connector.

The output of the amplifier boards was connected, through SMA to the BNC cable ($50\ \Omega$) to the Moku-Pro, which acted as the LIA for the setup. This setup is depicted in Fig. 5.8.

The voltage response of each board was carried out using the Moku-Pro frequency analyser tool. Sweeps were performed for each board for 8192 points in the frequency range of $70 \rightarrow 70 \times 10^3$ Hz, at $5\ \mu$V (after voltage division). Each point consisted of 5 cycles with

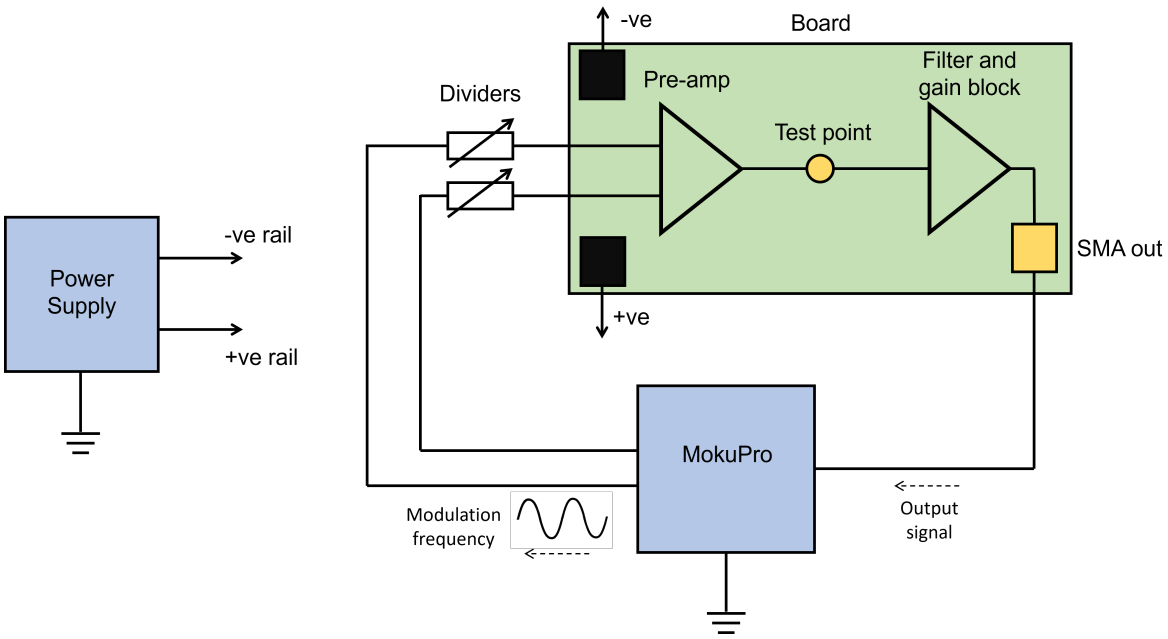

FIGURE 5.8: Schematic depicting the experimental layout utilised in carrying out frequency sweeps of the boards. The MokuPro acted as both the function generator and LIA. For test of the higher frequency board the power supply was set to $V = \pm 12$ V, and for the lower frequency board to $V = \pm 7$ V.

individual averaging for 5 ms and spaced with a 100 μs settling time. Frequency responses were conducted for the PAs chained with the GBs.

5.2.1.3 Results and Discussion

Given the frequency-specific nature of a QEPAS ADM, the design of our boards also had to take into account frequency responses. The 6th order Chebyshev filter, that was chosen operates by essentially combining three band pass filters together. The output of the whole filter essentially combines these together, which gives rise to a relatively flat response in the desired band pass region. The filter design tool that was used for the GB also provided the frequency response, which can be seen in Fig. 5.9 a).

Early testing focused on passing a signal to the boards and measuring the response at different frequencies, to be compared with the expected response from modeling. The first tests utilised the Moku-Pro's frequency analyser tool. Since this allowed testing to be done over a wide range of frequencies and simultaneously monitor the demodulated 1f signal, this was a good

starting analogue for a QEPAS signal, which would also require demodulation, and allowed for a direct comparison to the model's simulations. As seen in Fig. 5.9 b) the overall shape of both boards is close to expectations. Looking at the band-pass region for the lower frequency board we would expect the band-pass region to start rolling off below 11.60 kHz and above 13.64 kHz. From the frequency sweep, we can see that the board begins to roll off below 11.52 kHz and above 13.20 kHz. Likewise for the higher frequency board the modelling shows roll-off start below 29.07 kHz and above 33.78 kHz. The voltage sweep shows that the actual values are 28.37 kHz and 33.77 kHz, respectively.

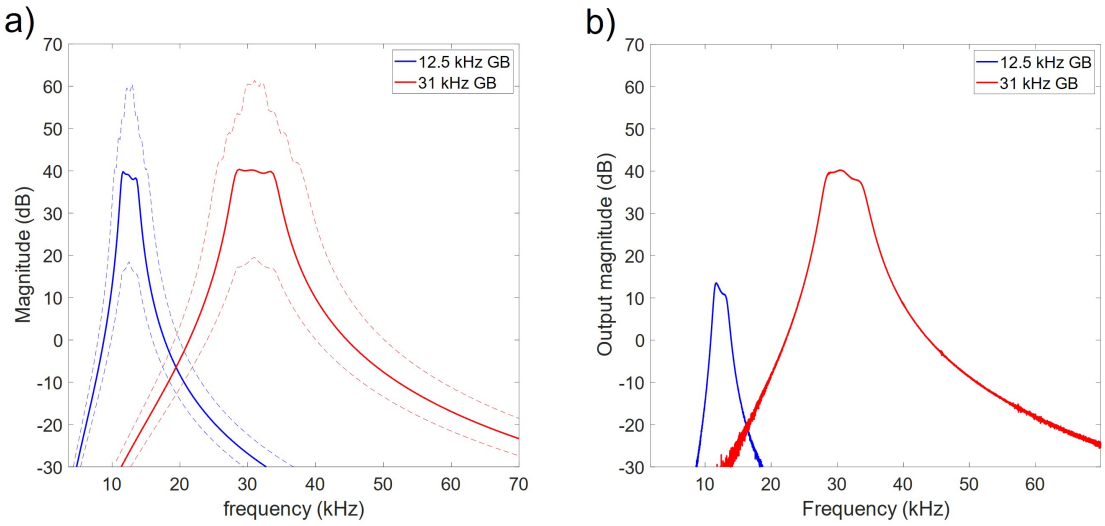

FIGURE 5.9: a) Simulated electronic responses of the GB as modeled using the filter design software tool. The dotted lines represent the maximum and minimum possible responses based on the tolerances of the parts used. Resistor tolerances were set to 1% and capacitors to 10%. b) Frequency response curves for each board to an input of 5 μV. The signals are are obtained from 5 100 ms cycles demodulated at 1f.

The simulated response, from the modeling software give a range that arises primarily from the tolerances of the resistor and capacitors. All resistors purchased for the boards had tolerances $\leq 1\%$, so a variation of 1% was used. However, the capacitor tolerances for the model were set at 10% as several components could not be sourced below this range. This introduced more variability in the potential responses of the boards. The response of the higher-frequency board is well within this tolerance and sits very close to the ideal designed response. However, the lower frequency board exhibits a response that indicates an overall

gain of ∼37 dB less than the higher frequency board, and this sits below the lower tolerance level.

5.2.2 Noise Floor Testing

To further evaluate the performance of the amplifier boards, focus shifted to characterising the noise floor - an essential step for their intended use in QEPAS. QTFs from Mad City Labs (large size) were sourced, with the standard centre frequency of 32.768 kHz. This enabled direct QTF noise floor testing with the higher frequency board, and will be used later to constructed a QEPAS ADM. Fast Fourier transform (FFT) analysis was chosen to assess how various conditions impacted the noise floor. However, initial attempts to integrate the QTF revealed a significant issue: its inclusion caused the amplifier circuit to enter a feedback loop, driving the op-amps to their maximum output and producing unreliable noise floor measurements. Consequently, the QTF was temporarily removed to address this issue, allowing accurate noise characterisation and improvement before full integration could be revisited.

5.2.2.1 Experimental Methods

The boards were powered using the battery bank, as previously described. The output was connected to a Rohde & Schwarz Digital Oscilloscope (RTB2002). Ffts were obtained with a resolution band width (RBW) of 50 Hz, a centre of 35 kHz, and a span of 70 kHz. The data presented consists of an average of 16 individual traces. This setup can be seen in Fig. 5.10. The input pins in this diagram represent where the input of the board could be loaded.

5.2.2.2 Results and Discussion

The necessity of incorporating a QTF meant that the noise floor had to be reduced. Given that the previous frequency sweeps had indicated that at least the GB filter was likely operating within expectations, the performance of the pre-amplifier was considered. Initially, we considered two likely sources for the build-up of noise when the QTF was incorporated. The

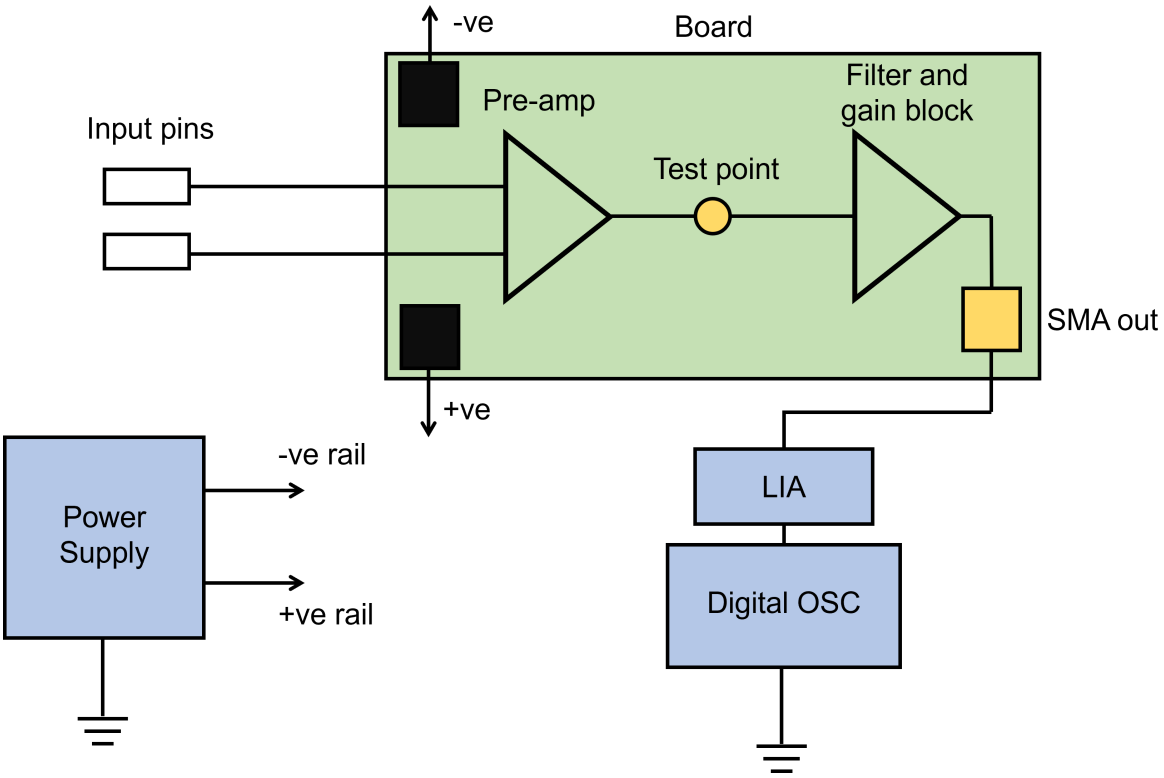

FIGURE 5.10: Schematic depicting the experimental layout utilised in taking ffts, to measure the noise floor of the boards. For test of the higher frequency board the power supply was set to $V = \pm 12$ V, and for the lower frequency board to $V = \pm 7$ V.

first was feedback within the board. If there was some capacitance between the inputs and outputs then, given the high gain of the system, it was possible that electrical energy could continue to accumulate within the amplifier until the op-amps reached their output limits. The second potential source was noise being added through the voltage rails to the op-amps. Although, all the op-amps had high PSRR, if unwanted noise managed to pass through then the extremely high internal gains of the transistors could be adding large unwanted signals to the QTF.

To address the first problem, a second high frequency board was printed and assembled with two modifications. Since the initial input between the QTF and the first op-amps is sensitive to noise, this area was elongated on the new PCB to enable larger physical separation of both the electrical components and routing wires from each other, reducing any potential electromagnetic coupling. The second modification involved reducing the gain from the first

stage of the pre-amplifier. Resistance in the R_1 position was reduced from 100 kΩ to 50 kΩ, bringing the gain down to 15.5 dB. The primary consideration here was reduce the impact of any feedback, although this would reduce the gain of a QEPAS signal it would also allow for better dissipation of any AC signal still coupled with the input. Another aspect that was considered was the thermal noise of the resistors. The effective voltage of thermal noise for a given frequency bandwidth of 1 Hz can be calculated from:

$$e_{th} = \sqrt{4kTR} \tag{5.1}$$

where, $k = 1.38 \times 10^{-23}$ JK^{-1} is Boltzmann's constant, T is the temperature, and R is the resistance [175]. This means that to reduce thermal noise, the frequency bandwidth, temperature, or resistance need to be reduced. Given that the system requirements do not enable practical modification of the first two, this leaves resistance as the only viable alternative. Therefore, the aforementioned drop in resistor values should also provide a drop in thermal noise. Using the noise modelling software above, decreasing the gain, by reducing the resistance, reduced the noise at $f = 32.7$ kHz from 651 μV/$\sqrt{\text{Hz}}$ to 343 μV/$\sqrt{\text{Hz}}$.

To address the second potential issue, the operation of the voltage regulators was re-assessed. The voltage regulators, which for the purposes of analysis includes both the op-amps and the surrounding resistor and capacitor components used to control them, do introduce a number of extra components that can potentially introduce more noise to the system. The initial design considerations counted on the noise of the individual components that comprised the regulators being offset by the regulators as a whole system. However, this may not have been the case, so to see if the regulators were contributing to the problem, they were bypassed. A thin copper wire was soldered between the output of the power jacks and the output of the regulator. All resistors and capacitors that were incorporated into the voltage regulator portion of the circuit were lifted, after removal of the solder. The lifting the components meant they were removed non-destructively, so that regulator functionality could be restored for further testing if it was found that they were not causing the issue.

FFTs were used to measure the noise floor before and after the modifications. The results shown in Fig. 5.11 demonstrate that both measures significantly reduced the noise floor. Within the band-pass region the noise floor dropped by ∼10 dB, and by up to ∼30 dB outside this region. Both solutions produced similar noise floors, though there were some differences in the exact shape of the passband region. At 32.768 kHz the bypassed board was only 2 dB lower than the reduced version.

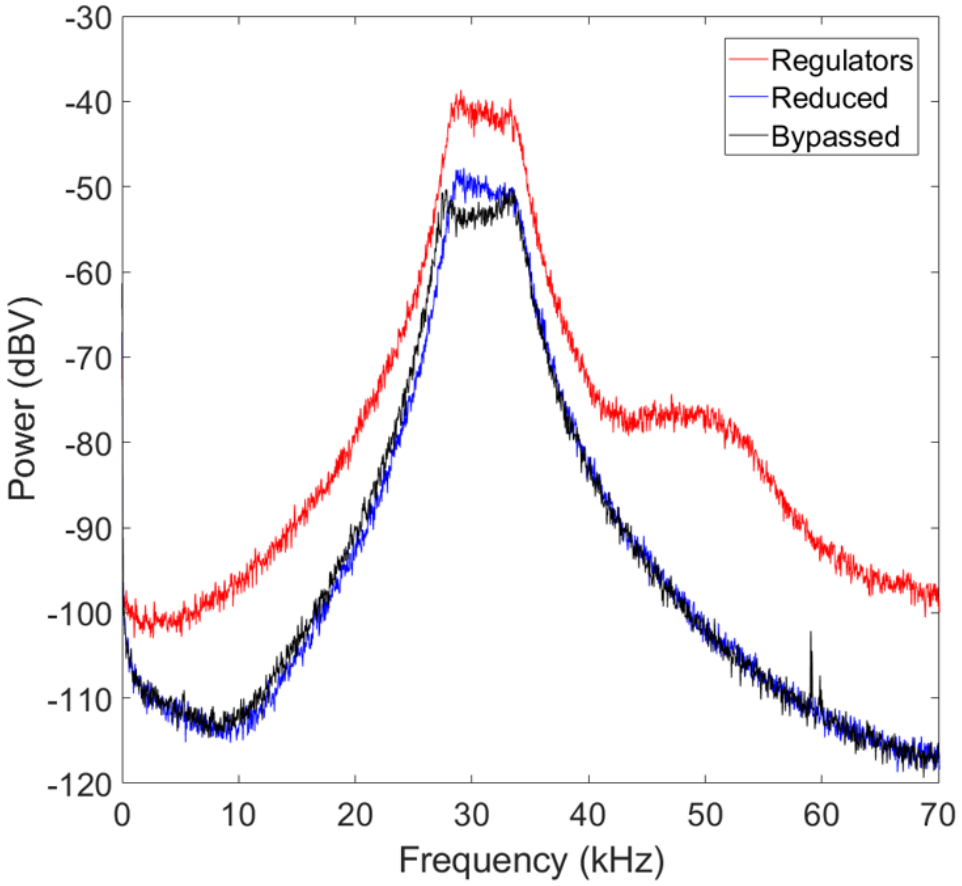

FIGURE 5.11: FFTs showing the noise floor for the 32 kHz board as the two fixes were applied. FFTs were obtained with an resolution band width of 50 Hz, and span of 70 kHz. Here we can see the (red) initial board before any modifications, (blue) board after the initial gain was reduced, (black) board with full gain and the voltage regulators being bypassed.

Given that both approaches produced similar results, further testing and development was carried out using only the bypassed board. The bypassed board allowed the reduced noise floor to be retained without sacrificing the gain of the initial PA. Given this, the next step was

to check the noise floor which a QTF fixed to the input prongs. Unlike the original board, the QTF could be inserted whilst the board output remained stable. This can be seen in the black trace of Fig. 5.12 a), where a peak can be seen at $\sim$32 kHz corresponding to the expected resonance of the QTF. Given that the resolution band width was 50 Hz, this was not used to determine f_0, although this trace did indicate that a QTF could be incorporated into the bypassed board.

Furthermore, in Fig. 5.12 a) the results for the noise floor tests are also shown for other inputs. Here, the input pins were either left bare or a resistor was input to each one. From these results, we can observe that the noise floor decreases with resistance, as expected from Eqn. 5.1. It should also be noted that when the pins are left bare the input resistance is 10 MΩ from the resistors bypassed to ground just before the first op-amps, which is in agreement with the bare pins producing the highest noise floor.

During noise floor tests, the contribution of potential electromagnetic interference was also investigated. As described above, guard shielding was incorporated into the boards around the QTF input pins, to protect from unwanted electromagnetic interference. Given the high gain across the whole board, the decision was made to additionally encompass the boards within a metal box, to shield the entire circuitry. As seen in Fig. 5.12 b), the noise floor of an unshielded board is largely the same as a shielded one. It is clear though that the shielding significantly helps to remove spurious unwanted signals. Some of these signals are suppressed by the GB filter, as seen between 55-70 kHz, however, it is noteworthy that there are five signal peaks between 32.3-33.6 kHz. Not only do these fit within the passband region, they also cover the expected resonance frequency of standard QTFs. This supports the need for careful shielding of the electrical components and, in addition to the shielding around the boards, it was also decided to shield components that attached to the input pins. For the customised connector used in the following section to emulate a QTF signal, the 3D printed sections were coated in metal tape.

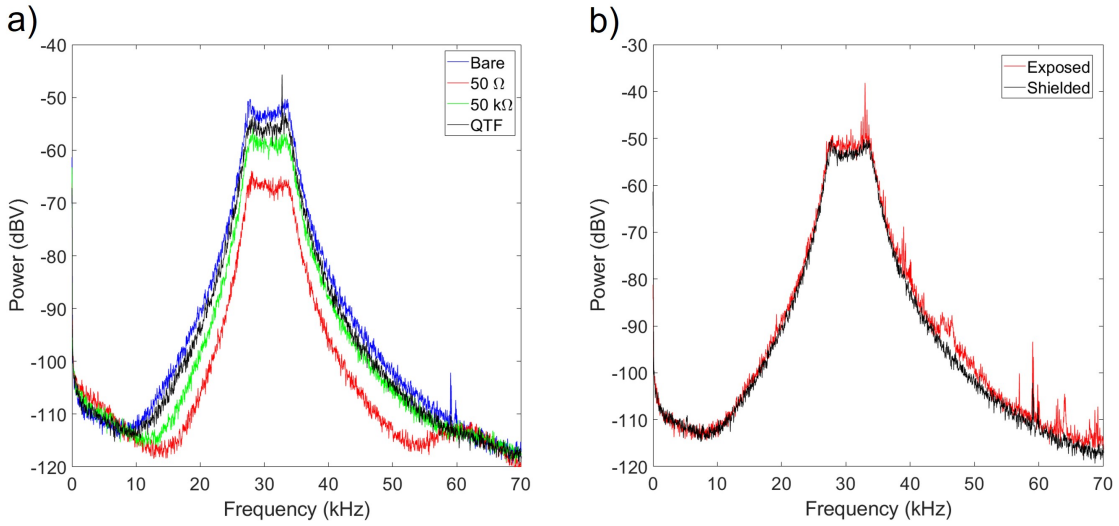

FIGURE 5.12: a) Noise floor of the 32 kHz board for differing input impedance. b) Fft tests showing the noise floor for the bypassed board (red) without any shielding, and (black) whilst the board is shielded in a metal box to protect from electromagnetic interference.

5.2.3 Emulating a Quartz Tuning Fork Signal

Most importantly for electrical characterisation was the simulation of a QTF signal and the determination as to whether it can be picked up by the use of a LIA. To emulate a QTF signal, two sine waves were generated at 12.5 kHz for the low-frequency board, and two were generated at 32.7 kHz for the high-frequency board. Using the custom-built connector, these emulated signals were passed to each of the input pins on the respective boards. The signals were phase offset by 90^o to match the expected differential signal of a QTF.

5.2.3.1 Experimental Methods

To emulate a QTF signal, two 32 kHz signals with a 90^o phase offset were generated and passed to each input pin. Voltage dividers were incorporated into each cable. The voltage dividers consisted of a central 50 kΩ resistor with a 50 Ω on either side, wired to ground. Signal generation and demodulation was performed using the Moku-pro. The LIA was set to a bandwidth of 0.7 Hz (corresponding to $\tau = 227$ ms), with a slope of 24 dB and a gain of 0. 1f signals were averaged over 30 s, and the error was determined by the standard deviation.

Testing was conducted for pre-amplifiers alone as well as the pre-amplifiers chained with the GBs. To switch between the two a series of soldier joints were incorporated into the design, so that the output of the pre-amplifiers after the second stage could be directly connected to the SMA output pin for direct monitoring; this would essentially bypass the GBs. The simplified schematic can be seen in Fig. 5.13. To chain the BG, solider joints would be lifted or deposited, according to the detailed design schematic seen in Appx. A. The metal shielding box has a removable base so that these modifications can be made without having to completely remove the board each time. Grounding the box also provided an extra level of electrostatic discharge (ESD) protection both while these modifications were being made and during testing.

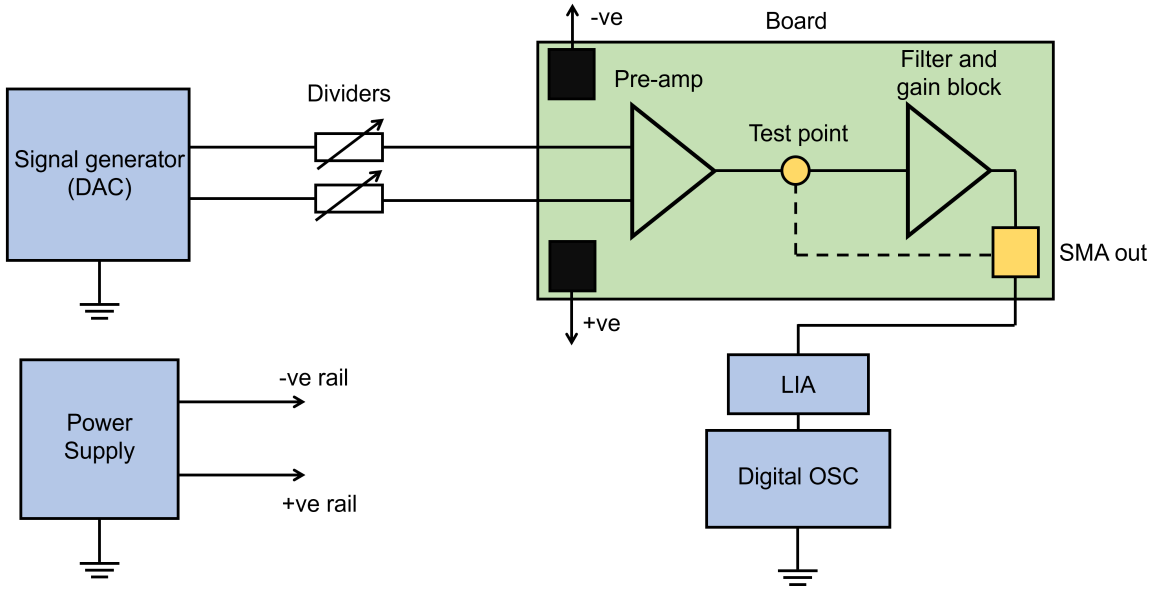

FIGURE 5.13: Schematic of the setup used to test emulated QTF signals.

5.2.3.2 Results and Discussion

Initially, only PAs were tested. As can be seen in Fig. 5.14 a), both boards were able to produce a measurable signal, down to 0.75 μV. This is well within the range of expected QTF signals, which indicates that they are operating as required, in that both the lower- and higher-frequency boards are capable of producing a measurable response from a QTF signal. Furthermore, regression analysis showed that the measured output voltage scaled linearly

with the input; both boards had $R^2 = 0.99$. The linear response is key in obtaining reliable QEPAS measurements. It also indicates that there is no nonlinear feedback occurring, which may have been occurring before the voltage regulators were bypassed.

A similar test was conducted where the GBs were chained to the PAs. Given the strong linear response of the PAs alone and the high gain of the GBs, even smaller signals were emulated. This time with a minimum of 0.21 μV being passed to the boards (as seen in Fig. 5.14 b)). The response of both boards was linear with an $R^2 = 0.99$. Combined with the previous results this demonstration shows linearity in both the PA and GB portions of the electrical circuits.

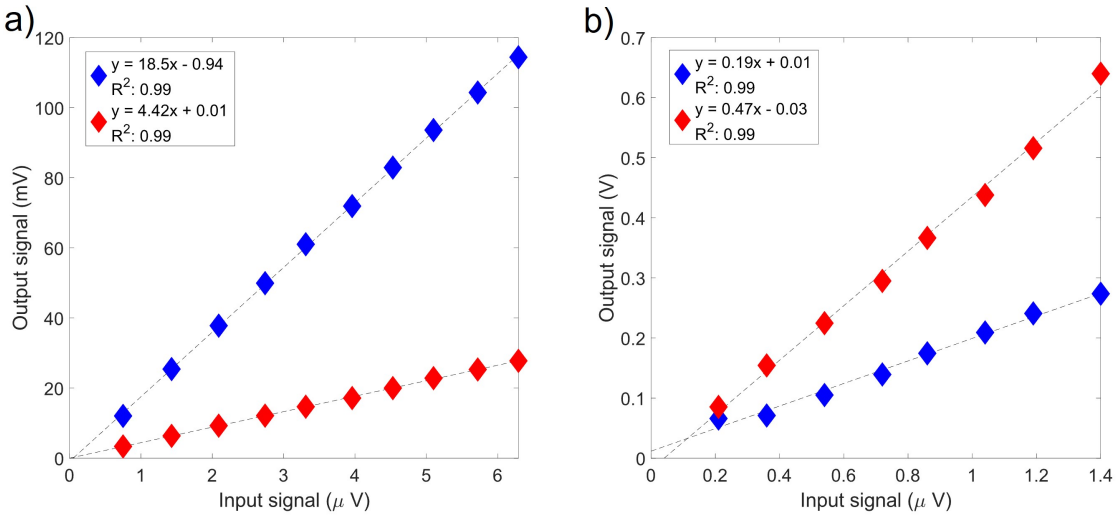

FIGURE 5.14: a) Voltage response of the pre-amplifier to an emulated QTF signal at 12.5 kHz (blue) and 32 kHz (red). b) Voltage response of the pre-amplifier chained with the gain block to an emulated QTF signal at 12.5 kHz (blue) and 32 kHz (red). Regression analysis was performed to confirm the linearity of the response; given the high R^2 values in all cases it is apparent that the boards operate with the expected linear response.

The input impedance is also worth noting here. The voltage dividers were customised to use resistors that were close to the expected resistance of a QTF; however, it was not possible to match the BNC cables and the signal generator (with impedance 50 Ω) to the QTF. Given this a direct voltage-to-voltage comparison should not be made between these tests and a QTF, however, they still provide a useful initial test point. Given that very low signals were successfully amplified and the responses were linear, this shows that the boards are

performing well within expectations and that the response is sufficient to obtain direct QEPAS measurements. Furthermore comparing the linear fits for the pre-amplifier to those with the GB chained we obtain gains of 20.2 dB for the lower-frequency board and 40.2 dB for the higher frequency board.

5.3 Chamber Design

Once electrical characterisation showed that the boards were capable of measuring the output from a QTF, it was pragmatic to setup and test this with an optically generated QEPAS signal. To this end, the following section covers first the design and build of an in-house produced QEPAS gas chamber and ADM, and then the proof-of-concept with the results for QEPAS measurements of methane.

5.3.1 Acoustic Detection Module

The QEPAS detection module was designed in two distinct sections. The first was the ADM, was designed and built around the QTF. It consisted of three separate components to facilitate the easy assembly of the final ADM package. The first component was a simple mounting bracket for the QTF. This consisted of a round socket to fit the base of the QTF, holding it in place, and an arm that extended out from this base. The purpose of the arm was to provide a point to clamp this component so that the QTF could be aligned in the assembly phase. The second component, the largest, was the main framework for the ADM. This was roughly a rectangular prism with a section removed for insertion of the QTF, and features to hold other components. A groove at the bottom of this section allowed the prongs of the QTF to extend below this structure, enabling connection to the amplifier boards. Two semicircular groves were embedded either side of this location to fit two hollow tubes that would make up the MRs. Next to this was a further inset to house a GRIN lens that would enable the excitation of an acoustic signal. The third component was a simple rectangular cap that fit around the optical fibre that connected to this grin lens. This enables the components to be

sealed, after placement, within the gas chamber. These designs can be seen in Fig. 5.15. For dimension-specific information, a technical drawing can also be found in Appx. A.

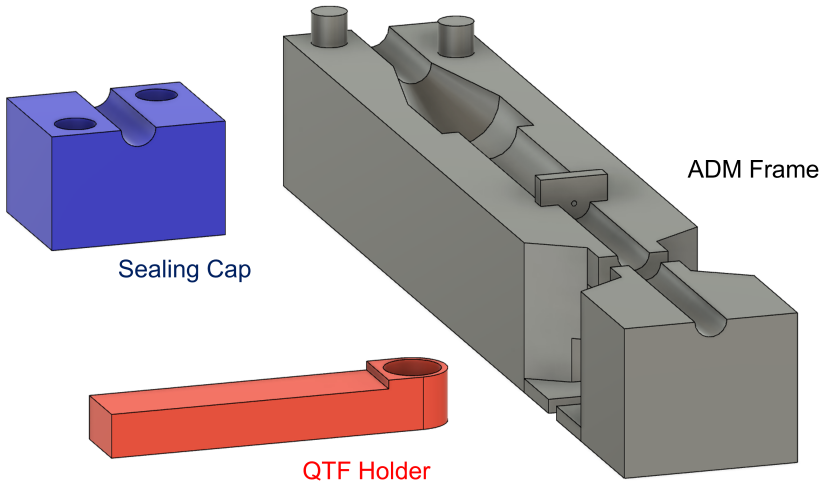

FIGURE 5.15: CAD designs of the main ADM framework (grey), QTF holder (red), and the cap for sealing the optical input to the module (blue).

A ThorLabs 50-1310M-FC GRIN lens fibre colimator was intended to be used in the ADM frame to colimate the output of the laser diode so a grove was designed specifically to fit and align it with the QTF. Since the beam diameter was expected to be 1.1 mm, larger than the prong distance of the QTF (0.3 mm), an aperture was included in the design of the framework to limit the laser intensity incident upon the QTF surface.

5.3.2 Gas Chamber

A gas chamber was also designed to house the ADM and allow controlled concentration measurements to take place. This section consisted of a main chamber and several smaller components that could be assembled together to create sealed QEPAS detection unit. The main gas chamber was designed to fit onto the metal boxes that shielded the amplifier boards. To this end the main chamber comprised of a T shape with two legs either side. Two legs protruded from the ends of the upper T section, these allowed for closer fitting to the metal

box, and two small extensions from each of these provided the possibility to bolt the chamber the box if needed. The main gas cell comprised of a narrow rectangular grove to fit the ADM once it was assembled. A hole was positioned to allow the metal prongs of the QTF to protrude through the chamber so that it could be connected to the input pins of an amplifier board. Consequently, the base of this grove was kept only 2 mm thick to leave more space for the metal connection wires of the QTF to reach the board. The rest of the walls around the centre structure were left thicker to help seal the chamber. In addition two large holes ($\varnothing = 13$ mm) were bored through each side to enable the placement of pneumatic connection points. Two small er components were printed to seal the chamber: a rectangular cap was to seal the chamber above the ADM at the lower T section above the ADM, and a rectangular block acted as a simple lid. The CAD designs for this chamber can be seen in Fig. 5.16.

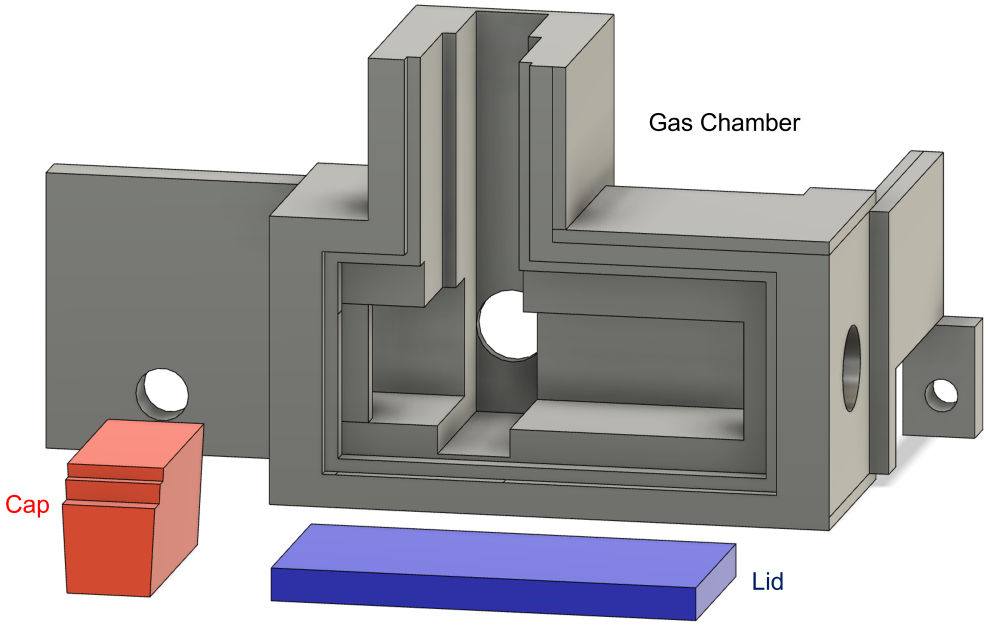

FIGURE 5.16: CAD designs of the gas chamber (grey), sealing cap (red), and the simple lid (blue).

5.3.3 Assembly

The framework components for both the ADM and the gas chamber were 3D printed. The ADM required high precision, given the need for careful optical alignment of the components.

As a result, these components were printed with the Form 3 resin printer, using setero-lithography (using Formlabs black V4 resin), with a resolution of 25 μm [176]. After the components were printed they were rinsed in an isopropyl alcohol bath before being cured in a Formlabs Form Cure oven. This printing method provided the resolution needed to align the optical components with the QTF and MR tubes.

The ADM framework was mounted on a custom-made 3D-printed base. This base was secured to a 3-axis optical stage with thumbscrew micrometers for precise movement. To hold the framework in place, Kapton tape was used to attach it to the 3D printed base, allowing for easy adjustments and alignment. An example is shown in Fig. 5.17 a), which shows an AMD frame while it is taped down during assembly. The QTF holder was simultaneously clamped in place. Firstly, the QTF was fitted to the round socket and glued in place using UV-cured optical adhesive. This stage is shown in Fig. 5.17 b), where the QTF has just been glued to the holder and the ADM framework can be seen secured to the stage in the background. Once the QTF was secured to the holder, the clamp was moved close to the ADM framework. The QTF was then positioned using the micrometers on the stage, whilst a binocular microscope positioned above the setup allowed for exact positioning to be monitored. The QTF and holder were then secured in place using optical adhesive and the clamp removed. The GRIN lens fibre colimator was then glued in place before each of the MR tubes were added. Finally, the cap was secured, before the whole ADM module was left to stand for 24 hours.

The gas chamber components were printed by extrusion using the Method X printer. This method was used here as the components were larger and required less precision that the smaller ADM parts. The components were printed from ABS-R using a water-soluble support structure. To remove the support structure, the prints were submerged for 4 hours immediately after printing. The components were then bulk dried with compressed air, before being placed in an oven at 100 ^{o}C for 4 hours. The components were then left to air dry for a further 48 hours.

To help seal the final chamber all the gas chamber components were chemically annealed to close the air gaps arising from extrusion layer printing. A gas chamber was made by lining the base and edges of a polypropylene box with non-residue microfiber cloth. The cloth was

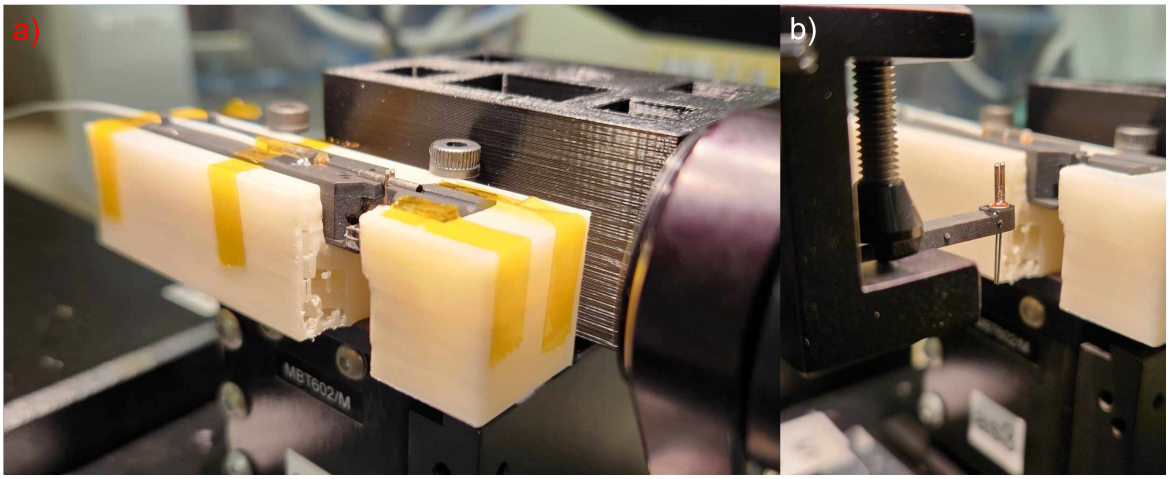

FIGURE 5.17: a) Picture of the the main ADM framework secured in place on the stage for alignment. b) The QTF, still in its holder prior to attachment onto the ADM.

then saturated in acetone, and the components were placed on a metal platform in the centre of the box to avoid direct contact with liquid acetone. The box was then sealed and left for 1 hour. The components were then removed and left to air dry for 48 hours (due to the volatile nature of acetone no further oven drying was used). The change to the printed surface can be seen in Fig. 5.18 which shows a comparison of the 3D printed surface before and after annealing.

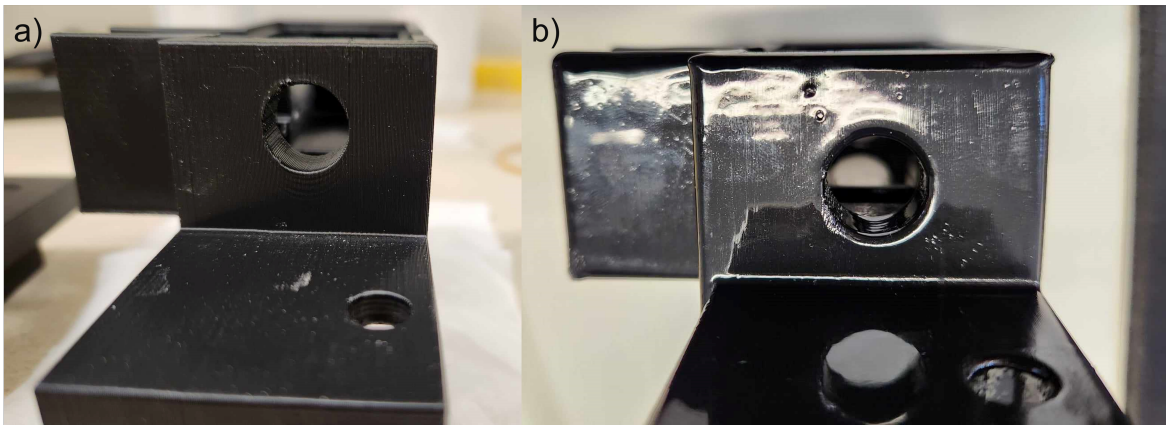

FIGURE 5.18: Pictures showing the comparison of the 3D printed plastic surface a) before and b) after chemical annealing.

The final chamber was then assembled by first adding the ADM module to the base of the gas chamber. Two straight threaded male to push (6 mm) adapters were then screwed to

the holes on either side of the chamber. After which both the cap and the lid were placed. All components were secured one at a time using epoxy glue, with a minimum of 2 hours between each to allow the glue to settle. Both the UV-cured resin and epoxy were selected due to relatively low out-gassing, though, as a precaution the chamber was left to stand for 48 hours before testing began.

5.4 Fixed Wavelength Testing

With the test chamber now assembled, optical testing commenced. The primary goal here was to provide proof of concept to show that the electronic amplifiers were capable of successfully measuring a QEPAS signal. In addition to measuring a QEPAS signal, for the purposes of gas detection, it was also important to determine the relations between methane concentration and the measured signal. This next section covers early fixed-wavelength measurements as a relatively straightforward starting methodology to achieve this. We will cover initial testing performed with the chamber, then optimisation of test parameters, followed by a further round of testing and a discussion of SNRs, and potential detection limits.

5.4.1 Initial Testing

5.4.1.1 Experimental Methods

The Eblana Photonics diode laser (EP1653-7-DM-B01-Fa) provided the light source for all optical measurements. The diode laser operating conditions and modulation were regulated with the TL101 laser control board. The wavelength was monitored and set using a Burliegh WA-1100 wavemeter, connected directly to the fibre output of the laser. Using this meter, the centre wavelength, power, and temperature were set using variable capacitors on the control board. The laser was centred at 1653.73 nm with an output of 3.905 ± 0.004 mW. No modulation was applied while aligning and setting the centre wavelength.

A fixed wavelength approach was taken to produce the acoustic signals. A high frequency sine wave ($f = 32.768$ Hz) was produced using the Moku-Pro's inbuilt signal generator, and

this signal was fed directly into the laser control board. The laser output was coupled directly to the GRIN lens in the chamber. The chamber itself was placed directly on the metal box that shielded the boards, with the QTF output pins directly connected to the press-pin mounts on the board.

The amplifier output was demodulated using the Moku-Pro's inbuilt LIA and recording software. The LIA bandwidth was set to 0.7 Hz (0.227 ms) with a slope of 24 dB/oct. This general setup is illustrated in Fig. 5.19. Signals were measured over a 30 s window, with the average taken as the signal value and the standard deviation (1σ) as the error.

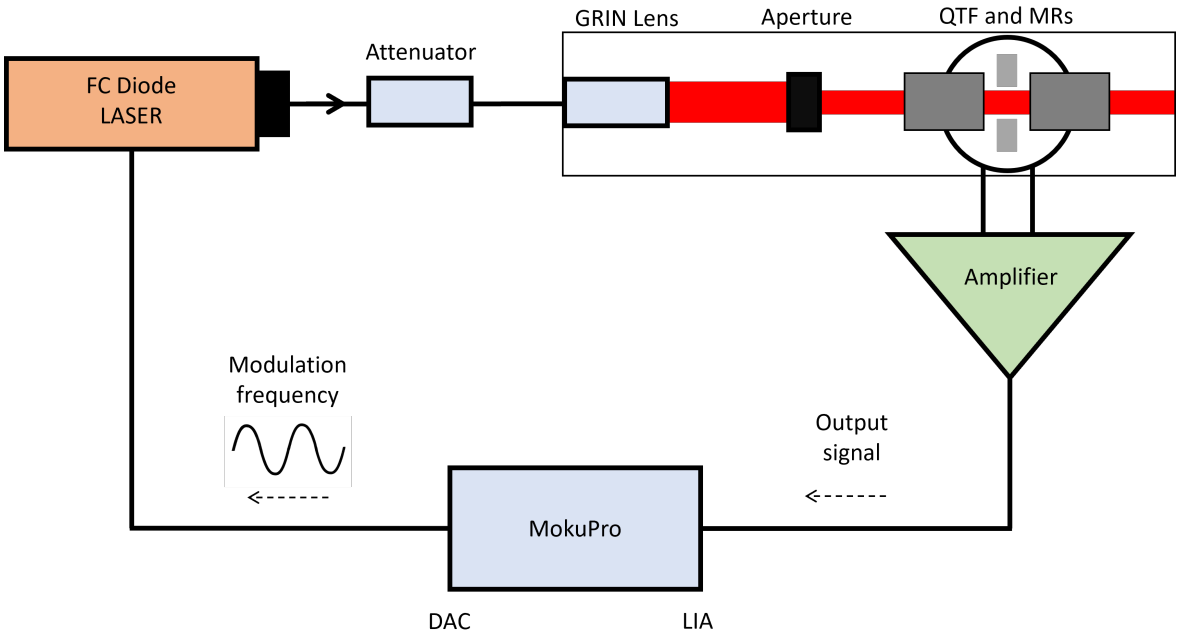

FIGURE 5.19: Schematic of the experimental setup to perform fixed wavelength measurements. The thin black box represents the components housed within the 3D printed gas chamber and ADM. The attenuator was connected in series using fibre couplers, only for the power dependence testing.

Methane was supplied using CAC calibration gas cylinders, which were connected to the board using pneumatic pipping. The chamber connected to the board is shown in the picture in Fig. 5.20 a). The setup for gas control can be seen in panel b). At the start of the test the gas cylinder was disconnected at valve 1, whilst 2 and 3 were left open and the vacuum pump run for 30 seconds to flush the chamber. To fill the chamber with a given concentration, valves

2 and 3 were opened first. Valve 1 was then opened for 10 s. After the pressure dropped back to the room level, both valves 2 and 3 were closed.

Concentration sweeps were performed by filling the chamber with increasing concentrations of methane ($0 \rightarrow 500$ ppm). The signal from the board was measured using the steps described above.

Optical background measurements were then taken by coupling a mechanical attenuator (AFW tech: VOA-C-1315-C-1-2) between the laser diode output and the chamber. The chamber was filled with an air mix (0 ppm methane) and the attenuator was completely closed. The attenuator was gradually opened and measurements were taken at 0.5 mW intervals. The laser power out of the attenuator was measured by illuminating a TL-labs photodetector (PM100D and attached S122C photosensor), with the output from the fibre.

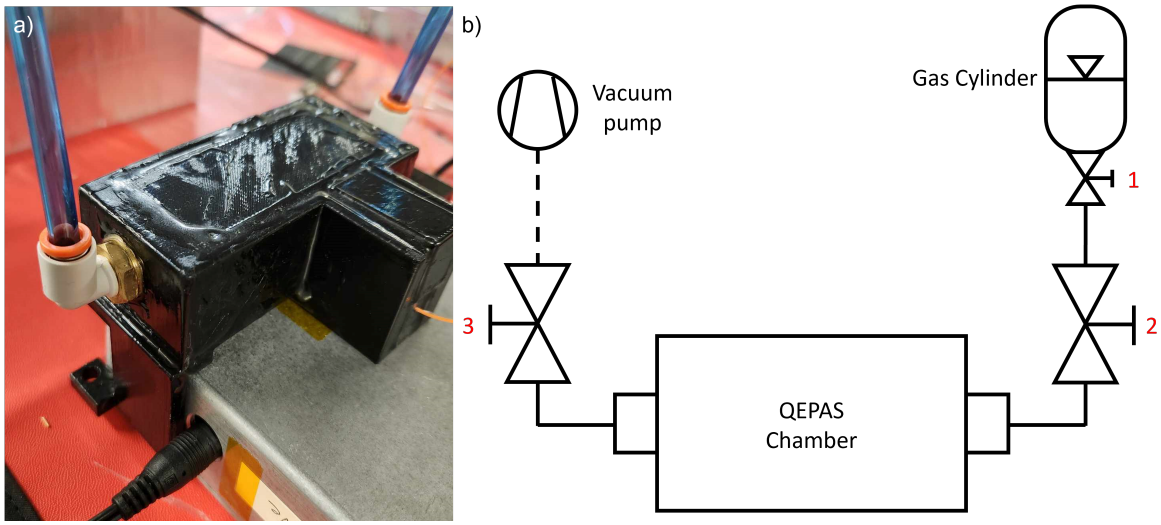

FIGURE 5.20: a) Picture of the enclosed gas chamber directly connected to the board for testing. Pneumatic piping is also connected for methane concentration control. b) Schematic of the experimental setup as it relates to controlling gas concentrations within the QEPAS chamber.

5.4.1.2 Results and Discussion

The first steps towards obtaining a QEPAS signal was to choose and then calibrate a suitable laser. Here we chose diode laser for several key reasons. Firstly, it was designed to operate around the known methane absorption peak at $\lambda = 1653.73$ nm [177]. Secondly, although the

output power was less than many of the other studies covered in the introduction (Chap. 4), the narrow linewidth and easy control over the output made it suitable for our purposes. Additionally, the laser was easy to source and requires relatively low power consumption.

Figure 5.21 shows the output of the laser for different temperature and current settings. Both the operating current and internal temperature could be monitored through dedicated output pins on the control board. From these tests, we determined that operating the board at $18.96\ ^{o}$C and 90 mA, providing an output of $\lambda = 1653.73$ nm and $P = 3.905 \pm 0.004$ mW. This puts the emission right on the methane absorption peak. Although a lower temperature would allow a higher operating current, and therefore greater output power, this would restrict the range of any modulation and risk condensation on the laser diode.

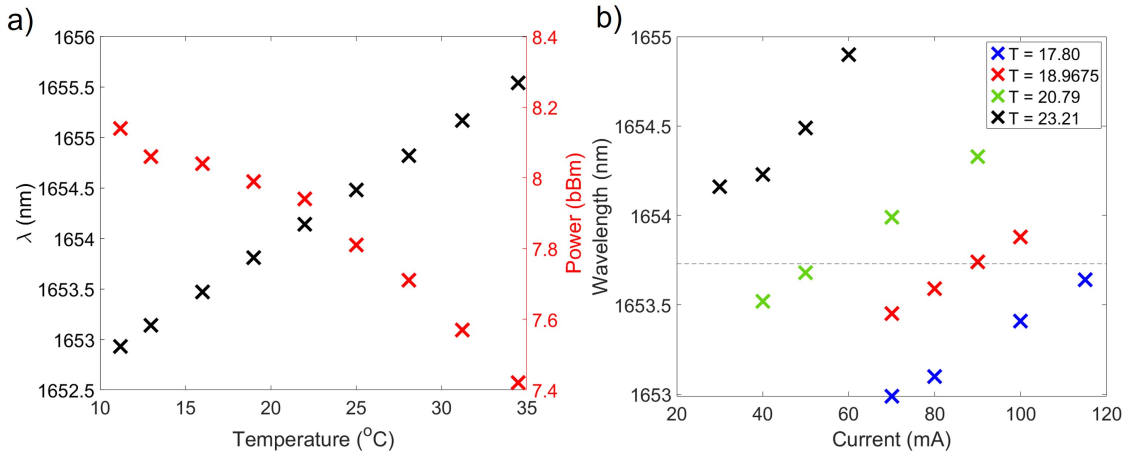

FIGURE 5.21: a) Plot showing the relation between the temperature of the laser diode, to both the wavelength and output power. b) Plot showing the relation between the laser current and the output wavelength, for different set temperatures. The horizontal dotted line (at $\lambda = 1653.73$ nm) corresponds to the targeted methane absorption peak.

With the laser operating conditions set, we performed initial concentration testing. As seen in Fig. 5.22 a) signals could be detected for all gas concentrations of methane. Importantly when methane was added the signal was stronger measurably different to the 0 ppm. Whilst this indicates that both the boards and the chamber are capable of detecting a photoacoustic signal, there are a few immediate problems with these results. The results show a clearly non-linear trend between methane concentration and the LIA signal. In addition, both the 100, and 200 ppm as well as the 200, and 500 ppm concentrations, whose measured signals are within error

of each other. This shows that, although methane can be detected, the concentration at these levels cannot be reliably determined. Furthermore, there is a large background component to the signals; the 0 ppm signal is half the magnitude of that at 500 ppm.

To determine whether the large background signal was optically generated, the chamber was filled with 0 ppm and an attenuator was incorporated into the setup. As can be observed in Fig. 5.22 b), there is a clear increase in the measured signal as the laser power is increased. Given that this was measured for 0 ppm, it indicates that there is a noticeable photothermal background component. Given the use of a simple aperture to restrict the beam diameter from the GRIN lens, this is not overly surprising. Furthermore, although the original aperture designed in CAD was set at the diameter of the QTF prong spacing, the printer was not able to adequately print the rounded hole and it was sealed during the development process. This required having to drill the hole, which likely left it larger than intended at 0.5 mm. However, the background signal does not, on its own, account for the nonlinear results. To help rule out other factors, the setup was further optimised.

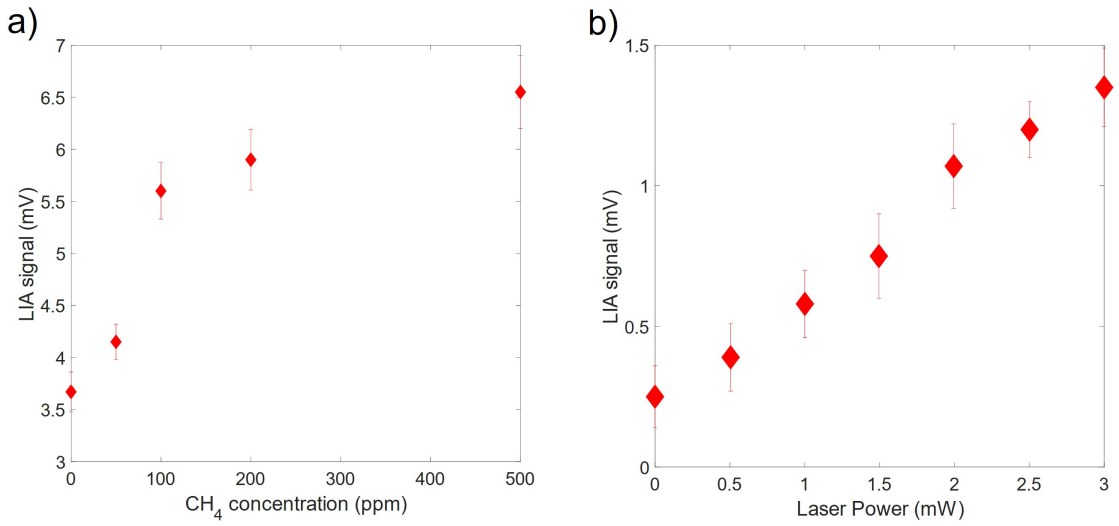

FIGURE 5.22: a) Methane concentration sweep and the corresponding measurement. LIA signal was measured as the static 1f response. b) Laser power test for a 0 ppm methane concentration showing the measured signal for varying input laser power signals. An attenuator was used to control the power to the chamber, whilst the laser operating conditions were kept static.

5.4.2 System Optimisation

5.4.2.1 Experimental Methods

Optimisation testing was performed following the same procedure as described in the previous section, using the setup shown in Fig. 5.19. To maximise signal strength, all optimisation tests were conducted with the chamber filled with methane at 500 ppm.

Firstly, the operating current of the laser, which sets the centre wavelength before any modulation is applied, was varied to optimise the signal. Since current directly influences both laser wavelength and power output, adjusting it allows for fine-tuning of the centre wavelength to maximise signal response. This was achieved by applying a DC offset, ranging from $-1 \rightarrow +1$ V, to the modulation signal. The corresponding signal for each set current was measured through a dedicated pin on the control board, using an Alignment 34401A digital multimeter.

The modulation depth was then optimised. The chamber was refilled with methane and the modulation depth was incrementally increased from $0 \rightarrow 2\ V_{pp}$ to determine the effect on the signal.

Finally, the modulation frequency was optimised by sweeping the frequency from $32.738986 \rightarrow 32.759006$ kHz. During this test, the chamber was once again filled with methane and a double Gaussian function was fitted to the results using MATLAB's `fit()` function, allowing the identification of the optimal modulation frequency for the maximum signal response.

5.4.2.2 Optimisation Results

The effect of varying the pre-modulation laser current, i.e. the centre wavelength, was tested first. The measured signal is shown in Fig. 5.23 a). From these results, a maximum was noted at a slight offset from the previous tests, so the current was increased to 93.5 mA. Following this the effects of modulation depth on the signal was then tested, and the corresponding results are presented in Fig. 5.23 b). Based on these findings, the modulation depth was

increased from $1 \rightarrow 2V_{pp}$, with $2V_{pp}$ being the maximum voltage difference applicable to the laser control board.

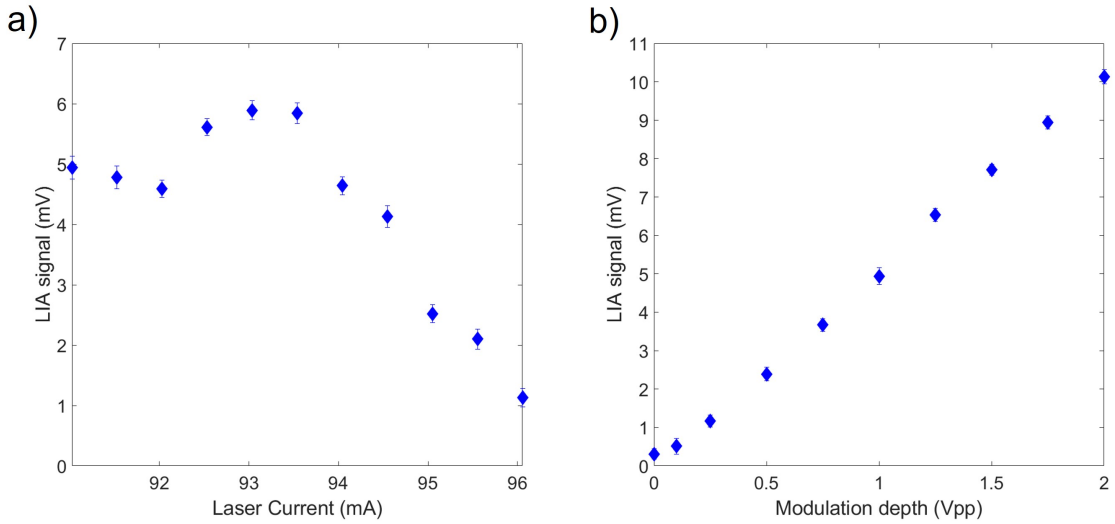

FIGURE 5.23: Calibration measurements performed with a set methane concentration of 500 ppm a) Measured signal for differing laser operating currents. Current shown here is the centre point, modulation was applied equally either side of this level. b) Sine wave modulation amplitude from the signal generator, and the corresponding measured signal.

Although optimising both the modulation depth and the centre operating current provided larger measured signals, optimising the modulation frequency had the greatest impact. As can be seen in Fig. 5.24, there is a signal difference of more 50 mV across a 30 Hz range. For initial testing, the laser was modulated at $f = 32.768$ Hz, the operating frequency given by the manufacturer [178]. After Gaussian fitting to the frequency test data, the new optimal operating frequency was determined as $f = 32.7595$ Hz. This alone accounts for a signal increase of $\sim 5\times$.

5.4.3 Further Testing

5.4.3.1 Experimental Methods

With these optimised parameters, concentration testing was repeated. For this the physical setup was kept the same as in Fig. 5.19, minus the attenuator. Each measurement was

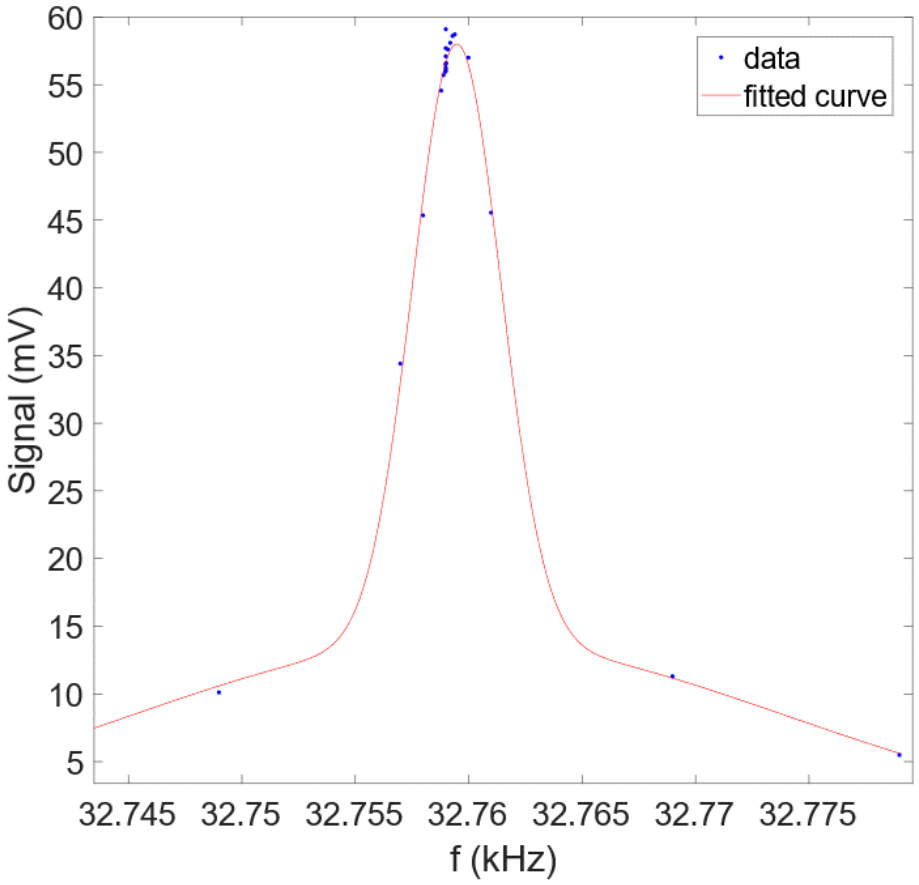

FIGURE 5.24: Frequency response of the QEPAS system for a methane concentration of 500 ppm. A double Gaussian fit determined the maximum signal to be occurring at 32.7595 kHz.

performed using the optimised parameters. The modulation frequency was set at 32.7595 kHz, with a modulation depth of 2 V_{pp}, and the current was adjusted accordingly.

Once more, a sweep was performed to measure the signal for increasing methane concentrations ($0 \rightarrow 500$ ppm). In addition a 3 minute settling time was introduced between the chamber being filled with methane and the start of the measurement cycle using the LIA.

5.4.3.2 Results and Discussion

The results here showed a large increase in the magnitude of the signal, as suggested by the optimisation results. The magnitude of the measured signals now reaching 62 mV for

a concentration of 500 ppm methane, compared to only 6.55 mV previously. There was an improvement in linearity between concentration and measured signal, with linear regression returning $R^2 = 0.97$, as seen in Fig. 5.25, and this linearity was expected for a QEPAS detection module [179]. Importantly, these results showed that the detection module is able to better differentiate methane concentrations than the previous results indicated.

Although an increase in signal magnitude is useful, it is more important to assess the SNR. For calculating the SNR, most QEPAS papers use the ratio of the peak strength to the variation of an interline region to determine the SNR [180]. However, this is not suitable for fixed-wavelength measurements. *Winkowski and Stacewicz*, who also made fixed wavelength measurements, calculated the SNR for their voltage amplifier using:

$$\text{SNR} = 20 \log \frac{V_{on}}{V_{off}} \tag{5.2}$$

where V_{on} is the signal voltage when the laser is on, and V_{off} is the voltage when the laser is off [162]. For a methane concentration of 500 ppm, this returned a SNR of 33.4, and consequently a MDL = 15.0 ppm, although. However, considering the large background signal that is generated in our ADM, the laser off state may not be a suitable benchmark. Here we decided to test another approach to check the SNR results. A more suitable comparison may then be the strength of the signal compared to its 1σ variation. If we subtract the signal voltage measured at 0 ppm (to account for the background), then, for a methane concentration of 500 ppm, we achieve an SNR of 33.3 and an MDL = 15.0 ppm. This close agreement indicates that both approaches are suitable.

Running SNR calculations for the previous measurements, prior to optimisation,we only reach an SNR of 18.31. This shows that optimisation has nearly doubled the SNR.

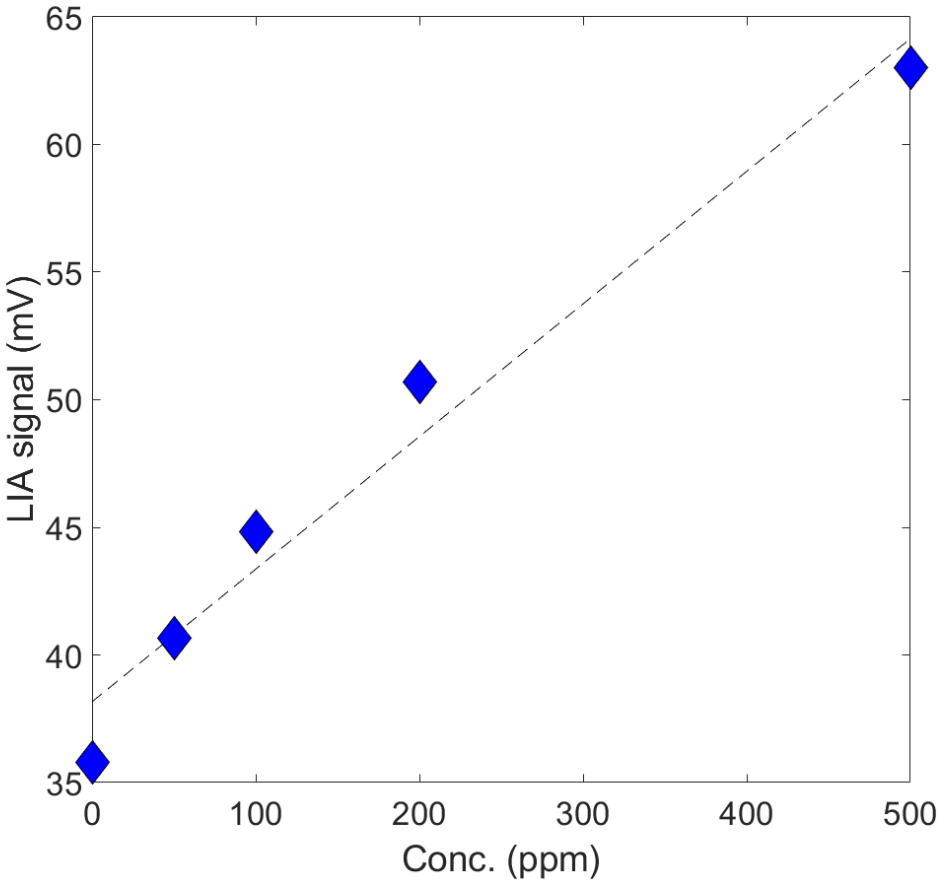

FIGURE 5.25: Concentration sweep for the QEPAS system. Measurements were obtained for a non-swept signal, demodulated at 1f.

5.5 Scanned Wavelength Tests

However, while fixed-wavelength measurement provides a starting point for analysing the effectiveness of a QEPAS detector and our amplifier, scanned wavelength measurements were needed to provide a suitable comparison with other detectors.

5.5.1 Experimental Methods

To conduct scanned wavelength measurement adjustments were made to the physical setup. The inbuilt function generator software of a Moku-Go was used to produce a high frequency sine wave (2 V_{pp}, 50 mHz), as well as a low frequency triangle wave ($f = 50$ mHz). Both

of these signals were combined using the adder board, and passed to the control board to modulate the laser. Once more the output of the Diode laser was coupled into the chamber, which was connected to the amplifier boards. The output signal was demodulated using a Stanford Research Systems LIA (SR830), and data recorded using a Rohde & Schwarz Digital Oscilloscope (RTB2002). This general setup can be seen in Fig. 5.26.

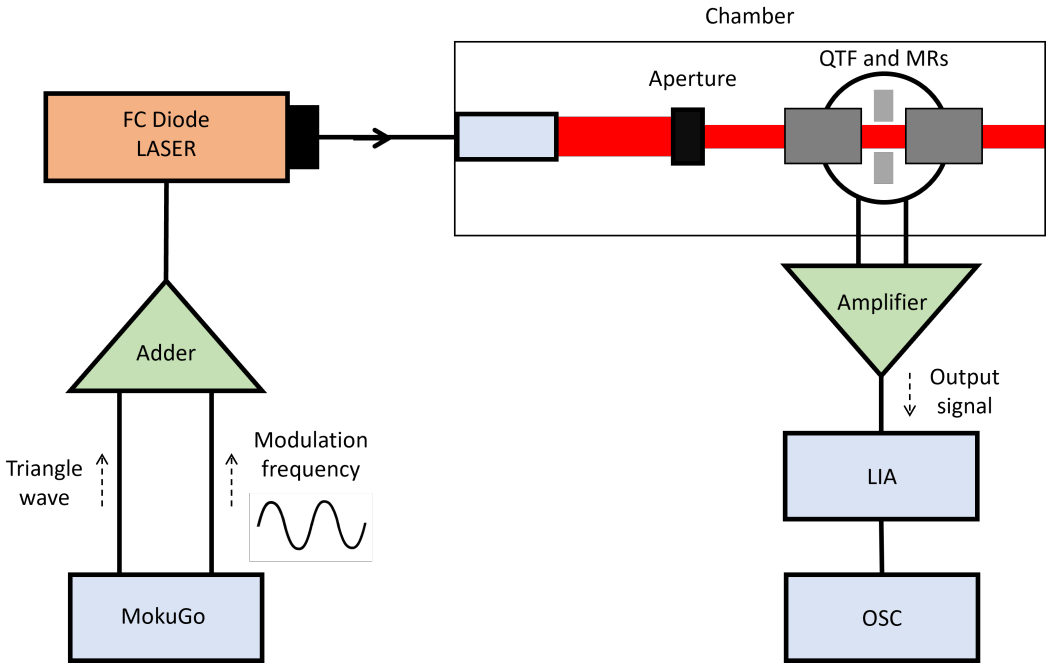

FIGURE 5.26: Schematic of the experimental setup used to perform scanned wavelength measurements.

The gas chamber was filled with methane using the methods described previously. Here signals were made using both 1f and 2f-QEPAS approaches. For the 1f-QEPAS measurement the high-frequency sine wave was set at $f = 32.7595$ Hz, and demodulated at the first harmonic. For the 2f-QEPAS measurement the high-frequency sine wave was set at $f = 32.7595$ Hz, and demodulated at the second harmonic. Initial scans were conducted using a methane concentration of 500 ppm and an 8 minute trace was recorded for the 1f and 2f-QEPAS signals separately. Following from this a concentration sweep was performed employing the same concentrations as the previous fixed wavelength tests, using the 1f-QEPAS frequency approach.

Each recorded trace was processed using MATLAB, where the average sweeps for each gas concentration and the corresponding maximum signals were calculated. Using MATLAB's built-in `peakfinder()` function, each trace was divided into individual sweeps based on the triangle wave, subsequently aligning the LIA signal with corresponding time codes. Given the bidirectional nature of the sweeps, odd- and even-numbered sweeps were separately analysed to maintain consistency; only sweeps as the laser is sweeping towards longer wavelengths are presented here for consistency, unless otherwise stated. An example of this asymmetry can be found in Appx. A

5.5.2 Results and Discussion

A methane concentration of 500 ppm was used for the first sweep test. This signal was demodulated at 1f and a signal peak of 18.7 ± 0.8 mV, as seen in Fig. 5.27 b). The signal in this figure shows an average for a trace recorded over 8 minutes. Individual sweeps were isolated in code using the ramp signal. The ramp was recorded simultaneously on the OSC and used for triggering. This allowed consistent averaging to be performed for different concentrations, as the ramp signal was kept constant across different tests. The shaded region shows the 1σ error for each data point along the trace. The standard deviation indicates that, overall, shape of the trace is consistent; however, the two peaks of the 1f signal are not fully resolved. Compared with the 1f response modelled in the previous chapter (Chap. 4), signal distortion is apparent. Following from this we also performed a 2f-QEPAS measurement. A methane concentration of 500 ppm produced a signal of 26.7 ± 1.2 mV. Using the calculations from above this gives us SNRs of 27.4 and 27.0 for the 1f and 2f-QEPAS measurements, respectively.

Using these SNR measurements, we arrive at MDLs of 18.3 and 18.6 ppm for the 1f and 2f signals, respectively, which would indicate a lower detection limit than static measurements. This not surprising given the visible distortion in the scanned signals. Of particular note is the 2f-QEPAS signal, where only a single peak can be clearly identified. This is likely a product of the large background signal, which is a product of direct photothermal heating of the MRs and QTF. Furthermore although a peak is notable in the 2f signal, it is not where it is expected.

The peak of the 2f signal should occur at the point where the laser crosses the peak of the absorption spectrum, which for our experiment should be at 5 seconds into the sweep, with some delay expected due to the high Q-factor. However, with the peak occurring much earlier, it may be a product of the photothermal distortion of the signal. As a result, with the clearer peak in the 1f scan, this was used for the concentration sweep. This warranted further studies to test the accuracy of the calculated MDLs. 1f-QEPAS traces were recorded for another concentration sweep. As can be seen in Fig. 5.27 c), the large background is distorting the signal and affecting the lower concentration measurements more than expected based on the MDL calculations.

Overall, the issues observed with the swept signals suggest that this chamber is not ideal for conducting a detailed comparison with other QEPAS detectors. Although MDLs indicate that the resolution of a 50 ppm signal should be achievable, the 1σ error margin shows that this signal cannot be distinguished from the 0 ppm baseline. This highlights the need for an improved QEPAS detector to better evaluate the performance of our amplifiers. However, it is important to emphasise that the chamber did produce a clear QEPAS signal, and fixed measurements suggest that achieving a lower MDL is feasible. Notably, this chamber was intentionally designed with simplicity in mind, primarily to assess whether the higher frequency board could effectively amplify a QEPAS signal. Although further work is necessary to fully characterise the board's performance, the current findings establish a proof-of-concept and align with the electronic tests, demonstrating that these boards are providing a measurable boost to the raw QTF signal.

5.6 Conclusions

We have described the design and construction of two QTF signal amplifiers based on VA topologies, tailored for lower and higher frequencies, respectively. The initial electrical characterisation of both boards revealed that the voltage regulator, originally intended to reduce noise on the power supply lines, was not suitable when a QTF was connected. However, bypassing the regulator allowed the boards to function as QTF signal amplifiers. Electronic

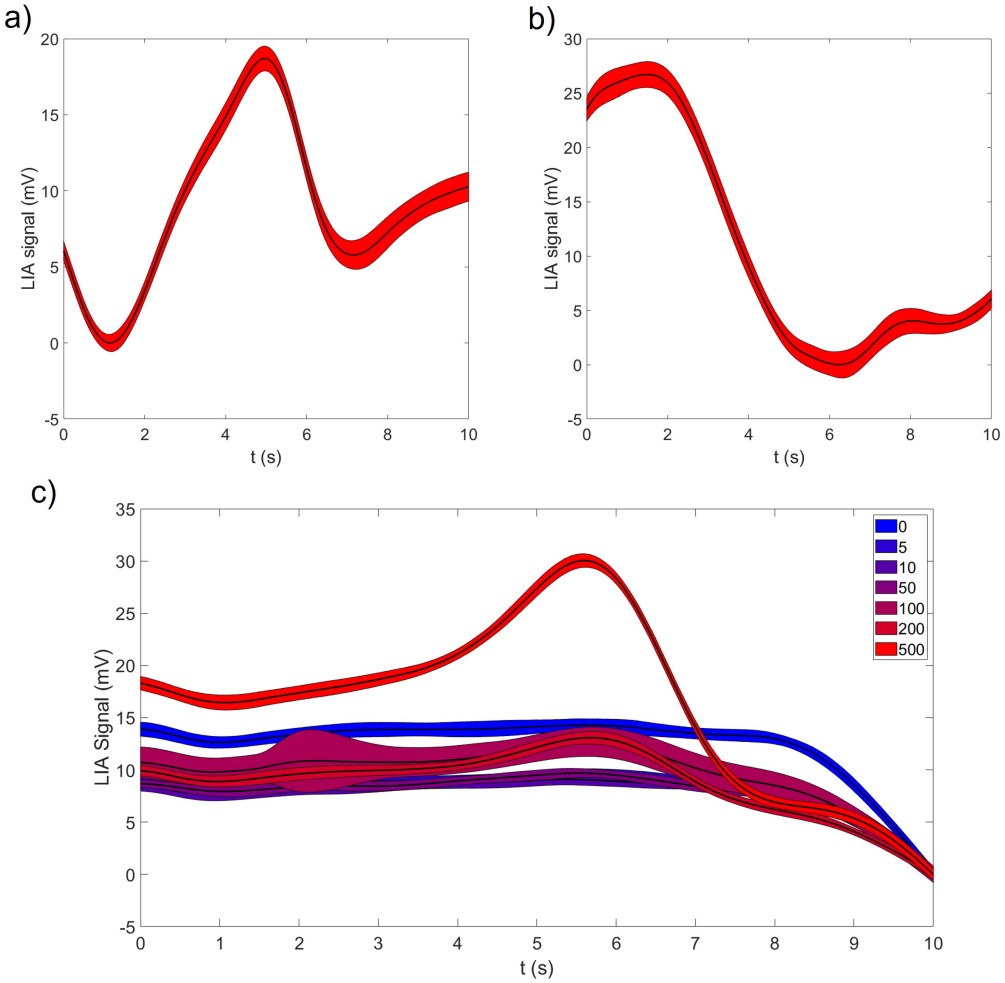

FIGURE 5.27: Averaged measurements for QEPAS sweeps. The colour shaded region shows the 1σ deviation for each point. a) Measurement for a 1f-QEPAS sweep, at a methane concentration of 500 ppm. b) Measurement for a 2f-QEPAS sweep, at a methane concentration of 500 ppm. c) 1f-QEPAS measurements for increasing concentrations of methane. Only the 500 ppm produced a signal that was could be reliably identified compared with a the 0 ppm signal.

emulation tests with a QTF confirmed that the boards were capable of amplifying signals as low as 0.21 mV.

Following these electronic tests, a QEPAS chamber was assembled using 3D-printed materials and chemically treated to seal the chamber from the environment. Using this chamber, QEPAS measurements were performed with a high-frequency amplifier board and a standard 32.768 kHz QTF. An SNR of 33.3 was achieved using a fixed-wavelength WMS approach,

at a methane concentration of 500 ppm. Although scanned wavelength signals produced MDLs of $\sim$18.5 ppm, further concentration testing showed this was likely lower than what the detection unit is actually capable of and that is not yet suitable to retrieve reliable concentration measurements using this approach. Additional improvements to the optical components of the chamber are required to fully evaluate the amplifier's capabilities and to facilitate direct comparisons with other QEPAS detection units reported in the literature.

In summary, the VA pre-amplifiers and gain blocks were successfully assembled, and electronic testing was conducted. We also successfully measured an optically generated QEPAS signal. Although more work is needed to fully characterise the performance of the higher frequency board, these results offer a proof of concept, indicating that this amplifier design is capable of amplifying a QTF signal.

CHAPTER 6

Chamber Optimisation and Further Testing

In this chapter, we develop upon the QEPAS detector in the previous chapter. Although the previous chamber in Chap. 5 provided a demonstration that the voltage amplifier (VA) board we designed was capable of detecting a QEPAS signal, it was clear that improvements to the acoustic detection module (ADM) were needed to provide a more thorough analysis of the electronic amplifiers performance. Here we present improvements to the optics of the ADM, whilst utilising and building upon the 3D printing design procedures laid out in the previous chapter. These improvements allow for the QEPAS unit to be used to conduct thorough testing of the higher frequency amplifier. We then test the pre-amplifier independently and with the gain block chained to the output. The performance of the VA design is compared to a transcendence amplifier that was built in house as a direct control. The optimised results are then compared to similar QEPAS units in the literature.

6.1 Improved Detector

6.1.1 Optical Design

To overcome the large background from the previous chapter, we focused on improving the optical throughput of the ASM. To achieve this, we replaced the commercial Thor Labs GRIN lens with a custom-designed component, made in-house. This component consisted of an SMPF0215-APC pigtail ferrule connected to a second focusing GRIN lens (LFRL-180-023-50). The ferrule and GRIN lens were housed in a single plastic sleeve (51-2800-1800 - GRIN/ferrule Sleeve). This setup can be seen in Fig. 6.1.

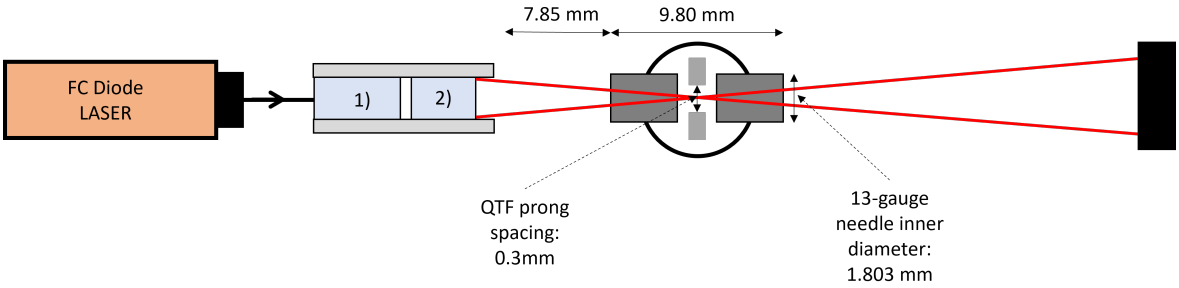

FIGURE 6.1: Schematic depicting the optical portion of the new chamber design. The laser is now emitted from 1) a pigtail fibre attached to a glass ferrule and 2) then focused by a GRIN lens, both housed in a ferrule.

In order to align the ferrule with the GRIN lens, the output face of the grin lens in the ferrule was positioned 10.5 mm from the surface of a CMOS detector. This distance was determined using simulations conducted in Ansys Zemax OpticStudio. The focal point at 1640 nm was modeled to match the design of the ADM, and then the focal point using this same arrangement and GRIN lens was modeled at 650 nm, with these simulation results presented in Fig. 6.2. The ferrule was then fitted to the GRIN lens, and the pig-tailed fibre was inserted. A red alignment laser (650 nm) then illuminated the ferrule, which was then adjusted until the beam was focused on the CMOS detector. With the positioning determined, the components were glued in place using UV optical adhesive.

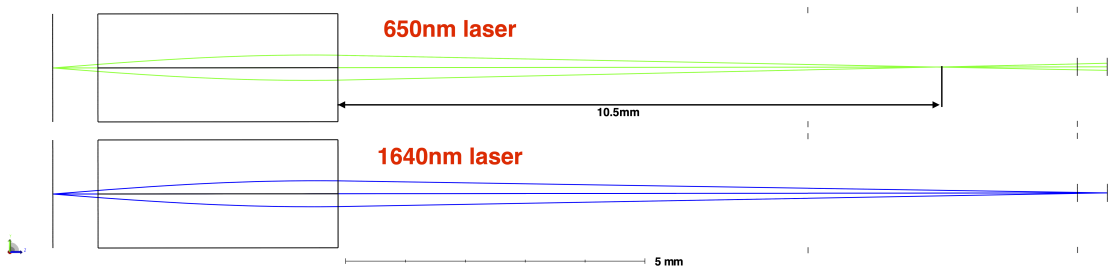

FIGURE 6.2: Zemax simulations to determine the focal point for the alignment laser at 650 nm compared to the expected operating regime at 1640 nm.

6.1.2 Assembly

The ADM was adapted from the design and assembly process presented in Section 5.3.1. The outside dimensions were kept the same as the previous module, for compatibility with the gas chamber. The GRIN lens template was changed to fit the new optical components, and in

addition, the area where the QTF holder was glued was widened to provide more flexibility during alignment. This new design can be seen in Fig. 6.3 and a detailed technical drawing can be seen in Appx. B.

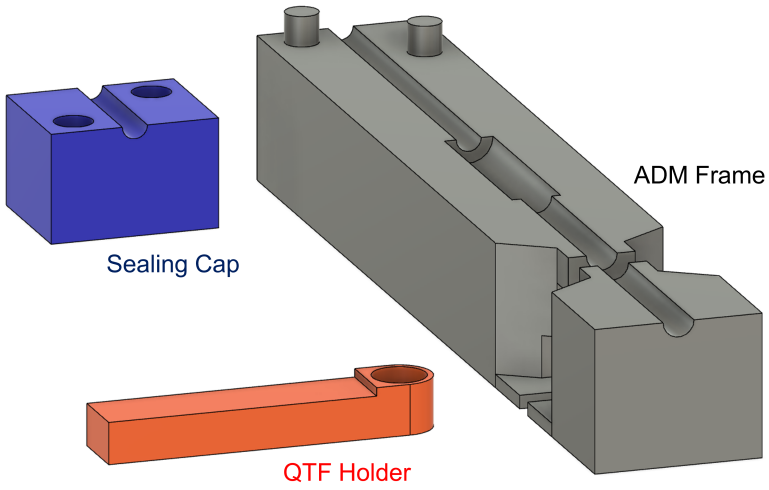

FIGURE 6.3: CAD designs for the new ADM to house the MRs, QTF, and updated optics.

The ADM module was then printed and assembled using the protocol described in Section 5.3.3. To ensure that all the components were aligned properties and the laser beam was not clipped by either the MRs or QTF, the GRIN lens was connected to the laser diode. The laser diode was switched on after each component was added in the assembly, and the power behind the ADM base was measured using a ThorLabs compact power meter (PM100D), with a 700-1800 nm photodetector (S122C). To avoid unwanted beam reflections, the laser was disconnected while components were being placed. Prior to the attachment of any components, the throughput power of the laser was 3.905 ± 0.004 mW.

After an initial optical power measurement, the QTF was mounted onto a clamped QTF holder and secured using UV-cured optical adhesive. Figure 6.4 a) shows this stage of the setup, with the QTF ready for alignment. Also seen in this figure is the mount for the optical detector, which is removed during initial alignment. Once aligned, the QTF is glued in place

with optical adhesive, and the long arm of the QTF holder was cut flush with the rest of the base. From this, the micro resonators (MRs) were secured. This time an additional 3D printed platform enabled a glass plate with 50 μm markings to be placed directly above the ADM, in conjunction with the overhead binocular microscope, and this was used to check the positioning of the MRs as performed using the stage. MRs can be seen prior to being secured with the optical adhesive in Fig. 6.4 b). Finally the cap was secured to the base to provide a seal around the fibre. After all the components were secured to the ADM, the throughput power of the laser was 3.902 ± 0.008 mW. Since this is within error of measurements prior to part placement, this indicates all optical power is passing through the MRs and QTF and should remove the previous photothermal background.

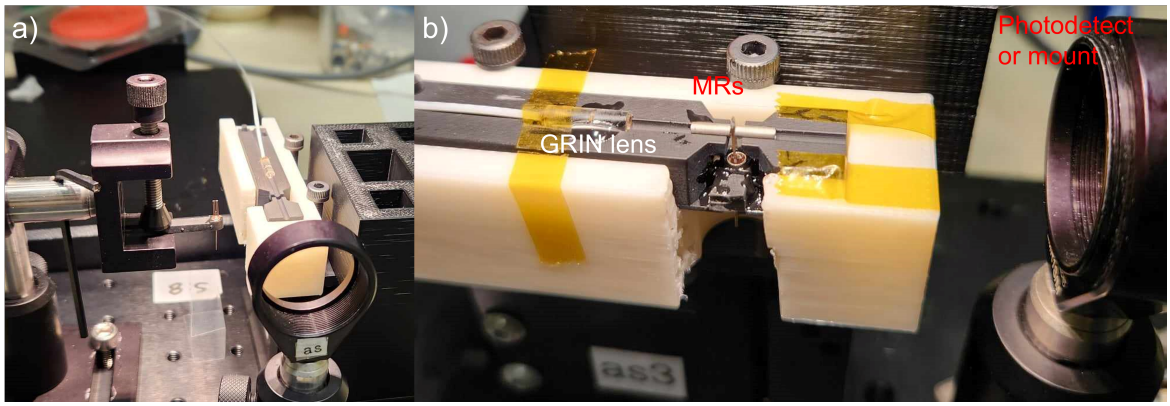

FIGURE 6.4: Pictures showing the assembly of the ADM module. a) Just prior to securing the QTF in place. The GRIN lens component can be seen already attached in a predefined grove. b) Later stage of assembly. The MR tubes, just prior to them being secured. Here kapton tape is also visible, this was used to hold components during alignment. Also visible is the 3D printed platform used to mount the alignment ruler for the MRs, which was removed to take the photo.

The design of the gas chamber remained unchanged from that in the previous chapter, as the ADM module did not change in overall size. Once again it was 3D printed using ABSR material, and chemically annealed to seal the plastic. The annealing process outlined in Section 5.3.3 was modified slightly. During assembly of the previous chamber, it was observed that the fine edges of the structures would warp under gravity as the acetone softened the plastic in the chamber, which can be seen in the comparison in Fig. 6.5. Consequently, the tank was opened and the components rotated every 20 minutes to help reduce the effect

of deformation. Though, it should be noted some deformation is fine as long as it does not affect the ability to fix the ADM in place and seal the chamber. The lid and cap components were left to anneal for 4 hours. Given their simpler structure, a longer annealing time could be maintained without any structural deformation that impacted the final assembly. After annealing, all components were left to stand for 72 hours. The ADM module was then incorporated and all components were sealed and secured using epoxy adhesive.

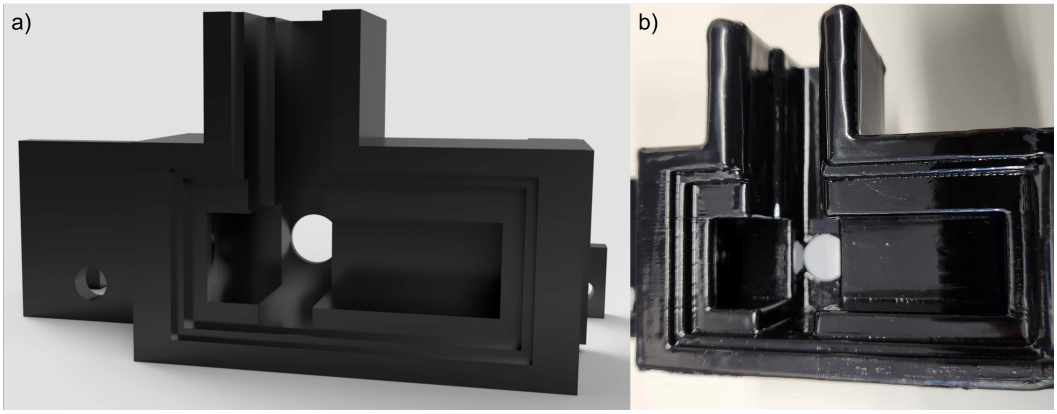

FIGURE 6.5: Comparison between a) a CAD rendering of the chamber design, with b) the final actual chamber after annealing. Visible warping to the sharp edges and corners can be seen.

6.1.3 Transcendence Amplifier Control

A transimpedence amplifier (TA) was also designed and assembled as a control, to directly compare the performance of our VA designs. This amplifier consisted of a single ended amplifier which had a feedback resistor of $10\ M\Omega$ around a single op-amp. The ADA4627 class op-amp was used here, identical to the parts used in the VA pre-amplifier. Bypass capacitors of $10\ \mu$f and 10 nf were added to each of the power rail inputs. These bypass capacitors again match those used in the VA board. The components were soldered using the procedure outlined in Section 5.1.4. In addition, a mount was designed to hold the TA board during testing. The holder was designed in Fusion 360, the design of which can be seen in Fig. 6.6 a). It was printed from ASBr using the Method X printer. A picture of the finished board, mounted in the holder, are shown in Fig. 6.6 b). Detailed schematics of the PCB and 3D-printed holder are provided in Appx. B.

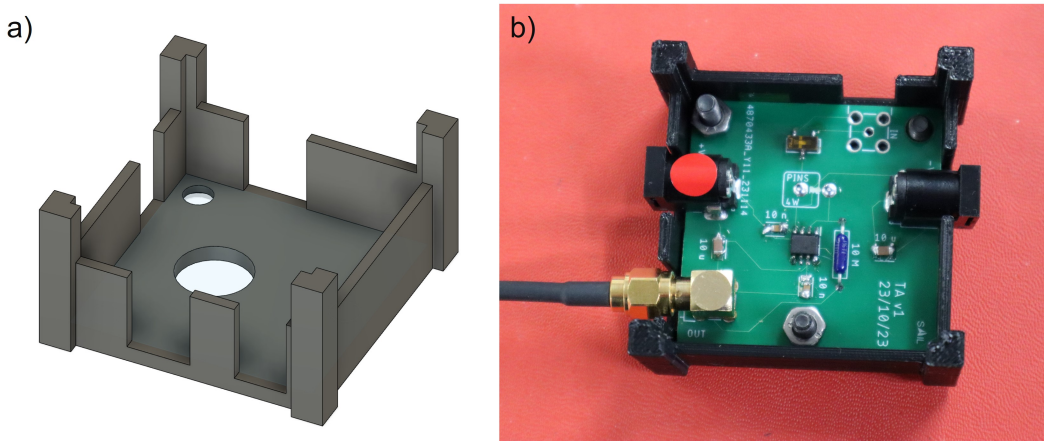

FIGURE 6.6: a) CAD design of the TA holder to secure it during testing. b) Picture showing the TA board fitted to the holder.

6.2 Scanned Wavelength Testing

6.2.1 Experimental Methods

The experimental setup followed from the procedure laid out in Section 5.5.1. The modulation signal was generated by the Moku-Go signal generator and consisted of a separately generated high-frequency sine wave component ($f = 32.759$ kHz for 1f or $f/2 = 16.378$ kHz for 2f) and a slow triangle wave ($f = 50$ mHz), which were combined using the adder board. This signal was then fed to the diode laser. The slow ramp swept the laser from $\lambda = 1653.68 \rightarrow 1653.78$ nm.

The new chamber was directly connected to the board; the QTF output wires were fit to the input pins of the electronic board. The board was kept shielded in its metal casing for all tests, with power supplied using the battery bank. The output was directly connected to a Stanford Research Systems LIA (SR830) and demodulated at the first or second harmonic, corresponding to the 1f or 2f-QEPAS techniques. This output was recorded using a Rohde & Schwarz Digital Oscilloscope (RTB2002). This setup can be seen in Fig. 6.7. All electronics, including the diode laser, were powered on and left to warm up and stabilise for 30 minutes before each round of testing.

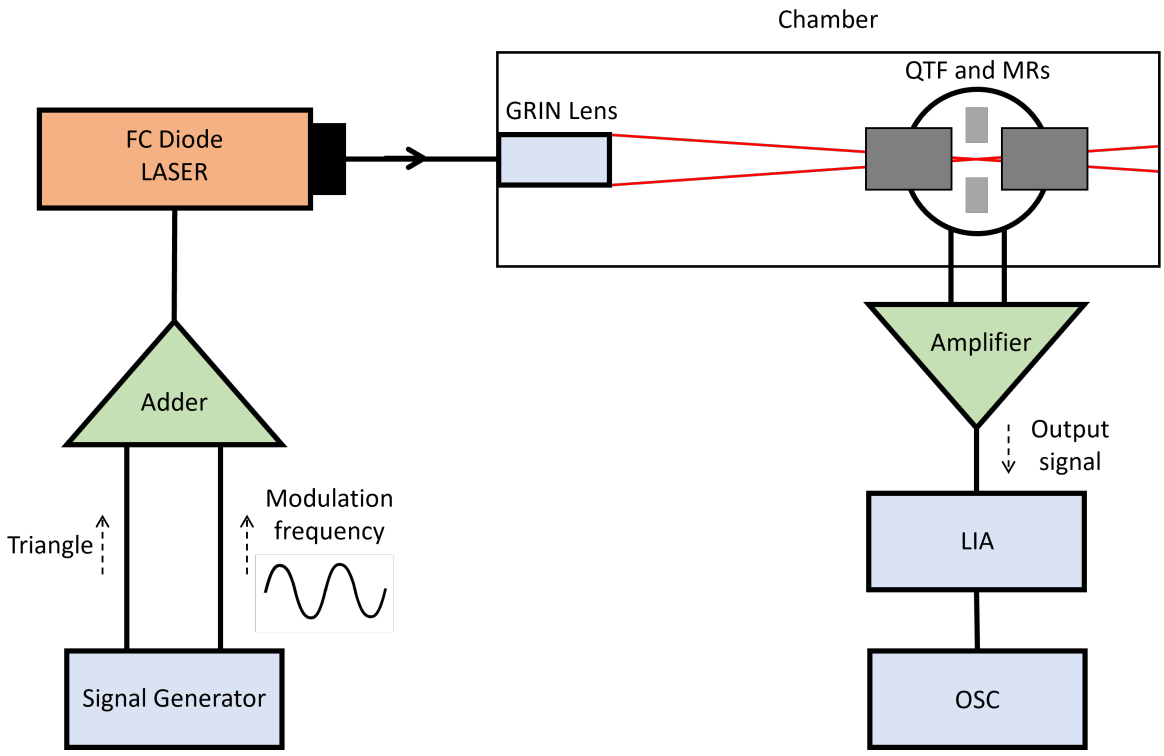

FIGURE 6.7: Schematic of the experimental setup used to test the QEPAS detection unit.

The chamber was connected for methane measurements using the gas setup outlined in Section 5.4.1.1 with the chamber being flushing for 10 seconds, for each concentration measured. Concentration tests/sweeps were performed by first filling the chamber with 0 ppm methane, and taking an 8 minute trace. Methane concentrations of 50, 100, 200, and 500 ppm, were then sequentially tested.

Modulation depth testing was carried out for both 1f and 2f measurements. Using the signal generator, the high frequency sine wave voltage was set at 1 V_{pp}. For each board, an initial 500 ppm methane concentration was used to fill the chamber, whilst it was connected to the VA. An 8 minute trace was recorded. This was repeated, increasing the set voltage by increments of 1 V_{pp} until a maximum of 10 V_{pp} was reached. The chamber was refilled after each voltage sweep. The modulation depth measurements were then repeated for a methane concentration of 50 ppm. Both concentrations were also repeated for the TA board as a control.

Traces were analysed in code by breaking up each individual sweep. MATLAB's inbuilt peak finder was used to identify the turning points of the ramp signal, which was recorded using the OSC alongside the LIA output, and used for triggering to ensure consistent sweep positioning. A single 3 dimensional matrix was then generated containing all the sweeps. From this a single array was generated for an average sweep and the corresponding 1σ variation at each point. Given the bidirectional nature of the sweeps, odd- and even-numbered sweeps were separately analysed to maintain consistency; only sweeps as the laser is sweeping towards longer wavelengths are presented in figures, for ease of depiction. For numerical results regarding signal peaks, SNRs, and MDLs these were calculated from the average sweeps of both directions.Testing here was conducted for both only of the pre-amplifier, as well as the signal with the gain block (GB) chained to the pre-amplifier.

The SNRs here are calculated as the ratio of the signal peak to the variation at the given peak. A separate function was developed to calculate the SNR during the analysis phase. Once the code had generated the average sweeps, and their corresponding deviations, both sweep directions were analysed and the SNR calculated from both.

A function was developed to provide a correction to account for diffusion and was applied to selected traces prior to the above analysis analysis. The function first used MATLABs inbuilt peak finder to identify the location and magnitude of the 1f, or 2f peaks in a given trace. Then a least-squares linear fit was applied to the peaks to determine the negative drift over time. The resulting function was then used to apply a time-based multiplication factor to the original trace which was then returned to the rest of the code.

6.2.2 Results and Discussion

The first factor investigated using this new chamber was the modulation depth, and it's affect on the SNR. To facilitate this, a simple modification was made to the adder board. The ratio of the gain for the adder board is determined in a very similar manner to that of the voltage amplifier, being the ratio of the feedback resistor to the resistor on each input channel. The high frequency sine wave channel was reduced to $1/3$ of its original resistance (down to

$R = 14.71\ \Omega$), by soldering an additional two parallel 68.8 kΩ resistors. The board was originally designed to decrease the signal, without having to reduce the output of the signal generator. This was done to allow it to operate well above any potential noise floor. The new ratio decreased the signal by a smaller fraction, enabling much higher modulation depths to be reached, granting greater flexibility.

With this modification to the adder board, modulation depth testing was performed for an initial methane concentration of 500 ppm. In Fig. 6.8 a) we can see an increase in signal as the modulation depth is increased. Looking at the SNRs in panel b), we can see that there is a sharp increase from $3\% \rightarrow 12\%$, before the SNR levels off. Similar testing for the TA board was also performed Appx. B, which showed the SNR followed the same general increase.

A similar trend can be seen for the 2f-signal in Fig. 6.8 c) and d). However, here, looking at the shape of the 2f- curves, we can see an increase in the signal at around 1 s as the overall signal begins to distort. As can be seen in Fig. 6.8 e), this distortion also occurs at this lower concentration, though is proportionally larger. In addition, for modulation depths greater than 17%, the voltage of the main absorption peak becomes lower than the side peaks. Looking at the SNRs in Fig. 6.8 f), the general increase also levels off after this point. Considering all of this, the decision was made to fix the modulation depth at 28% and 14% for the 1f and 2f QEPAS measurements, respectively. It is also worth noting that, unlike the previous chamber, the signal shape here is closer to the expected distribution for each demodulation. For ease of reading, the demodulation signals modelled in Chap. 4 have been reproduced in Fig. 6.9.

To characterise the performance of the voltage amplifier and gain block a series of concentration tests were then conducted, providing direct measurements for methane. The much cleaner shape seen in the previous modulation depth testing is carried through here, demonstrating that the optical design here is significantly better suited to provide cleaner QEPAS measurements.

Firstly the pre-amplifier, without the gain block, was tested. Both 1f and 2f signals were clearly measured, as expected from the modulation depth tests. For the 1f measurements, as seen in Fig. 6.10 a), a maximum signal of 1.32 mV was recorded for a methane concentration of 500 ppm. For the 2f signal, a maximum of 0.70 mV was recorded. Most importantly for

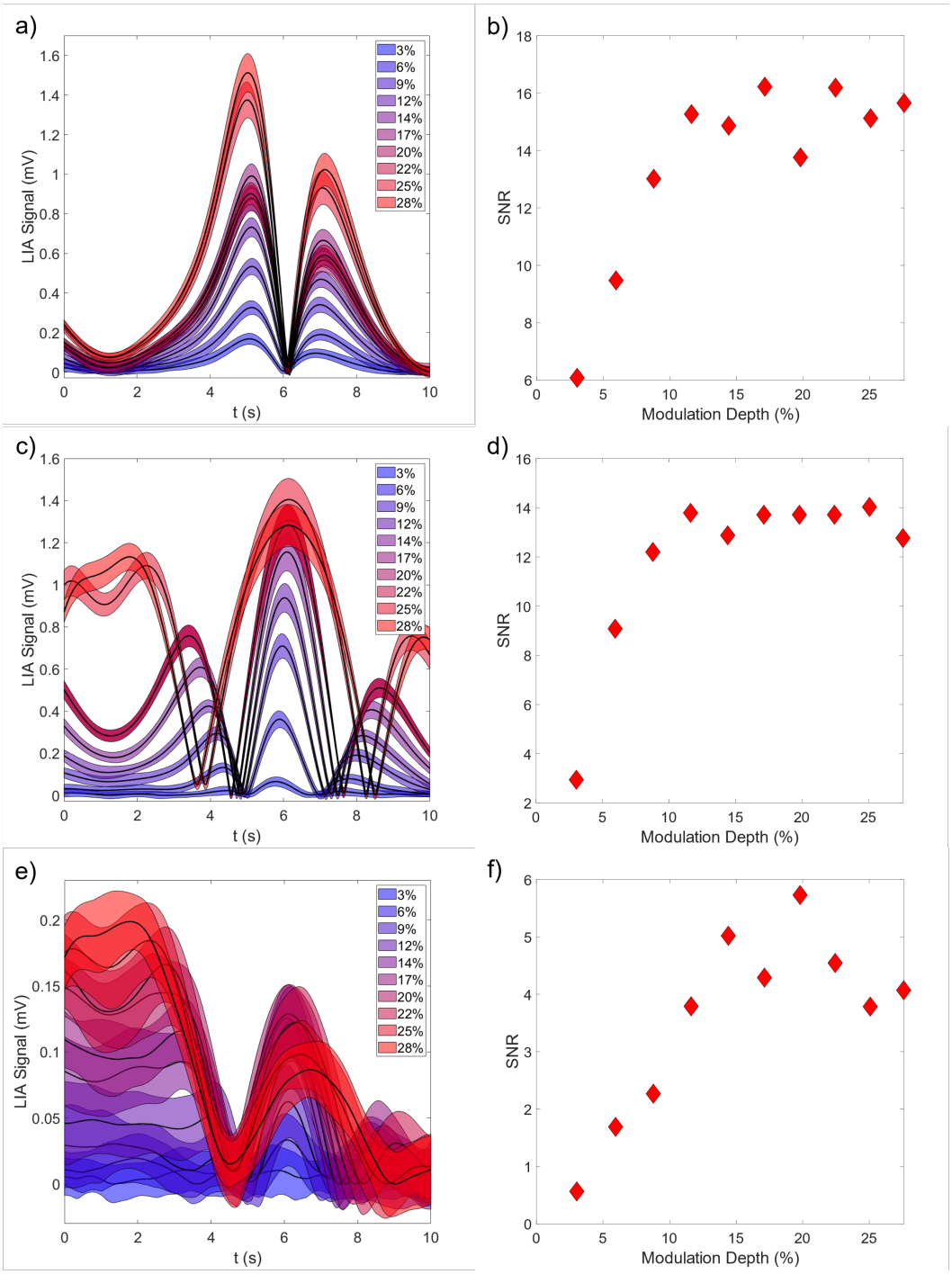

FIGURE 6.8: Modulation depth testing for the new QEPAS chamber. a) 1f-QEPAS results for increasing modulation depths, at a methane concentration of 500 ppm. b) Corresponding SNRs for the modulation depth increases. c) 2f-QEPAS modulation depth testing for a methane concentration of 500 ppm, along with d) the corresponding SNRs. e) 2f-QEPAS results for a concentration of 50 ppm, along with f) the corresponding SNRs.

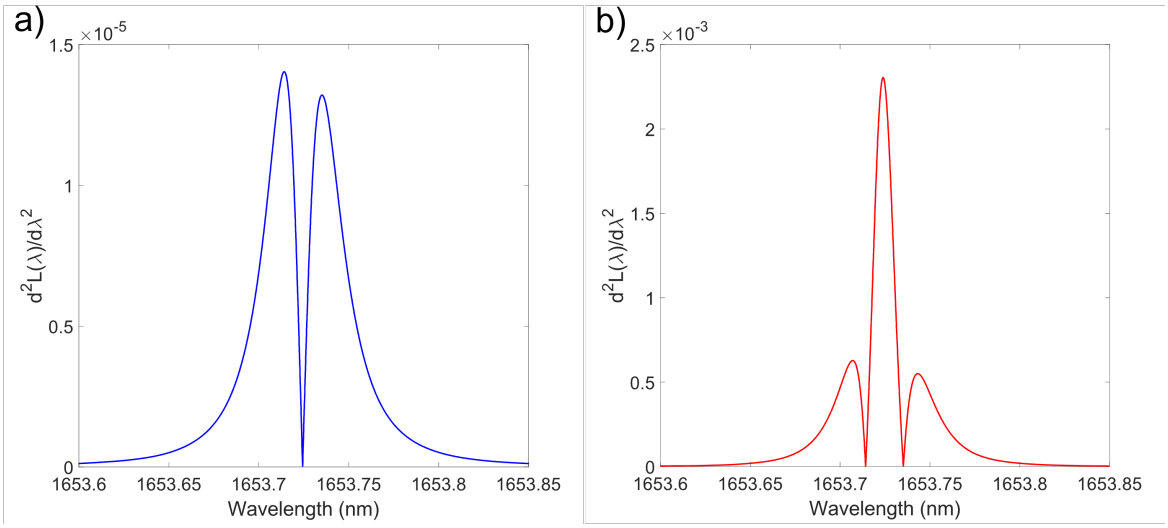

FIGURE 6.9: Modelled demodulated methane absorption peak at 1653.7 nm, using a concentration of 500 ppm, and a pressure of 1 atm. a) Model of the 1f-QEPAS response. b) Model of the 2f-QEPAS response.

a gas detection is determine the correlation between gas concentration and a given signal. To this end we we fit a linear equations to the concentration sweeps. As seen in Fig. 6.10 c) and d) both 1f and 2f measurements returned highly linear correlations. For the 1f an $R^2 = 0.99$ was achieved, with a slightly lower measurement for 2f at $R^2 = 0.98$. The most likely reason for the reduced R^2 in the 2f sweep, was due to the 0 ppm concentration being higher than expected. Observing the sweep, the presence of a QEPAS signal suggests residual methane. However, at this point this contributions from background signals cannot be ruled out; consequently we will explore this more in future sections.

Concentration sweeps with the GB chained showed significant signal amplification. For a methane concentration of 500 ppm, maximum signals of 73.5 mV and 52.0 mV were recorded for the 1f and 2f-QEPAS measurements respectively. Giving a gain increase of 35 and 38 dB from the pre-amplifier signal. Although this is slightly less than the suggested emulated results (which indicated a gain of 41.7 dB). However, some variance between these measurements is expected due to the difference in the impedance between the QTF and the input connections used in the emulated signal tests. Furthermore, as seen in Fig. 6.11 panels c) and d), the correlation between the concentration and the measured signal is highly linear, with both 1f

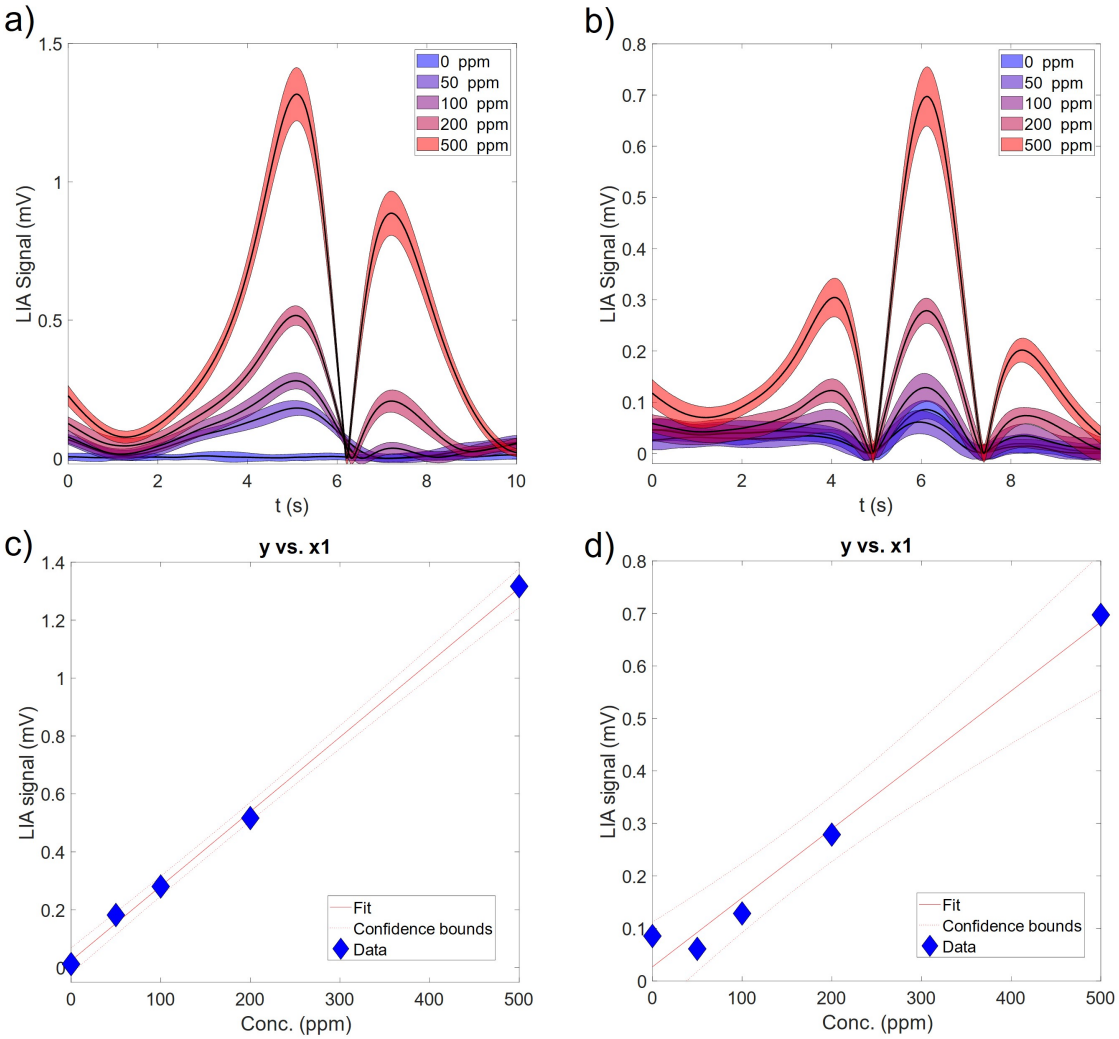

FIGURE 6.10: Concentration sweep results for the pre-amplifier. a) 1f-QEPAS signal, with the average trace shown as black lines and the shaded region showing the 1σ variation around each point in the trace. b) 2f-QEPAS signal. c) Maximum 1f-QEPAS signal for each concentration and linear fitting results. Here an $R^2 = 0.99$ achieved. d) Maximum 2f-QEPAS signal with linear regression fitting. ($R^2 = 0.98$)

and 2f measurements returning an $R^2 = 0.99$. This demonstrates that neither the pre-amplifier nor the gain block is adding any detectable non-linearity to the signals.

We then tested the chamber using a TA board for controlled tests. The press-fit pins included in the board design allowed the gas chamber to be detached and reattached from any given board. Not only did this allow for easy maintenance, it also allowed the chamber to be connected

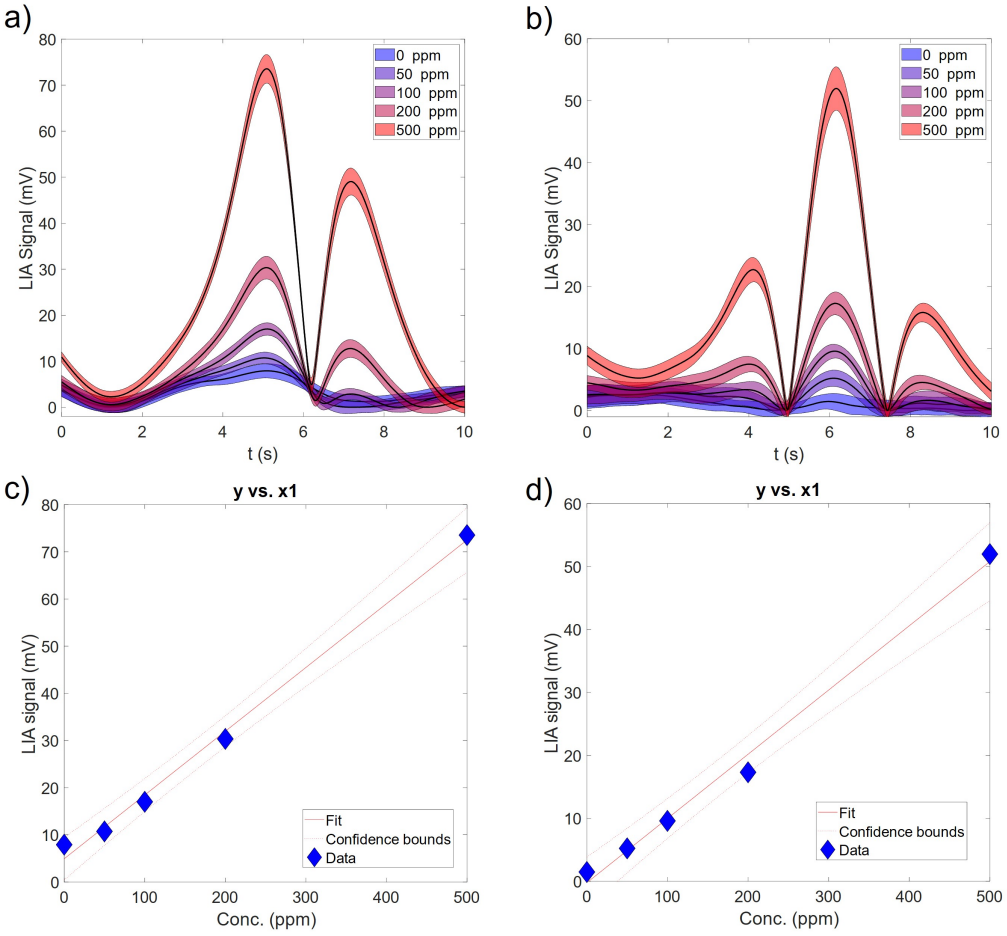

FIGURE 6.11: Concentration sweep results for the pre-amplifier, chained with the GB. a) 1f-QEPAS signal, with the average trace shown as black lines and the shaded region showing the 1σ variation around each point in the trace. b) 2f-QEPAS signal. c) Maximum 1f-QEPAS signal with linear regression fitting. ($R^2 = 0.99$) d) Maximum 2f-QEPAS signal with linear regression fitting. ($R^2 = 0.99$)

with different boards so that a direct comparison could be made between the electronics, without any variation of the QTF, MRs, or optical components and their exact positioning.

Concentration testing was then performed using the TA, again capturing the 1f and 2f QEPAS signals. As can be seen in Fig. 6.12 a) and b) the signals measured using the TA board are significantly weaker than those measured for the VA, even without the use of the gain block. Maximum signals of 19 μV and 12 μV were obtained for a methane concentration of 500 ppm. Previous studies had shown, given the better voltage response of quartz, that a signal of an order of magnitude greater can be achieved using the VA design [162]. The VA pre-amplifiers

produced a signal of more than an order of magnitude greater than the TA. When the gain block is used, we achieve a signal nearly 3 orders of magnitude greater than the TA. The TA board still produces the expected response for the 1f and 2f measurements, as is expected from this control setup. Given the similarities in shape between the TA and VA signals, this also suggests that neither of the boards, or gain block, are distorting the signal from the ADM. As can be seen in Fig. 6.12 c) and d), the QEPAS signal is also linearly proportional to the methane concentration, as with the previous boards.

However, the signal magnitude on is not a sufficient metric to fully assess the performance of our amplifier designs. Although signal magnitude is important, especially in cases where signal detection and process are limited, if noise also increases proportionally, then the boards are unlikely to provide better performance.

In the previous chapter, the SNR was calculated as the ratio of the average signal strength, when the laser was centred on the 1653.7 nm methane absorption peak and only the high-frequency modulation was applied, to the 1σ variation of that signal. This provided a method to assess the signals and account for the large background to the signals. By recording average signals and determining the standard deviation at each point, we can apply a similar approach to the signals here.

Focusing on the SNR for a methane concentration of 500 ppm, we can see that our VA board improves the signal quality (as shown in Fig. 6.13). For the 2f measurements, the TA board only achieved SNRs just above 8, whilst the pre-amplifier was above 13, and up to 25.8 with the GB. Overall, this follows the trend we expected and shows that the overall large gain provided by the pre-amplifier with the gain block not only improves the magnitude of the signal, it also improves the SNR.

However, there are some issues with these results. In particular, the SNRs were generally lower than expected. A study by *Winkowski & Stacewicz* [162], reported an SNR improvement of $1.7\times$, compared to our similar improvement of $1.6\times$ with the pre-amplifier and 1.8x with the gain block (specifically for the 2f measurements). It is important to note that the SNRs were calculated differently, and their study focused on water vapour rather than methane.

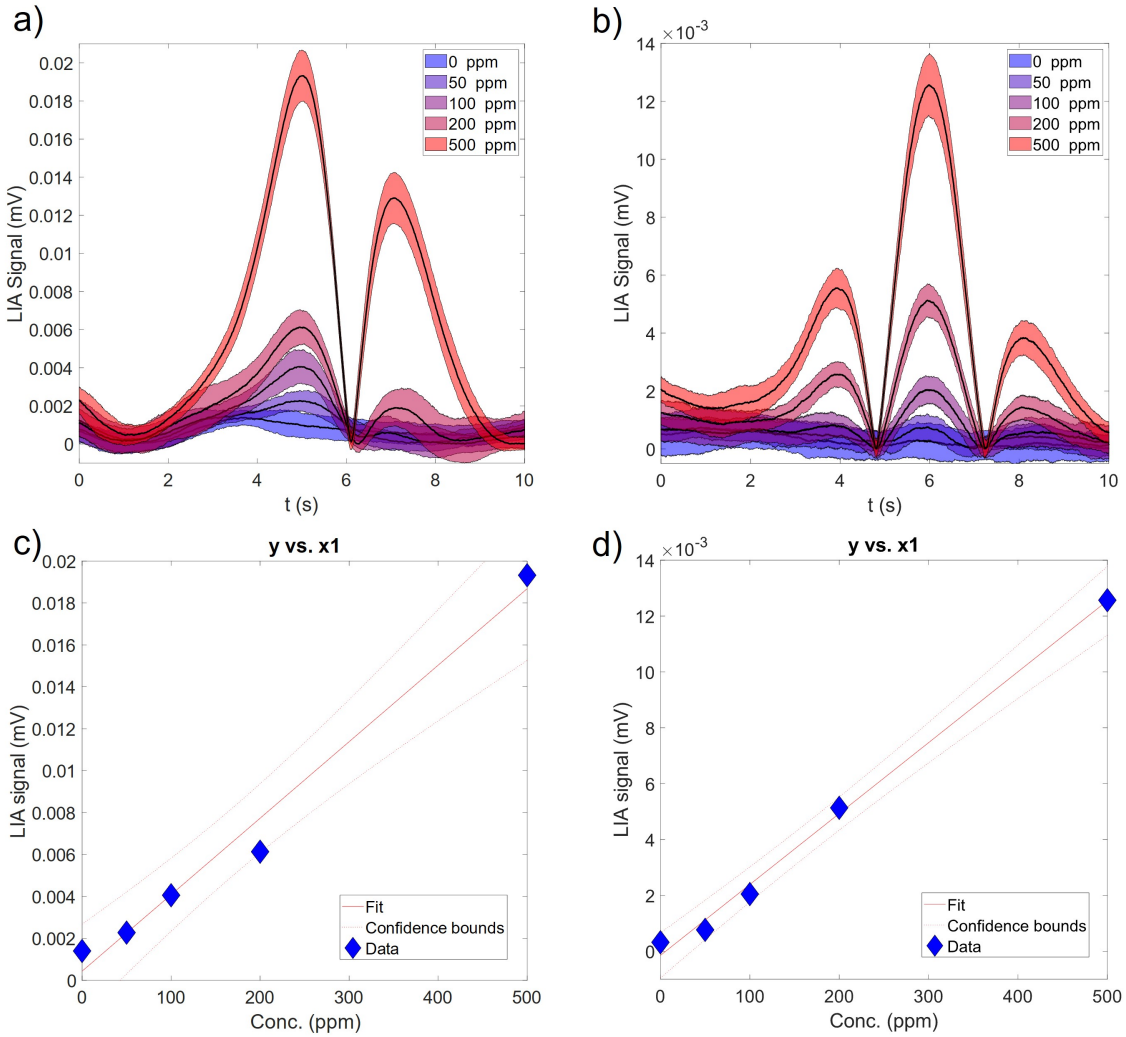

FIGURE 6.12: Concentration sweep results for the transimpedence amplifier control. a) 1f-QEPAS signal, with the average trace shown as black lines and the shaded region showing the 1σ variation around each point in the trace. b) 2f-QEPAS signal. c) Maximum 1f-QEPAS signal with linear regression fitting. ($R^2 = 0.98$) d) Maximum 2f-QEPAS signal with linear regression fitting. ($R^2 = 0.99$)

However, the relative increase in SNR between the TA and VA designs remains our focus here. A more detailed comparison with literature results will be discussed later in this chapter (Section 6.3.2.2).

The MDL offers another metric for analysis. Using the SNR from the 500 ppm methane concentration, we obtained a 2f MDL of 60.2 ppm for the TA and 33.7 ppm for the pre-amplifier and gain block. Although this shows that the VA outperforms the TA, the MDL

is still higher than expected, when compared to the previous fixed wavelength results that returned an MDL of 15.0 ppm, with a less optimal optical arrangement. Furthermore, the 1f results are not as expected. As discussed previously, we anticipated the 2f-QEPAS signal to have a higher SNR than the 1f, and while this holds for the TA, it does not apply to the VA, particularly with the gain block. Several factors may contribute to this discrepancy. The 1f measurement exhibits a linear response, whereas the 2f is non-linear, reflected in the modulation depth settings — 28% for 1f versus 14% for 2f. This difference is also evident in the overall magnitude of the signal, which was higher for 1f than 2f. Background noise not related to the QEPAS measurements could also explain the better SNRs. Typically, the 2f signal is preferred due to its non-linear response and reduced background noise. However, the balanced design of the VA incorporates more noise-reducing features than the TA. It is possible that the VA design diminished the usual advantages of 2f demodulation, making the increase in the driving level of 1f more beneficial.

One aspect that may be effecting the 1σ variation for the sweeps above, and subsequent SNR and MDL calculations, is a general drop in signal over the 8 minute traces recorded. The example trace in Fig. 6.14 a) clearly shows this drop. A likely cause of this drop is gas diffusion from the 3D printed cell. Additional testing was conducted, where the chamber was filled with 500 ppm methane a signal was measured every 10 minutes over a period of 100 minutes. Figure 6.14 b) shows that there is a consistent decrease throughout this period, indicating probable gas diffusion.

In addition to this the Allan deviation was also calculated for a longer series of data over the course of 2 hours. This data was recorded for the 2f-QEPAS signal using the PA (without the GBs chained). As can be seen in Fig. 6.15 a) the effect of this gas diffusion dominates the measurement after $\tau = 1$ s, with a decrease in sensitivity reflected in an increased concentration detection limit. Given that the chamber is designed for eventual use in environments with constant gas flow, with an emphasis on faster signal acquisition this is not a major concern, though it does warrant careful consideration moving foward with the analysis. Despite this, however, the Allan deviation returned a minimum concentration of 15.0 ppm, which agrees with the previous analysis. Also, a correction factor, using a 3rd degree polynomial fit was

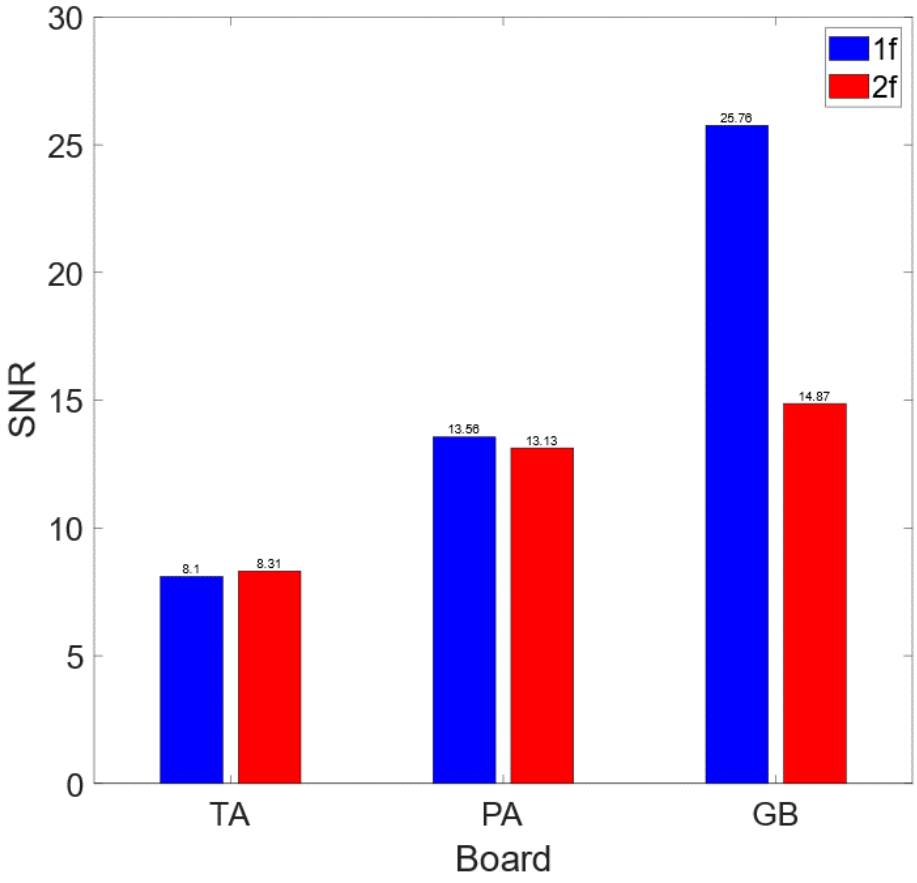

FIGURE 6.13: 1f and 2f-QEPAS SNR comparison for a methane concentration of 500 ppm.

applied to the data to account for the decrease in signal over time. As can be seen in Fig. 6.15 b) this showed that as the time constant was increased the signal did stabilise, and indicates a possible detection limit of 4.6 ppm, however, this should be taken lightly given the corrections applied.

To try and isolate this factor from the rest of the results we developed a simple function to correct for the decrease in peak magnitude across the 8 minute traces, used for the concentration measurements. The drift correction function used MATLAB's inbuilt peak finder function to identify the decrease in signal for a given trace, then after regression analysis a linear function was then used to correct this decrease. This removed the variation due to the drift and the SNRs were recalculated. The downstream intention for this study, is that future QEPAS

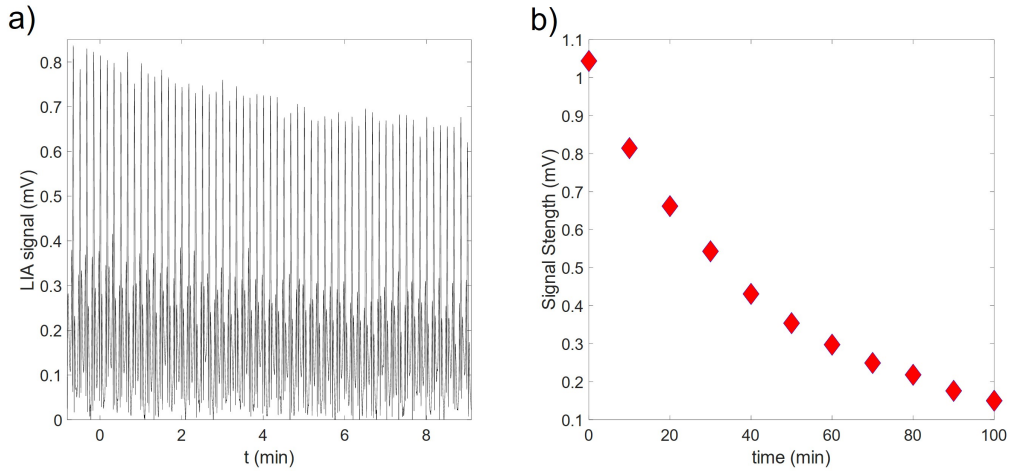

FIGURE 6.14: a) 2f-QEPAS trace connected to the pre-amplifier. The decrease in signal can be clearly seen. b) Results for diffusion tests, with a 2f-QEPAS being measured every 10 minutes.

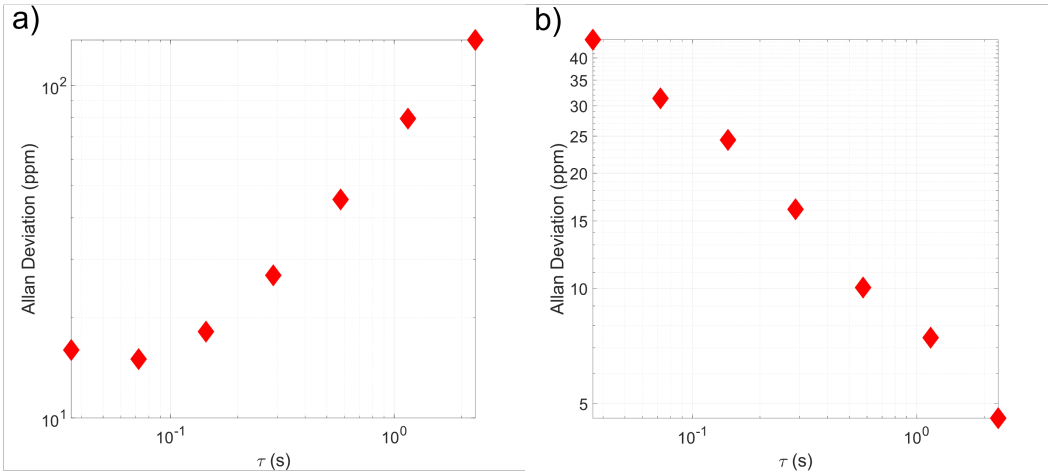

FIGURE 6.15: Allan variance for a) Allan variance calculated for 2f-QEPAS traces recorded over the course of 104 minutes. b) Allan variance after a correction for gas diffusion was applied to the data.

detection modules will be used for continuous monitoring. This would entail constant gas flow through the system, so the effects of gas diffusion here would not be an issue, and so this correction was aimed at providing insight into the performance of the chamber if diffusion was not a factor.

Although an improvement was expected, as can be seen in Fig. 6.16, there was a significant increase in the SNRs. The pre-amplifier now outperforms the TA by a factor of 2.1x for the

2f signal and 3.6x for 1f measurements. These results do still show that for the VA the 1f measurement obtains a better signal than the 2f measurement. Additionally, however, the gain block is now adding noise to the signal for the 1f and 2f measurements compared with the pre-amplifier alone. Despite this the MDL using the best case scenario (1f, pre-amplifier) is now 10.6 ppm.

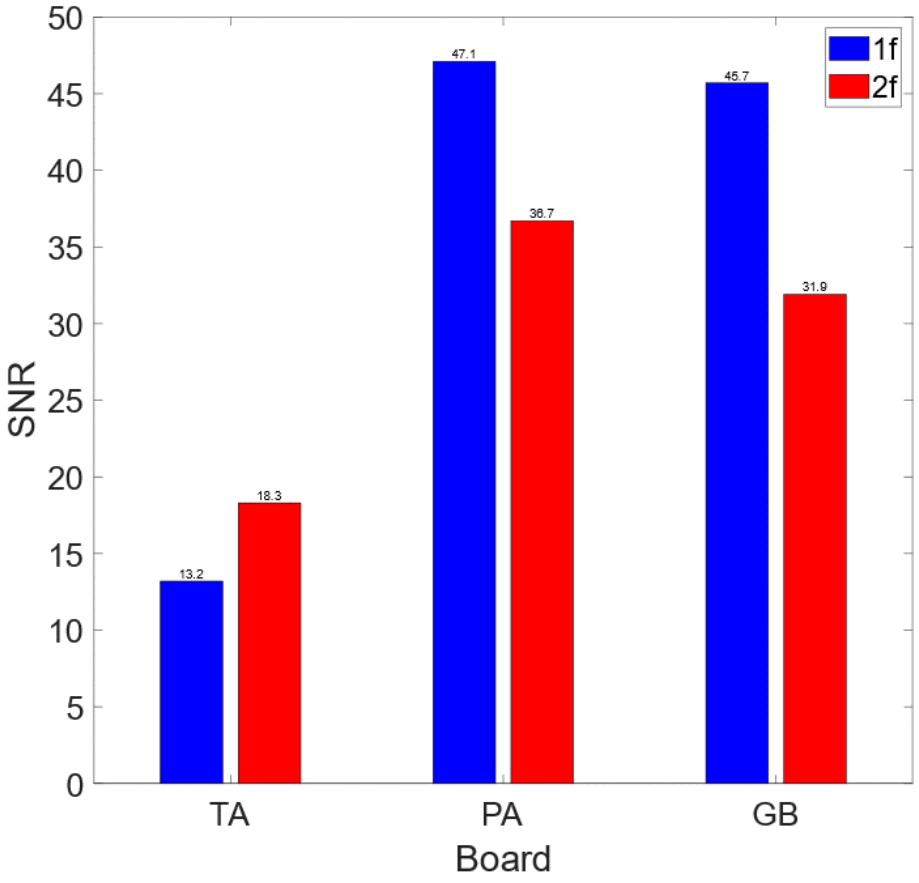

FIGURE 6.16: 1f and 2f-QEPAS results for a methane concentration of 500 ppm, after the drift correction has been applied.

In summary, this section has outlined the operation and direct QEPAS measurements made using a new gas chamber and QEPAS ADM. We showed that this new system was capable of making full QEPAS measurements. After the correction had been applied, an MDL of nearly half that recorded in the previous chapter was reached. However, this correction also showed that the GB reduced the SNR compared to the PA.

6.3 Optimised Configuration for Improved Signal Measurement

Recognising the need for further optimisation, we introduced improvements and conducted additional measurements to see if the results could be improved and to verify the consistency of some of the unexpected findings in the previous section. This section covers the improvements and additional measurements, along with direct comparisons of our QEPAS system to comparable ones in the literature.

6.3.1 Experimental Optimisation

6.3.1.1 Experimental Methods

The physical setup and procedure was similar to that laid out in Section 6.2.1. However, this time high frequency sine wave was generated using the built-in function generator in the Stanford Research Systems LIA (SR830), as can be seen in Fig. 6.17. Furthermore, all cables and pipes for the setup were removed and the experiment was reconnected, with the lengths of the pipes and cables shortened where possible. Overall, the design and connection points did not change from the previous experiment, with the focus being directed towards the efficiency of how the experiment was setup to reduce noise and enhance the measured response. Concentration testing and data analysis was conducted in the same manner as previously outlined. Traces were, however, recorded for only 4 minutes to reduce the effects of gas diffusion. All data analysis was performed using the same code as in the previous section.

6.3.1.2 Results and Discussion

Several changes were implemented to improve the consistency of the experimental setup and to confirm if the discrepancies, particularly around the 1f vs 2f results and the performance of the gain block after the drift correction had been applied, could be repeated. The most significant change was switching to using the LIA's inbuilt function generator, as this is known

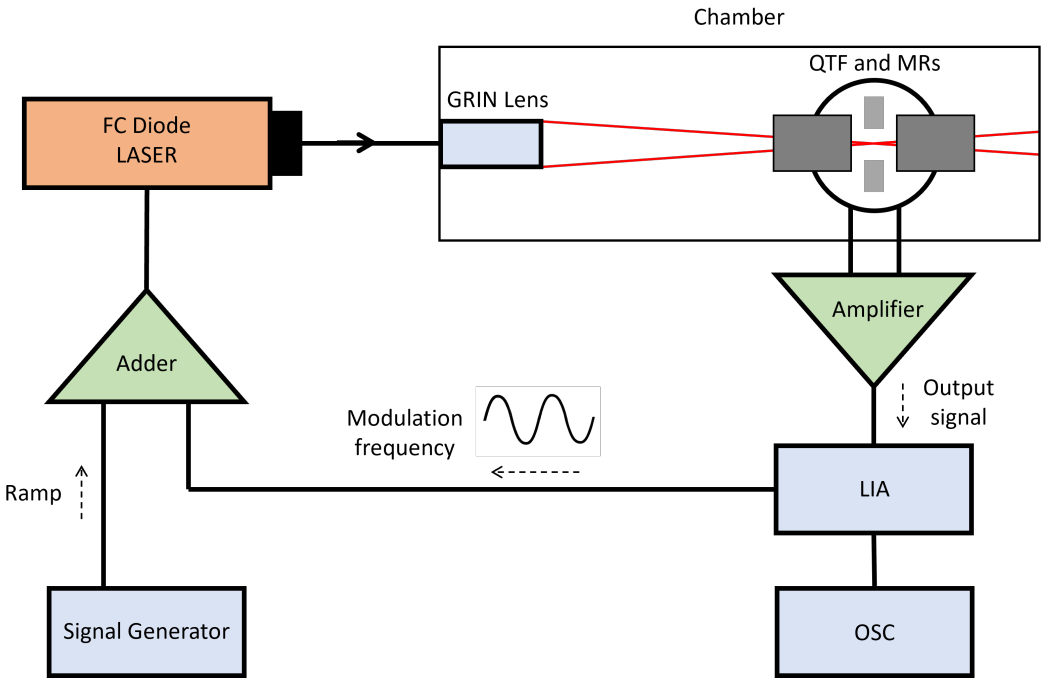

FIGURE 6.17: Schematic of the experimental setup using the LIA's inbuilt function generator to produce the HF sine wave used to produce the differential WMS signal.

to increase the SNR and reduce jitter noise [119]. In addition, the LIA provided a cleaner signal than the previous signal generator.

Further changes were also made to the physical setup and connection of both the gas chamber and the electronics. As noted in the previous section, several of the 0 ppm measurements appeared as though not all the methane had been properly cleared from the chamber. The pneumatic piping between points 1 and 2 was re-fitted with shortened lengths to reduce total volume. In addition, the flush time of the 0 ppm air mixture was increased to 30 seconds. To also reduce the impact of any gas diffusion, the length of time traces were recorded was reduced to 4 minutes.

Additionally, the lengths of the SMA and BNC electronic cables were minimised where possible. The primary focus of this minimisation was on the distance between the pre-amplifier output and the LIA. These were the first experimental components setup, with the others being connected around them. In addition, the LIA, OSC, function generator and adder circuits were all connected to the same circuit breaker to help establish a common ground.

The ground for the LIA was floated to isolate the board from mains noise as much as possible. In addition to helping to reduce noise, these changes also bring the setup closer to that of a self-contained remote sensor that would be isolated from other electrical sources and have shorter connection lengths by necessity. For the electronic modulation parameters, these were kept consistent with the previous setup to isolate the changes made to the physical setup being isolated from other parameters. See appendix Appx. B for a comparison of the modulation drive voltages between the Moku-Go and LIA DAC signals.

The concentration tests were then rerun for the pre-amplifier, without the gain block chained. The overall magnitude of the 1f signal was reduced, with a maximum of 0.40 mV for a methane concentration of 500 ppm. The deviation around the peak was reduced for these measurements (see Fig. 6.18 a)). A trade-off for using the LIA's inbuilt generator was reduced control over the set modulation frequency, and this may be the cause for the reduced signal. However, if the SNR has been improved, then this is not an issue. For the 2f measurements, a general increase was noted with a maximum of 1.2 mV for a methane concentration of 500 ppm. In addition, shown in Fig. 6.18 b), is a reduction in the 1σ deviation of the signal peaks. Both the 1f and 2f-QEPAS measurements once more showed a linear response to changes in concentration, as can be seen in Fig. 6.18 panels c) and d).

The results obtained after the gain block was chained followed the same trends seen for the PA. As can be seen in Fig. 6.19 a) the magnitude of the 1f signals was lower than in the previous setup, although once again the deviation has been reduced. The 2f measurement not only had a relative reduction in deviation, the magnitude of the signal was increased (as shown in Fig. 6.19 b)). Figure 6.19 panels c) and d) also show that the linear response to concentration is maintained. Additionally, the average sweeps for the 0 ppm methane air mix shows a much flatter response for both the 1f and 2f measurements, indicating that reducing the pipe lengths and increasing the flush time is sufficiently purging the chamber between tests. The 1f measurement does show a slight increase between $2 \rightarrow 6$ s, which is likely a background signal and not from the remaining methane, given the much flatter 2f results (at 0 ppm). This fits with expectations in the literature that a 1f signal is expected to be more susceptible to a larger background than the 2f signal [85].

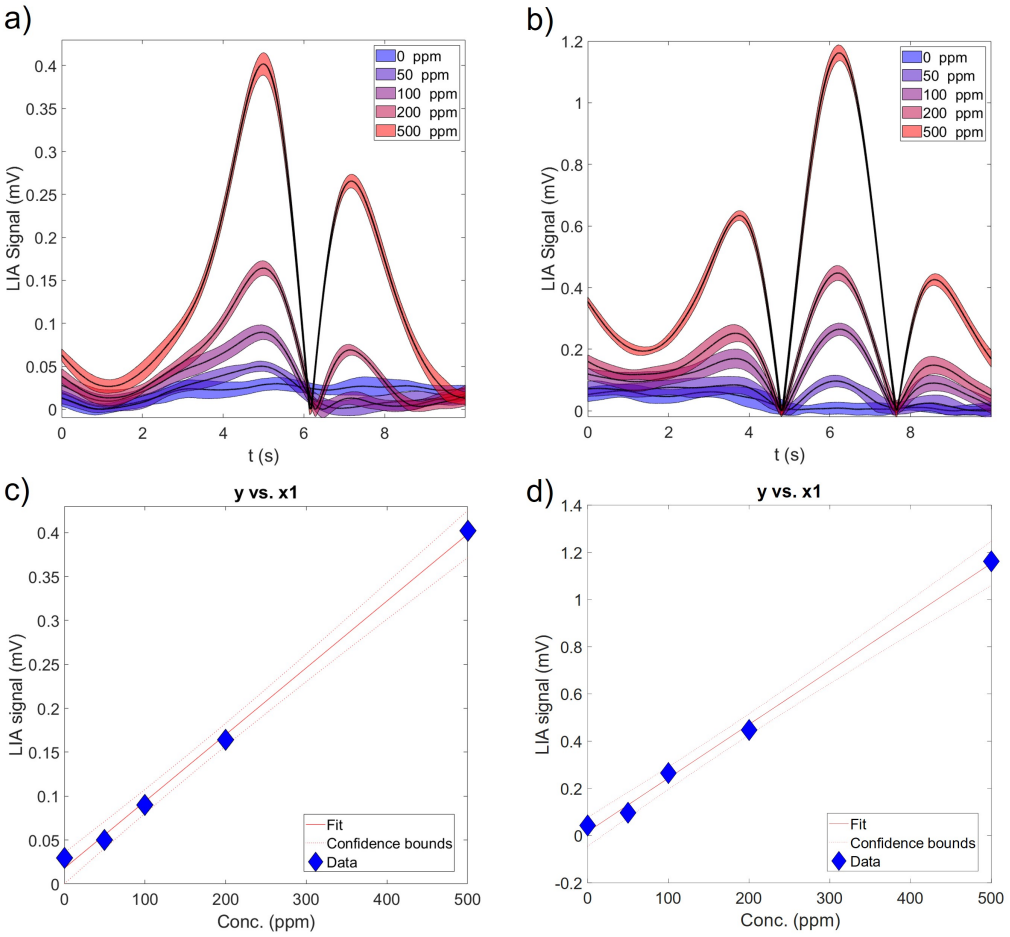

FIGURE 6.18: Concentration sweep results for the pre-amplifier, after experimental optimisation. a) 1f-QEPAS signal, with the average trace shown as black lines and the shaded region showing the 1σ variation around each point in the trace. b) 2f-QEPAS signal. c) Maximum 1f-QEPAS signal with linear regression fitting. ($R^2 = 0.99$) d) Maximum 2f-QEPAS signal with linear regression fitting. ($R^2 = 0.99$)

The TA board showed the same general change in signal magnitudes, with a general reduction for the 1f signal and an increase for the 2f. The deviation for the 1f signal was generally reduced, especially for the higher concentrations of 200 and 500 ppm methane. However, as is clearly visible in Fig. 6.20 a) both 50 and 100 ppm signal peaks are within error of the 0 ppm air measurement. This is an important point to note when comparing the performance of the TA to the VA design. Before looking at the SNRs this shows that the VA design is outperforming the TA control at lower concentrations. Performance is better for the 2f signal, with reduced overlap at lower concentrations. However, the 50 and 100 ppm signals are

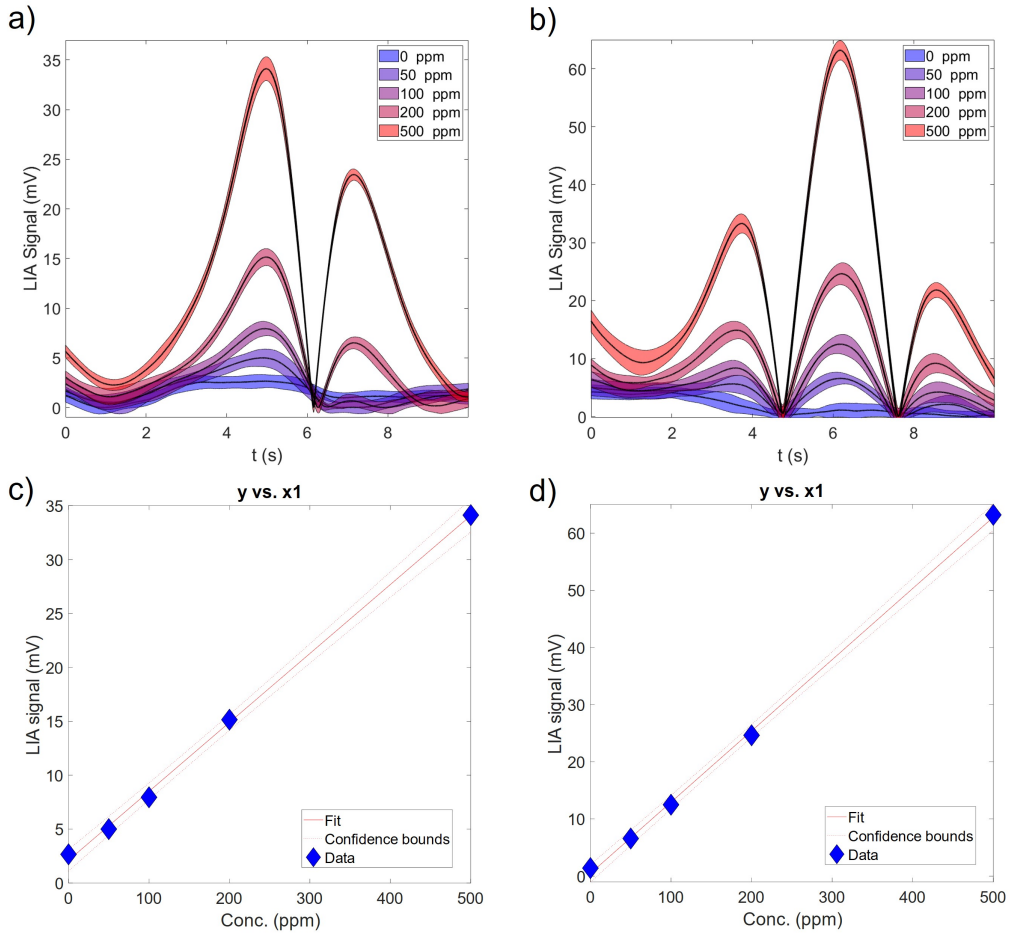

FIGURE 6.19: Concentration sweep results for the pre-amplifier chained to the gain block, after experimental optimisation. a) 1f-QEPAS signal, with the average trace shown as black lines and the shaded region showing the 1σ variation around each point in the trace. b) 2f-QEPAS signal. c) Maximum 1f-QEPAS signal with linear regression fitting. ($R^2 = 0.99$) d) Maximum 2f-QEPAS signal with linear regression fitting. ($R^2 = 0.99$)

within error of each other. These results are reflected in the linear analysis for both. As can be seen in Fig. 6.20 c), the lower concentrations show a flatter, non-linearity to the electronic response. This is reflected in the slightly lower $R^2 = 0.97$. The 2f maintains the linear signal response to concentration, as can be observed in Fig. 6.20 d), with an $R^2 = 0.99$. However, this suggests that lower concentrations should be considered when assessing the MDL and SNRs of the different amplifier designs.

With these results, let us look at the SNRs and MDLs to compare with the previous setup and with similar QEPAS detectors in the literature. Starting with the SNRs for the 500 ppm

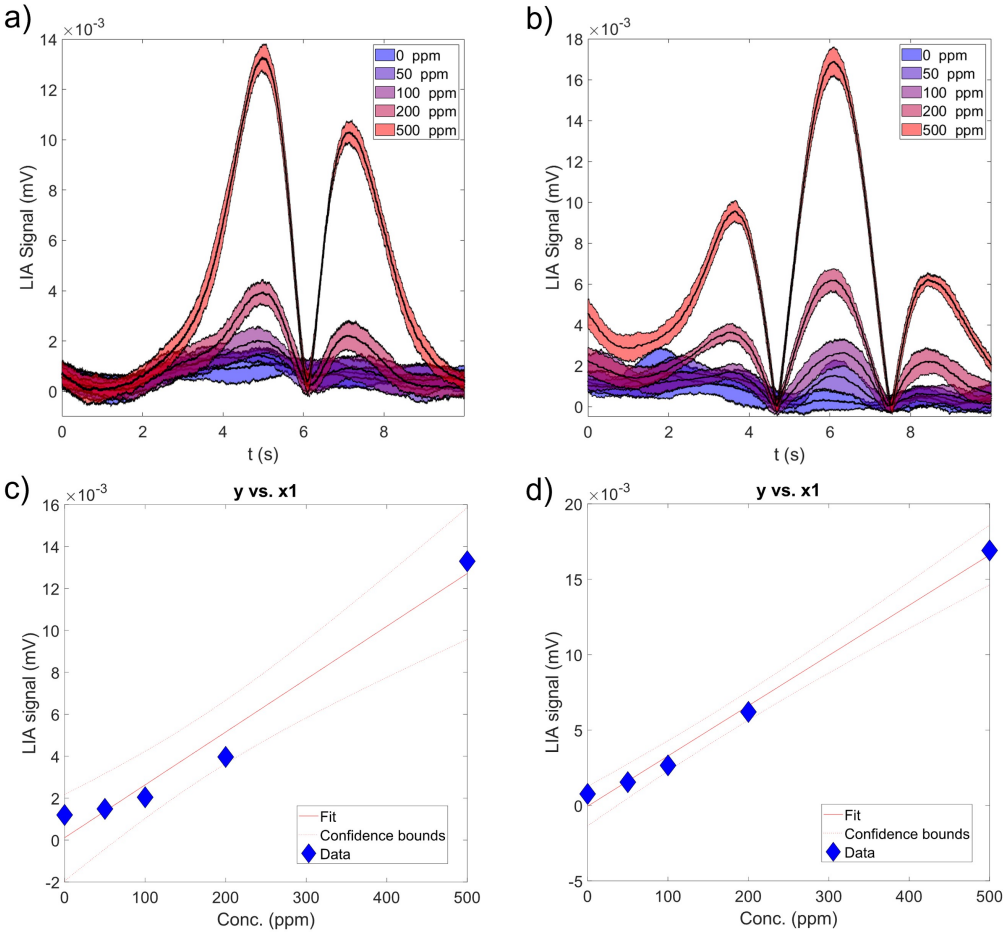

FIGURE 6.20: Concentration sweep results for the transimpedence amplifier. a) 1f-QEPAS signal, with the average trace shown as black lines and the shaded region showing the 1σ variation around each point in the trace. b) 2f-QEPAS signal. c) Maximum 1f-QEPAS signal with linear regression fitting. ($R^2 = 0.97$) d) maximum 2f-QEPAS signal with linear regression fitting. ($R^2 = 0.99$)

methane concentration tests, there was an increase for all three setups. These SNRs are shown in Fig. 6.21 a), with the 1f measurements being fairly close to each other, and the 2f being noticeably higher for the VA board (both pre-amplifier alone and with the gain block) than for the TA. For the TA the SNR roughly tripled for both the 1f and 2f measurements, in comparison with the previous setup. Looking at the 1f and 2f measurements separately for a moment. The 1f results show SNRs that, although much higher than previously, shows a much smaller difference between the VA and TA configurations, although the gain block does seem to provide an improved SNR. For the 2f results, there is the same decrease as previously

when the gain block is chained, with the SNR reducing by 30%. However, both are still higher than the TA.

Compared with the previous setup the largest increase, however, was for the 2f measurements utilising only the pre-amplifer. This also produced the highest SNR, without drift correction, measured so far. Using this SNR, we achieve an MDL for methane of 11.7 ppm. Looking back at the literature review, this indicates that our chamber performs slightly better than *Chen et al* [129] who achieved an MDL for methane of 14.93 ppm. This study is the closest analogue to our own as they reported a 3D printed chamber as well. They targeted an absorption feature at 1651 nm which had a slightly higher, but comparable absorption co-efficient to our targeted peak at 1653.7 nm. One notable difference, however, is that their study utilised a high power laser diode that emitted ~ 38 mW, an order of magnitude higher than the 3.919 ± 0.002 mW (prior to modulation) that was used for the detector in this thesis. Given that a QEPAS signal is proportional to the laser power, this suggests that the use of our VA has enabled us to achieve a signal that would otherwise require much more power and cost-demanding optics.

It is worth noting a few differences between the SNR calculations used here and the general approach in the literature. The most common approach is to use the ratio of the maximum signal peak divided by the 1σ variation of the interline region, i.e. when the laser wavelength is not on any absorption feature. Although the use of the maximum of the 1f or 2f signals is consistent, we use the variation of the peak itself. There are two primary reasons for this. This first is that most literature SNRs are calculated for a single 2f wavelength sweep, and so does not allow for variation in the peak to be observed. Given that we recorded repeated sweeps, this enabled us to observe the deviation in each, along with any potential trends. Since the magnitude of the peak is used to determine the concentration, it was useful to see if the peak experienced a variation that was not accounted for by monitoring the interline regions. Secondarily was the wavelength range covered using our detector. Since the long-term goal of this project is to develop remote detectors that can take relatively fast measurements, a relatively narrow wavelength range of $1653.68 \rightarrow 1653.73$ nm was used. This was to allow for somewhat faster sweeps by minimising downtime. This did appear to prevent the signal from dropping all the way back to the 0 ppm level in-between scans. This is evidenced

by the increasing signal measured at around one second for higher concentrations. This is because there is not enough time for the energy to fully dissipate from the ADM resonator in-between scans. However, given that all the 2f signals maintain a high linear response to concentration, this does not seem to be impacting the ability of the detector to monitor higher concentrations. Furthermore, future applications will be targeted towards monitoring much lower concentrations of methane, where this effect does not appear to be present.

The SNRs were also calculated for a methane concentration of 500 ppm using the 1σ variation from the interline region to ensure the validity of our findings. Table 6.1 compares these results: SNRs calculated using the 1σ variation of the signal peak with those obtained using the interline variation to assess signal stability. Notably, the SNRs are higher across all cases when measured using the interline variation. This suggests that our method presents a more conservative assessment compared to the main method used in the literature.

TABLE 6.1: Comparison of the SNRs using the variation in signal peaks compared with the variation of the interline region. Results here are for a methane concentration of 500 ppm

Amplifier	**Peak SNR (1f/2f)**	**Interline SNR (1f/2f)**
TA	27.54/23.78	32.8/27.3
VA	30.1/42.78	46.6/61.4
VA with GB	35.1/33.0	48.8/40.5

To remove the effect of gas diffusion, we applied the drift correction to all of these data sets. These results, shown in Fig. 6.21 b), are more consistent with expectations. The pre-amplifier outperforms the TA's SNR by 18.52 and 35.7, for the 1f and 2f measurements, respectively. These results also show that the gain block further increases the SNR for both the 1f and 2f signals. This is in line with design intentions and expectations. The reason the drift correction may have made such a difference is that the whole VA board (especially the gain block) provide significant amplification. The deviation that arises from gas diffusion, rather than inherent noise, would have a larger impact on the magnitude of the signal. However, for the TA, where little improvement was noted, the magnitude of electrical noise in the signal is greater in comparison to the decrease arising from diffusion. Therefore, correcting for this drift provided much less of a change to the SNR.

For the pre-amplifier, the 2f signals now exhibit a higher SNR than the 1f signals, which aligns with theoretical expectations and reports in the literature. The adjustments made to more carefully measure the QEPAS signals suggest that the previous discrepancies are likely attributable to the ability to drive the 1f signal at a higher modulation depth, rather than any inherent properties of the board. However, this remains an interesting aspect for future investigation. Here, the only results still showing a higher 1f signal are those associated with the TA board, but the difference is marginal at just 2%. Given that the relative 1σ variation around each peak is significantly larger, no definitive conclusions can be drawn, and this difference does not suggest that the 1f signal offers any inherent advantage in this context. Furthermore, considering earlier results did not indicate superior 1f performance of the TA, these findings do not imply any unexpected behaviour in the experimental setup.

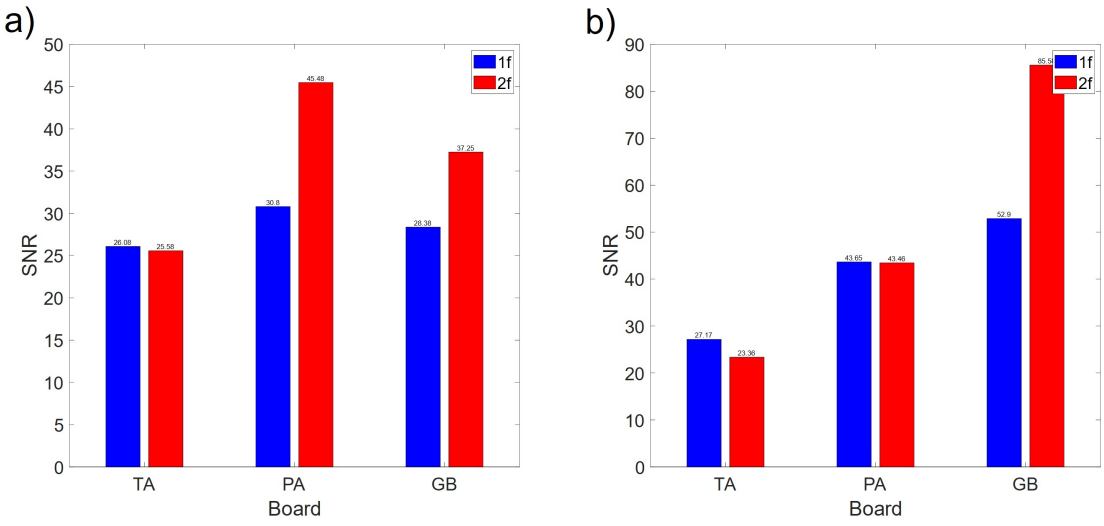

FIGURE 6.21: Bar charts showing the SNRs for different amplifier board layouts at a methane concentration of 500 ppm. a) 1f and 2f results without correction. b) Results after the drift correction has been applied.

However, as noted above, the performance of the TA appeared poorer at lower concentrations. Given this, we also analysed the SNR and MDLs for the lowest 50 ppm methane concentration traces. As can be seen in Fig. 6.22 a), the magnitude of all the SNRs are much lower, as expected from a weaker signal from the less concentrated cell. However, the trends remain largely the same as the previous results. A maximum SNR of 6.24 was obtained for the 2f measurement using the pre-amplifier, which in turn provides an MDL of 8.01 ppm. Compared

to the 2f MDL of only 27.6 ppm for the TA, indicating that the advantages of the VA design are more pronounced at for weaker signals. For a full summary of all the MDLs, see appendix Appx. B.

Once again, the results were analysed after applying a drift correction. As seen in Fig. 6.22 b), this led to a slight increase in SNR, although it was less pronounced than with the 500 ppm concentration. If the drift was due to gas diffusion, then less diffusion at lower concentrations would be expected. Additionally, the larger background from the 1f measurements is relatively much higher at these concentrations compared to the 2f signal, making the benefits of locking to the second harmonic more evident. In all cases, with and without drift correction, the 2f signals outperformed the 1f, as expected.

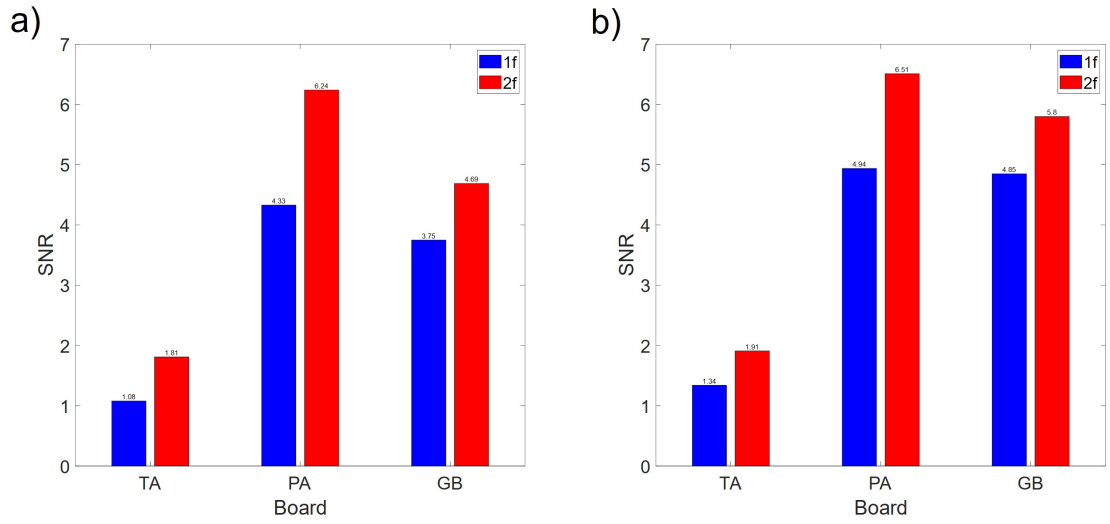

FIGURE 6.22: Bar charts showing the SNRs for the amplifier board layouts at the lowest a methane concentration of 50 ppm. a) 1f and 2f results without correction. b) 1f and 2f results after a drift correction has been applied.

Although the gain block does not seem to be improving the SNR compared to the pre-amplifier alone, it is still important to note the magnitude of signal amplification that is still performed. For the non-drift corrected 2f measurements, the gain block further increases the signal of the pre-amplifier from $0.97 \rightarrow 6.6$ mV at a concentration of 50 ppm, and from $1.2 \rightarrow 63.2$ mV at a concentration of 500 ppm. Compared to the raw output of the TA, which only produces a $17\ \mu$V signal for a concentration of 500 ppm, this is a gain of 71.4 dB. Although there is a need for future improvements, this does demonstrate that the use of the gain block is a suitable

approach for providing significant electronic amplification, whilst maintaining relatively low power requirements.

6.3.2 Longer Scan Times

6.3.2.1 Experimental Methods

Additional tests were performed with a reduced sweep speed. The frequency of the triangle sweep signal was reduced to 25 mHz and the measurements were retaken for a methane concentration of 500 ppm. All other test conditions were kept consistent with those outlined in Section 6.3.1.1. Given that the 2f-QEPAS method is the primary one used in the literature, and the above results show that the optimised setup also consistently obtains better SNRs with this method, we focused only on that for these measurements. In addition we also tested the pre-amplifier for the lower frequency board as a proof of concept.

6.3.2.2 Results and Discussion

Following expectations, the SNRs show an increase over those found in previous tests. Although the TA also saw an increase in SNR, the VA designs provide a higher SNR, giving an MDL of 16.3 ppm. Additionally, the gain block demonstrated an improvement in the SNR when chained to the pre-amplifier. The pre-amplifier and gain block produced the highest SNR obtained, without drift correction, in this thesis so far. In turn, this indicates an MDL of 7.8 ppm. The lower frequency pre-amplifier also demonstrated a larger SNR than the TA. Given that the only significant difference between the pre-amplifier designs was the choice of op-amps, this was to be expected. Additionally, the lower frequency pre-amplifier board is still returned a lower SNR than the higher frequency design, reflective of the design choices behind the selection of the op-amps.

These results further support that our QEPAS detector is capable of outperforming the previously mentioned study of a 3D printed QEPAS chamber by *Chen et al* [129], achieving almost half the MDL. Generally, the experimental refinements in this chapter have decreased the MDLs, however, here that also held true for the TA. The pre-amplifier (with and without

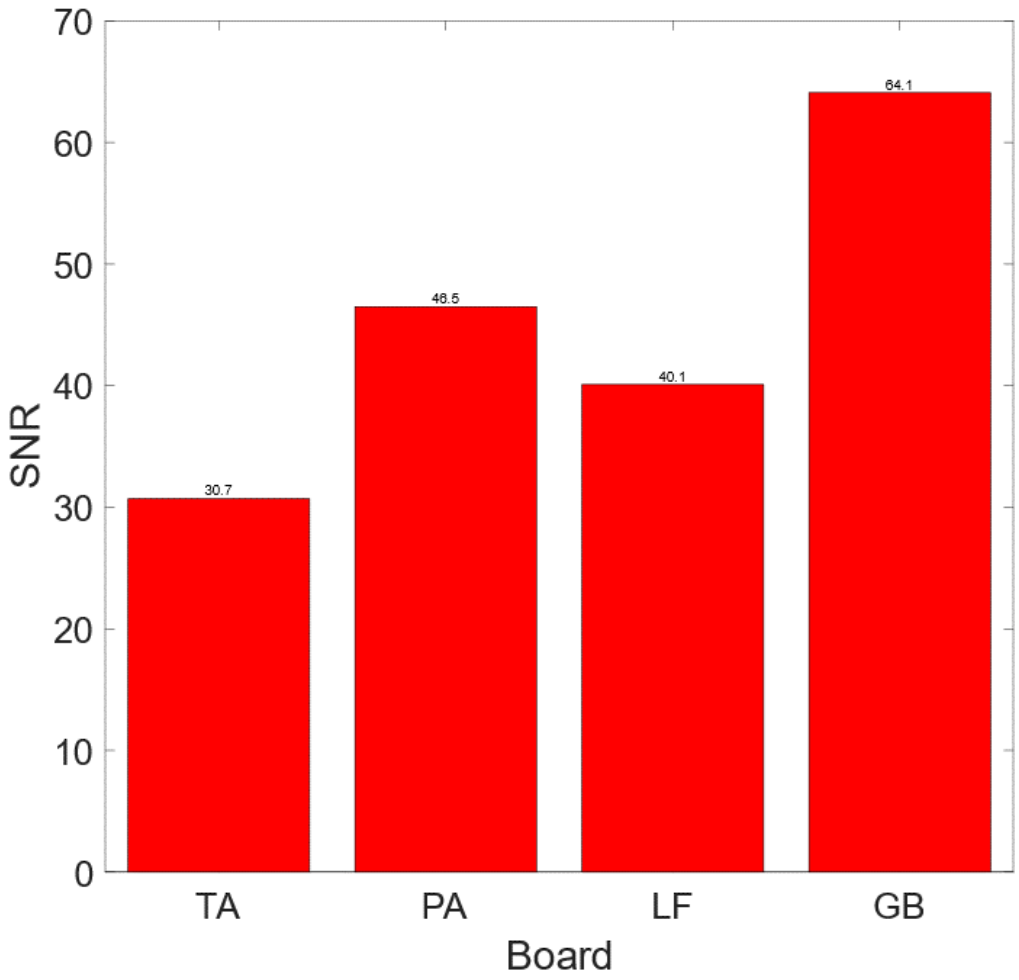

FIGURE 6.23: Bar chart showing the SNRs from 2f-QEPAS measurements for different amplifier board layouts at a methane concentration of 500 ppm for a slower sweep speed of 25 mHz. Additionally, the response of the lower frequency pre-amplifier (LF) is also included. No baseline correction has been applied.

the gain block) does outperform the TA as expected, the relative improvement is somewhat less than anticipated. However, based on previous analyses at lower concentrations, this likely reflects an overestimation of the TA's actual performance near the MDLs reported here, while the findings for the VA are likely more accurate.

Upon revisiting several more of the methane detection studies detailed in the literature review, we note several others with comparable MDLs to the most recent results using the VA pre-amplifier and gain block. *Li et al* [135] achieved a slightly lower MDL of 7.0 ppm. However, there are a few differences between our setups. The first is that, although they were operating a DFB emitting a roughly similar output (maximum of 6.2 mV), they were also targeting a much stronger absorption feature (at $\lambda = 2.3$ μm). Additionally, they also employed a customised QTF operating at $f = 30.72$ kHz. Considering these two procedural differences, it is likely that we would expect to be working with a weaker signal, even though our detection limits are almost equal.

Another paper that stands out is the study conducted by *Medduni et al* [136] who achieved a detection limit of 0.76 ppm. This study, importantly, also targeted the same absorption feature as our detection unit. However, they used a more powerful fibre-coupled DFB (~ 12 mW), and a custom QTF operating at $f_0 = 12.5$ kHz. The custom QTF used here was shown to provide an increase in SNR of 4.2 compared to the standard one used in our detector [112]. These two factors suggest a raw QEPAS signal $\sim 12\times$ greater than ours. Given that our 2f MDL is $10.2\times$ higher, indicating slightly better performance from our detection unit.

For a more direct comparison, we calculated the normalised noise equivalent absorption (NNEA) for our chamber. This takes into account differences in laser power, detector bandwidth, and specific absorption peaks. For our chamber, using the most recent 2f-QEPAS results for the pre-amplifier chained to the gain block, a NNEA of 1.0×10^{-8} cm^{-1}W$/\sqrt{\text{Hz}}$ was obtained. This confirms that our chamber performs better than the aforementioned 3D-printed chamber (2.20×10^{-7} cm^{-1}W$/\sqrt{\text{Hz}}$). The study by *Medduni et al* does not report an NNEA for comparison, although the study by *Li et al* reports an initial NNEA of 7.3×10^{-9} cm^{-1}W$/\sqrt{\text{Hz}}$. Whilst this is slightly lower than ours it still shows that our chamber is competitive, especially when considering the main goal here of achieving a low-cost practical approach to the construction of gas detectors.

It is also important to note that our experiments were conducted in dry air, and water vapour is known to enhance signal strength. Specifically, the presence of water vapour provides alternative energy pathways that increase the V-T relaxation rate, increasing the measured

signal by making photonic to acoustic energy transfer more efficient [181]. Some studies have even shown that the presence of water vapour (2% humidity) can increase measured signals by 40% [182]. Therefore, in regard to taking environmental measurements at atmospheric humidity levels, our results likely underestimate the performance of our detector under field conditions. These results demonstrate clear progress in terms of chamber design and construction, offering a solid basis for further refinement and optimisation in future iterations.

6.4 Conclusion

Based on the limitations described in the previous chapter (Chap. 5), we present an improved version of the gas chamber, constructed by building upon the design and assembly methods also described previously. Using this new chamber, we performed 1f and 2f-QEPAS measurements using a scanned wavelength approach. After initial calibration, these measurements showed that the issues of the previous chamber had been overcome. However, these initial signals provided lower than expected SNRs. As a result, the experimental setup and methodology were reworked to improve signal measurement. Results taken using this setup were much closer to expectations and demonstrated improved performance of the QEPAS detection unit. Not only did these results show that the electronic amplifiers are suitable for use in detecting QEPAS signals from a QTF, but most importantly they showed an improvement over a traditional TA. Although there is still work to be done to further improve the MDL and NNEA of this chamber, these results indicate the validity of our approach to achieve a direct optical comparison of different electronic amplifier designs.

CHAPTER 7

Conclusions and Future Work

In this thesis, we explored novel approaches to gas detection using modulation absorption spectroscopy. Two innovative techniques were examined: cross-correlation and wavelength modulation spectroscopy. For cross-correlation spectroscopy, we present a unique notch filter and demonstrate experimental methodologies that enable its use in highly selective gas detection. For wavelength modulation spectroscopy, we employ flexible design and construction methodologies to build QEPAS detection units, facilitating a direct comparison of specialised electronic amplifiers.

Here, a novel complex aperiodic FBG is presented for the notch-filter, where the reflection and transmission spectra were customised to match the absorption features of the P-band of acetylene C_2H_2, forming a "photonic" molecule. This is the first use of such a complex device made specifically for direct fingerprint molecular detection. We also present experimental methodology for the use of this device in the detection of acetylene. The results demonstrate that, not only is this device capable of detecting differing amounts of the target gas, it is also highly immune to contaminate gases. Simulations were used to demonstrate that the impact of interlopers, such as cyanide HCN with overlapping absorption features, is predictable thus, suggesting the potential versatility of such devices.

We aim to apply this technique with other gases in the future to target the pressing need for methane sensors for use in environmental monitoring. Acetylene was an ideal gas for proof-of-concept; however, gases such as methane CH_4, and nitrous oxide NO_2, would make great next targets. This work would include detailed calibration curves and specific analysis to enable these devices to be used for determining specific concentrations, rather than the proof of concept demonstrated here. Although the present work focused on relative

measurements and detection/non-detection scenarios, next-generation experiments should enable calibrated determination of the optical path integrated molecular count. The compact, lightweight, and robust nature of the photonic componentry used here bodes well for future potential integration into portable detectors for real-world sensing applications. With the future development of portable detectors, field measurements to measure trace greenhouses gases on large scales will be possible.

A key focus of this research was enhancing electrical amplifiers for QEPAS gas detection. By building on prior work, we designed and tested new voltage amplifiers (VAs). These VA-based pre-amplifier (PA) designs have two primary variants: one designed to operate at lower frequencies and one designed to operate at higher frequencies, enabling their use in the amplification of both standard and custom QTFs. Further gain block (GB) filters were also designed and we showed that they could be chained to these PAs to provide further signal enhancement. The plug and play design of these boards also allows for easy incorporation into a QEPAS unit. Combined with the flexible, cost effective nature of our gas chamber designs this work marks a notable advancement towards creating highly sensitive, yet cost effective QEPAS sensors.

Detailed designs of each board are presented herein, along with the build and assembly details as well as electronic testing and characterisation. Electronic characterisation included frequency response tests of the PAs chained with their respective GB. The higher frequency board was shown to match the expected frequency response and gain levels. The lower frequency board showed the expected frequency response, however, did not provide the expected gain. This was followed up with noise floor testing, using fft analysis, and the response of each board to an emulated QTF signal. The results for the emulated signals showed that both boards provided the expected linear response, both from the PA and GB components. These tests also showed that the PA of the low frequency board provided even higher gain than the PA for the high frequency board. Comparing the PA performance to that with the GB, the lower than expected frequency response was from the GB, indicating that the PA was still suitable for use in QEPAS.

The higher frequency board is capable of measuring QEPAS signals, at least via a specially designed, 3D printed QEPAS detection chamber that incorporated a standard $f = 32.768$ kHz QTF. We also present the design of this chamber in two parts. The first part used high-resolution resin printing to build a framework for the QEPAS ADM. The second part used standard extrusion printing to construct a gas chamber to house the ADM for testing. In addition to the assembly of the QEPAS module with these parts, we also present a chemical annealing process that provides a better material finish for gas detection testing. Using this chamber we were able to achieve proof-of-concept for the high-frequency amplifier design's capability of detecting methane. Using a fixed wavelength approach, we were able to reach a minimum detection limit (MDL) of 15.0 ppm for methane. However, the simple optical design of this chamber was unable to produce reliable results for a scanned-wavelength approach.

Subsequently, a new detector was developed with improved optics to provide better analysis of our electronic amplifiers. Using this detector, it was possible to measure 1f and 2f-QEPAS responses with a scanned wavelength approach. We also designed and assembled a transimpedance amplifier to act as a control. However, these results had much higher MDLs than expected, when compared to the MDLs measured using the fixed wavelength approach with the older chamber. As a result, the experimental setup was reworked and more reliable data was collected. For methane, these results returned a best case MDL of 11.00 ppm uncorrected, and a best case MDL of 6.43 ppm corrected.

Final testing using a slower scan speed was then carried out. These results showed that even without correction the GB was capable of both amplifying the signal from the PA by 35 dB, and increasing the SNR. This returned an MDL of 7.80 ppm, and an NNEA of 1.0×10^{-8} cm^{-1}W$/\sqrt{\text{Hz}}$. While there is still considerable room for improvement here, this did demonstrate improved performance of our detection unit compared to a comparable setup. Most importantly, all of the testing done using the improved detector demonstrated improved signal measurement when using the VA board designs over a traditional TA. An increase of 71.4 dB to the raw signal, as well as a SNR of more than double, could be achieved when using our electronic amplifiers. Overall, this demonstrates that the procedures and designs used in this study are suitable for providing a direct optical comparison for QTF amplifier. To

the best of our knowledge, this is the first time a VA amplifier has been successfully used in a methane detector.

One of the more pressing areas is to develop the detector further for future use in field testing. To achieve the goal of environmental monitoring, the MDL still requires some improvement. However, this unit could also potentially be adapted to function as a safety detection unit for use in confined spaces. The cost-effective nature of the 3D printing and assembly techniques would be beneficial in developing numerous gas chambers and ADMs for use in more dangerous environments. To this end, now that the operating conditions are better understood, the development of a hardware-based LIA would likely allow the current setup to be converted into a more portable version. Combined with the FPGA signal generators and detection units already used in this study, developing a portable unit using this approach would be a suitable avenue for field testing.

One of the benefits of QEPAS is that many parts of the physical setup are hardware agnostic to other components. For example, whilst the electronic amplifier is tied to the QTF, it is not tied to the optical source of the setup. This means that improvements shown here can be applied to other systems. Another path towards environmental monitoring, therefore, would be to incorporate design elements from other QEPAS detectors with the electronic amplifiers presented here. The use of a more powerful diode laser or a fibre amplifier would, for example, improve the signal. Our setup could be used to test the performance of our amplifier designs for other methodologies, such as beat-frequency QEPAS or photothermal QEPTS. Given this hardware flexibility, it would also be interesting to use our detector with optics for detecting other gases. The amplifier board would still improve the signal and would allow our detector to be used in a wider range of environments.

Improving the electronic noise levels of the boards, naturally, would be significant for future application of this technology. Now that our amplifier designs have been demonstrated to work, however, less flexibility is needed for the parts during and after assembly. To this end, the next step should be to develop a fully surface mount design with all parts mounted industrially during assembly. This would reduce the footprint of the amplifiers, thus increasing their suitability for incorporation into a small remote detection unit. Future designs could

also incorporate more PCB layers. More layers would allow for better isolation and shielding of the most noise-sensitive parts. More layers would also enable other options, such as uninterrupted ground pours and reduced vias. In combination with other noise reduction design elements, such as thicker layers and better low-noise materials (e.g. Rogers or Isola laminates). These elements would enable the significant gain to be maintained, while further reducing the electronic noise that such gain is highly susceptible to.

Overall, the primary goal of this work was to investigate novel approaches for gas detection. This took the form of two main avenues of research: to demonstrate that it is possible to use a customised complex aperiodic FBG device for gas detection, which is currently the only result of its kind in the world; as well as, to develop a simple and cost-effective technique for producing QEPAS detectors for the monitoring of methane, which allowed for direct testing of electronic amplifier performance. Despite some limitations relating to the sensitivity of our QEPAS detector, we were nevertheless able to demonstrate a method of direct optical comparison. The gas chamber and ADM were manufactured using widely available 3D printing and assembly methods, which provide high levels of design flexibility whilst maintaining cost effectiveness. We are confident that this will help lay the groundwork towards developing practical, portable gas detectors capable of highly sensitive and selective fingerprint detection.

Bibliography

[1]A. I. Filkov, T. Ngo, S. Matthews, S. Telfer and T. D. Penman, 'Impact of Australia's catastrophic 2019/20 bushfire season on communities and environment. Retrospective analysis and current trends', en, Journal of Safety Science and Resilience **1**, 44–56 (2020).

[2]A. Gissing and N. Bibby, 'Readiness for the next major bushfire emergency', EN, Australian Journal of Emergency Management, The **35**, Publisher: Emergency Management Australia, 13 (2020).

[3]B. Jalaludin, F. Johnston, S. Vardoulakis and G. Morgan, 'Reflections on the Catastrophic 2019–2020 Australian Bushfires', en, The Innovation **1**, 100010 (2020).

[4]M. Ladds, A. Keating, J. Handmer and L. Magee, 'How much do disasters cost? A comparison of disaster cost estimates in Australia', en, International Journal of Disaster Risk Reduction **21**, 419–429 (2017).

[5]N. H. Saji, B. N. Goswami, P. N. Vinayachandran and T. Yamagata, 'A dipole mode in the tropical Indian Ocean', en, Nature **401**, Number: 6751 Publisher: Nature Publishing Group, 360–363 (1999).

[6]M. J. McPhaden, S. E. Zebiak and M. H. Glantz, 'ENSO as an Integrating Concept in Earth Science', en, Science **314**, Publisher: American Association for the Advancement of Science Section: Review, 1740–1745 (2006).

[7]S. Harris and C. Lucas, 'Understanding the variability of Australian fire weather between 1973 and 2017', en, PLOS ONE **14**, Publisher: Public Library of Science, e0222328 (2019).

[8]C. W. Team, *Climate Change 2023: Synthesis Report. Contribution of Working Groups I, II and III to the Sixth Assessment Report of the Intergovernmental Panel on Climate Change*, Synthesis Report (Intergovernmental Panel on Climate Change (IPCC), Geneva, Switzerland, 2023), pp. 35–115.

[9]D. A. Lashof and D. R. Ahuja, 'Relative contributions of greenhouse gas emissions to global warming', en, Nature **344**, Number: 6266 Publisher: Nature Publishing Group, 529–531 (1990).

[10]J. Lelieveld, P. J. Crutzen and F. J. Dentener, 'Changing concentration, lifetime and climate forcing of atmospheric methane', en, Tellus B **50**, _eprint: https://onlinelibrary.wiley.com/doi/pdf/10.1034/j 0889.1998.t01-1-00002.x, 128–150 (1998).

[11]D. R. Tyner and M. R. Johnson, 'Where the Methane Is—Insights from Novel Airborne LiDAR Measurements Combined with Ground Survey Data', Environmental Science & Technology **55**, Publisher: American Chemical Society, 9773–9783 (2021).

[12]S. Schwietzke, O. A. Sherwood, L. M. P. Bruhwiler, J. B. Miller, G. Etiope, E. J. Dlugokencky, S. E. Michel, V. A. Arling, B. H. Vaughn, J. W. C. White and P. P. Tans, 'Upward revision of global fossil fuel methane emissions based on isotope database', en, Nature **538**, Number: 7623 Publisher: Nature Publishing Group, 88–91 (2016).

[13]B. Hmiel, V. V. Petrenko, M. N. Dyonisius, C. Buizert, A. M. Smith, P. F. Place, C. Harth, R. Beaudette, Q. Hua, B. Yang, I. Vimont, S. E. Michel, J. P. Severinghaus, D. Etheridge, T. Bromley, J. Schmitt, X. Faïn, R. F. Weiss and E. Dlugokencky, 'Preindustrial 14CH4 indicates greater anthropogenic fossil CH4 emissions', en, Nature **578**, Number: 7795 Publisher: Nature Publishing Group, 409–412 (2020).

[14]Z. Du and J. Li, 'Spectroscopic Gas Sensing Systems', en, in *Handbook of II-VI Semiconductor-Based Sensors and Radiation Detectors: Vol. 3: Sensors, Biosensors and Radiation Detectors*, edited by G. Korotcenkov (Springer International Publishing, Cham, 2023), pp. 335–360.

[15]L. Sommer, *Analytical Absorption Spectrophotometry in the Visible and Ultraviolet: The Principles*, en, Google-Books-ID: bUt_21vaGPkC (Elsevier, Dec. 2012).

[16]M. Kwaśny and A. Bombalska, 'Optical Methods of Methane Detection', en, Sensors **23**, Number: 5 Publisher: Multidisciplinary Digital Publishing Institute, 2834 (2023).

[17]S. Suchalkin, G. Belenky and M. A. Belkin, 'Rapidly Tunable Quantum Cascade Lasers', IEEE Journal of Selected Topics in Quantum Electronics **21**, Conference Name: IEEE Journal of Selected Topics in Quantum Electronics, 1–9 (2015).

[18]R. F. Curl, F. Capasso, C. Gmachl, A. A. Kosterev, B. McManus, R. Lewicki, M. Pusharsky, G. Wysocki and F. K. Tittel, 'Quantum cascade lasers in chemical physics', Chemical Physics Letters **487**, 1–18 (2010).

[19]C. Robert, 'Simple, stable, and compact multiple-reflection optical cell for very long optical paths', EN, Applied Optics **46**, Publisher: Optica Publishing Group, 5408–5418 (2007).

[20]K. Chen, B. Zhang, S. Liu, F. Jin, M. Guo, Y. Chen and Q. Yu, 'Highly sensitive photoacoustic gas sensor based on multiple reflections on the cell wall', Sensors and Actuators A: Physical **290**, 119–124 (2019).

[21]M. Zhang, B. Zhang, K. Chen, M. Guo, S. Liu, Y. Chen, Z. Gong, Q. Yu, Z. Chen and M. Liao, 'Miniaturized multi-pass cell based photoacoustic gas sensor for parts-per-billion level acetylene detection', Sensors and Actuators A: Physical **308**, 112013 (2020).

[22]Y. He, Y. Ma, Y. Tong, X. Yu and F. K. Tittel, 'A portable gas sensor for sensitive CO detection based on quartz-enhanced photoacoustic spectroscopy', en, Optics & Laser Technology **115**, 129–133 (2019).

[23]G. F. Marshall and G. E. Stutz, eds., *Handbook of Optical and Laser Scanning*, English, Accepted: 2020-09-21T13:35:04Z (Taylor & Francis, 2012).

[24]M. A. Linne, *Spectroscopic Measurement: An Introduction to the Fundamentals*, en, Google-Books-ID: Q9PKEAAAQBAJ (Elsevier, Jan. 2024).

[25]X. Liu, S. Cheng, H. Liu, S. Hu, D. Zhang and H. Ning, 'A Survey on Gas Sensing Technology', en, Sensors **12**, Number: 7 Publisher: Molecular Diversity Preservation International, 9635–9665 (2012).

[26]G. Berden, R. Peeters and G. Meijer, 'Cavity ring-down spectroscopy: Experimental schemes and applications', International Reviews in Physical Chemistry **19**, Publisher: Taylor & Francis _eprint: https://doi.org/10.1080/014423500750040627, 565–607 (2000).

[27]D. Romanini, I. Ventrillard, G. Méjean, J. Morville and E. Kerstel, 'Introduction to Cavity Enhanced Absorption Spectroscopy', en, in *Cavity-Enhanced Spectroscopy and Sensing*, Vol. 179, edited by G. Gagliardi and H.-P. Loock, Series Title: Springer Series in Optical Sciences (Springer Berlin Heidelberg, Berlin, Heidelberg, 2014), pp. 1–60.

[28]R. Beer and R. H. Norton, 'Analysis of spectra using correlation functions', EN, Applied Optics **27**, Publisher: Optica Publishing Group, 1255–1261 (1988).

[29]F. Wang, S. Jia, Y. Wang and Z. Tang, 'Recent Developments in Modulation Spectroscopy for Methane Detection Based on Tunable Diode Laser', en, Applied Sciences **9**, Number: 14 Publisher: Multidisciplinary Digital Publishing Institute, 2816 (2019).

[30]M. A. Bolshov, Y. A. Kuritsyn and Y. V. Romanovskii, 'Tunable diode laser spectroscopy as a technique for combustion diagnostics', Spectrochimica Acta Part B: Atomic Spectroscopy **106**, 45–66 (2015).

[31]S. Shen, W. Li, M. Wang, D. Wang, Y. Li and D. Li, 'Methane near-infrared laser remote detection under non-cooperative target condition based on harmonic waveform recognition', Infrared Physics & Technology **120**, 103977 (2022).

[32]W.-q. Wang, L. Zhang and W.-h. Zhang, 'Analysis of Optical Fiber Methane Gas Detection System', Procedia Engineering **52**, 401–407 (2013).

[33]J. Sang, X. Yang, T. He and J. Li, 'High sensitive detection of atmospheric methane using infrared laser absorption spectroscopy', in 14th National Conference on Laser Technology and Optoelectronics (LTO 2019), Vol. 11170 (May 2019), pp. 82–89.

[34]M. Rahme, P. Tuthill, C. Betters, M. Large and S. Leon-Saval, 'A new gas detection technique through cross-correlation with a complex aperiodic FBG', Scientific Reports **14**, Publisher: Nature Publishing Group, 9939 (2024).

[35]S. Sivanandam, R. Cheriton, P. Zavyalova, P. R. Herman, E. Deibert, E. Tonita, V. Artyshchuk, E. d. Mooij, S. Janz and A. Densmore, 'Astrophotonic solutions for spectral cross-correlation techniques', in Ground-based and Airborne Instrumentation for Astronomy IX, Vol. 12184 (Aug. 2022), pp. 552–561.

[36]R. F. Griffin, 'A PHOTOELECTRIC RADIAL-VELOCITY SPECTROMETER', en, Ap J. . . **148** (1967).

[37]J. M. Fletcher, H. C. Harris, R. D. McClure and C. D. Scarfe, 'A PHOTOELECTRIC RADIAL-VELOCITY SPECTROMETER ON THE 1,2 M TELESCOPE OF THE DOMINION ASTROPHYSICAL OBSERVATORY', en, Publications of the Astronomical Society of the Pacific **94**, Publisher: The Astronomical Society of the Pacific, 1017 (1982).

[38]R. Cheriton, A. Densmore, S. Sivanandam, E. d. Mooij, P. Cheben, D.-X. Xu, J. H. Schmid and S. Janz, 'Fiber Fabry–Perot astrophotonic correlation spectroscopy for remote gas

identification and radial velocity measurements', EN, Applied Optics **60**, Publisher: Optica Publishing Group, 10252–10263 (2021).

[39]P. Tuthill, 'Australian Provisional Patent 2022901208 - Optical Sensor and System', 2022901208 (2022).

[40]S. Frans and K. Christoph, 'Apparatus for determining presence of a gas', NL2020863B1 (Nov. 2019).

[41]C. Fuchs, J. Kuhn, N. Bobrowski and U. Platt, 'Quantitative imaging of volcanic SO_2 plumes using Fabry–Pérot interferometer correlation spectroscopy', English, Atmospheric Measurement Techniques **14**, Publisher: Copernicus GmbH, 295–307 (2021).

[42]A. L. Verlaan, W. A. Klop, H. Visser, H. v. Brug and J. Human, 'Higs-instrument: design and demonstration of a high performance gas concentration imager', in International Conference on Space Optics — ICSO 2016, Vol. 10562 (Sept. 2017), pp. 1720–1726.

[43]D. Pereira-Martín, J. M. Luque-González, J. G. Wangüemert-Pérez, A. Hadij-ElHouati, Í. Molina-Fernández, P. Cheben, J. H. Schmid, S. Wang, W. N. Ye, J. Čtyroký and A. Ortega-Moñux, 'Complex spectral filters in silicon waveguides based on cladding-modulated Bragg gratings', EN, Optics Express **29**, Publisher: Optica Publishing Group, 15867–15881 (2021).

[44]R. Cheriton, S. Sivanandam, A. Densmore, E. D. Mooij, D. Melati, M. K. Dezfouli, P. Cheben, D. Xu, J. H. Schmid, J. Lapointe, R. Ma, S. Wang, L. Simard and S. Janz, 'Spectrum-free integrated photonic remote molecular identification and sensing', EN, Optics Express **28**, Publisher: Optica Publishing Group, 27951–27965 (2020).

[45]P. Gatkine, N. Jovanovic, J. Jewell, J. K. Wallace and D. Mawet, 'An on-chip astrophotonic spectrograph with a resolving power of 12,000', in UV/Optical/IR Space Telescopes and Instruments: Innovative Technologies and Concepts X, Vol. 11819 (Aug. 2021), pp. 171–180.

[46]J. Sandsten, H. Edner and S. Svanberg, 'Gas imaging by infrared gas-correlation spectrometry', EN, Optics Letters **21**, Publisher: Optica Publishing Group, 1945–1947 (1996).

[47]K. S. C. Kuang, R. Kenny, M. P. Whelan, W. J. Cantwell and P. R. Chalker, 'Embedded fibre Bragg grating sensors in advanced composite materials', en, Composites Science and Technology **61**, 1379–1387 (2001).

[48]Y. Xu, Z. Zhou, Y. Guo, L. Liu, Y. Xu, C. Qiao and Y. Jia, 'Carbon dioxide detection using polymer-coated fiber Bragg grating based on volume dilation mechanism and molecular dynamics simulation', en, Applied Surface Science **584**, 152616 (2022).

[49]Y. Xu, Z. Zhao, L. Liu, Y. Xu, C. Qiao and Y. Jia, 'Simultaneous detection of carbon dioxide and relative humidity using polymer-coated fiber Bragg gratings', Sensors and Actuators B: Chemical **368**, 132216 (2022).

[50]C. Li, X. Peng, J. Liu, C. Wang, S. Fan and S. Cao, 'D-Shaped Fiber Bragg Grating Ultrasonic Hydrophone With Enhanced Sensitivity and Bandwidth', Journal of Lightwave Technology **37**, Conference Name: Journal of Lightwave Technology, 2100–2108 (2019).

[51]H. A. Mohammed, B. Adel Esttaifan and M. H. Yaacob, 'Highly sensitive fiber Bragg grating based gas sensor integrating polyaniline nanofiber for remote monitoring', en, Optical Fiber Technology **71**, 102901 (2022).

[52]W. Ali and I. A. Murdas, 'Fiber bragg grating FBG as temperature sensor for the human body in review', AIP Conference Proceedings **2660**, Publisher: American Institute of Physics, 020049 (2022).

[53]A. Rahnama, E. Alimohammadian, P. Zavyalova, J. Li, K. M. Aghdami and P. R. Herman, 'Spatial Light Shaping of Uniform Femtosecond Laser Sheets for Fabricating Fiber Bragg Gratings', EN, in OSA Advanced Photonics Congress (AP) 2020 (IPR, NP, NOMA, Networks, PVLED, PSC, SPPCom, SOF) (2020), paper ITh2B.4 (July 2020), ITh2B.4.

[54]J. Bland-Hawthorn, M. Englund and G. Edvell, 'New approach to atmospheric OH suppression using an aperiodic fibre Bragg grating', EN, Optics Express **12**, Publisher: Optica Publishing Group, 5902–5909 (2004).

[55]J. Bland-Hawthorn, S. C. Ellis, S. G. Leon-Saval, R. Haynes, M. M. Roth, H.-G. Löhmannsröben, A. J. Horton, J.-G. Cuby, T. A. Birks, J. S. Lawrence, P. Gillingham, S. D. Ryder and C. Trinh, 'A complex multi-notch astronomical filter to suppress the bright infrared sky', en, Nature Communications **2**, Number: 1 Publisher: Nature Publishing Group, 581 (2011).

[56]S. C. Ellis, J. Bland-Hawthorn, J. S. Lawrence, J. Bryant, R. Haynes, A. Horton, S. Lee, S. Leon-Saval, H.-G. Löhmannsröben, J. Mladenoff, J. O'Byrne, W. Rambold, M. Roth and C. Trinh, 'GNOSIS: an OH suppression unit for near-infrared spectrographs', SPIE

7735, Conference Name: Ground-based and Airborne Instrumentation for Astronomy III ADS Bibcode: 2010SPIE.7735E..16E, 773516 (2010).

[57]A. Horton, S. Ellis, J. Lawrence and J. Bland-Hawthorn, 'PRAXIS: a low background NIR spectrograph for fibre Bragg grating OH suppression', in Modern Technologies in Space- and Ground-based Telescopes and Instrumentation II, Vol. 8450 (Sept. 2012), pp. 652–657.

[58]S. G. Leon-Saval, T. A. Birks, J. Bland-Hawthorn and M. Englund, 'Multimode fiber devices with single-mode performance', EN, Optics Letters **30**, Publisher: Optica Publishing Group, 2545–2547 (2005).

[59]S. C. Ellis, J. Bland-Hawthorn, S. Bauer, S. Case, R. Content, T. Fechner, D. Giannone, R. Haynes, E. Hernandez, A. J. Horton, U. Klauser, J. S. Lawrence, S. G. Leon-Saval, H.-G. Löhmannsröben, S.-S. Min, N. Pai, M. Roth, L. Waller and R. Zhelem, 'PRAXIS: an OH suppression optimised near infrared spectrograph', in Advances in Optical Astronomical Instrumentation 2019, Vol. 11203 (Jan. 2020), pp. 69–70.

[60]V. N. Venkatesan and R. Ramalingam, 'Numerical and experimental investigation of FBG strain response at cryogenic temperatures', en, IOP Conference Series: Materials Science and Engineering **171**, Publisher: IOP Publishing, 012133 (2017).

[61]A. Othonos, 'Fiber Bragg gratings', Review of Scientific Instruments **68**, Publisher: American Institute of Physics, 4309–4341 (1997).

[62]G. L. Edvell, 'Optical structure writing system', en, US8693826B2 (Apr. 2014).

[63]B. Bell Alexander Graham, 'On the production and reproduction of sound by light', American Journal of Science **3**, 305–324 (1880).

[64]M. Viengerov, 'New method of gas analysis based on tyndall-roentgen optoacoustic effect', Doklady Akademii Nauk SSSR **19**, 8 (1938).

[65]E. L. Kerr and J. G. Atwood, 'The Laser Illuminated Absorptivity Spectrophone: A Method for Measurement of Weak Absorptivity in Gases at Laser Wavelengths', EN, Applied Optics, Vol. 7, Issue 5, pp. 915-921, Publisher: Optica Publishing Group, 10.1364/AO.7.000915 (1968).

[66]F. H. Tyas, J. G. Nikita, D. K. Apriyanto, Mitrayana and M. N. Amin, 'The Performance of CO2 Laser Photoacoustic Spectrometer In Concentration Acetone Detection As Biomarker

For Diabetes Mellitus Type 2', en, Journal of Physics: Conference Series **1011**, Publisher: IOP Publishing, 012056 (2018).

[67]M. J. Navas, A. M. Jiménez and A. G. Asuero, 'Human biomarkers in breath by photoacoustic spectroscopy', Clinica Chimica Acta **413**, 1171–1178 (2012).

[68]C. Popa, N. Verga, M. Patachia, S. Banita, C. Matei, D. Dumitras, A. St and C. Davila, 'ADVANTAGES OF LASER PHOTOACOUSTIC SPECTROSCOPY IN RADIOTHERAPY CHARACTERIZATION', en,

[69]D. C. Dumitras, M. Petrus, A.-M. Bratu and C. Popa, 'Applications of Near Infrared Photoacoustic Spectroscopy for Analysis of Human Respiration: A Review', en, Molecules **25**, Number: 7 Publisher: Multidisciplinary Digital Publishing Institute, 1728 (2020).

[70]D. C. Dumitras, D. C. Dutu, C. Matei, R. Cernat, S. Banita, M. Patachia, A. M. Bratu, M. Petrus and C. Popa, 'Evaluation of ammonia absorption coefficients by photoacoustic spectroscopy for detection of ammonia levels in human breath', en, Laser Physics **21**, 796–800 (2011).

[71]C. Popa, 'Infrared spectroscopy study of the influence of inhaled vapors/smoke produced by cigarettes of active smokers', Journal of Biomedical Optics **20**, Publisher: SPIE, 051003 (2014).

[72]X. Yin, L. Dong, H. Wu, L. Zhang, W. Ma, W. Yin, L. Xiao, S. Jia and F. K. Tittel, 'Highly sensitive photoacoustic multicomponent gas sensor for SF_6 decomposition online monitoring', EN, Optics Express **27**, Publisher: Optica Publishing Group, A224–A234 (2019).

[73]F. G. Linhares, M. A. Lima, G. A. Mothe, M. P. P. de Castro, M. G. da Silva and M. S. Sthel, 'Photoacoustic spectroscopy for detection of N2O emitted from combustion of diesel/beef tallow biodiesel/sugarcane diesel and diesel/beef tallow biodiesel blends', en, Biomass Conversion and Biorefinery **9**, 577–583 (2019).

[74]G. A. Shah, G. M. Shah, M. I. Rashid, J. C. J. Groot, B. Traore and E. A. Lantinga, 'Bedding additives reduce ammonia emission and improve crop N uptake after soil application of solid cattle manure', Journal of Environmental Management **209**, 195–204 (2018).

[75]A.-M. Bratu, C. Popa, M. Bojan, P. C. Logofatu and M. Petrus, 'Non-destructive methods for fruit quality evaluation', en, Scientific Reports **11**, Publisher: Nature Publishing Group, 7782 (2021).

[76]A. J. Schmithausen, M. Trimborn and W. Büscher, 'Methodological Comparison between a Novel Automatic Sampling System for Gas Chromatography versus Photoacoustic Spectroscopy for Measuring Greenhouse Gas Emissions under Field Conditions', en, Sensors **16**, Number: 10 Publisher: Multidisciplinary Digital Publishing Institute, 1638 (2016).

[77]A. Miklós, P. Hess and Z. Bozóki, 'Application of acoustic resonators in photoacoustic trace gas analysis and metrology', Review of Scientific Instruments **72**, 1937–1955 (2001).

[78]Y. Yan, Y. Zheng, H. Sun and J. Duan, 'Review of Issues and Solutions in High-Power Semiconductor Laser Packaging Technology', English, Frontiers in Physics **9**, Publisher: Frontiers, 10.3389/fphy.2021.669591 (2021).

[79]D. Dumitras, D. Dutu, C. Matei, A.-M. Bratu (Magureanu), M. Petrus and C. Popa, 'Laser photoacoustic spectroscopy: Principles, instrumentation, and characterization', Journal of Optoelectronics and Advanced Materials **9**, 3655–3701 (2007).

[80]S. Xiong, X. Yin, Q. Wang, J. Xia, Z. Chen, H. Lei, X. Yan, A. Zhu, F. Qiu, B. Chen, Q. Wang, L. Zhang and K. Zhang, 'Photoacoustic Spectroscopy Gas Detection Technology Research Progress', en, Applied Spectroscopy **78**, Publisher: SAGE Publications Ltd STM, 139–158 (2024).

[81]A. A. Kosterev, Y. A. Bakhirkin, R. F. Curl and F. K. Tittel, 'Quartz-enhanced photoacoustic spectroscopy', EN, Optics Letters **27**, Publisher: Optical Society of America, 1902–1904 (2002).

[82]Y. Ma, 'Review of Recent Advances in QEPAS-Based Trace Gas Sensing', en, Applied Sciences **8**, Number: 10 Publisher: Multidisciplinary Digital Publishing Institute, 1822 (2018).

[83]J.-M. Friedt and É. Carry, 'Introduction to the quartz tuning fork', American Journal of Physics **75**, Publisher: American Association of Physics Teachers, 415–422 (2007).

[84]A. A. Kosterev, F. K. Tittel, D. V. Serebryakov, A. L. Malinovsky and I. V. Morozov, 'Applications of quartz tuning forks in spectroscopic gas sensing', Review of Scientific Instruments **76**, Publisher: American Institute of Physics, 043105 (2005).

[85]P. Patimisco, G. Scamarcio, F. K. Tittel and V. Spagnolo, 'Quartz-Enhanced Photoacoustic Spectroscopy: A Review', en, Sensors **14**, Number: 4 Publisher: Multidisciplinary Digital Publishing Institute, 6165–6206 (2014).

[86]T. D. Rossing, D. A. Russell and D. E. Brown, 'On the acoustics of tuning forks', American Journal of Physics **60**, 620–626 (1992).

[87]P. P. Ong, 'Little Known Facts about the Common Tuning Fork', en, Physics Education **37**, ERIC Number: EJ658220, 540–42 (2002).

[88]H. Zheng, H. Lin, L. Dong, Z. Huang, X. Gu, J. Tang, L. Dong, W. Zhu, J. Yu and Z. Chen, 'Quartz-Enhanced Photothermal-Acoustic Spectroscopy for Trace Gas Analysis', en, Applied Sciences **9**, Number: 19 Publisher: Multidisciplinary Digital Publishing Institute, 4021 (2019).

[89]M. R. Mohebbifar, 'High-sensitivity detection and quantification of CHCl3 vapors in various gas environments based on the photoacoustic spectroscopy', en, Microwave and Optical Technology Letters **61**, _eprint: https://onlinelibrary.wiley.com/doi/pdf/10.1002/mop.31880, 2234–2241 (2019).

[90]D. W. Dye, 'The piezo-electric quartz resonator and its equivalent electrical circuit', en, Proceedings of the Physical Society of London **38**, 399 (1925).

[91]G. Aoust, R. Levy, M. Raybaut, A. Godard, J.-M. Melkonian and M. Lefebvre, 'Theoretical analysis of a resonant quartz-enhanced photoacoustic spectroscopy sensor', en, Applied Physics B **123**, 63 (2017).

[92]H. Zheng, L. Dong, Y. Ma, H. Wu, X. Liu, X. Yin, L. Zhang, W. Ma, W. Yin, L. Xiao and S. Jia, 'Scattered light modulation cancellation method for sub-ppb-level NO_2 detection in a LD-excited QEPAS system', EN, Optics Express **24**, Publisher: Optica Publishing Group, A752–A761 (2016).

[93]P. Patimisco, A. Sampaolo, L. Dong, F. K. Tittel and V. Spagnolo, 'Recent advances in quartz enhanced photoacoustic sensing', Applied Physics Reviews **5**, 011106 (2018).

[94]Y. Ma, Y. He, Y. Tong, X. Yu and F. K. Tittel, 'Quartz-tuning-fork enhanced photothermal spectroscopy for ultra-high sensitive trace gas detection', EN, Optics Express **26**, Publisher: Optica Publishing Group, 32103–32110 (2018).

[95]K. Liu, X. Guo, H. Yi, W. Chen, W. Zhang and X. Gao, 'Off-beam quartz-enhanced photoacoustic spectroscopy', EN, Optics Letters **34**, Publisher: Optica Publishing Group, 1594–1596 (2009).

[96]Y. Ma, X. Yu, G. Yu, X. Li, J. Zhang, D. Chen, R. Sun and F. K. Tittel, 'Multi-quartz-enhanced photoacoustic spectroscopy', Applied Physics Letters **107**, Publisher: American Institute of Physics, 021106 (2015).

[97]H. Zheng, Y. Liu, H. Lin, B. Liu, X. Gu, D. Li, B. Huang, Y. Wu, L. Dong, W. Zhu, J. Tang, H. Guan, H. Lu, Y. Zhong, J. Fang, Y. Luo, J. Zhang, J. Yu, Z. Chen and F. K. Tittel, 'Quartz-enhanced photoacoustic spectroscopy employing pilot line manufactured custom tuning forks', en, Photoacoustics **17**, 100158 (2020).

[98]*AB38T-32.768KHZ | Abracon 32.768kHz Crystal ±20ppm Cylindrical Can, Radial 3.2 x 8.3mm | RS*.

[99]R. Rousseau, N. Maurin, W. Trzpil, M. Bahriz and A. Vicet, 'Quartz Tuning Fork Resonance Tracking and application in Quartz Enhanced Photoacoustics Spectroscopy', en, Sensors **19**, Number: 24 Publisher: Multidisciplinary Digital Publishing Institute, 5565 (2019).

[100]H. Wu, L. Dong, X. Yin, A. Sampaolo, P. Patimisco, W. Ma, L. Zhang, W. Yin, L. Xiao, V. Spagnolo and S. Jia, 'Atmospheric CH4 measurement near a landfill using an ICL-based QEPAS sensor with V-T relaxation self-calibration', en, Sensors and Actuators B: Chemical **297**, 126753 (2019).

[101]G. Menduni, A. Zifarelli, A. Sampaolo, P. Patimisco, M. Giglio, N. Amoroso, H. Wu, L. Dong, R. Bellotti and V. Spagnolo, 'High-concentration methane and ethane QEPAS detection employing partial least squares regression to filter out energy relaxation dependence on gas matrix composition', en, Photoacoustics **26**, 100349 (2022).

[102]Y. Ma, G. Yu, J. Zhang, X. Yu and R. Sun, 'Sensitive detection of carbon monoxide based on a QEPAS sensor with a 2.3 um fiber-coupled antimonide diode laser', en, Journal of Optics **17**, Publisher: IOP Publishing, 055401 (2015).

[103]N. Liberatore, R. Viola, S. Mengali, L. Masini, F. Zardi, I. Elmi and S. Zampolli, 'Compact GC-QEPAS for On-Site Analysis of Chemical Threats', en, Sensors **23**, Number: 1 Publisher: Multidisciplinary Digital Publishing Institute, 270 (2023).

[104]V. Spagnolo, A. A. Kosterev, L. Dong, R. Lewicki and F. K. Tittel, 'NO trace gas sensor based on quartz-enhanced photoacoustic spectroscopy and external cavity quantum cascade laser', en, Applied Physics B **100**, 125–130 (2010).

[105]S. Borri, P. Patimisco, A. Sampaolo, H. E. Beere, D. A. Ritchie, M. S. Vitiello, G. Scamarcio and V. Spagnolo, 'Terahertz quartz enhanced photo-acoustic sensor', Applied Physics Letters **103**, 021105 (2013).

[106]N. Petra, J. Zweck, A. A. Kosterev, S. E. Minkoff and D. Thomazy, 'Theoretical analysis of a quartz-enhanced photoacoustic spectroscopy sensor', en, Applied Physics B **94**, 673–680 (2009).

[107]P. Patimisco, A. Sampaolo, L. Dong, M. Giglio, G. Scamarcio, F. K. Tittel and V. Spagnolo, 'Analysis of the electro-elastic properties of custom quartz tuning forks for optoacoustic gas sensing', Sensors and Actuators B: Chemical **227**, 539–546 (2016).

[108]A. Sampaolo, P. Patimisco, L. Dong, A. Geras, G. Scamarcio, T. Starecki, F. K. Tittel and V. Spagnolo, 'Quartz-enhanced photoacoustic spectroscopy exploiting tuning fork overtone modes', Applied Physics Letters **107**, 231102 (2015).

[109]F. K. Tittel, A. Sampaolo, P. Patimisco, L. Dong, A. Geras, T. Starecki and V. Spagnolo, 'Analysis of overtone flexural modes operation in quartz-enhanced photoacoustic spectroscopy', eng, Optics Express **24**, A682–692 (2016).

[110]H. Zheng, L. Dong, P. Patimisco, H. Wu, A. Sampaolo, X. Yin, S. Li, W. Ma, L. Zhang, W. Yin, L. Xiao, V. Spagnolo, S. Jia and F. K. Tittel, 'Double antinode excited quartz-enhanced photoacoustic spectrophone', Applied Physics Letters **110**, 021110 (2017).

[111]H. Wu, X. Yin, L. Dong, K. Pei, A. Sampaolo, P. Patimisco, H. Zheng, W. Ma, L. Zhang, W. Yin, L. Xiao, V. Spagnolo, S. Jia and F. Tittel, 'Simultaneous dual-gas QEPAS detection based on a fundamental and overtone combined vibration of quartz tuning fork', Applied Physics Letters **110**, 121104 (2017).

[112]P. Patimisco, A. Sampaolo, M. Giglio, S. d. Russo, V. Mackowiak, H. Rossmadl, A. Cable, F. K. Tittel and V. Spagnolo, 'Tuning forks with optimized geometries for quartz-enhanced

photoacoustic spectroscopy', EN, Optics Express **27**, Publisher: Optica Publishing Group, 1401–1415 (2019).

[113]Y. Liu, H. Lin, B. A. Z. Montano, W. Zhu, Y. Zhong, R. Kan, B. Yuan, J. Yu, M. Shao and H. Zheng, 'Integrated near-infrared QEPAS sensor based on a 28 kHz quartz tuning fork for online monitoring of CO2 in the greenhouse', en, Photoacoustics **25**, 100332 (2022).

[114]L. Dong, A. A. Kosterev, D. Thomazy and F. K. Tittel, 'QEPAS spectrophones: design, optimization, and performance', en, Applied Physics B **100**, 627–635 (2010).

[115]S. Schilt, A. A. Kosterev and F. K. Tittel, 'Performance evaluation of a near infrared QEPAS based ethylene sensor', en, Applied Physics B **95**, 813–824 (2009).

[116]D. V. Serebryakov, I. V. Morozov, A. A. Kosterev and V. S. Letokhov, 'Laser microphotoacoustic sensor of ammonia traces in the atmosphere', en, Quantum Electronics **40**, Publisher: IOP Publishing, 167 (2010).

[117]S. Dello Russo, M. Giglio, A. Sampaolo, P. Patimisco, G. Menduni, H. Wu, L. Dong, V. M. N. Passaro and V. Spagnolo, 'Acoustic Coupling between Resonator Tubes in Quartz-Enhanced Photoacoustic Spectrophones Employing a Large Prong Spacing Tuning Fork', en, Sensors **19**, Number: 19 Publisher: Multidisciplinary Digital Publishing Institute, 4109 (2019).

[118]N. Ogawa and F. Kaneko, 'Open end correction for a flanged circular tube using the diffusion process', en, European Journal of Physics **34**, Publisher: IOP Publishing, 1159 (2013).

[119]M. L. Meade, *Lock-in amplifiers: Principles and applications*, Publication Title: IEE Electrical Measurement Series ADS Bibcode: 1983lapa.book.....M (Jan. 1983).

[120]T. Liang, S. Qiao, Y. Chen, Y. He and Y. Ma, 'High-sensitivity methane detection based on QEPAS and H-QEPAS technologies combined with a self-designed 8.7 kHz quartz tuning fork', Photoacoustics **36**, 100592 (2024).

[121]L. S. Rothman, I. E. Gordon, A. Barbe, D. C. Benner, P. F. Bernath, M. Birk, V. Boudon, L. R. Brown, A. Campargue, J. .-. Champion, K. Chance, L. H. Coudert, V. Dana, V. M. Devi, S. Fally, J. .-. Flaud, R. R. Gamache, A. Goldman, D. Jacquemart, I. Kleiner, N. Lacome, W. J. Lafferty, J. .-. Mandin, S. T. Massie, S. N. Mikhailenko, C. E. Miller, N. Moazzen-Ahmadi, O. V. Naumenko, A. V. Nikitin, J. Orphal, V. I. Perevalov, A. Perrin,

A. Predoi-Cross, C. P. Rinsland, M. Rotger, M. Šimečková, M. A. H. Smith, K. Sung, S. A. Tashkun, J. Tennyson, R. A. Toth, A. C. Vandaele and J. Vander Auwera, 'The *HITRAN* 2008 molecular spectroscopic database', Journal of Quantitative Spectroscopy and Radiative Transfer, HITRAN **110**, 533–572 (2009).

[122]J. M. Supplee, E. A. Whittaker and W. Lenth, 'Theoretical description of frequency modulation and wavelength modulation spectroscopy', EN, Applied Optics **33**, Publisher: Optica Publishing Group, 6294–6302 (1994).

[123]H. Yi, K. Liu, W. Chen, T. Tan, L. Wang and X. Gao, 'Application of a broadband blue laser diode to trace NO_2 detection using off-beam quartz-enhanced photoacoustic spectroscopy', EN, Optics Letters **36**, Publisher: Optica Publishing Group, 481–483 (2011).

[124]T. Yang, W. Chen and P. Wang, 'A review of all-optical photoacoustic spectroscopy as a gas sensing method', Applied Spectroscopy Reviews **0**, Publisher: Taylor & Francis _eprint: https://doi.org/10.1080/05704928.2020.1760875, 1–28 (2020).

[125]Z. Shang, S. Li, B. Li, H. Wu, A. Sampaolo, P. Patimisco, V. Spagnolo and L. Dong, 'Quartz-enhanced photoacoustic NH3 sensor exploiting a large-prong-spacing quartz tuning fork and an optical fiber amplifier for biomedical applications', en, Photoacoustics **26**, 100363 (2022).

[126]J. P. Waclawek, H. Moser and B. Lendl, 'Compact quantum cascade laser based quartz-enhanced photoacoustic spectroscopy sensor system for detection of carbon disulfide', EN, Optics Express **24**, Publisher: Optica Publishing Group, 6559–6571 (2016).

[127]C. Bauer, U. Willer, R. Lewicki, A. Pohlkötter, A. Kosterev, D. Kosynkin, F. K. Tittel and W. Schade, 'A Mid-infrared QEPAS sensor device for TATP detection', en, Journal of Physics: Conference Series **157**, 012002 (2009).

[128]Y. Ma, Y. He, L. Zhang, X. Yu, J. Zhang, R. Sun and F. K. Tittel, 'Ultra-high sensitive acetylene detection using quartz-enhanced photoacoustic spectroscopy with a fiber amplified diode laser and a 30.72 kHz quartz tuning fork', Applied Physics Letters **110**, Publisher: American Institute of Physics, 031107 (2017).

[129]Y. Chen, T. Liang, S. Qiao and Y. Ma, 'A Miniaturized 3D-Printed Quartz-Enhanced Photoacoustic Spectroscopy Sensor for Methane Detection with a High-Power Diode

Laser', en, Sensors **23**, Number: 8 Publisher: Multidisciplinary Digital Publishing Institute, 4034 (2023).

[130]M. Zatorska, G. Gomółka and M. Nikodem, 'Near-infrared quartz-enhanced photoacoustic spectroscopy system for ppb-level methane detection', EN, Optics Continuum **2**, Publisher: Optica Publishing Group, 266–273 (2023).

[131]A. Elefante, G. Menduni, H. Rossmadl, V. Mackowiak, M. Giglio, A. Sampaolo, P. Patimisco, V. M. N. Passaro and V. Spagnolo, 'Environmental Monitoring of Methane with Quartz-Enhanced Photoacoustic Spectroscopy Exploiting an Electronic Hygrometer to Compensate the H2O Influence on the Sensor Signal', en, Sensors **20**, Number: 10 Publisher: Multidisciplinary Digital Publishing Institute, 2935 (2020).

[132]A. Sampaolo, G. Menduni, P. Patimisco, M. Giglio, V. M. N. Passaro, L. Dong, H. Wu, F. K. Tittel and V. Spagnolo, 'Quartz-enhanced photoacoustic spectroscopy for hydrocarbon trace gas detection and petroleum exploration', en, Fuel **277**, 118118 (2020).

[133]C. F. Twomey, G. Biagi, A. A. Ruth, M. Giglio, V. Spagnolo, L. O'Faolain and A. J. Walsh, 'Evanescent wave quartz-enhanced photoacoustic spectroscopy employing a side-polished fiber for methane sensing', Photoacoustics **36**, 100586 (2024).

[134]J. B. Christensen, L. Høgstedt, S. M. M. Friis, J.-Y. Lai, M.-H. Chou, D. Balslev-Harder, J. C. Petersen and M. Lassen, 'Intrinsic Spectral Resolution Limitations of QEPAS Sensors for Fast and Broad Wavelength Tuning', en, Sensors **20**, Number: 17 Publisher: Multidisciplinary Digital Publishing Institute, 4725 (2020).

[135]Y. Li, R. Wang, F. K. Tittel and Y. Ma, 'Sensitive methane detection based on quartz-enhanced photoacoustic spectroscopy with a high-power diode laser and wavelet filtering', en, Optics and Lasers in Engineering **132**, 106155 (2020).

[136]G. Menduni, F. Sgobba, S. D. Russo, A. C. Ranieri, A. Sampaolo, P. Patimisco, M. Giglio, V. M. N. Passaro, S. Csutak, D. Assante, E. Ranieri, E. Geoffrion and V. Spagnolo, 'Fiber-Coupled Quartz-Enhanced Photoacoustic Spectroscopy System for Methane and Ethane Monitoring in the Near-Infrared Spectral Range', en, Molecules **25**, Number: 23 Publisher: Multidisciplinary Digital Publishing Institute, 5607 (2020).

[137]A. Zifarelli, G. Menduni, M. Giglio, A. Elefante, A. Sukhinets, A. Sampaolo, P. Patimisco, S. Fangyuan, W. Chongwu, Q. J. Wang and V. Spagnolo, 'Compact and Versatile QEPAS-Based Sensor Box for Simultaneous Detection of Methane and Infrared Absorber Gas Molecules in Ambient Air', English, Frontiers in Environmental Chemistry **3**, Publisher: Frontiers, 10.3389/fenvc.2022.926233 (2022).

[138]G. Menduni, A. Zifarelli, E. Kniazeva, S. Dello Russo, A. C. Ranieri, E. Ranieri, P. Patimisco, A. Sampaolo, M. Giglio, F. Manassero, E. Dinuccio, G. Provolo, H. Wu, D. Lei and V. Spagnolo, 'Measurement of methane, nitrous oxide and ammonia in atmosphere with a compact quartz-enhanced photoacoustic sensor', Sensors and Actuators B: Chemical **375**, 132953 (2023).

[139]C. Lin, X. Yan and Y. Huang, 'An all-optical off-beam quartz-enhanced photoacoustic spectroscopy employing double-pass acoustic microresonators', Optics Communications **503**, 127447 (2022).

[140]W. Ye, W. Liu, W. Luo, J. Xiao, L. He, Y. Huang and D. Zhu, 'Calibration-free near-infrared methane sensor system based on BF-QEPAS', Infrared Physics & Technology **133**, 104784 (2023).

[141]M. Behringer, 'High-Power Diode Laser Technology and Characteristics', en, in *High Power Diode Lasers: Technology and Applications*, edited by F. Bachmann, P. Loosen and R. Poprawe (Springer, New York, NY, 2007), pp. 5–74.

[142]M. E. Webber, M. Pushkarsky and C. K. N. Patel, 'Fiber-amplifier-enhanced photoacoustic spectroscopy with near-infrared tunable diode lasers', EN, Applied Optics **42**, Publisher: Optica Publishing Group, 2119–2126 (2003).

[143]I. Vurgaftman, R. Weih, M. Kamp, J. R. Meyer, C. L. Canedy, C. S. Kim, M. Kim, W. W. Bewley, C. D. Merritt, J. Abell and S. Höfling, 'Interband cascade lasers', en, Journal of Physics D: Applied Physics **48**, Publisher: IOP Publishing, 123001 (2015).

[144]J. R. Meyer, W. W. Bewley, C. L. Canedy, C. S. Kim, M. Kim, C. D. Merritt and I. Vurgaftman, 'The Interband Cascade Laser', en, Photonics **7**, Number: 3 Publisher: Multidisciplinary Digital Publishing Institute, 75 (2020).

[145]M. S. Vitiello and P. De Natale, 'Terahertz Quantum Cascade Lasers as Enabling Quantum Technology', en, Advanced Quantum Technologies **5**, _eprint: https://onlinelibrary.wiley.com/doi/pdf/10.1002 2100082 (2022).

[146]Y. Yao, A. J. Hoffman and C. F. Gmachl, 'Mid-infrared quantum cascade lasers', en, Nature Photonics **6**, Publisher: Nature Publishing Group, 432–439 (2012).

[147]A. A. Kosterev, P. R. Buerki, L. Dong, M. Reed, T. Day and F. K. Tittel, 'QEPAS detector for rapid spectral measurements', en, Applied Physics B **100**, 173–180 (2010).

[148]H. Wu, L. Dong, H. Zheng, Y. Yu, W. Ma, L. Zhang, W. Yin, L. Xiao, S. Jia and F. K. Tittel, 'Beat frequency quartz-enhanced photoacoustic spectroscopy for fast and calibration-free continuous trace-gas monitoring', en, Nature Communications **8**, Bandiera_abtest: a Cc_license_type: cc_by Cg_type: Nature Research Journals Number: 1 Primary_atype: Research Publisher: Nature Publishing Group Subject_term: Photoacoustics;Sensors Subject_term_id: photoacoustics;sensors, 15331 (2017).

[149]T. Wei, A. Zifarelli, S. Dello Russo, H. Wu, G. Menduni, P. Patimisco, A. Sampaolo, V. Spagnolo and L. Dong, 'High and flat spectral responsivity of quartz tuning fork used as infrared photodetector in tunable diode laser spectroscopy', Applied Physics Reviews **8**, 041409 (2021).

[150]A. Stylogiannis, N. Kousias, A. Kontses, L. Ntziachristos and V. Ntziachristos, 'A Low-Cost Optoacoustic Sensor for Environmental Monitoring', en, Sensors **21**, Number: 4 Publisher: Multidisciplinary Digital Publishing Institute, 1379 (2021).

[151]Y. He, Y. Ma, Y. Tong, X. Yu and F. K. Tittel, 'Ultra-high sensitive light-induced thermoelastic spectroscopy sensor with a high Q-factor quartz tuning fork and a multipass cell', EN, Optics Letters **44**, Publisher: Optica Publishing Group, 1904–1907 (2019).

[152]Q. Zhang, J. Chang, Z. Cong and Z. Wang, 'Quartz tuning fork enhanced photothermal spectroscopy gas detection system with a novel QTF-self-difference technique', en, Sensors and Actuators A: Physical **299**, 111629 (2019).

[153]Y. Ma, Y. He, P. Patimisco, A. Sampaolo, S. Qiao, X. Yu, F. K. Tittel and V. Spagnolo, 'Ultra-high sensitive trace gas detection based on light-induced thermoelastic spectroscopy and a custom quartz tuning fork', Applied Physics Letters **116**, Publisher: American Institute of Physics, 011103 (2020).

[154]Y. Chen, T. Liang, S. Qiao, Y. He and Y. Ma, 'Highly sensitive detection of methane based on LITES and H-LITES techniques', Infrared Physics & Technology **140**, 105370 (2024).

[155]J. Tichý*, J. Erhart, E. Kittinger* and J. Přívratská, 'Principles of Piezoelectricity', en, in *Fundamentals of Piezoelectric Sensorics: Mechanical, Dielectric, and Thermodynamical Properties of Piezoelectric Materials*, edited by J. Tichý, J. Erhart, E. Kittinger and J. Přívratská (Springer, Berlin, Heidelberg, 2010), pp. 1–14.

[156]J. Tichý, J. Erhart, E. Kittinger and J. Prívratská, *Fundamentals of Piezoelectric Sensorics: Mechanical, Dielectric, and Thermodynamical Properties of Piezoelectric Materials*, en, Google-Books-ID: gAYmeaiO8SMC (Springer Science & Business Media, July 2010).

[157]W. Q. Liu, Z. H. Feng, R. B. Liu and J. Zhang, 'The influence of preamplifiers on the piezoelectric sensor's dynamic property', Review of Scientific Instruments **78**, 125107 (2007).

[158]Z. Lu, K. S. Yeo, W. M. Lim, M. A. Do and C. C. Boon, 'Design of a CMOS Broadband Transimpedance Amplifier With Active Feedback', IEEE Transactions on Very Large Scale Integration (VLSI) Systems **18**, Conference Name: IEEE Transactions on Very Large Scale Integration (VLSI) Systems, 461–472 (2010).

[159]R. M. Cerda, *Understanding Quartz Crystals and Oscillators*, en, Google-Books-ID: uppVAwAAQBAJ (Artech House, May 2014).

[160]F. N. Mokogwu, A. Ng, A. Marzuki and I. Ukaegbu, 'Variable Input Transimpedance Amplifier for Perovskite and Thin-film Photovoltaics Sensing Applications', in 2022 International Conference on Communications, Information, Electronic and Energy Systems (CIEES) (Nov. 2022), pp. 1–4.

[161]T. Starecki and P. Z. Wieczorek, 'A High Sensitivity Preamplifier for Quartz Tuning Forks in QEPAS (Quartz Enhanced PhotoAcoustic Spectroscopy) Applications', en, Sensors **17**, Number: 11 Publisher: Multidisciplinary Digital Publishing Institute, 2528 (2017).

[162]M. Winkowski and T. Stacewicz, 'Low noise, open-source QEPAS system with instrumentation amplifier', en, Scientific Reports **9**, Number: 1 Publisher: Nature Publishing Group, 1838 (2019).

[163]G. Menduni, A. Sampaolo, P. Patimisco, M. Giglio, S. Dello Russo, A. Zifarelli, A. Elefante, P. Z. Wieczorek, T. Starecki, V. M. N. Passaro, F. K. Tittel and V. Spagnolo, 'Front-End

Amplifiers for Tuning Forks in Quartz Enhanced PhotoAcoustic Spectroscopy', en, Applied Sciences **10**, Number: 8 Publisher: Multidisciplinary Digital Publishing Institute, 2947 (2020).

[164]P. Z. Wieczorek, T. Starecki and F. K. Tittel, 'Improving the Signal to Noise Ratio of QTF Preamplifiers Dedicated for QEPAS Applications', en, Applied Sciences **10**, Number: 12 Publisher: Multidisciplinary Digital Publishing Institute, 4105 (2020).

[165]M. D. Gioia, G. Menduni, A. Zifarelli, A. Sampaolo, P. Patimisco, M. Giglio, C. Marzocca and V. Spagnolo, 'Study of the effect of the low-pass filter time constant on the noise level of quartz-enhanced photoacoustic spectroscopy sensors', in Quantum Sensing and Nano Electronics and Photonics XIX, Vol. 12430 (Mar. 2023), pp. 208–216.

[166]Y. Ma, 'Recent Advances in QEPAS and QEPTS Based Trace Gas Sensing: A Review', Frontiers in Physics **8**, 268 (2020).

[167]R. Cui, H. Wu, F. K. Tittel, V. Spagnolo, W. Chen and L. Dong, 'Folded-optics-based quartz-enhanced photoacoustic and photothermal hybrid spectroscopy', Photoacoustics **35**, 100580 (2024).

[168]*ADA4627-1ARZ Analog Devices | Mouser*, en-au.

[169]*LMC6001 data sheet, product information and support | TI.com*.

[170]A. Devices, *Analog Devices Filter Wizard*.

[171]*ADA4001-2ARZ*, en-us.

[172]JLCPCB, *JLCPCB - PCB Manufacturing Service*.

[173]A. Devices, *Analog Devices Signal Chain Designer*.

[174]L. Instruments, *Liquid Instruments - Test and Measurement Solutions*.

[175]D. Walter, A. Bülau and A. Zimmermann, 'Review on Excess Noise Measurements of Resistors', en, Sensors **23**, Number: 3 Publisher: Multidisciplinary Digital Publishing Institute, 1107 (2023).

[176]*Compare Formlabs SLA 3D Printers' Tech Specs*, en.

[177]L. Tian, J. Sun, S. Zhang, A. A. Kolomenskii, H. A. Schuessler, Z. Wang, J. Xia, J. Chang and Z. Liu, 'Near-infrared methane sensor with neural network filtering', Sensors and Actuators B: Chemical **354**, 131207 (2022).

[178] *Quartz Crystal Tuning Forks | Scanning Probe Microscopy, AFM, NSOM, and Nanoprobe Accessories*.

[179] L. Dong, V. Spagnolo, R. Lewicki and F. K. Tittel, 'Ppb-level detection of nitric oxide using an external cavity quantum cascade laser based QEPAS sensor', EN, Optics Express **19**, Publisher: Optica Publishing Group, 24037–24045 (2011).

[180] A. Sampaolo, P. Patimisco, M. Giglio, A. Zifarelli, H. Wu, L. Dong and V. Spagnolo, 'Quartz-enhanced photoacoustic spectroscopy for multi-gas detection: A review', en, Analytica Chimica Acta, 338894 (2021).

[181] A. Kosterev, Y. Bakhirkin, F. Tittel, S. McWhorter and B. Ashcraft, 'QEPAS methane sensor performance for humidified gases', en, Applied Physics B **92**, 103–109 (2008).

[182] M. Zatorska and M. Nikodem, 'Ppb-Level Detection of Methane Using Quartz Enhanced Photoacoustic Spectroscopy (QEPAS) Combined with Bismuth-Doped Fiber Amplifier', in 2023 Conference on Lasers and Electro-Optics Europe & European Quantum Electronics Conference (CLEO/Europe-EQEC), ISSN: 2833-1052 (June 2023), pp. 1–1.

APPENDIX A

Electronic Designs and Schematics

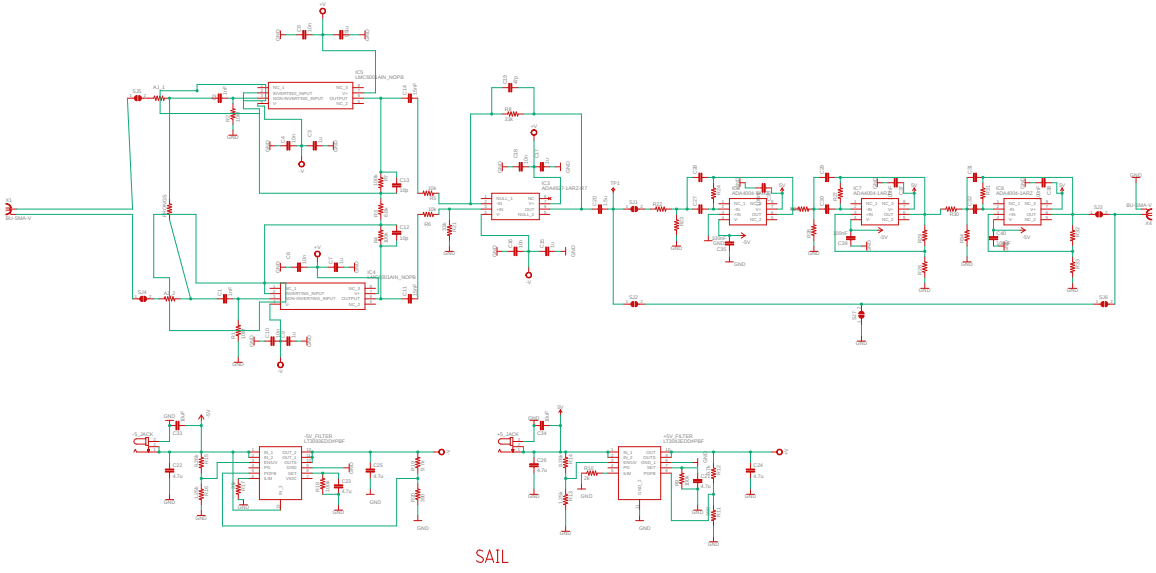

FIGURE A.1: Detailed schematic of the lower frequency board.

ADM Frame

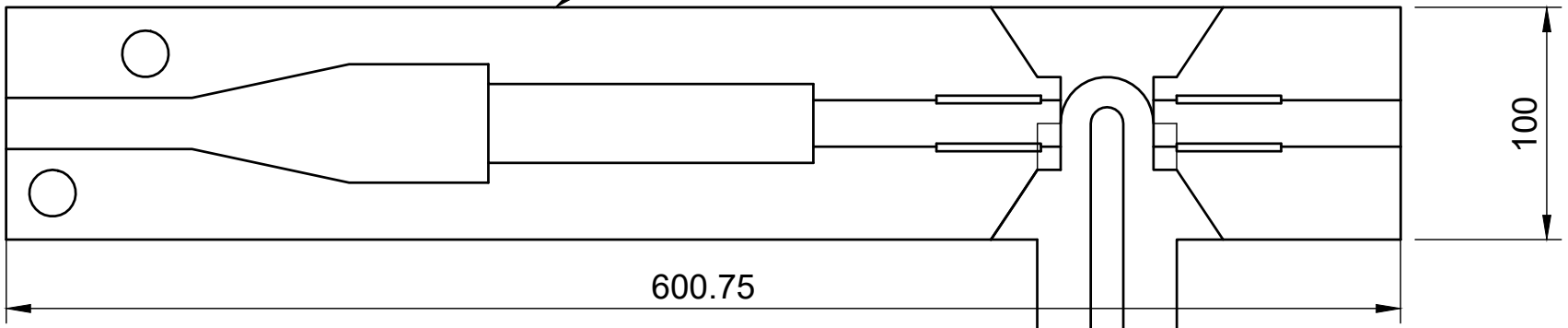

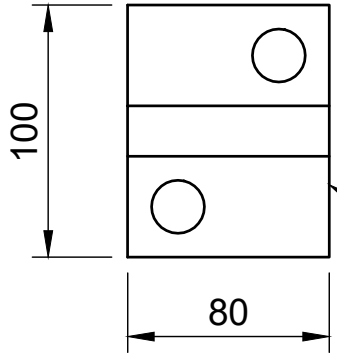

Sealing Cap

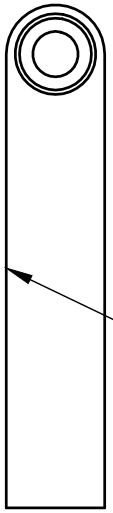

QTF Holder

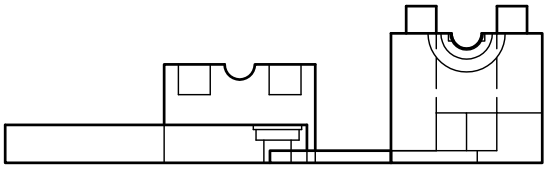

Created by Matthew Rahme Document type Scale Drawing	Top Scale 1:3 Side Scale 1:5
Title Inner_chamber V2	DWG No. 1
	Sheet 1/1

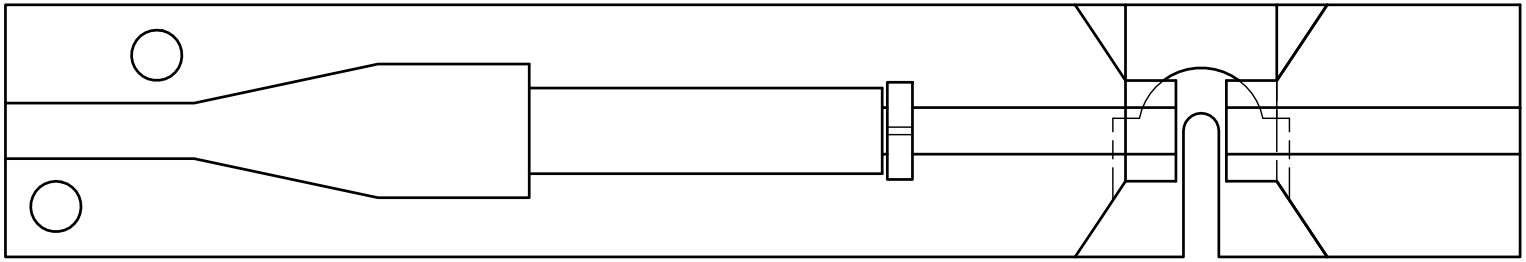

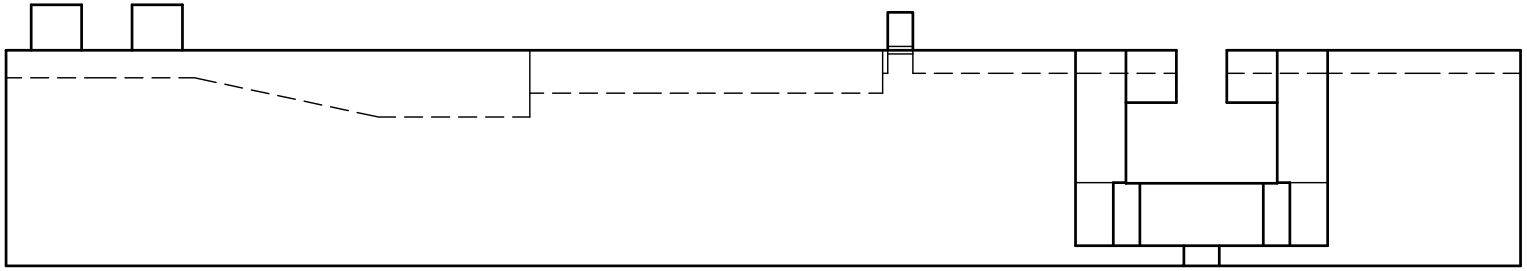

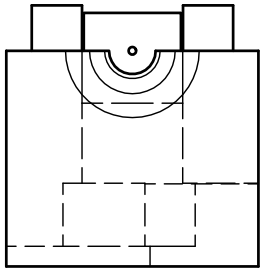

Created by Matthew Rahme	Scale 1:3
Title Aperture	DWG No. 1.1
	Sheet 1/1

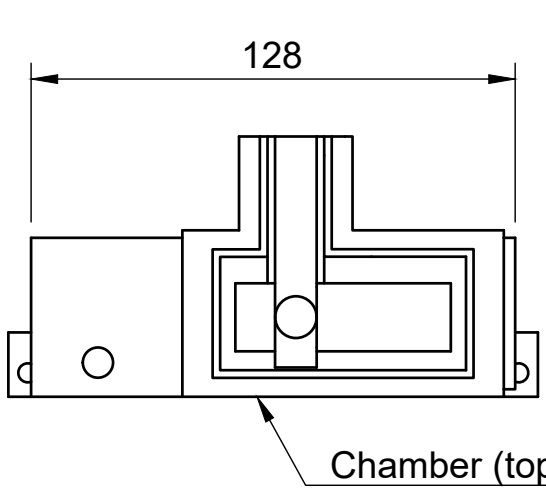

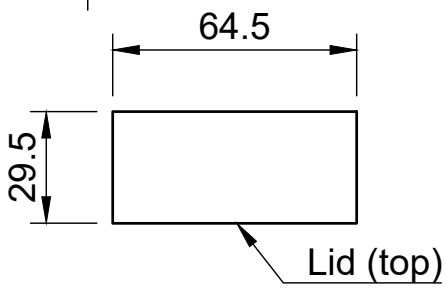

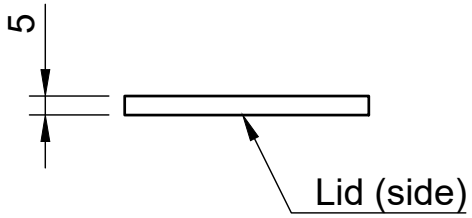

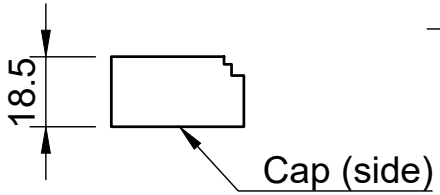

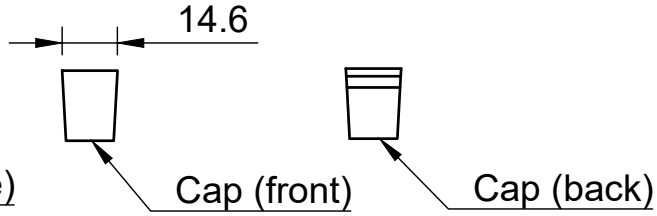

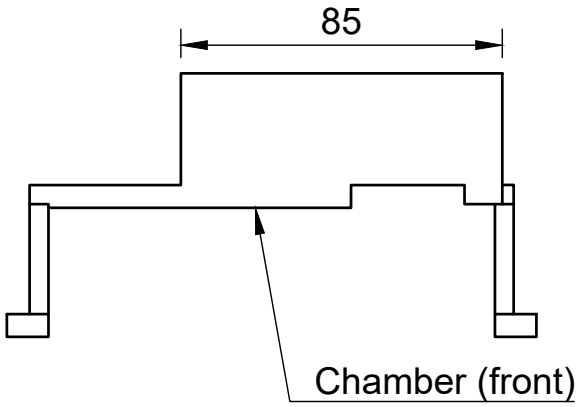

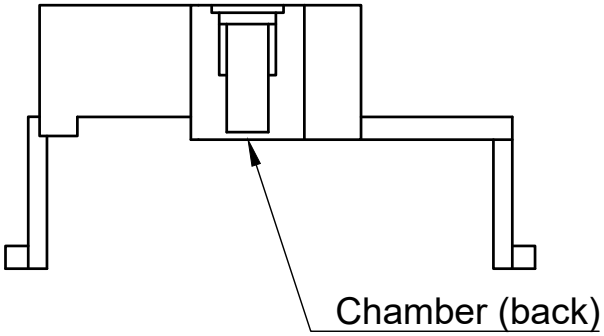

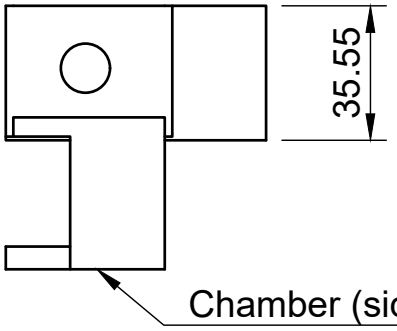

Created by Matthew Rahme	Scale 2:1
Title Gas Chamber	DWG No. 3
	Sheet 1/1

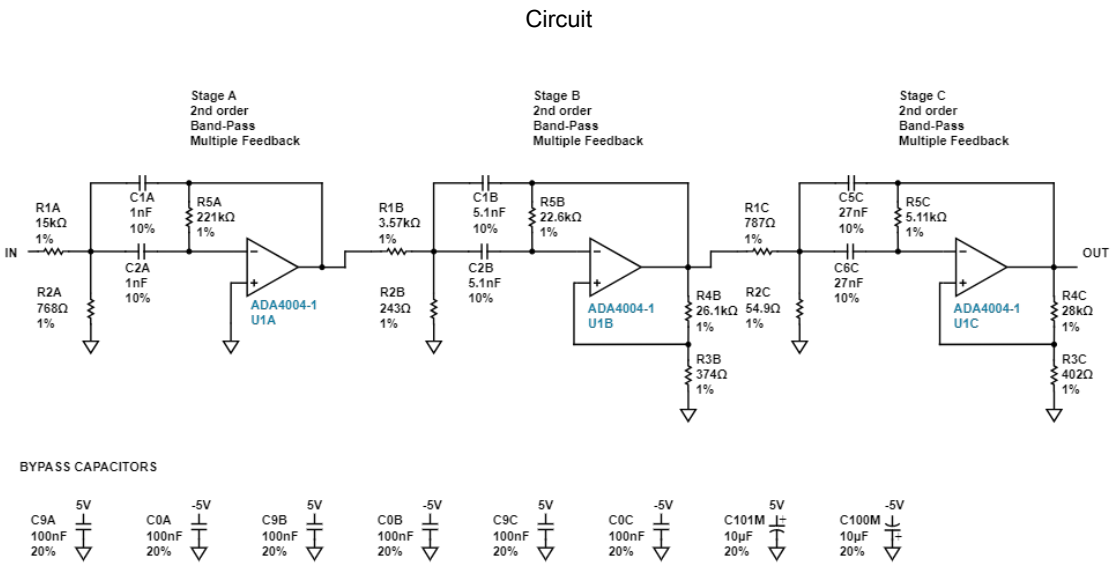

FIGURE A.2: Detailed schematic with the parts for the lower frequency Gain-bock filter centred at 12.5 kHz.

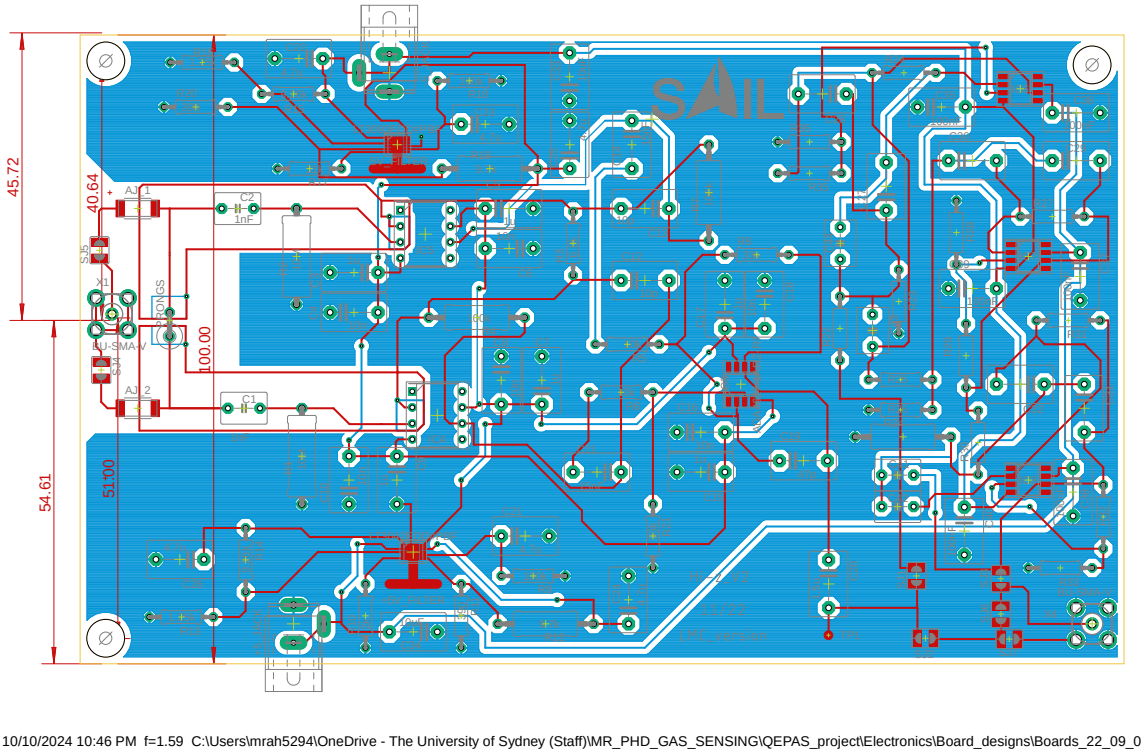

FIGURE A.3: Design of the lower frequency PCB

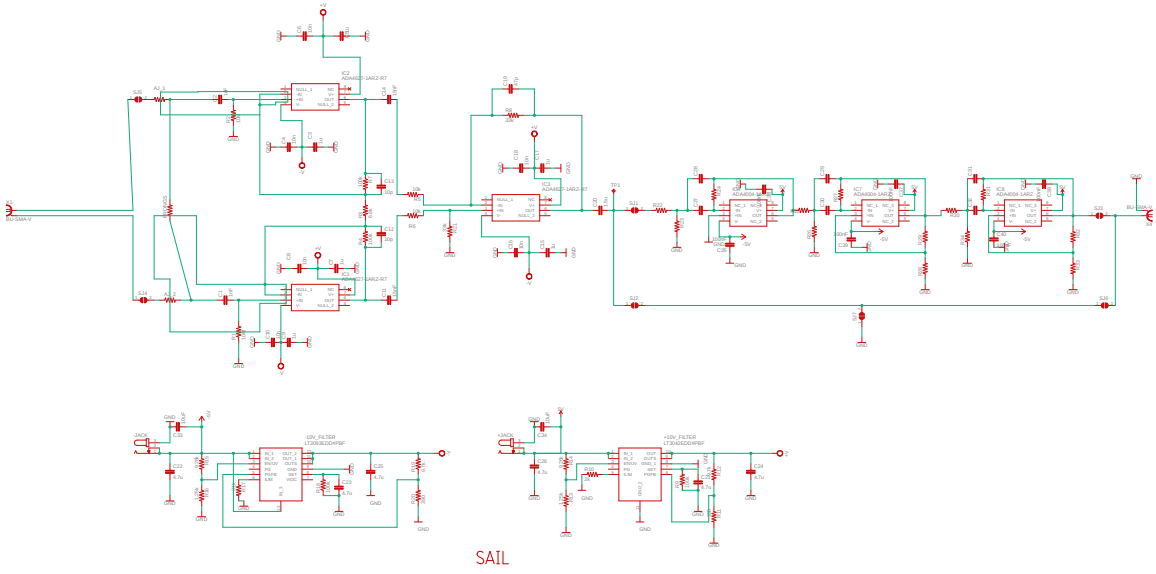

FIGURE A.4: Detailed schematic of the higher frequency board.

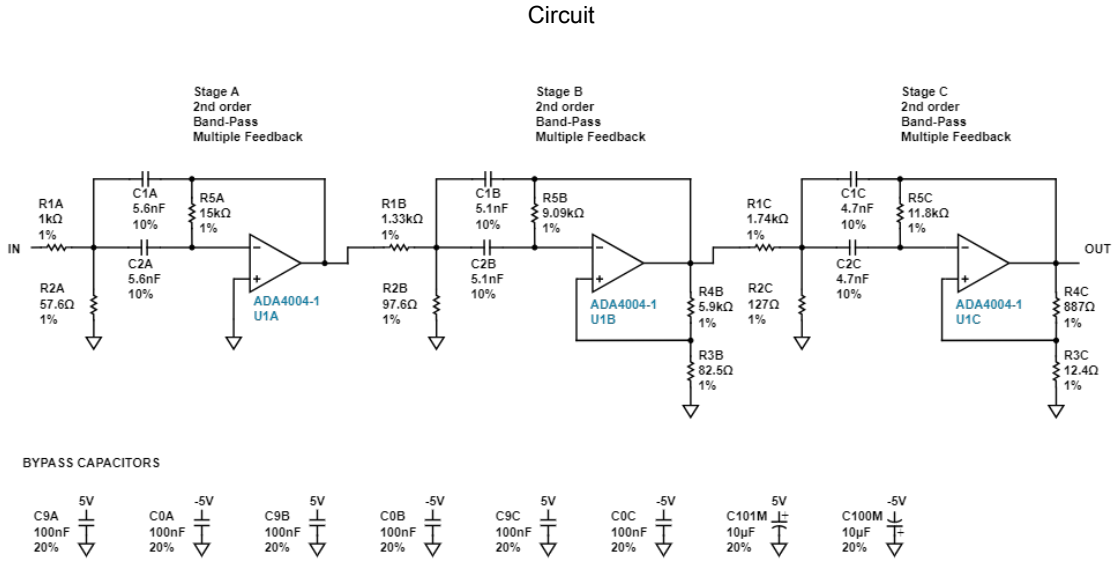

FIGURE A.5: Detailed schematic with the parts for the higher frequency Gain-bock filter centred at 31 kHz.

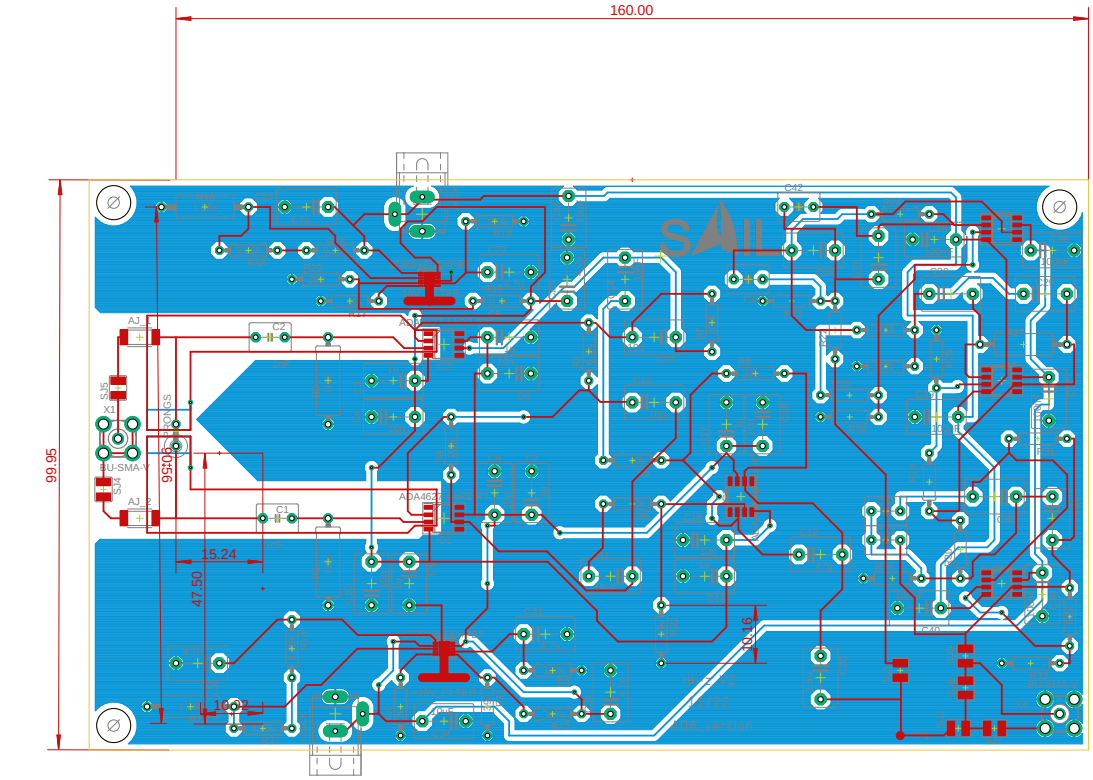

FIGURE A.6: Design of the higher frequency PCB

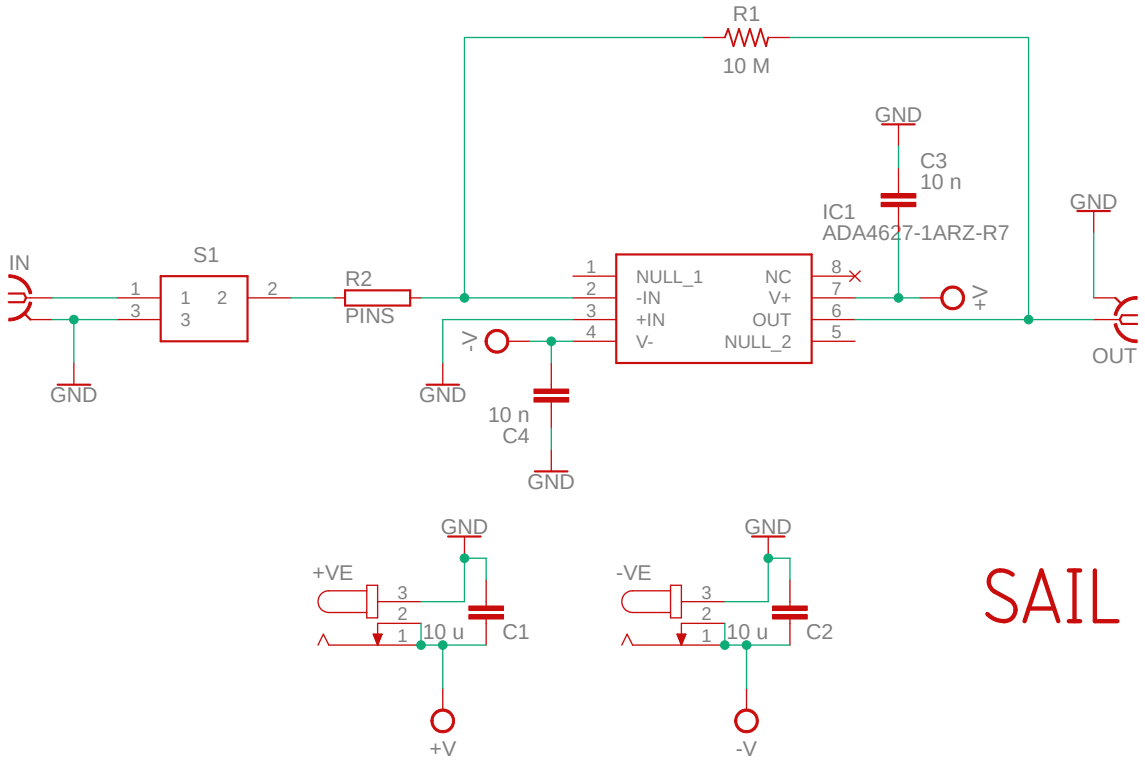

FIGURE A.7: Detailed schematic of the TA control board.

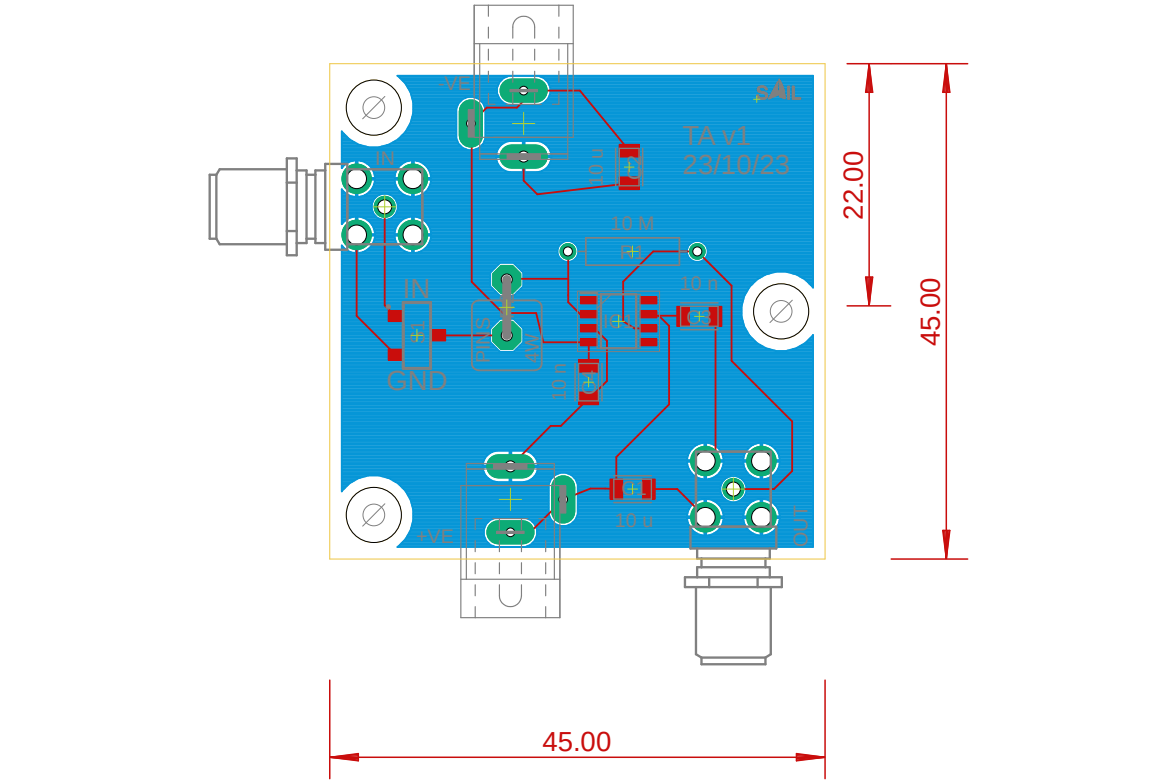

FIGURE A.8: CAD design of the TA PCB

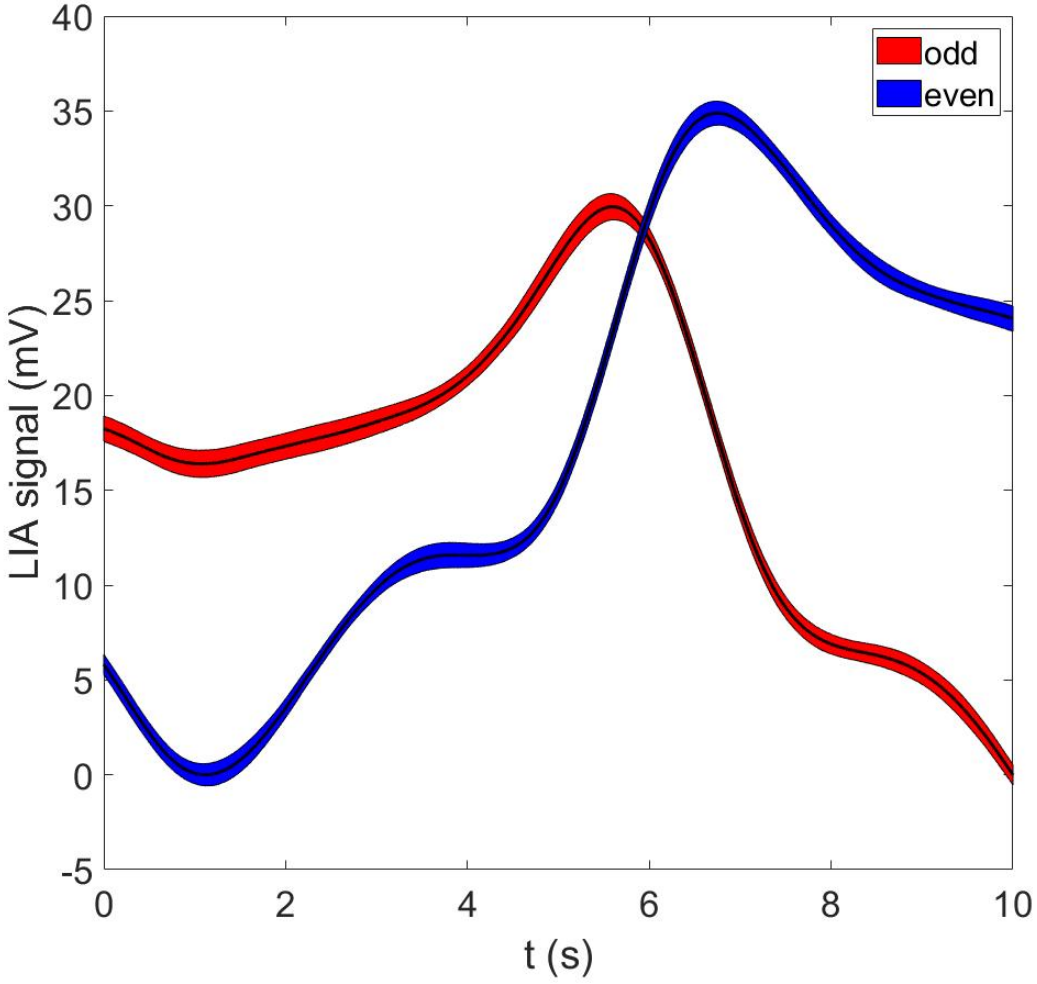

FIGURE A.9: Example showing the asymmetry for the different sweep direction of the laser

APPENDIX B

Improved Schematics and Further Scanned Results

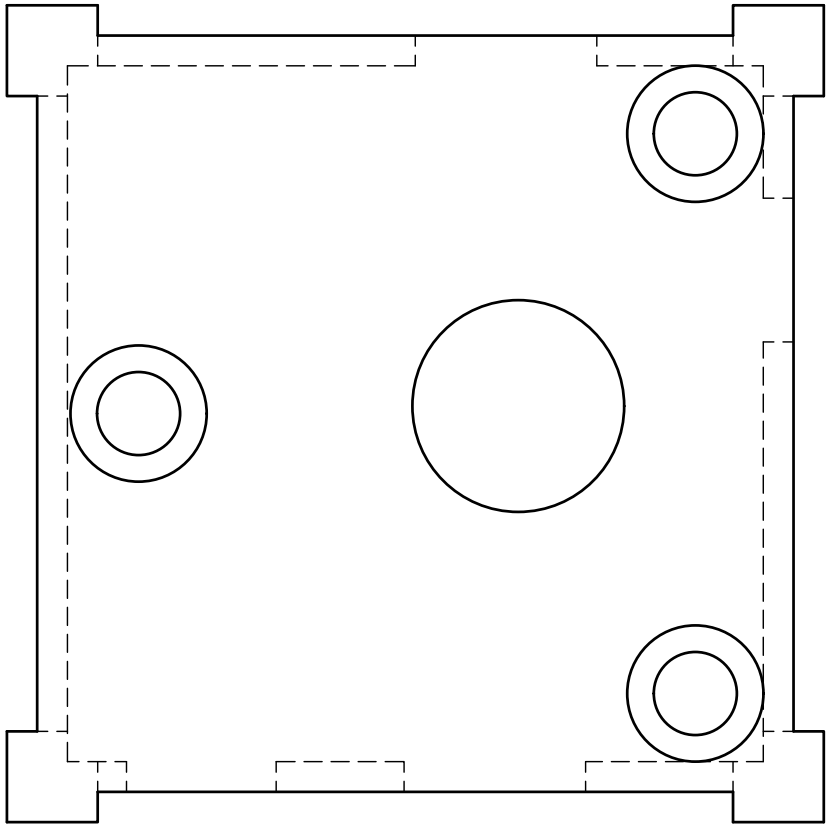

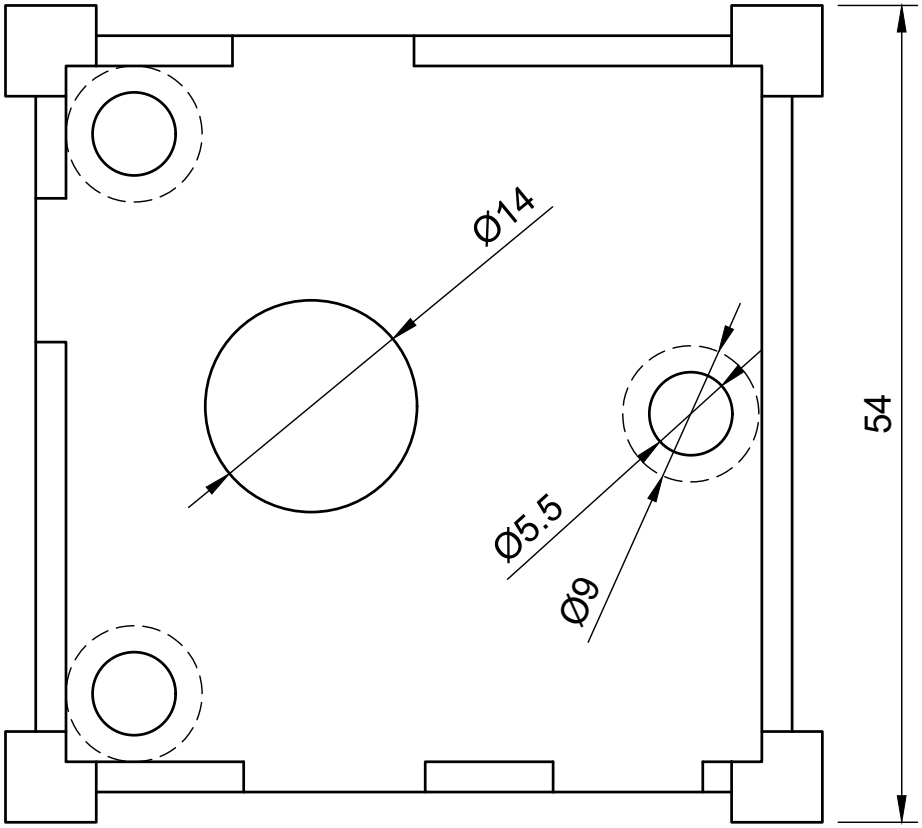

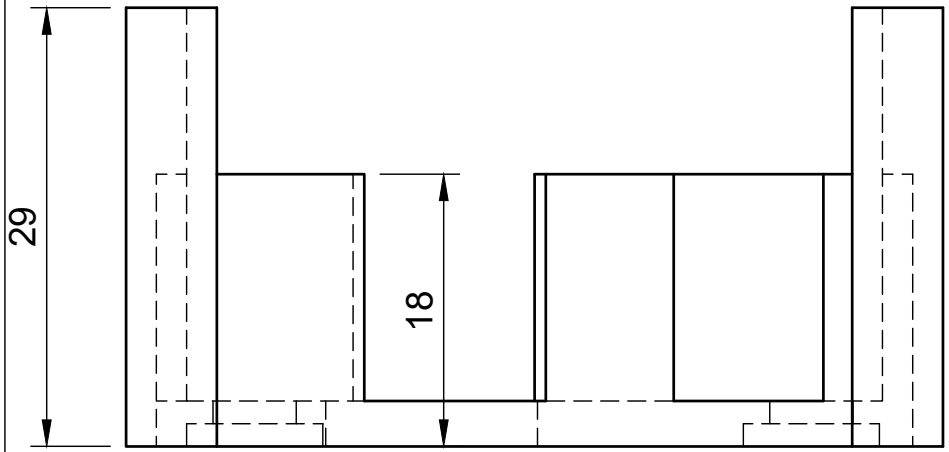

Created by	Scale
Matthew Rahme	2:1
Title	**DWG No.**
TA_holder	4

Sheet 1/1

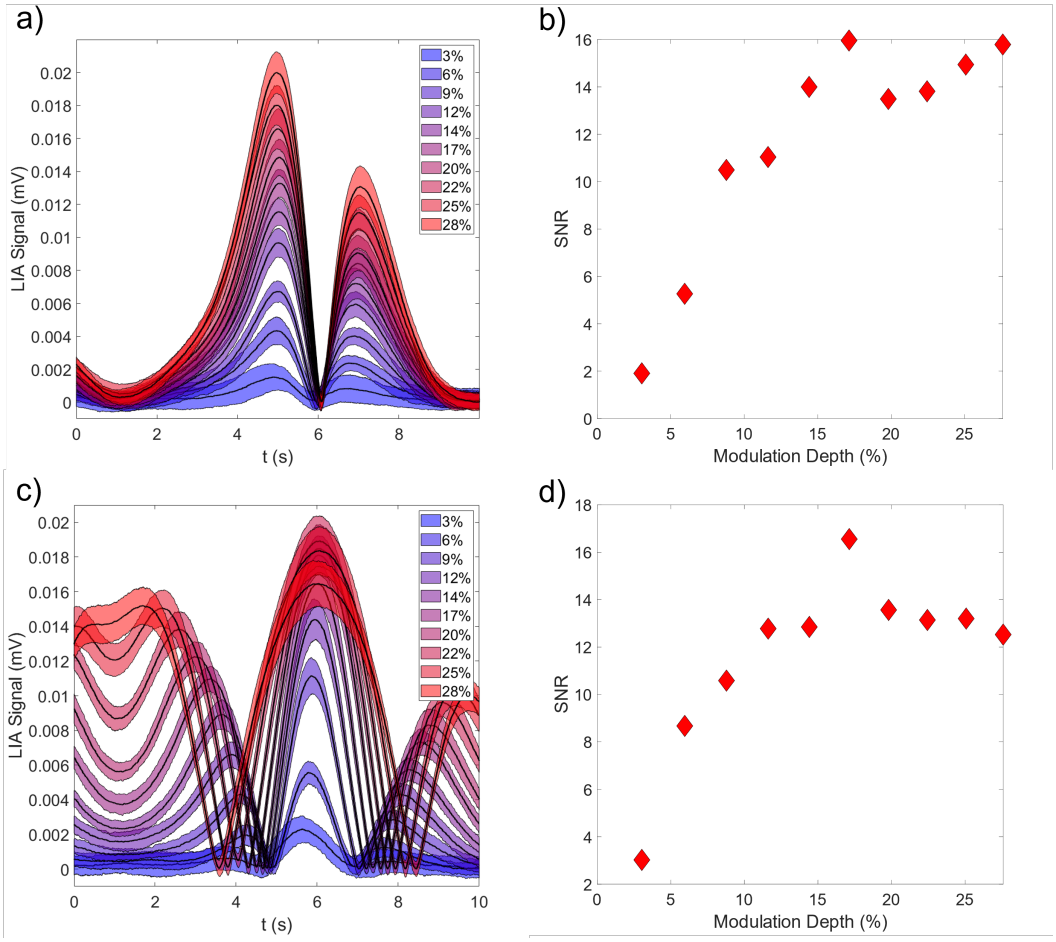

FIGURE B.1: Modulation depth testing for the new QEPAS chamber, coupled with the TA control board. a) 1f-QEPAS results for increasing modulation depths, at a methane concentration of 500 ppm. b) Corresponding SNRs for the modulation depth increases. c) 2f-QEPAS modulation depth testing for a methane concentration of 500 ppm, along with d) the corresponding SNRs.

TABLE B.1: Results summary for the first round of experiments performed with the new chamber. Data here is a summary of 1f and 2f-QEPAS measurements for a methane concentration of $500 ppm$.

Amplifier	**1f-Raw sig (mV)**	**1f-SNR**	**1f-MDL (ppm)**	**2f-Raw sig (mV)**	**2f-SNR**	**2f-MDL (ppm)**
TA	0.018	8.10	61.7	0.013	8.31	60.2
VA	1.32	13.6	36.9	0.70	13.1	38.07
VA with GB	73.5	24.8	20.2	52.0	14.9	33.7

TABLE B.2: Results summary for the first round of experiments performed with the new chamber. Data here is a summary of 1f and 2f-QEPAS measurements for a methane concentration of $500ppm$, after a drift correction has been applied.

Amplifier	**1f-Raw sig (mV)**	**1f-SNR**	**1f-MDL (ppm)**	**2f-Raw sig (mV)**	**2f-SNR**	**2f-MDL (ppm)**
TA	0.22	13.2	37.8	0.013	18.3	27.3
VA	1.47	47.1	10.6	0.771	36.7	13.6
VA with GB	77.0	45.7	11.0	55.4	31.9	15.75

TABLE B.3: Results summary for the second round of experiments performed with the new chamber. Data here is a summary of 1f and 2f-QEPAS measurements for a methane concentration of $500ppm$.

Amplifier	**1f-Raw sig (mV)**	**1f-SNR**	**1f-MDL (ppm)**	**2f-Raw sig (mV)**	**2f-SNR**	**2f-MDL (ppm)**
TA	0.013	27.54	18.15	0.017	23.78	21.03
VA	0.4	30.07	16.63	1.2	42.78	11.69
VA with GB	34.12	35.14	14.23	63.19	33.00	21.03

TABLE B.4: Results summary for the second round of experiments performed with the new chamber. Data here is a summary of 1f and 2f-QEPAS measurements for a methane concentration of $500ppm$, after a baseline drift correction has been applied.

Amplifier	**1f-Raw sig (mV)**	**1f-SNR**	**1f-MDL (ppm)**	**2f-Raw sig (mV)**	**2f-SNR**	**2f-MDL (ppm)**
TA	0.013	27.08	18.5	0.017	26.6	18.8
VA	0.42	45.6	11.0	1.19	62.3	8.03
VA with GB	35.6	50.3	9.93	65.1	77.7	6.43

TABLE B.5: Results summary for the second round of experiments performed with the new chamber, however, the SNR has been calculated using the variation of the interline region and not the variation of the signal peak. Data here is a summary of 1f and 2f-QEPAS measurements for a methane concentration of $500ppm$.

Amplifier	**1f-Raw sig (mV)**	**1f-SNR**	**1f-MDL (ppm)**	**2f-Raw sig (mV)**	**2f-SNR**	**2f-MDL (ppm)**
TA	0.013	34.6	14.5	0.017	27.7	18.0
VA	0.40	46.6	10.7	1.2	63.0	7.94
VA with GB	34.12	35.14	14.23	63.19	42.1	11.9

TABLE B.6: Results summary for the second round of QEPAS testing. Data here is a summary of 1f and 2f-QEPAS measurements for a methane concentration of 50 ppm.

Amplifier	**1f-Raw sig (μV)**	**1f-SNR**	**1f-MDL (ppm)**	**2f-Raw sig (mV)**	**2f-SNR**	**2f-MD (ppm)**
TA	1.49	1.08	46.4	1.50	1.81	27.6
VA	50.2	4.33	11.5	96.8	8.01	6.24
VA with GB	$5.00x10^3$	3.75	13.3	$6.59x10^3$	4.69	10.67

TABLE B.7: Results summary for the second round of QEPAS testing. Data here is a summary of 1f and 2f-QEPAS measurements for a methane concentration of 50 ppm, after a drift correction had been applied.

Amplifier	**1f-Raw sig (μV)**	**1f-SNR**	**1f-MDL (ppm)**	**2f-Raw sig (mV)**	**2f-SNR**	**2f-MDL (ppm)**
TA	1.94	1.34	37.4	1.45	1.91	26.2
VA	52.8	4.94	10.1	103	6.51	7.68
VA with GB	$5.12x10^3$	4.85	10.3	$5.79x10^3$	5.80	9.43

TABLE B.8: Results summary for the slower ramp sweep ($25\ mHz$). Data here is a summary of the 2f-QEPAS measurements for a methane concentration of $500ppm$. LF here refers to the pre-amplifier on the board designed to operate at lower frequencies.

Amplifier	**2f-Raw sig (mV)**	**2f-SNR**	**2f-MDL (ppm)**
TA	0.019	31.8	15.7
VA	1.16	51.8	9.65
VA with GB	64.57	64.4	7.76
LF	0.677	48.7	10.3